INVESTIGATING THE EARLY MOLECULAR EVENTS FOLLOWING EXPOSURE OF LUNG CELLS TO NANOPARTICLES USING ADVANCED OPTICAL MICROSCOPIES

Hana Kokot

Doctoral Dissertation
Jožef Stefan International Postgraduate School
Ljubljana, Slovenia

Supervisor: Prof. Dr. Janez Štrancar, Jožef Stefan International Postgraduate School, Ljubljana, Slovenia, and Jožef Stefan Institute, Ljubljana, Slovenia

Evaluation Board:
Prof. Dr. Igor Križaj, Chair, Jožef Stefan International Postgraduate School, Ljubljana, Slovenia and Jožef Stefan Institute, Ljubljana, Slovenia
Prof. Vladimir Lobaskin, Member, University College of Dublin, Dublin, Ireland
Acad. Prof. Dr. Robert Zorec, Member, Faculty of Medicine, University of Ljubljana, Ljubljana, Slovenia

MEDNARODNA PODIPLOMSKA ŠOLA JOŽEFA STEFANA
JOŽEF STEFAN INTERNATIONAL POSTGRADUATE SCHOOL

Hana Kokot

INVESTIGATING THE EARLY MOLECULAR EVENTS FOLLOWING EXPOSURE OF LUNG CELLS TO NANOPARTICLES USING ADVANCED OPTICAL MICROSCOPIES

Doctoral Dissertation

PROUČEVANJE ZGODNJIH MOLEKULARNIH DOGODKOV PO IZPOSTAVITVI PLJUČNIH CELIC NANODELCEM S POMOČJO NAPREDNIH OPTIČNIH MIKROSKOPIJ

Doktorska disertacija

Supervisor: Prof. Dr. Janez Štrancar

Ljubljana, Slovenia, September 2022

Acknowledgments

I am thankful for the funding received by the Slovenian Research Agency Young Researcher Program (PR-08331) and the EU Horizon 2020 SmartNanoTox Project (Grant No. 686098). Thank you also to the members of the Evaluation board of this dissertation and the committee members of my Seminars for their valuable comments and suggestions.

A big thank you goes to my supervisor Janez Štrancar – not only for his scientific and financial support, but also for all the inspiration and amazing discussions, and for encouraging us to ask "stupid" questions, nurture our curiosity, to grow and to persevere.

I am grateful to the scientists who courteously permitted me to enrich the discussions in this work with their micrographs. This data proved to be indispensable for deeper understanding of the system and confirming the mechanisms of nanoparticle toxicity. I would like to thank

- Pernille Høgh Danielsen, Kristina Bram Knudsen, and Ulla Vogel (National Research Centre for the Working Environment, Copenhagen, Denmark) for their ex vivo alveolar micrographs,
- Carola Endes and David Kutschke (Institute of Lung Biology and Disease, Helmholtz Zentrum München, Neuherberg, Germany) for their ex vivo BAL micrographs,
- Carolina Ballester Lopez, Martin Irmler, Johannes Beckers, and Tobias Stoeger (Institute of Lung Biology and Disease and Institute of Experimental Genetics, Helmholtz Zentrum München, Neuherberg, Germany) for their transcriptomics data,
- and my lab members: Patrycja Zawilska for her micrographs of inhibited endocytosis, Aleksandar Sebastijanović for his micrographs of neurons, exocytotic vesicles and position data of macrophage movement in co-culture, and Mojca Pušnik and Tilen Koklič for their micrographs of the mitochondrial (de)fragmentation.

Also, thank you Polona Umek, Ulla Vogel and the Joint Research Centre for the nanoparticles used in this study, and Stane Pajk for his flurescent probe SAG-38.

I would like to thank my lab-mates from the Laboratory of Biophysics (LBF) for their assistance and support with these experiments: Boštjan Kokot with live nebulization of nanoparticles and the dose dependence experiments; Ana Krišelj, Boštjan Kokot, Aleksandar Sebastijanović, and Petra Čotar with measurements of the cauliflower-forming potential and toxicity of various nanoparticles; Aleksandar Sebastijanović, Ana Krišelj, Ana Jandrlić, Tilen Koklič and Janez Štrancar with the ELISA experiment; Rok Podlipec, Iztok Urbančič and Janez Štrancar with the implementation of reflectance microscopy on our fluorescence microscope; and my master's student Tanja Vajs who quantified cauliflower growth. Also, thanks to Ana, Maja, Patrycja, Boštjan, Aleks, Katarina, Neža,

Petra, and Monika for relieving me of many of the lab-management-related duties during these years.

I am thankful for being a part of two amazing groups: thank you to all the current and former members of our Laboratory of Biophysics and the SmartNanoTox project for your positive critical comments, stimulating discussions, and all the unforgettable moments and memories we acquired over the years.

Thanks also to Janja Mirtič, Barbara Sterle Zorec, Julijana Kristl, and Tilen Knaflič, for their support and for showing me alternative approaches to situations.

Thanks to all of my other teachers and mentors – both official and unofficial – who knowingly or unknowingly helped me on my journey.

Thanks to my family, in-laws and friends for all they have taught me, for celebrating the good times and lending an ear or a helping hand when needed.

Thank you, Boštjan, for walking by my side; it would not have been half as amazing without you.

Abstract

The potential toxicity of nanoparticles in our environment and consumer products is currently determined by costly and timely animal-based testing, which limits the rate of nanoparticle testing, causing a desperate need for alternative testing strategies. A promising alternative – mechanism-based prediction – employs a set of high-throughput cell-based tests that target the key events connecting nanoparticle exposure to the adverse outcomes. However, this approach requires understanding of the molecular mechanisms of nanoparticle toxicity, which is sadly still lacking.

To alleviate this knowledge gap and devise targeted in vitro tests for mechanism-based toxicity prediction, we discerned the early molecular events caused by exposure of alveolar cells to TiO_2 nanotubes – a model nanoparticle that interacts strongly with biomolecules and causes long-lasting lung inflammation in mice. We investigated the relations between these events in epithelial and macrophage cell lines by live-cell fluorescence microscopy – including 3D- and time-acquisition, lifetime imaging and super-resolution STED microscopy – and tracked the nanoparticles by fluorescent labelling and reflectance microscopy. We further confirmed our findings by transcriptomics and in vivo experiments performed using the same nanotubes.

Importantly, we discovered nanoquarantine: a novel cell-defense mechanism in which lung epithelial cells excrete and quarantine nanoparticles on their surface, forming large bio-nano composites termed cauliflowers and effectively lowering the nanoparticle dose. We also observed it with other nanoparticles (e.g. crystalline silica DQ12, TiO_2 rutile NM-105, but not TiO_2 anatase NM-101 or carbonaceous nanoparticles) and other cell lines (neurons, but not alveolar macrophages). The other key events in chronic inflammation are immune cell death (re-exposing other cells to the nanoparticles) and pro-inflammatory signaling (causing the influx of fresh immune cells). The combination of these processes leads to continuous cycling of nanoparticles between the alveolar cells, causing continuous pro-inflammatory signaling, observed as chronic inflammation.

Further, we described the cell response by a theoretical model which can mimic the inflammatory outcomes by modifying only the three nanoparticle-specific rates of the key events. To determine them, we devised three simple and quick in vitro assays, the results of which can be combined with the theoretical model to predict the inflammatory potential of nanoparticles.

As shown in this dissertation, microscopy-based real-time tracking of cellular events coupled with complementary approaches improves our understanding of nanotoxicity mechanisms, providing the much-needed boost for mechanism-based prediction of nanosafety, a time- and cost-efficient animal-free alternative for toxicity testing.

Povzetek

Vsakodnevno smo izpostavljeni velikim količinam raznovrstnih nanodelcev, od katerih lahko nekateri resno ogrožajo naše zdravje – izpostavljenost nanodelcem namreč močno prispeva k razvoju pljučnih, srčno-žilnih, in nevrodegenerativnih obolenj. Po nekaterih ocenah izpostavljenost nanodelcem že sedaj skrajša naše življenje za nekaj let, problem pa postaja čedalje bolj pereč zaradi povečane proizvodnje in uporabe novih nanodelcev, ter nastajanja nanodelcev pri uporabi in razgradnji večine materialov.

Precejšen delež škodljivih učinkov nanodelcev lahko pripišemo njihovim majhnim dimenzijam (vsaj ena njihova dimenzija je manjša od 100 nm) in, posledično, ogromni specifični površini, tj. razmerju med površino in maso. Za razliko od večjih delcev lahko nanodelci prečkajo biološke bariere (koža, črevesna stena in pljučni mešički – alveoli) ter preidejo v limfo in kri, od koder se razširijo po celotnem telesu. Največ nanodelcev pride v naše telo skozi pljučne mešičke, saj so ti močno izpostavljeni nanodelcem, imajo veliko površino, razdalja med zrakom in krvjo je v njih zelo majhna, odstranjevanje delcev iz pljučnih mešičkov pa je izredno počasno. V pljučnih mešičkih nanodelci najprej interagirajo s pljučnim surfaktantom – mešanico lipidov in proteinov – nato pa pridejo v stik z izjemno tankimi alveolarnimi epitelijskimi celicami ter alveolarnimi makrofagi (imunskimi celicami pljučnih mešičkov). Ker je večina nanodelcev anorganskega izvora, jih makrofagi ne zmorejo razgraditi, kot to uspešno počnejo s virusi in bakterijami. Večina nanodelcev se zato dolgo časa zadržuje v alveolu, nekaj pa jih preide skozi sloj epitelija v limfo, ter potencialno skozi žilni endotelij v kri.

Trenutno se za določanje možnih zdravju škodljivih lastnosti nanodelcev uporabljajo draga in dolgotrajna testiranja na živalih. Ker na potencialno toksičnost nanodelca vpliva kompleksna kombinacija njegovih lastnosti, je potrebno testirati vsak material posebej, to pa posledično močno omejuje količino testiranih nanodelcev v obtoku. Obetavno alternativo ponuja napovedna toksikologija, ki s pomočjo cenejših in hitrejših visokozmogljivih celičnih testov (t. i. in vitro testov) ciljno preverja zgodnje ključne dogodke, za katere je znano, da vodijo do škodljivih zdravstvenih izidov. Žal ta pristop temelji na poznavanju in razumevanju molekularnih mehanizmov toksičnosti nanodelcev, ki pa je trenutno še vedno zelo pomanjkljivo. Poleg kompleksnosti bioloških sistemov otežuje razvoj razumevanja mehanizmov toksičnosti tudi dejstvo, da je izredno težko primerjati rezultate različnih študij. Že majhne razlike med nanodelci lahko namreč privedejo do popolnoma različnih zdravstvenih izidov. Posledično je potrebno celotno študijo toksičnosti opraviti z isto serijo nanodelcev – od opazovanja zgodnjih dogodkov na mikroskopskih skalah nekaj minut/ur po izpostavitvi, vse do vidnih simptomov na ravni tkiv in organizma nekaj mesecev po izpostavitvi nanodelcem.

Da bi ublažili omenjeno vrzel v znanju o molekularnih mehanizmih toksičnosti in posledično razvili in vitro teste za napovedovanje zdravju škodljivih učinkov vdihnjenih nanodelcev na podlagi poznanih mehanizmov, smo se posvetili odkrivanju in razumevanju zgodnjih molekularnih dogodkov, ki jih povzroči izpostavljenost alveolarnih celic nanocevkam TiO_2. Te nanodelce smo izbrali kot modelne nanodelce, ker so predstavniki

skupine široko uporabljenih nanodelcev – titan dioksidnih nanodelcev. Poleg tega omenjene nanocevke močno interagirajo z biološkimi molekulami, zato lahko povzročijo puščanje modelnih lipidnih mehurčkov, razpad celične membrane in celično smrt pri nekaterih celicah, pri miših pa že enkratna izpostavljenost tem nanocevkam povzroči močno nekajmesečno vnetje pljuč.

Pri svojih raziskavah smo uporabljali celični liniji pljučnih epitelijskih celic LA-4 in alveolarnih makrofagov MH-S, katerim smo s fluorescenčnimi sondami označili določene strukture in organele, ter nato opazovali žive celice s konfokalno fluorescenčno mikroskopijo s prostorskim in časovnim zajemom slike. Svoje ugotovitve smo potrdili s transkriptomiko ter in vivo rezultati (histološkimi rezinami alveolov in bronhoalveolarnimi izpirki miši), pri čemer so bili vsi poskusi opravljeni z isto serijo nanodelcev, zato so medsebojno primerljivi.

Ključen prispevek k razumevanju dogajanja v celicah po izpostavitvi nanodelcem je bil razvoj metodologije za spremljanje položaja in porazdelitve nanodelcev v živih celicah s fluorescenčno mikroskopijo. Za nanocevke TiO_2 smo namreč razvili postopek za stabilno, preverljivo in ponovljivo fluorescenčno označevanje nanodelcev s komercialno dostopnimi fluorescenčnimi sondami. Ker smo nanocevke označili s fotostabilnimi sondami z ustreznim emisijskim spektrom, smo lahko poleg tega s superločljivostno STED mikroskopijo določili njihovo lego v strukturah na 50 nm natančno – torej z nekajkrat boljšo ločljivostjo od konfokalne mikroskopije, pri kateri bi bila ločljivost zaradi uklonske limite omejena na približno 300 nm. Za določevanje gostote agregacije nanocevk v vzorcu smo izkoristili dejstvo, da na življenjski čas fluorescence uporabljenih sond vpliva gostota agregatov, kar smo merili z mikroskopijo življenjskega časa fluorescence (FLIM).

Da bi preverili, ali so mehanizmi škodljivosti nanodelcev, katere smo odkrili s fluorescenčno označenimi nanocevkami TiO_2, značilni tudi za druge nanodelce, smo le-tem sledili v živih celicah prek detekcije svetlobe, ki se sipa na nanodelcih – torej z uporabo t. i. odbojne mikroskopije. Ker tovrstna detekcija temelji na intrinzični lastnosti urejenih struktur, da sipajo svetlobo, smo lahko z njo sledili katerimkoli nanodelcem brez predhodnega označevanja s fluorescenčnimi sondami.

Ključen rezultat zgoraj opisanega časovnega in prostorskega sledenja nanodelcem v živih celicah je odkritje nanokarantene – novo-opisanega procesa, pri katerem celice pljučnega epitelija izločajo internalizirane nanodelce na svojo površino ter jih pri tem obdajo z lipidi in drugimi biološkimi molekulami. Tako s časom zrastejo veliki bionano-kompoziti na površini epitelijskih celic, ki jih lahko opazimo tudi in vivo v mišjih pljučnih mešičkih. Opažene kompozite smo zaradi njihove značilne oblike, strukture in barve na fluorescenčnih slikah poimenovali »cvetače«. Ker se nanodelci v teh strukturah ne morejo premikati, se s procesom nanokarantene učinkovito zniža aktivna doza (tj. količina nanodelcev v sistemu, ki lahko prosto interagirajo z biološkimi molekulami), kar posledično poveča verjetnost za preživetje celic. Nanokaranteno lahko torej vidimo kot enega od mehanizmov celične obrambe. Pojav nanokarantene smo opazili pri večih vrstah nanodelcev (npr. nanocevkah TiO_2, kristaliničnem silicijevem dioksidu DQ12, rutilu TiO_2 NM-105, ne pa pri anatazi TiO_2 NM-101 ali ogljikovih nanocevkah) in celičnih linijah (pri pljučnih epitelijskih celicah LA-4 in nevronih SH-SY5Y, ne pa pri makrofagih MH-S).

Drugi ključen dogodek za razvoj kroničnega vnetja v alveolu je smrt imunskih celic. Opazili smo, da makrofagi internalizirajo tako proste nanodelce kot tudi nanodelce, katerega so pljučne epitelijske celice že imobilizirale v cvetačah na svoji površini. Makrofagi po internalizaciji razgradijo biološke molekule okoli nanodelcev (t. i. korono), zaradi česar sami sebe izpostavijo nativni površini nanodelca, katera pogosto močno interagira z biološkimi strukturami. Pri posledični smrti makrofaga (opaženi tudi v mišjih alveolih) se internalizirani nanodelci sprostijo v okolico, kjer lahko zopet interagirajo s preostalimi

celicami. Cikel kroženja nanodelcev med epitelijskimi in imunskimi celicami v alveolu je tako sklenjen.

Brez dotoka novih imunskih celic, ki bi nadomestile umrle makrofage, bi se zgoraj opisani cikel kroženja nanodelcev prej ali slej ustavil. V realnem primeru pa pro-vnetna signalizacija (ki je večinoma uravnavana s strani epitelijskih celic) povzroči dotok svežih imunskih celic v alveol, kar lahko privede do neprestanega kroženja nanodelcev med alveolarnimi celicami ter nepretrgane pro-vnetne signalizacije (kroničnega vnetja).

Zgoraj opisano novo-odkrito védenje o ključnih dogodkih v alveolu smo opisali s poenostavljenim teoretičnim modelom. Model vsebuje šest diferencialnih enačb prvega reda za šest spremenljivk (površina nanodelcev v epitelijskih celicah, v cvetačah, v makrofagih, prostih nanodelcev, ter površina epitelijskih in imunskih celic), poleg sedem fiksnih parametrov pa vsebuje tudi tri parametre, ki so specifični za vsako vrsto nanodelcev posebej: toksičnost tox, učinkovitost nanokarantene cff, in potencial za sprožitev pro-vnetne signalizacije ob nanokaranteni $signalEff$. S spreminjanjem le-teh v smiselnem območju vrednosti lahko model posnema različne vnetne izide, ki jih opazimo v živo: akutno (prehodno) vnetje, kronično (dolgotrajno) vnetje, in resne poškodbe epitelijskega tkiva. Fazni prostor teh treh parametrov lahko uporabimo za grafično ponazoritev njihovega vpliva na jakost in trajanje vnetja, ter posledično grafično razvrščanje nanodelcev.

Da bi lahko te tri parametre eksperimentalno določili s preprostimi in hitrimi in vitro testi za katerekoli izbrane nanodelce, smo omenjeni teoretični model poenostavili za opis obnašanja monokulture epitelijskih celic, monokulture makrofagov, ter njune kokulture. Iz teh modelov ter meritev nekajdnevnega obnašanja omenjenih treh celičnih sistemov lahko enostavno in hitro določimo ključne tri parametre izbranih nanodelcev, katere nato vključimo v teoretični model dogajanja in vivo, ter s tem računsko napovemo morebitni dolgotrajni vnetni potencial nanodelcev.

Kot je prikazano v tem delu, lahko sledenje celičnim dogodkom in nanodelcem v realnem času v živih celicah v kombinaciji s komplementarnimi pristopi izboljša naše razumevanje mehanizmov nanotoksičnosti, ter tako omogoča razvoj časovno in stroškovno učinkovitega napovedovanja varnosti nanodelcev na osnovi mehanizmov brez testiranja na živalih. Poleg tega pa prikazani rezultati brez dvoma poleg odgovorov na zastavljena vprašanja tudi odpirajo množico novih, razburljivih vprašanj za bodoče raziskave.

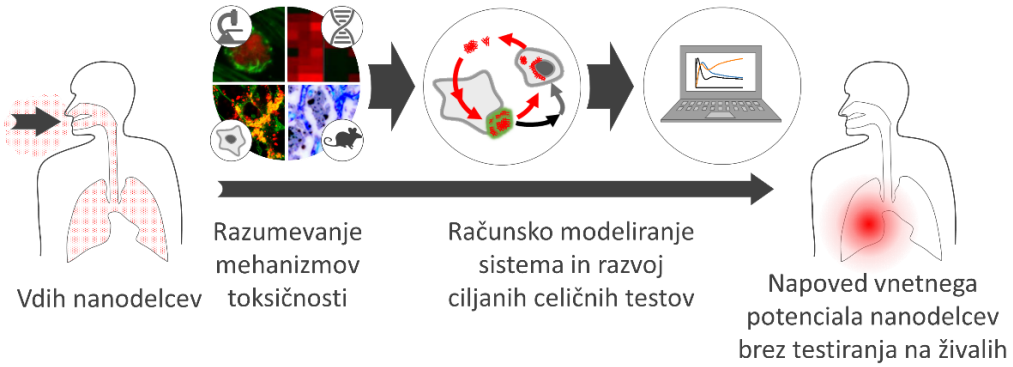

Slika: Z uporabo naprednih optičnih mikroskopij in komplementarnih eksperimentalnih tehnik smo razjasnili mehanizem, prek katerega nanodelci povzročajo kronično vnetje v alveolih. Na podlagi modeliranja tega novo-odkritega mehanizma smo razvili ciljane celične teste, s katerimi lahko napovemo vnetni potencial nanodelcev brez testiranja na živalih.

Contents

List of Figures **xvii**

List of Tables **xxi**

Abbreviations **xxiii**

Symbols **xxv**

1 Introduction **1**
1.1 Exposure to Nanoparticles Can Affect Human Health ... 1
1.1.1 Nanoparticles in our Bodies ... 1
1.2 Current Safety Testing Needs an Alternative ... 4
1.3 Mechanism-Based Testing of Nanoparticle Safety as an Alternative to Animal Testing ... 5
1.3.1 Current Issues Preventing Mechanism-Based Nanosafety Assessment ... 5
1.4 Investigating Toxicity Mechanisms Using TiO_2 Nanotubes ... 7
1.4.1 TiO_2 Nanotubes Cause Lipid Wrapping and Chronic Inflammation ... 7
1.5 Goals of the Dissertation ... 9

2 Methodology **13**
2.1 Microscopy ... 13
2.1.1 Microscopy of Living Cells ... 13
2.1.2 Fluorescence Microscopy ... 14
2.1.3 Confocal Fluorescence Microscopy ... 17
2.1.4 Stimulated Emission Depletion (STED) Microscopy ... 18
2.1.5 Fluorescence Lifetime Imaging Microscopy (FLIM) ... 20
2.2 Detection of Non-Fluorescent Nanoparticles ... 21
2.2.1 Reflectance Microscopy ... 22
2.2.2 Quality-Controlled Nanoparticle Labelling ... 25
2.3 In Vitro Model ... 27
2.4 Materials ... 28
2.4.1 Chemicals ... 28
2.4.2 Fluorophores and Stains: ... 28
2.4.3 Nanoparticles ... 28
2.4.4 Materials ... 29
2.4.5 Software ... 29
2.5 Methods ... 29
2.5.1 Preparation and Characterization of Nanoparticles ... 29
2.5.1.1 Synthesis and Labelling of TiO_2 Nanotubes ... 29
2.5.1.2 Nonlabelled Nanoparticles ... 29
2.5.1.3 Characterization of the Nanoparticles ... 30
2.5.2 Culturing of Cell Lines ... 30

2.5.3 Preparation of in Vitro Samples for Imaging and Cell Tests 30
2.5.4 In Vitro Imaging 31
2.5.4.1 Confocal Fluorescence Microscopy and STED Microscopy 31
2.5.4.2 FLIM 32
2.5.4.3 Imaging of Nanoparticles with Reflectance Microscopy 32
2.5.5 In Vitro Cell Tests 33
2.5.5.1 Measuring Cell Viability 33
2.5.5.2 Determining the Cauliflower-Forming Potential of Nanoparticles 34
2.5.5.3 Detecting Released Cytokines with ELISA 34
2.5.6 Model of Chronic Inflammation Following Nanoparticle Exposure 35
2.5.7 Analysis of In Vivo BAL Cell Numbers 35

3 Results and Discussion – Key Events in Nanoparticle-Exposed Alveolar Cells 37
3.1 Macrophages Die Trying to Defend the Epithelium from Nanoparticles 38
3.1.1 Macrophages Immediately Start to Internalize Nanoparticles 38
3.1.2 The Macrophages are Full of Nanoparticles Several Days After Exposure 40
3.1.3 Macrophages Die After Internalizing the Nanoparticles 41
3.1.4 Macrophages Do Not Manage to Internalize All Nanoparticles 45
3.1.5 Short Summary 47
3.2 Nanoquarantine – an Unexpected Cellular Defense Mechanism 47
3.2.1 Epithelial Cells Immediately Start to Internalize Nanoparticles 47
3.2.2 Surface-Bound Bio-Nano Structures (Cauliflowers) Grow on Epithelial Cells In Vitro and In Vivo 50
3.2.3 Cauliflowers Form by Exocytosis of Nanoparticles 54
3.2.4 Cauliflower Formation is Accompanied by Increased Lipid Synthesis 55
3.2.5 Nanoquarantine Is Also Observed with Other Nanoparticles and Cell Lines 57
3.2.6 Nanoquarantine – a Cell Defense Mechanism? 58
3.2.7 Short Summary 60
3.3 Inter-Cellular Nanoparticle Cycling Governs Chronic Inflammation 60
3.3.1 Dying Cells Re-Expose Other Cells by Releasing the Nanoparticles 61
3.3.2 Macrophages Degrade and Internalize Cauliflowers 62
3.3.3 Epithelial Cells Are the Major Modulator of Signaling for Immune Cell Influx 63
3.3.4 Short Summary 64
3.4 Combining it All Together – the Chronic Cycle of Inflammation 65

4 Results and Discussion – Development of the Predictive Model 67
4.1 Mathematical Equations Describe the Network of Events 67
4.2 The Model Can Replicate the Typical In Vivo Outcomes – Acute and Chronic Inflammation, and the "All Dead" Situation 71
4.3 Phase Space of the Three Nanoparticle-Dependent Parameters: the Nanoparticle Sorter Cube 73
4.4 Translating the Model to In Vitro Conditions 75
4.5 Determination of the Nanoparticle-Specific Model Parameters Using Targeted In Vitro Tests 78
4.5.1 Determination of the Toxicity Rate (***tox***) 79

4.5.2 Determination of the Quarantining Rate (Cauliflower Formation Rate, $\boldsymbol{cff}$) 82
4.5.3 Determination of Signaling Efficiency (*signalEff*) 84

5 Conclusions **89**
5.1 Prediction Model 90
5.2 Methodology 91
5.3 Open Questions 92
5.4 Final Remarks 93

Appendix A Supplementary Information **95**
A.1 Over-Sonicated TiO_2 Nanotubes Can Disrupt the Cell's Cytoskeleton 95
A.2 Nanoquarantine is Observed with Many Nanoparticles 95
A.3 ELISA 99
A.3.1 Selection of Nanoparticles for the ELISA Assay 99
A.3.2 Obtaining Concentrations from Time-Resolved ELISA Measurements 100
A.3.3 Obtaining a Measure for the Effective Change in Cytokine Concentrations Between the Samples and Controls 103
A.3.4 Coupling the Effective Measure $\boldsymbol{value}$ to the In Vivo PMN Data 103
A.4 The Metric for Comparing the In Vivo Inflammatory Potential of Various Nanoparticles 106
A.4.1 The Issue with LOAEL and NOAEL 106
A.4.2 An Alternative: % PMN at a Defined Surface Dose 107
A.5 Dynamic Interior of Macrophages After Two Days 108
A.6 Transcriptomics 109
A.7 In Vivo BAL Cell Numbers 110
A.8 Speed of Macrophages 112
A.9 Can Nanoparticles Between Macrophages Glue Them Together? 113
A.10 Theoretical Time-Courses of In Vitro Mono- and Co-Cultures 115

References **119**

Bibliography **129**

Biography **133**

List of Figures

Figure 1.1: Different modes of exposure of the human body to nanoparticles, possible translocations of nanoparticles between organs, and nanoparticle excretion; »GI tract« stands for gastro-intestinal tract. 2
Figure 1.2: The majority of nanoparticles that are inhaled through the nose are deposited in the alveolar region of the lungs. 3
Figure 1.3: Schematic of the air-blood barrier in the alveolus. 4
Figure 1.4: A schematic of an adverse outcome pathway with the typical spatial and time-scales of the key events, and the scope of most in vitro and in vivo approaches. 5
Figure 1.5: The dose dependence of the viability of LA-4 lung epithelial cells (determined using propidium iodide and Hoechst 33342 staining) after 6 days of incubation with nanoparticles (NP) – TiO_2 nanotubes, reproduced from [51] under a CC-BY license. 8
Figure 1.6: The correlation between the number of macrophages at day 1 and number of neutrophils at day 28 after nanoparticle instillation in mice; high neutrophil numbers correspond to stronger inflammation. 9
Figure 2.1: By enabling a cell-by-cell analysis of events, microscopy provides additional information on the events and toxicity mechanisms – for instance, the variation in the events between cells (left), and their correlation with the amount of internalized nanoparticles (right)... 13
Figure 2.2: One of the advantages of fluorescence microscopy (right) over bright-field transmission microscopy (left) is that different components of the sample can be specifically labelled and thus distinguished in the false-color micrographs. 15
Figure 2.3: Left: Jablonski energy diagram of the energy levels, timing and lateral intensity distribution of excitation (green), internal conversion (gray) and emission (orange) during fluorescence. 15
Figure 2.4: A scheme of the microscope that was used in our experiments. 16
Figure 2.5: A side-by-side comparison of non-confocal (left) and confocal (right) fluorescence micrographs of the same cells in the horizontal (xy, above) and vertical (xz, below) plane. 18
Figure 2.6: Left: Jablonski energy diagram of the energy levels of **A** fluorescence and **B** stimulated emission; right: fluorescence excitation (green), fluorescence emission spectrum (orange) and stimulated emission spectrum (red). 19
Figure 2.7: A comparison of side-view (xz) micrographs of the same 40 nm-large Crimson fluorescent bead (used to acquire the Point Spread Function of the microscope during an alignment phase), acquired by (from left to right): confocal microscopy, 2D STED, a combination of 30% 2D STED and 70% 3D STED, and 3D STED microscopy. 20
Figure 2.8: A fluorescence lifetime-coded image is obtained by fitting the time-distribution of detected photons with a monoexponential decay (middle) in each pixel of the image. 21
Figure 2.9: Schematic of the two setups for detecting light that is backscattered from the sample by the nanoparticles: reflectance microscopy (shown in green) and reflectance confocal microscopy (shown in dark red). 23
Figure 2.10: Comparison of three modes of optical detection of nanoparticles using a 60x water immersion objective. 23
Figure 2.11: Detection of nonlabelled multi-walled carbon nanotubes (MWCNT, left) and nonlabelled TiO_2 nanotubes (middle and right) in a sample with living cells using a 60x water immersion objective. 24

Figure 2.12: Comparison of a reflectance (green) and confocal fluorescence micrograph (magenta) of labelled TiO_2 nanotubes on a monolayer of LA-4 cells when using a low-magnification 10x air objective. 24
Figure 2.13: Overview of **A** the process of fluorescent labelling of nanoparticles, **B** potential experimental artefacts that originate from faulty labelling, and **C** checkpoints to control the labelling procedure and ensure reliable and reproducible experimental results. 26
Figure 2.14: Schemes and micrographs of potential experimental artefacts that stem from faulty labelling. LA-4 epithelial cells (cell membranes were labelled with CellMask Orange) were incubated with purposefully modified TiO_2 nanotubes, labelled with Alexa Fluor 647 (shown in red). 27
Figure 3.1: Splitting the system into simple subsystems lowers the complexity of interactions. 38
Figure 3.2: Macrophages internalize various sizes of nanotube aggregates. 39
Figure 3.3: Macrophages are full of nanoparticles several days after exposure. 40
Figure 3.4: Dead macrophages and a haze of non-aggregated nanoparticles in macrophages can be observed after a few days of nanoparticle exposure. 41
Figure 3.5: Exposure to large surface doses of TiO_2 nanotubes lowers the viability of macrophages. 42
Figure 3.6: Dead cells and cell debris are present in both in vitro and in vivo lavages. 43
Figure 3.7: Time-courses of the macrophage and neutrophil numbers in the bronchoalveolar lavage fluid (BAL) of instilled mice. 44
Figure 3.8: The relation between macrophage and neutrophil numbers a day after exposure (acute inflammation) is nicely discerned, whereas the relation between initial macrophage depletion and neutrophil numbers after a month of exposure (prolonged inflammation) is not as simple. 45
Figure 3.9: Macrophages do not manage to internalize all the nanoparticles. 46
Figure 3.10: The macrophages slow down during the exposure to nanoparticles. 46
Figure 3.11: The nanotubes enter the cell through multiple mechanisms – mostly by endocytosis, but also through other routes, e.g. fast endocytic processes and direct translocation. 49
Figure 3.12: The major route of nanoparticle internalization is endocytosis, with other routes also present. 50
Figure 3.13: Cauliflowers are larger and more frequent at higher surface doses of exposure. 51
Figure 3.14: Cauliflowers grow with time. 52
Figure 3.15: The characteristic appearance and structure of cauliflowers on the surface of lung epithelial cells. 53
Figure 3.16: Cauliflowers are present also in the alveoli of mice, exposed to the same TiO_2 nanotubes. 53
Figure 3.17: The characteristic size of nanoparticle aggregates in the cauliflowers is very similar to the size of lysosomes and exocytotic vesicles. 55
Figure 3.18: Nanoparticle exposure elevates the lipid metabolism of cells but does not majorly influence the size of lipid droplets. 56
Figure 3.19: Cauliflowers can be observed in neurons, but not in macrophages. 57
Figure 3.20: Various nanoparticles induce formation of cauliflowers. 58
Figure 3.21: The mitochondrial network fragments soon after exposure to TiO_2 nanotubes, but is restored after two days. 59
Figure 3.22: The LA-4 epithelial cells and MH-S macrophages can be distinguished by their morphology. 61
Figure 3.23: Nanoparticles that are released from macrophages are internalized into epithelial cells. 62
Figure 3.24: Macrophages internalize and condense nanoparticles from cauliflowers. 63
Figure 3.25: Inflammatory signaling is strongly modulated in the cell cultures. 64
Figure 3.26: Simplified schematic of the cycle of events with the most important events leading to chronic inflammation; “NPs” stands for nanoparticles. 65
Figure 4.1: Theoretical in vivo time-courses for nine chosen sets of nanoparticle (NP) parameters. 72
Figure 4.2: The nanoparticle sorter cube with theoretical end-points at three different exposure doses (nanoparticle-to-alveolus 1:1, 10:1 and 100:1) and two time-points corresponding to acute and chronic inflammation (1 day and 10 days after exposure, respectively). 74

Figure 4.3: By using a multi-step approach, the model parameters can easily be determined from targeted in vitro tests. ... 78
Figure 4.4: The toxicity rate *tox* (R1) can be determined from the measured relative increase of surface of viable macrophages (M1) in a macrophage monoculture after 1 – 4 days of exposure to the nanoparticles (surface dose 10:1). ... 79
Figure 4.5: The viability and surface coverage of macrophages can be determined from fluorescence micrographs (top row, 10x objective). ... 81
Figure 4.6: Determining the cff from the epithelial monoculture. ... 82
Figure 4.7: A proof-of-concept example of machine-learning-based detection of cauliflowers in a fluorescence micrograph. ... 83
Figure 4.8: Theoretically predicted endpoints for nanoparticles A-I (same as in Figure 4.1 and Figure 4.2) performed on the basis of two nanoparticle parameters – *tox* and cff. ... 84
Figure 4.9: The signaling efficiency $signalEff$ (R3) can be determined from the measured percent of PMN in bronchoalveolar lavages after one day (M3), combined with the previously determined tox (R1) and cff (R2). ... 85
Figure 4.10: Effective change in cytokine concentrations, calculated from the fitted measured time course of TMB absorption. ... 86

Figure A.1: Nanoparticles can disrupt the cell's cytoskeleton. ... 95
Figure A.2: A micrograph of the control – non-exposed LA-4 – with a more contrasted red channel (scattering) than figures in the table above. ... 98
Figure A.3: A scheme of the TMB substrate reaction in the sandwich ELISA. ... 101
Figure A.4: Time evolution of the absorbance of TMB in several samples and the zoom-in on the first 200 seconds. Note the instabilities of the spectrofluorimeter spanning mostly from ca. 300 s to 1300 s, which are highly undesirable both in the time-resolved and endpoint ELISA measurements. ... 101
Figure A.5: The slopes b of the measured samples; they are proportional to concentrations of cytokines for each cytokine separately. ... 102
Figure A.6: Resulting values, calculated from the fitted slopes of measured time traces of TMB absorption. ... 103
Figure A.7: Graphs of PMN influx compared to the six largest principal components (PC1 – PC6). The line that connects the nanoparticles in order of their PMN influx is non-monotonous. ... 104
Figure A.8: Graphs of PMN influx compared to various combinations of the first four principal components. ... 105
Figure A.9: The results of solving a set of linear equations using an increasing number of principal component vectors. ... 105
Figure A.10: Graphical representation of the problematic nature of LOAEL and NOAEL as toxicity metrics. ... 106
Figure A.11: A comparison of dose-dependence curves for three toxicity metrics. ... 108
Figure A.12: The micrographs show the dynamics of MH-S cells (membranes labeled with CellMask Orange, left micrograph) after several days of incubation with TiO_2 nanotubes (labelled with Alexa 647, middle and right micrographs). ... 109
Figure A.13: A heatmap presenting the GSEA normalized enrichment score (NES) of the upregulated Hallmark pathways in the transcriptome profile (total RNA) of mono- and cocultures of LA-4 and MH-S cells, exposed to a 10:1 surface dose of TiO_2 nanotubes for 4 and 48 hours... 110
Figure A.14: Time-courses of the numbers of various cell types in the bronchoalveolar lavage fluid (BAL) of instilled mice. ... 111
Figure A.15: The time-courses are compared for five different metal oxides at the same surface dose (ratio between the nanoparticle and lung surface being 1:1). ... 112
Figure A.16: Presence of nanoparticles between macrophages – does it glue them together? ... 113
Figure A.17: Clustering of cells in BAL cytospins after nanoparticle exposure hints on large attraction between the cells. ... 114
Figure A.18: A control measurement of the affinity of CellMask Orange to the TiO_2 nanotubes. ... 115

Figure A.19: Theoretical time-courses of an in vitro coculture of epithelial cells and macrophages for the chosen sets of nanoparticle parameters. 116
Figure A.20: Theoretical time-courses of an in vitro monoculture of epithelial cells for the chosen sets of nanoparticle parameters. 117
Figure A.21: Theoretical time-courses of an in vitro macrophage monoculture for the chosen set of nanoparticle parameters. 118

List of Tables

Table 2.1: A short overview of the settings that were most commonly used for live-cell imaging shown in this work. 31
Table 4.1: An overview and description of the variables used in the system. 68
Table 4.2: An overview and description of the 10 parameters used in the system. 69
Table 4.3: An overview of the variables in all four models. 77
Table 4.4: An overview of the parameters in all four models.. 78

Table A.1: Table of criteria for the qualitative determination of the extent of quarantine, termed "Cauliflower-Forming Potential" (CFP) 96
Table A.2: The determined extent of nanoquarantine (CFP, left column) and typical xy micrographs of LA-4 cells (cell membranes labelled with CellMask Orange, shown in green) after a 2-day incubation with a 10:1 surface dose of various nonlabelled nanoparticles (detected via backscattered light, shown in red) 97
Table A.3: Overview of the main characteristics of the tested nanoparticles, including the observed CFP. 98
Table A.4: A table of chosen nanoparticles for ELISA assay, information on their physicochemical characteristics and the inflammation they induce in vivo at a 1:1 surface dose. 100

Abbreviations

AEAPMS	...	3-(2-aminoethylamino)propyltrimethoxysilane; silane linker connecting the fluorescent label to the TiO_2 nanotubes
AO	...	adverse outcome
AOP	...	adverse outcome pathways
APD	...	avalanche photodiode; detector
ATTC	...	American Type Culture Collection
BAL	...	bronchoalveolar lavage
BET	...	specific surface area (nanoparticle surface area per nanoparticle mass [m^2/g]) determined by the Brunauer, Emmett and Teller theory
CFP	...	cauliflower-forming potential; a metric for the extent of nanoquarantine
DQ12	...	crystalline silica, quartz
ELISA	...	enzyme-linked immunosorbent assay
FAS	...	fatty acid synthase; key enzyme for synthesis of fatty acids
FBS	...	fetal bovine serum
FLIM	...	fluorescence lifetime imaging microscopy
GSEA	...	gene set enrichment analysis; method for calculating enrichment of gene sets from transcriptomics data
H2020	...	Horizon 2020; European Union research and innovation programme
HRP	...	horseradish peroxidase; enzyme in ELISA
JRC	...	Joint Research Centre
KLD	...	Karhunen-Loève decomposition; a mathematical procedure similar to PCA
LA-4	...	cell line of type II pneumocytes (alveolar epithelial cells)
LCIS	...	live cell imaging solution; isotonic saline buffered with HEPES to pH 7.4
LOAEL	...	lowest observed adverse effect level; lowest dose with observed adverse effect
KE	...	key event
MIE	...	molecular initiating event
MWCNT	...	multi-walled carbon nanotubes
MH-S	...	cell line of alveolar macrophages
NES	...	normalized enrichment score; a metric for the enrichment of pathways in the GSEA analysis
NC	...	nanocubes
NOAEL	...	no observed adverse effect level; highest dose with no observed adverse effect
NP	...	nanoparticle

NT	...	nanotube
OXPHOS	...	oxidative phosphorylation
PBS	...	phosphate-buffered saline; isotonic saline buffer with pH 7.4
PC		principal components; new orthogonal basis obtained by PCA
PCA		principal component analysis; a mathematical method that reduces the dimensionality of the data
PI	...	propidium iodide; a fluorophore that stains nuclei of cells with compromised plasma membrane (dead cells)
PMN	...	polymorphonuclear cells; neutrophils, eosinophils and basophils
PMT	...	photomultiplier tube; detector
STED	...	stimulated emission depletion (microscopy)
2D STED	...	STED which improves only the lateral resolution
3D STED	...	STED which improves only the axial resolution
70% 3D STED	...	a combination of 30 % 2D STED and 70% 3D STED, improves both the lateral and axial resolution
TMB	...	3,3',5,5'-tetramethylbenzidine; substrate in ELISA
UV light	...	ultraviolet light
TCSPC	...	time-correlated single-photon counting (module); used in FLIM measurements

Symbols

α	...	ratio between the surface (projected area) of macrophages and the surface area of alveoli in mice
$Absorbance$	...	detected absorbance in ELISA measurements
b	...	the ELISA slope obtained by fitting the time-resolved ELISA measurements
cff	...	rate of cauliflower formation (nanoparticle-dependent)
$cfuEff$	...	ratio between endocytosis rates of cauliflowers and of free nanoparticles
coc	...	the ELISA slope of the non-exposed coculture
D_{xy}	...	minimal resolvable lateral distance
D_z	...	minimal resolvable axial distance
$delay$	...	delay between signal excretion and infiltration of new macrophages
ε	...	molar absorptivity of the TMB substrate
$elisaData$	...	the set of calculated values from ELISA measurements for the set of eight cytokines
$endo$	...	rate of nanoparticle internalization
λ	...	wavelength of light in vacuum
l	...	height of the sample in the well
$la4Max$	...	maximal projected surface of epithelial cells compared to the lung surface area
$la4Rep$	...	replication rate of epithelial cells
I	...	detected intensity
$influxMhs$	...	the influx of immune cells
$macrophageSurface$	...	norming factor for surface of macrophages
$mhsRep$	...	replication rate of macrophages in vitro
n	...	refractive index of the medium
NA	...	numerical aperture of the focusing lens
neg	...	the ELISA slope of the negative control (12.5% FBS)
NP	...	the ELISA slope of the sample, incubated with nanoparticles
$npCF$	...	surface area of nanoparticles in cauliflowers normed to the surface area of the lung
$npFree$	...	surface area of freely-floating nanoparticles normed to the surface area of the lung
$npLa4$	...	surface area of nanoparticles inside epithelial cells normed to the surface area of the lung
$npMhs$	...	surface area of nanoparticles inside macrophages normed to the surface area of the lung

pos	...	the ELISA slope of the positive controls (the antigen standards)
r	...	radius of macrophage
$signalEff$	...	signaling efficiency: how many immune cells are infiltrated compared to the lipid production (nanoparticle-dependent)
S_A	...	surface area of alveoli in mice
$sLa4$	...	surface (i.e. projected area) of epithelial cells normed to the surface area of the lung
$sMhs$	...	surface (i.e. projected area) of macrophages (and other immune cells) normed to the surface area of the lung
S_M	...	projected area of alveolar macrophages in mice
τ	...	fluorescence lifetime of the fluorophore
t	...	time (in the model $t = 1$ corresponds to 1 day)
$timecf$	...	norming factor for exocytosis saturation
tox	...	toxicity of nanoparticles (nanoparticle-dependent)
v	...	velocity
$value$	...	the metric for comparing ELISA slopes of different cytokines
$transfData$	...	the KLD-transformed input *elisaData* in the basis of principal component vectors
$transfMatrix$	...	the KLD transformation between the values for cytokines and principal components
$weights$	...	the weights for the principal component vectors used to calculate the measured PMN influx
$\#MHS$	...	number of macrophages measured in vivo at a 1:1 surface dose
$\#PMN$	...	number of PMN cells measured in vivo at a 1:1 surface dose
$\#PMN(ctrl)$	...	number of PMN cells measured in vivo at a 0:1 surface dose (sham control)
$\%PMN$	...	the increase of the number of PMN cells compared to the control, normed to the number of macrophages in the control
$\%PMN1$	...	the number of PMN cells, normed to the total number of cells in the alveolus

Chapter 1

Introduction

1.1 Exposure to Nanoparticles Can Affect Human Health

Despite being daily exposed to potentially hazardous particulate matter through our water, food and the air we breathe, we still do not understand its influence on human health, yet alone predict its adverse effects before they become evident. This is becoming a serious issue as more and more novel nanoparticles (particulate matter with at least one dimension in the range from 1 to 100 nm) are manufactured and widely used in food, cosmetics, textiles, medicine and in various industrial applications, thus additionally contributing to the already present exposure from naturally occurring nanoparticles (e.g. particles in volcanic ash and fine dust) and incidentally produced nanoparticles (example by diesel engines and solid fuel combustion) [1]–[7].

Through the years, various health risks have been correlated to both every-day and work-related inhalation of natural and man-made nanoparticles [3], [8]–[12]. These include asthma, lung cancer, heart disease, chronic inflammation, cardiovascular effects, asbestosis, silicosis, pulmonary fibrosis, chronic obstructive pulmonary disease, and brain damage with accelerated cognitive decline. Overall, inhalation of polluted air majorly increases the mortality rate and was recently associated with eight million yearly premature deaths worldwide, corresponding to a loss of life expectancy of three years [13], [14]. Notably, one of the major culprits in this study was deemed to be exposure to particulate matter smaller than 2.5 µm, especially nanoparticles.

Not surprisingly, the combination of emerging indications of health risks that are associated with exposure to nanoparticles on one side, and the quick development and introduction of nanotechnology into our lives on the other, have sparked research in the field of nanosafety (sometimes called "nanotoxicology" or "toxicology of ultrafine particles"), which focuses on testing, understanding and ultimately predicting nanoparticle toxicity.

1.1.1 Nanoparticles in our Bodies

Several decades of nanosafety research has confirmed that nanoparticles interact with our body differently than larger particles due to their large specific surface area (surface-to-mass ratio), which is a direct consequence of their small size [15]. As an example, 1 g of 10 nm-large TiO_2 nanospheres contains 10^{18} particles, which in total have a 100.000-times larger surface area (40 m^2) than the same mass of bulk TiO_2 (2.4 cm^2). This large specific surface area governs many of the unique properties of nanoparticles, including their interactions with their surroundings. It therefore does not come as a surprise that even

some non-toxic materials can induce toxic effects when their size approaches the nano range [16].

In our body, the nanoparticles first come into contact with a biological barrier – a thin layer of cells that is specialized for maintaining the exchange of material with the environment, and has evolved to simultaneously protect the inner-lying tissues from bacteria, viruses, harmful substances, and naturally occurring particulate matter. In contrast to larger particles, nanoparticles can pass through these biological barriers, enter the lymph and bloodstream and from there relocate to various organs, including the liver, bone marrow, heart and brain, where they further interact with the biological milieu (Figure 1.1). Because the biological barriers are not all equally robust, the exposure route can greatly affect the outcome of nanoparticle exposure [1]–[3].

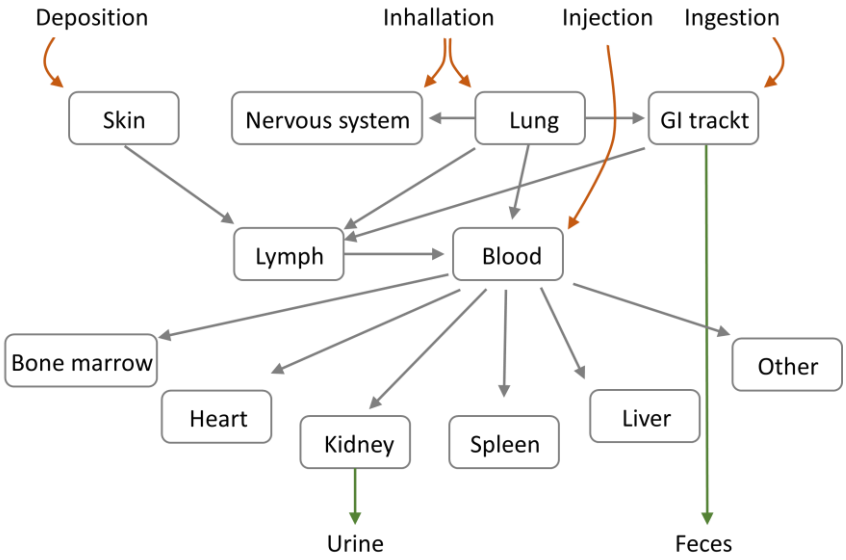

Figure 1.1: Different modes of exposure of the human body to nanoparticles, possible translocations of nanoparticles between organs, and nanoparticle excretion; »GI tract« stands for gastro-intestinal tract. Adapted from [2] (public domain).

The sturdiest biological barrier in the human body is the skin, which is frequently exposed to nanoparticles from cosmetics and textiles. It was once deemed to be unpassable to nanoparticles due to a 5 – 20 µm thick layer of dead skin cells (epidermis) covering the living cells in the dermis. However, some nanoparticles were observed to enter the human body even through intact skin, let alone damaged or diseased skin [17], [18].

The gastro-intestinal tract is another gate of entry into our body and is relevant mostly for nanoparticles in food and water. It is also partially relevant for inhaled airborne particulate matter that is trapped in the mucus that protects the airways and subsequently transported towards the pharynx by the mucociliary escalator where it is translocated into the gastro-intestinal tract. Many nanoparticles pass through the gastro-intestinal tract with seemingly no effect and are excreted, while others interfere with the gut function and microbiome, cause inflammation and/or translocate into the bloodstream [19].

Last but not least, one of the most troublesome routes of exposure is through our breathing pathways, which are constantly exposed to airborne nanoparticles. It has been shown that nanoparticles are able to enter the brain through or along the olfactory nerve from the nasal cavity and remain in the brain, possibly causing neuro-degenerative diseases [20], [21]. Luckily, a notable fraction of the inhaled nanoparticles is trapped by the mucus that lines the tracheobronchial regions and upper airways, with the latter also trapping the

majority of larger, micron-sized particles, as shown in Figure 1.2. The trapped particulate matter is efficiently cleared from the airways by the mucociliary escalator into the gastro-intestinal tract. However, more than half of the inhaled nanoparticles deposit in the alveoli in the lungs, from where they can pass into the lymph and/or bloodstream and relocate to other organs. This route of exposure is considered to be extremely vulnerable to nanoparticle-induced risks due to the large surface area of the alveoli (140 m^2), extremely small distance between the air interface and the blood (0.2 – 2 µm), as well as slow clearance and large deposition of nanoparticles in the alveoli [2], [22]. Hence, this work will focus on the toxicity of inhaled nanoparticles in the alveolus.

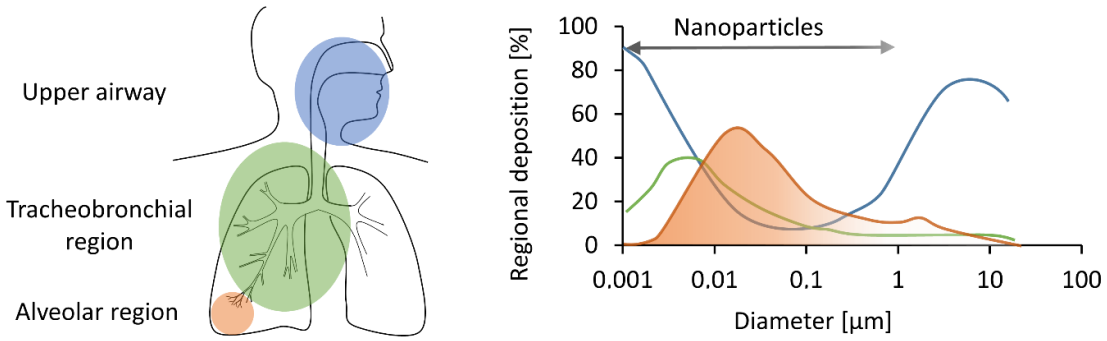

Figure 1.2: The majority of nanoparticles that are inhaled through the nose are deposited in the alveolar region of the lungs. Data from the International Commission on Radiological Protection (ICRP 1994), adapted from [2] (public domain).

As shown in Figure 1.3, the nanoparticles that reach the alveolus first come into contact with lung surfactant – a mixture of phospholipids and proteins, which not only acts as an immune barrier, but also lowers the compliance of the lungs during breathing, thus reducing the amount of energy and strain during inhalation and preventing alveolar collapse during exhalation [23], [24]. After passing through the lung surfactant, the particles can come into contact with one of the three types of cells in the alveolus.

The rim of the alveolus is formed by two types of alveolar epithelial cells (pneumocytes): most of the cells are pneumocytes type I, which are extremely thin cells that are incapable of undergoing cell division, but still have all the usual cell organelles. Their main role is to form a physical barrier between the air and blood which should be as thin as possible to enable efficient gas exchange. The second type of alveolar epithelial cells – pneumocytes type II – are thicker and are in charge of excretion and recycling the lung surfactant and regulating the volume in ion content of the alveolar liquid. If needed, these cells divide and differentiate into type I pneumocytes, and are also involved in the innate immune response of the alveolus – both directly and indirectly by modulating the response of immune cells [25], [26].

The third cell type in the alveolus are macrophages – the immune cells of the alveolus, which are located on the pneumocytes in the alveolar lumen. They recognize foreign bodies in the alveolus and remove them by engulfing and digesting them. This works excellently for viruses and bacteria, but not for nanoparticles because they are mostly not biodegradable. Nevertheless, macrophages are able to remove some of the nanoparticles from the alveolus by internalizing them and relocating with the internalized nanoparticles either into the lymph or upwards via the mucociliary escalator to the pharynx where they are swallowed into the gastro-intestinal tract. The clearance rate of nanoparticles from the alveolus varies from particle to particle – it can be anywhere from 0.1 % to 80 % of the nanoparticles in 24 hours [2], [27]. The nanoparticles that manage to pass through the

surfactant and through/between pneumocytes reach the interstitial space, which consists of an extracellular matrix – (fused) basal lamina – and interstitial fluid, from where they can translocate to the lymph, or pass through/between the capillary endothelial cells into the capillaries [2].

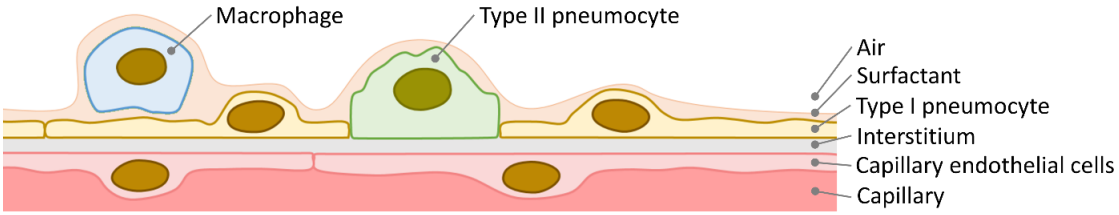

Figure 1.3: Schematic of the air-blood barrier in the alveolus. Note that the barrier in the schematic is shown flattened out and is not drawn in proportion.

1.2 Current Safety Testing Needs an Alternative

The toxicity of nanoparticles is governed not only by the route of exposure and received dose but also by a complex combination of physicochemical properties of nanoparticles, such as their shape, size, chemistry, crystal structure, surface charge, surface chemistry, adsorbed materials, and bio-persistence [28]. The key issue in nanoparticle safety is that some nanoparticles might be safe even at high exposure doses, while other, only slightly different nanoparticles, induce long-lasting inflammation and subsequent adverse outcomes [16], [29]. It is therefore clear that in order to ensure the safety of numerous novel nanoparticle-containing products, each and every one of them should be thoroughly tested before entering the market.

Today, regulated safety testing of novel compounds and materials is mostly done on animals, such as mice and rats. However, animal-based tests cannot fulfil the current needs of the industry and society for testing the entire plethora of potentially hazardous nanoparticles. Not only are they expensive and time-consuming – consequently limiting the number of nanoparticles and their combinations which can be tested – they also cannot directly predict potential harmful outcomes for humans due to large interspecies differences, which result in species-specific outcomes to material exposure [30], [31]. On top of that, more and more major governing bodies have started phasing out animal-based experiments, further increasing the already urgent need for designing inexpensive and reliable nanoparticle safety tests and predictions [32].

A promising replacement for animals are complex cellular superstructures (e.g. organoids, tissues/organs on a chip) – in vitro models that closely mimic their in vivo counterparts. Even more cost- and time-efficient are simple in vitro tests that use cultured cells or non-living biological systems (e.g. model membranes) and are thus more suitable for high-throughput screening of materials. However, because neither of these can currently be maintained for long enough to reproduce chronic and long-term effects, they are suitable only for short-term studies of acute effects [32]–[34]. This is a major issue in nanotoxicology because many nanoparticles are not biodegradable and remain in the body long after exposure, causing chronic or delayed responses.

1.3 Mechanism-Based Testing of Nanoparticle Safety as an Alternative to Animal Testing

Lately, a promising alternative approach that is able to mitigate the limited outreach of in vitro models has emerged. Suitably termed "mechanism-based nanosafety", it is based on acquiring detailed knowledge on the mechanisms of nanoparticle toxicity and causally connecting several key events on various spatial and time-scales into adverse outcome pathways (AOPs), as shown in Figure 1.4 [35].

An adverse outcome pathway is initiated by a molecular initiating event (MIE), i.e. the first crucial interaction between the nanoparticles and the biological milieu, which leads to a series of interconnected key events (KEs), comprising of cellular and tissue responses to the molecular initiating event that lead to the adverse outcome (AO) – the undesired harmful effect on the level of organs, organisms, or even populations. As shown in Figure 1.4, the events in the AOP happen on a wide range of time- and spatial scales, and therefore can only be discerned using a combination of complementary experimental approaches and techniques.

Importantly, when the intricate connections between key events and the adverse outcomes are well understood, one can utilize this knowledge to devise cost- and time-effective high-throughput in vitro tests that can be used to predict the adverse outcomes by targeting the key events in the adverse outcome pathways [32], [36]–[38]. Sadly, despite the enormous amount of published research on nanosafety, the biggest obstacle to the development of mechanism-based nanosafety is still our lack of knowledge about the relations between nanoparticle properties, early molecular events, and the symptoms that later on evolve into complex diseases [39]–[41].

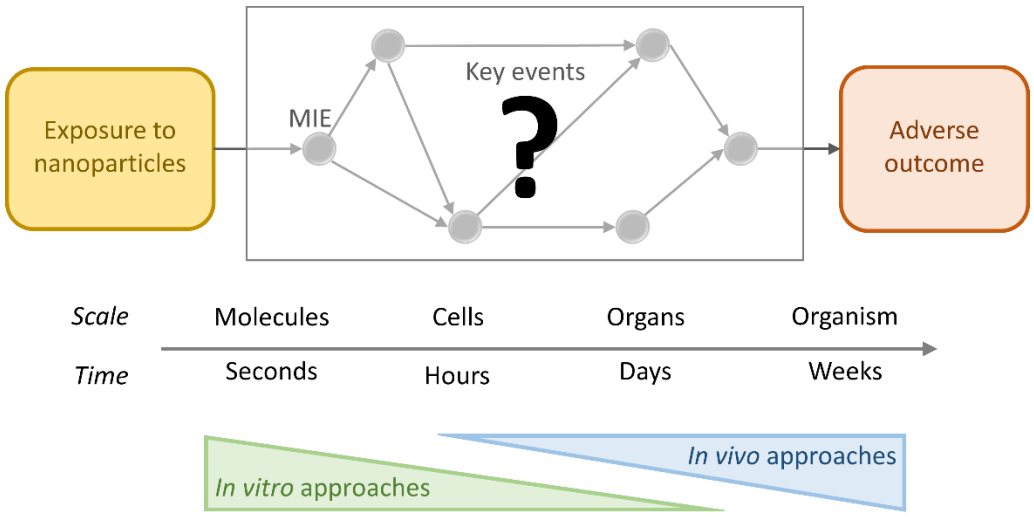

Figure 1.4: A schematic of an adverse outcome pathway with the typical spatial and time-scales of the key events, and the scope of most in vitro and in vivo approaches. MIE stands for "molecular initiating event".

1.3.1 Current Issues Preventing Mechanism-Based Nanosafety Assessment

One of the reasons (alongside the complexity of the biological systems) for the lack of knowledge regarding the nanotoxicity mechanisms as well as for slower progress of

nanosafety assessment in general is that it is difficult to join and compare the results from different studies. Some of the major causes for this situation and suggestions how to avoid them are discussed below.

- **Use of different nanoparticles in studies.** A plethora of nanoparticles are used in different studies, and although the nanoparticles are usually well-characterized, they are rarely used in follow-up studies by other groups using complementary approaches. Even when using the same nanoparticles from the same source, the properties of nanoparticles from different batches can vary [42]. This can be avoided by using the same batch of well-characterized nanoparticles in all experiments, or by obtaining the nanoparticles from a specialized distribution source such as the JRC Nanomaterials Repository, which purposefully sources large batches of typical industrial nanoparticles, characterizes them and distributes the same batch to different research groups [43].

- **Poorly defined exposure doses of nanoparticles used in the studies.** A crucial element in the toxicity measurements is the dose response of the system: the larger the dose, the larger the effect of the nanoparticles. Because nanoparticles come in a variety of shapes and sizes, the toxicity ranking of the tested nanoparticles can change drastically between different dose metrics and should thus be defined in a sensible way [44], [45]. Although many dose metrics can be found in the literature (e.g. the cumulative mass, number, volume or surface area of nanoparticles), the currently most effective dose metric for nanoparticles appears to be their surface dose (the ratio between the cumulative surface of nanoparticles and the surface of cells/lung) because most nanoparticles interact via their surface and are not soluble [44], [45]. Sadly, the results of many studies are reported only in one dose metric without sufficient data to recalculate to other dose metrics, which could easily be avoided if all the appropriate specific surfaces, volumes and concentrations were reported as well.

- **Nanoparticle-induced artefacts in assays.** Nanoparticles often interfere with many classical biochemical spectroscopy-based assays, which are routinely used for testing toxicity of soluble chemicals (MTT, LDH, DCF, WST-1, BCA assay, Alamar blue assay, etc.) [46]–[49]. The interference is usually caused by scattering of light from the nanoparticles, absorption of light by the nanoparticles or interaction of nanoparticles with the reagents of the assays. Luckily, the standard protocols can sometimes be modified to avoid nanoparticle-induced artefacts [46]–[49]. Because the interference is both test- and nanoparticle-specific, it should always be tested and reported alongside the published data.

- **Lack of complementary experiments.** Early molecular events are difficult to discern by vivo approaches as they happen soon after the exposure on a scale below 10 micrometers, whereas the symptoms that are related to the complex responses on and above the tissue level later on are out of reach of in vitro experiments. Hence, multiple complementary in vitro and in vivo approaches should be performed on the same batch of nanoparticles to cover the entire time- and spatial scale of the AOPs (Figure 1.4).

At this point, one might be under the impression that the complexity of nanoparticle interactions with cells and tissues is so complex that mechanistic understanding and its generalization seem practically unattainable. However, as shown in this work, a combination of various appropriately modified complementary state-of-the-art

experimental techniques, performed in vitro and in vivo using the same nanoparticles, proves to be the much-needed tool for filling in the gaps of an adverse outcome pathway, thus paving the way to predictive nanotoxicology.

1.4 Investigating Toxicity Mechanisms Using TiO_2 Nanotubes

In this work, the mechanisms of nanoparticle toxicity will be investigated for a model nanoparticle (TiO_2 nanotubes) by using a combination of advanced experimental techniques and complementary in vitro, in vivo and in silico approaches. On the way, the here-determined key events and mechanisms will be tested for other nanoparticles as well.

Anatase TiO_2 nanotubes were chosen as the model nanoparticle because they fit the following crucial criteria:

- TiO_2 is one of the most commonly used nanoparticles in consumer products – it is found in food, cosmetics, paper, textiles, inks, coatings, plastics, ceramics, etc., and has an estimated yearly production of 7 million tons [50], [51];
- these TiO_2 nanotubes have been shown to strongly interact with biological molecules and cause adverse outcomes both in vitro (disruption of vesicles and cell membranes, loss of cell viability) [52] and in vivo (strong pulmonary inflammation that persisted for several months after exposure) [29];
- the TiO_2 nanotubes can be stably fluorescently labelled in-house with various commercial dyes that have been carefully optimized for specific advanced microscopy approaches, thus enabling high-resolution nanoparticle tracking in live cells, as well as detection and characterization of key events using other advanced microscopies [52]–[54].

1.4.1 TiO_2 Nanotubes Cause Lipid Wrapping and Chronic Inflammation

In a recently published in vitro study, the anatase TiO_2 nanotubes were observed to wrap lipids from model membranes (both small and giant unilamellar lipid vesicles), leading to the outflow of material from the membranes, formation of mobile wrapped nanotubes, and sedimentation of newly-formed clusters of nanotubes and vesicles. In some cases, the strong interaction between the nanotubes and lipid membranes even led to disintegration of giant lipid vesicles [52].

Moreover, when MCF-7 breast cancer cells were exposed to these nanotubes at a high surface dose (ratio between nanoparticle surface area and cell surface was 100:1) for two days in the same study, a haze of wrapped nanoparticles was observed around the cell using fluorescence microscopy, several mitochondria were located unusually far from the nucleus, and the cell plasma membrane could not be fluorescently labelled [52]. All this pointed to the disintegration of the plasma membrane.

Shockingly, when the authors exposed LA-4 type II lung epithelial cells to the same nanoparticles, the majority of the exposed cells retained their viability and integrity of the cell plasma membrane even at equally large exposure doses (ratio of nanoparticle surface area to cell surface 100:1), as shown in Figure 1.5 [52]. Because the intense membrane wrapping is a consequence of the strong affinity between the nanotubes and lipid membranes, it should not depend on the cell type. Hence, this indicates that LA-4 cells

might possess and employ a cellular defense mechanism that somehow retains the integrity of the plasma membrane.

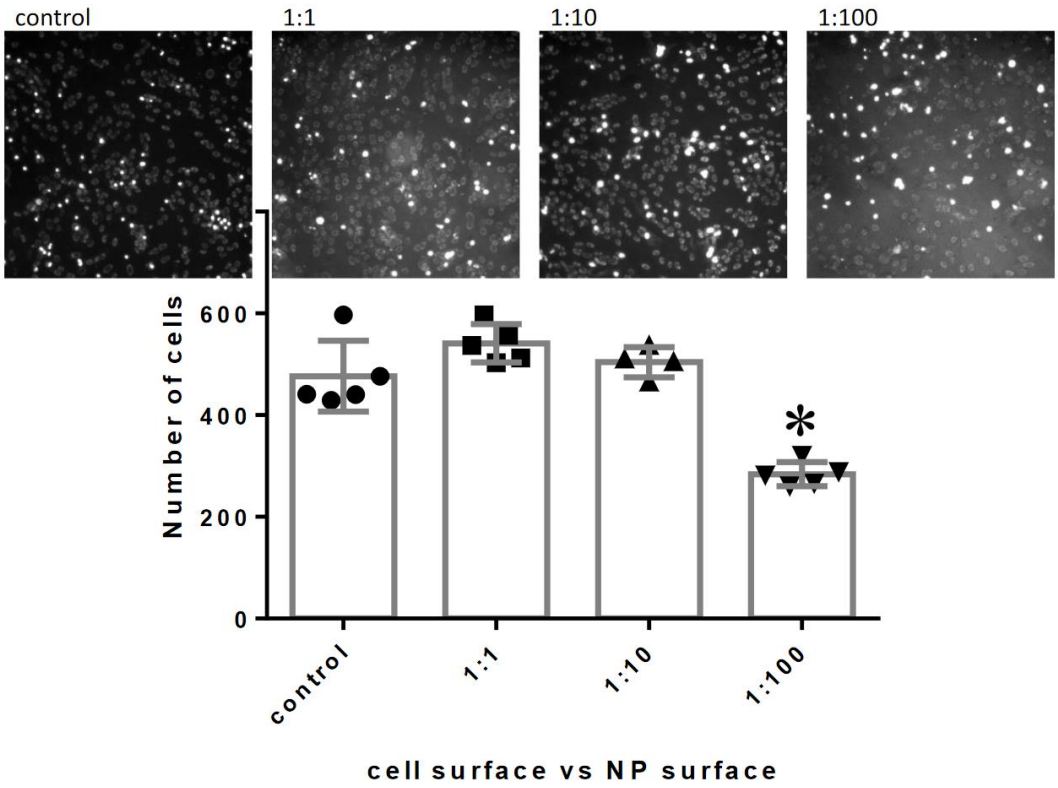

Figure 1.5: The dose dependence of the viability of LA-4 lung epithelial cells (determined using propidium iodide and Hoechst 33342 staining) after 6 days of incubation with nanoparticles (NP) – TiO_2 nanotubes, reproduced from [51] under a CC-BY license.

In vivo, instillation of the same TiO_2 nanotubes in mice resulted in strong and long-lasting pulmonary inflammation, denoted by a noticeable infiltration of inflammatory cells into the lung even a month after exposure [29]. Unexpectedly, the inflammatory response of the anatase TiO_2 nanotubes was more similar to the highly toxic amorphous silica (a.k.a. quartz, DQ12) than to the other three anatase TiO_2 nanoparticles tested in the same study (nanocubes and two rectangular/spherical particles). Although the tested anatase particles were similar in size and chemical composition, only the nanotubes induced significant and long-lasting inflammation, as was determined by the number of neutrophils in the lungs.

In the same study, they determined that the TiO_2 nanotubes were located almost exclusively in the lysosome-phagosome structures of macrophages three months following exposure [29]. Crucially, all four tested anatase nanoparticles were observed in the lungs even at 6 months after the exposure, regardless of whether or not the inflammation had already subsided. This indicates that the length of inflammation does not depend only on particle clearance.

Interestingly, after some additional analysis of the data published in [29], it seems that the exposures that induce the strongest and longest inflammation (the TiO_2 nanotubes and DQ12 at high doses) might correlate with a notable depletion of macrophages at day 1 following exposure (see Figure 1.6).

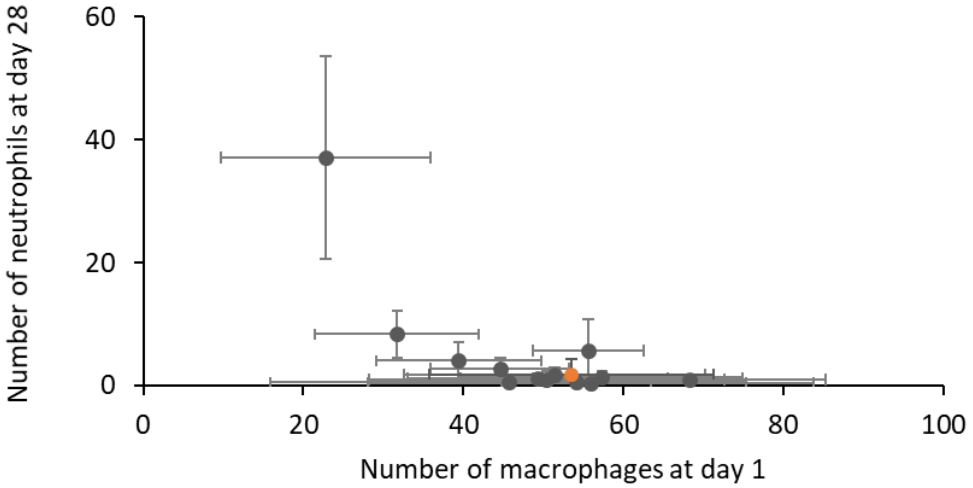

Figure 1.6: The correlation between the number of macrophages at day 1 and number of neutrophils at day 28 after nanoparticle instillation in mice; high neutrophil numbers correspond to stronger inflammation. The data for five metal oxides at several doses is shown in grey and the control value is shown in orange; raw data was obtained from [28] (CC-BY).

Another interesting observation from the same study was the presence and accumulation of proteinaceous matter in the alveolus for some nanoparticles – a condition termed "secondary type of pulmonary alveolar proteinosis" that can sometimes occur after exposure to nanoparticles, including certain quartz, talc and titanium nanoparticles [29]. Although it occurred only in the mice that were exposed to the nanoparticles that induced chronic inflammation (the TiO_2 nanotubes and DQ12), the possible causal connection between the two events was not discussed in the paper.

Many of the intriguing observations described above are still not understood – for example the retained cell viability of lung epithelial cells despite strong affinity between the nanoparticles and the plasma membrane, the in vivo accumulation of proteinaceous matter in the alveolus, and the possible role of macrophage death and accumulation of proteinaceous matter in sustaining inflammation. Hence, in order to understand these events and their potential link to the outcome – chronic inflammation – it is essential to employ a mechanistic study of the events in the nanoparticle-exposed alveolus. Then, we might be able to understand how adverse outcomes, such as chronic inflammation, evolve even after a single exposure to nanoparticles, and ultimately use the acquired knowledge to predict them.

1.5 Goals of the Dissertation

The purpose of this dissertation is

- to improve the current understanding of cellular and sub-cellular events and their inter-relations in the nanoparticle-exposed alveolus using a combination of advanced optical techniques and complementary approaches

and

- to employ this newly-gained knowledge on the relations between the key events for prediction of nanoparticle toxicity.

The goals of the dissertation are as follows:

- devise a quality-controlled procedure for the fluorescent labelling of TiO_2 nanotubes to ensure stable, reliable, repeatable, and well-characterized labelling,
- unravel cellular and sub-cellular events in the in vitro alveolar cell cultures exposed to nanoparticles, including potential cellular defense mechanisms,
- determine the relations between the detected events,
- associate the events with in vivo events for the same nanoparticles,
- describe the key relations between the detected events using a theoretical model,
- devise simple and quick in vitro assays to target the key events in the theoretical model, and
- use the results of the in vitro assays as an input to the theoretical model to predict the nanoparticle toxicity.

Hypotheses:

- Based on the retained cellular viability of lung epithelial cells in vitro after exposure to TiO_2 nanotubes [52] shown in Figure 1.5, we hypothesize that lung epithelial cells possess defense mechanisms that enable them to survive exposures to nanoparticles even at extremely large doses.
- Based on the previous hypothesis and the noticeable reduction of the number of macrophages after exposure to TiO_2 nanotubes in vivo [29] shown in Figure 1.6, we hypothesize that alveolar macrophages do not employ the aforementioned defense mechanisms and are hence more likely to die from nanoparticle exposure than epithelial cells at the same exposure dose.
- Based on the in vivo data showing a possible correlation between the reduction of the number of macrophages at day 1 following exposure and long-lasting inflammation [29] shown in Figure 1.6, we hypothesize that re-exposure of cells to the nanoparticles that have been released from other dying cells (e.g. macrophages) prolongs the inflammation and possibly explains how a single exposure can cause chronic inflammation.

Implications for science

Widespread use of the exciting applications offered by new nanoparticles is held back by slow and expensive animal-based safety testing. Sadly, development of alternative testing strategies is hindered by our current lack of understanding of the mechanisms governing the development of adverse outcomes.

Luckily, recent advances in advanced, high-resolution live-cell microscopies and omics provide an unprecedented opportunity for understanding the early molecular events, as well as their relations. Notably, they can track molecular, sub-cellular and inter-cellular events in real time with resolution of 10 nm under physiological conditions in complex live-cell environments on time scales ranging from seconds to days. This enables the discovery of new events, investigation of interactions between nanoparticles and the biological milieu,

determining their relations to complex cellular responses, and matching them with in vivo observations on the same nanoparticles.

As shown in this dissertation, the ability of real-time tracking of the complex network of events enables the understanding of the causality between the events. When coupled with complementary advanced approaches, a wide range of spatial and time-scales of possible key events can be investigated. This provides the much-needed boost for the construction of the adverse outcomes pathways, the ultimate key to mechanism-based prediction of nanosafety, and leads to development of time- and cost-efficient animal-free alternatives for toxicity testing.

Chapter 2

Methodology

2.1 Microscopy

A plethora of experimental techniques can be used to study the mechanisms of nanoparticle toxicity in an in vitro model. In contrast to the (mostly spectroscopic) techniques that determine the superimposed response of the entire population of cells in the sample at once (e.g. various assays), microscopies deliver cell-associated information via imaging a subset of cells. Although this can result in a lower statistic, it enables a unique view on the processes in the sample. Because it is image-based, it enables localization of nanoparticles, visualization of events, determining the heterogeneous spectrum of the cellular responses, correlation of events with nanoparticle location both inside a cell and its distribution between cells, as well as visual recognition of many potential nanoparticle-induced artefacts (Figure 2.1).

In the following text, general concepts of the live-cell microscopy techniques used in the experimental section of this work will be outlined, with more details easily accessible in any of the excellent resources on this subject, for example [55]–[66].

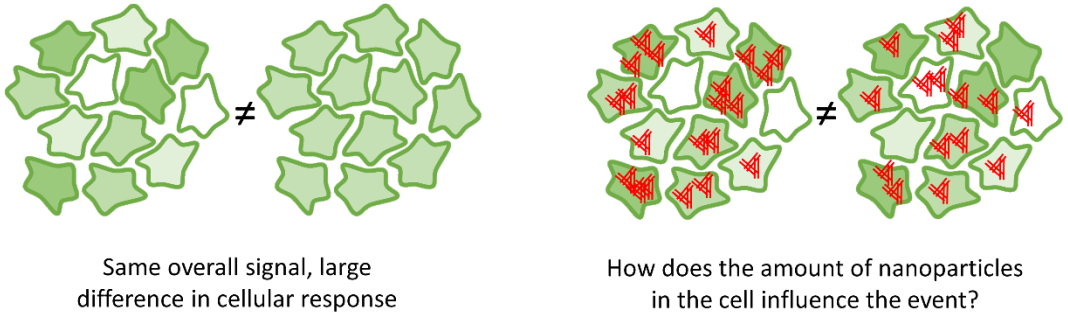

Figure 2.1: By enabling a cell-by-cell analysis of events, microscopy provides additional information on the events and toxicity mechanisms – for instance, the variation in the events between cells (left), and their correlation with the amount of internalized nanoparticles (right).

2.1.1 Microscopy of Living Cells

One of the currently most powerful experimental techniques for studying early molecular events is live-cell microscopy. In contrast to imaging of fixed cells, it enables one to observe the time evolution of events in a cell, type of diffusion/transport of nanoparticles through the system, dynamic interactions between the nanoparticles and the cell, and the cellular

response in real-time. Such knowledge about the spatial and temporal order of events can provide valuable hints about the causal relations between the observed events.

When imaging living cells, it is important to provide them with conditions that are as similar to the interior of the body as possible. This not only means an appropriate temperature (37 °C), but also correct osmolarity and pH of the surrounding medium. For measurements that are up to a few hours long, this can be achieved by imaging the cells in a closed container in a medium which is iso-osmolar and does not require CO_2 to keep the pH at physiological values (e.g. the HEPES-buffered live cell imaging solution – LCIS – that is used in this work). For longer imaging, the cells should be imaged in the bicarbonate-based culture medium inside a stage-top incubator that provides the correct temperature, humidity and concentration of CO_2.

To study events inside a living cell, it is also crucial to use an illumination source of an appropriate wavelength. Although light with a shorter wavelength enables better resolution of the acquired micrographs, its photons also have higher energy and consequently also cause more damage to the biological structures. Hence, imaging of live cells is usually performed using light in the visible spectrum with a tendency towards higher wavelengths as light in the near UV already potently damages DNA and biomolecules. Nevertheless, as even high intensities of light in the visible spectrum can be toxic for living cells, the intensity of the excitation light should be reduced as much as possible by optimizing the optical setup to minimize losses and improve the detection efficiency.

2.1.2 Fluorescence Microscopy

Although conventional transmission optical microscopy enables one to see cells and their interior, the signal is not specific, making it hard to detect nanoparticles and determine their sub-cellular location. It also possesses very low contrast because the image is formed by the decrease in the intensity of light that is transmitted through the sample due to scattering and/or absorption of light by the cells, organelles and nanoparticles. On the other hand, its alternative – fluorescence microscopy – is one of the most commonly used optical microscopies in cell biology especially due to its high contrast, high specificity and high sensitivity [60], [64] (see Figure 2.2).

As its name suggests, fluorescence microscopy is based on a phenomenon termed fluorescence: the innate ability of some molecules, atoms and nanostructures to absorb light in a certain range of wavelengths and emit it at a higher wavelength in a few nanoseconds. This difference in wavelengths between the absorbed and emitted light is termed the Stokes shift and is caused by a quick loss of energy of the excited electron before emitting the photon, causing the emitted photon to have less energy than the absorbed photon, and hence a longer wavelength [65]. A scheme representing the process and an example of an excitation and emission spectrum are presented in Figure 2.3.

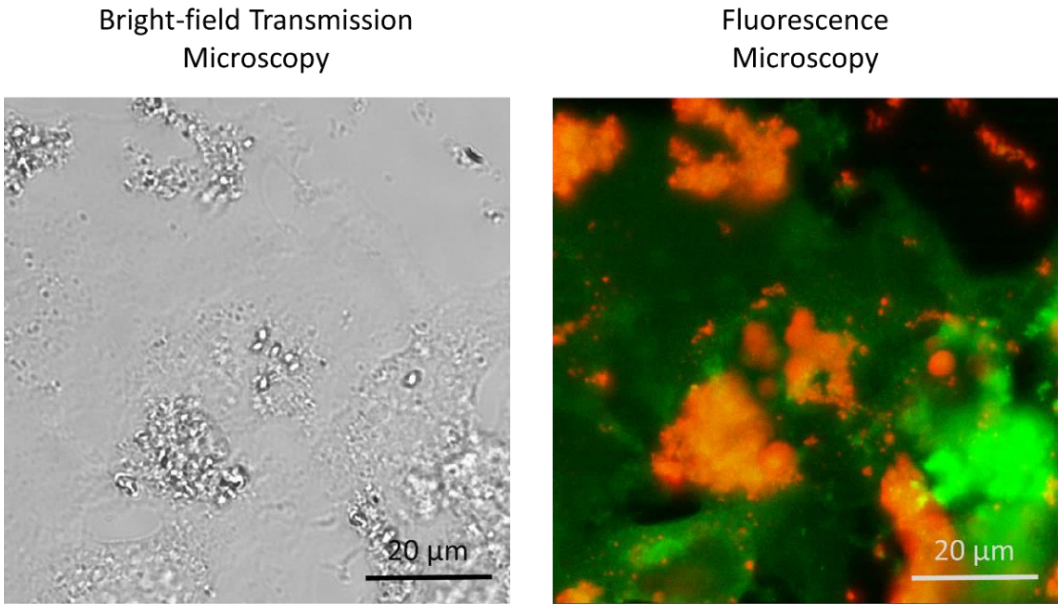

Figure 2.2: One of the advantages of fluorescence microscopy (right) over bright-field transmission microscopy (left) is that different components of the sample can be specifically labelled and thus distinguished in the false-color micrographs. In this example, LA-4 cells were incubated with TiO_2 nanotubes for two days. Because spectrally different probes were used for labelling cells (CellMask Orange, shown in green) and nanoparticles (Alexa 647, shown in red), the two can be easily discerned in the fluorescence micrographs (right).

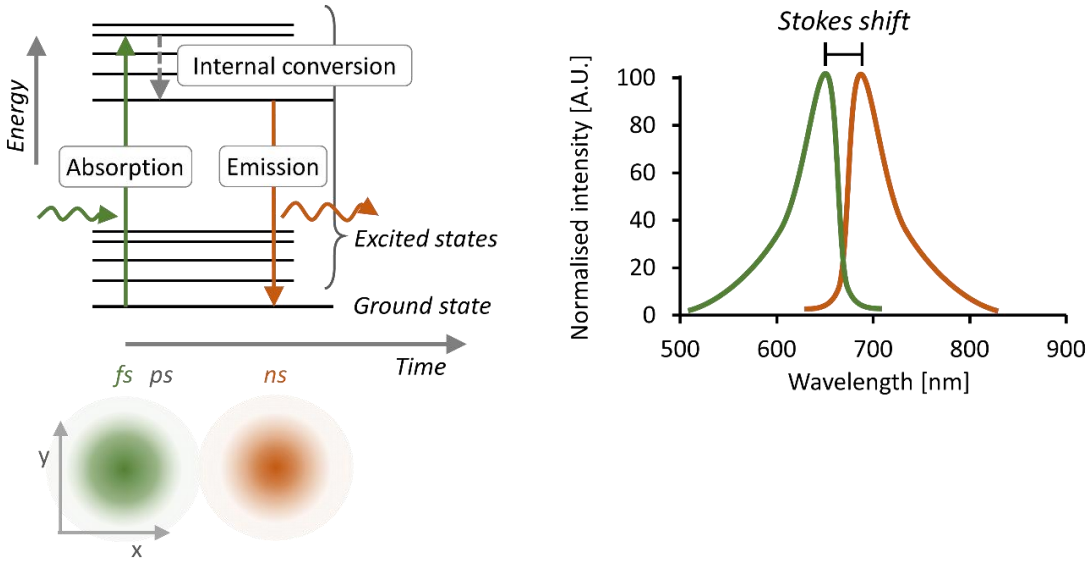

Figure 2.3: Left: Jablonski energy diagram of the energy levels, timing and lateral intensity distribution of excitation (green), internal conversion (gray) and emission (orange) during fluorescence. Right: fluorescence excitation (green) and emission spectrum (orange). The difference between the energy levels is inversely proportional to the wavelength of the absorbed and emitted photon.

It is exactly this Stokes shift that increases contrast in a fluorescence microscope, a scheme of which is shown in grey in Figure 2.4. Because the excitation and emitted light are spectrally different, they can be split by a dichroic beam splitter which reflects the excitation light but transmits the emitted light. Hence, the emitted light reaches the detector whereas the back-scattered excitation light with a different wavelength does not, producing an image with very low background (as shown in Figure 2.2), which in turn increases the contrast of the method.

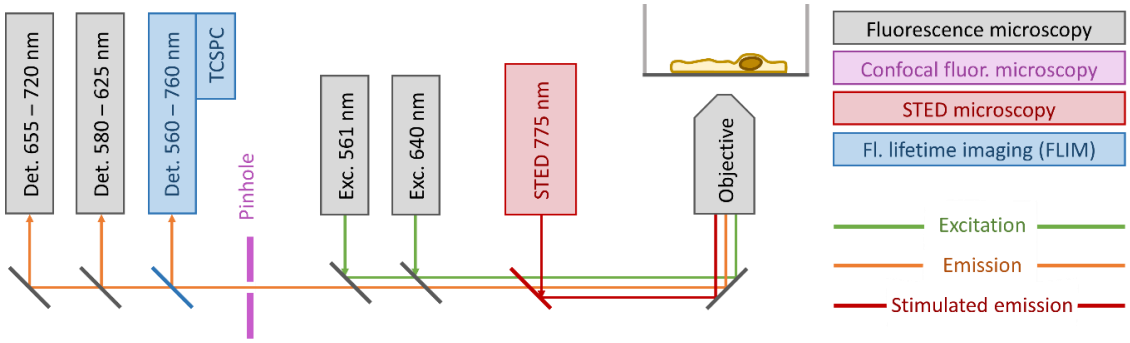

Figure 2.4: A scheme of the microscope that was used in our experiments. The grey elements represent the components of a basic fluorescence microscope, the green and orange lines represent excitation and emission light, respectively, "Exc." denotes excitation lasers and "Det." denotes detectors. Other colored elements are additions that enable better localization (magenta), increased resolution (red) and gather additional information about the system (blue), as explained in Sections 2.1.3, 2.1.4 and 2.1.5, respectively.

After a molecule absorbs a photon, it can relax to its ground state not only by fluorescence but also through other processes, such as internal conversion into heat or transfer of energy to a neighboring molecule [65]. The efficiency of the fluorescence process, termed "quantum efficiency", is described by the ratio between the number of fluorescently emitted photons and the number of absorbed photons and is usually quite low for most biological molecules (less than a few percent). Hence, in order to locate the structures of interest, they are usually labelled with special dyes that have a high quantum efficiency to enable their detection and lower the required intensity of the excitation light. At the same time, labelling structures of interest with special dyes is also the key to the specificity of fluorescence microscopy, as multiple dyes with well-separated spectra can be introduced in the sample to label different structures / molecules in the cell, and be excited and detected independently from one another.

Living cells can be fluorescently labelled in various ways: by fluorescent probes, genetically-encoded fluorescence proteins, quantum dots, nanobodies, and, self-labelling proteins [55], [57], [59], [63], [64]. In this work, we mostly used fluorescent probes which either partition into the plasma membrane of living cells or pass through it and passively label specific cellular components by partitioning that is driven by physical interactions. The most often used alternative – transfection with vectors that encode the synthesis of fluorescent proteins of interest – was not needed for our experiments as we did not focus on the interaction of nanoparticles with specific proteins. For the same reason, we also avoided specific targeted labelling of proteins using nanobodies (i.e. single-domain antibodies), self-labelling proteins (e.g. SNAP-, Halo- and CLIP- tags), and protein labelling using click-chemistry. We intentionally avoided the use of quantum dots because of their nano-size (5-50 nm), which could cause major interference with the interactions between cells and nanoparticles which we planned to observe. In all the methods listed above, special care should be taken to keep the concentration of fluorescent molecules in

the cell as low as possible to prevent their interference with biological structures and processes.

Besides having an appropriate excitation and emission spectrum, the dyes used for live-cell fluorescence microscopy should also be non-toxic to the cells both in absence and presence of light (non-toxic and non-phototoxic) and their emission signal should not decrease significantly during the experiment (in other words, they should be photostable to reduce photobleaching) [55], [65], [67]. One should also be aware that the cell medium fluoresces on its own and that phenol red, which is present in most media, can decrease (quench) the fluorescence of dyes [68].

2.1.3 Confocal Fluorescence Microscopy

Because the signal detected by a basic fluorescence microscope (described in Section 2.1.2 and shown in grey in Figure 2.4) originates from the entire volume of the cell, it is associated not only with the cellular components in the focal plane, but also with all the structures that are above and below it. Although these structures are out of focus, i.e. blurred, their signal decreases the contrast of the micrograph and the localization ability. This can be improved by inserting two pinholes into the conjugated planes of the light path, blocking most of the out-of-focus light and enabling fine optical sectioning of the sample with a slice thickness of up to 500 nm; an example of micrographs obtained by this so-called confocal fluorescence microscopy is shown in Figure 2.5. In practice, confocality can be achieved by adding a spinning disk between the dichroic beam splitter and the objective in the case of wide-field illumination, or by placing a pinhole in the conjugated plane of the sample just before the detector when using a laser scanning microscope. We used the latter in our setup, which is indicated by the magenta dashed line in Figure 2.4.

It is important to note that a smaller pinhole size decreases the thickness of the optical slice, but also lowers the intensity of the detected signal because it blocks a large portion of the emitted light [55]. In addition, the thickness of the optical slice remains the same below a certain pinhole size (app. 0.7 Airy units) due to the diffraction limit, which limits the minimal resolvable lateral and axial distances D_{xy} and D_z according to the wavelength of light in vacuum λ, numerical aperture of the focusing lens NA, and refractive index of the medium n to

$$D_{xy} = \lambda/(2\ NA) \tag{2.1}$$

and

$$D_z = 1.4\ \lambda\ n\ /\ NA^2 \tag{2.2}$$

[66]. The most commonly used pinhole size in this work is 1.1 Airy unit, which provides a good compromise between signal intensity and thickness of the optical slices for our samples.

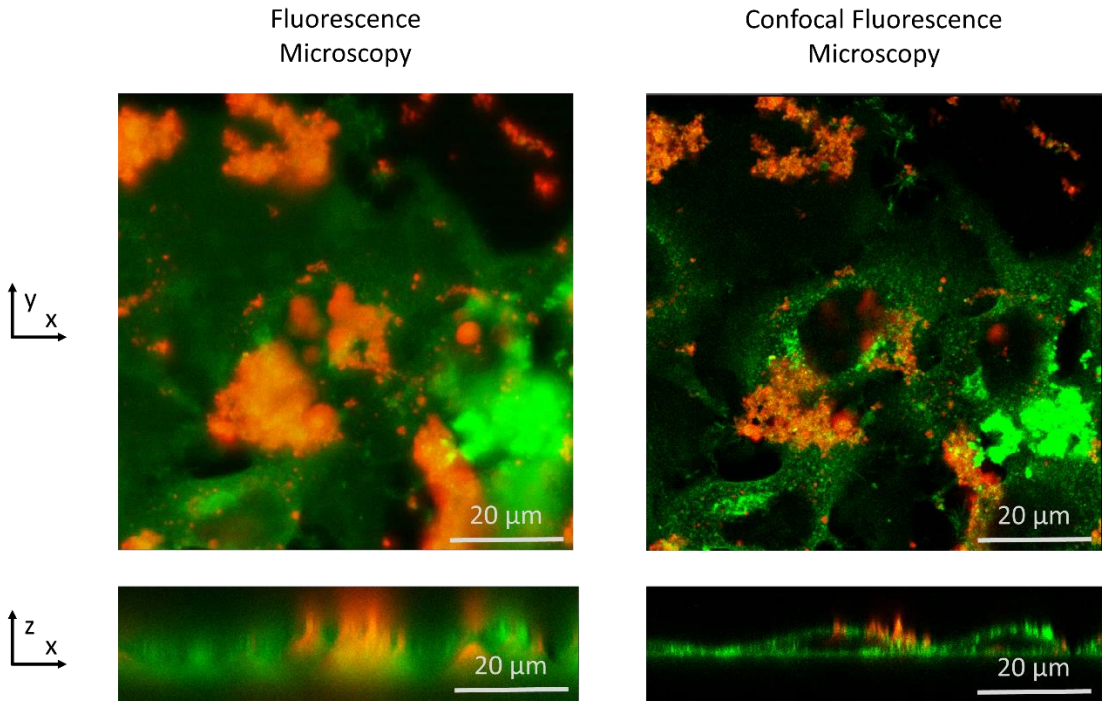

Figure 2.5: A side-by-side comparison of non-confocal (left) and confocal (right) fluorescence micrographs of the same cells in the horizontal (xy, above) and vertical (xz, below) plane. The confocal micrographs of LA-4 cells (their cell membranes were labelled with CellMask Orange, shown in green) after a 2-day incubation with TiO_2 nanotubes (fluorescently labelled with Alexa 647, shown in red) show remarkable improvement in optical sectioning and thus also in the ability to (co)localize fluorescently labelled components in the sample.

2.1.4 Stimulated Emission Depletion (STED) Microscopy

According to equations (2.1) and (2.2), the highest resolution of a typical confocal optical microscope with a numerical aperture 1.2, excitation at 600 nm, and refractive index of the medium 1.3, is limited by the diffraction limit to approximately 250 nm in the lateral and 550 nm in the axial direction [66]. For roughly a century, it was believed that because of this diffraction limit, the only way to increase the resolution is by decreasing the wavelength of the excitation light and consequently increasing the phototoxic burden to the observed sample. However, in the last two decades, several super-resolution techniques have emerged, each of them implementing a work-around to seemingly overcome the diffraction limit and improve resolution to few tens or even few nanometers, approaching the size of antibodies and other proteins.

One of these super-resolution techniques is stimulated emission depletion microscopy (STED microscopy), which was conceptually devised by S. W. Hell and J. Wichmann [69], as well as V. A. Okhonin [70]. To achieve such high resolution, STED microscopy (whose setup is shown on the scheme in Figure 2.4 using grey, magenta and red elements) employs a STED laser beam that is uniquely shaped by a phase mask and is used to de-excite fluorescence excited states in most of the excitation volume except for its central part before the emission occurs (Figure 2.6) [60]. The first part of the energy transitions in a fluorophore is the same as in laser-scanning microscopy: the fluorophores are excited by a focused excitation laser pulse in a diffraction-limited area, which is followed by a quick loss

of energy of the excited electron (to the lowest energy level of the first excited state). Before the emission occurs, a doughnut-shaped higher-wavelength STED laser pulse is directed onto the sample to stimulate the electron relaxation of those excited fluorophores that are not located in the center of the doughnut. The consequently stimulated emitted photons have the same wavelength as the STED laser light and are prevented from reaching the detectors by a filter. Later, the remaining excited fluorophores, which are mostly located in the center of the doughnut, relax and emit light, which is detected in the same way as in the case of laser-scanning confocal microscopy.

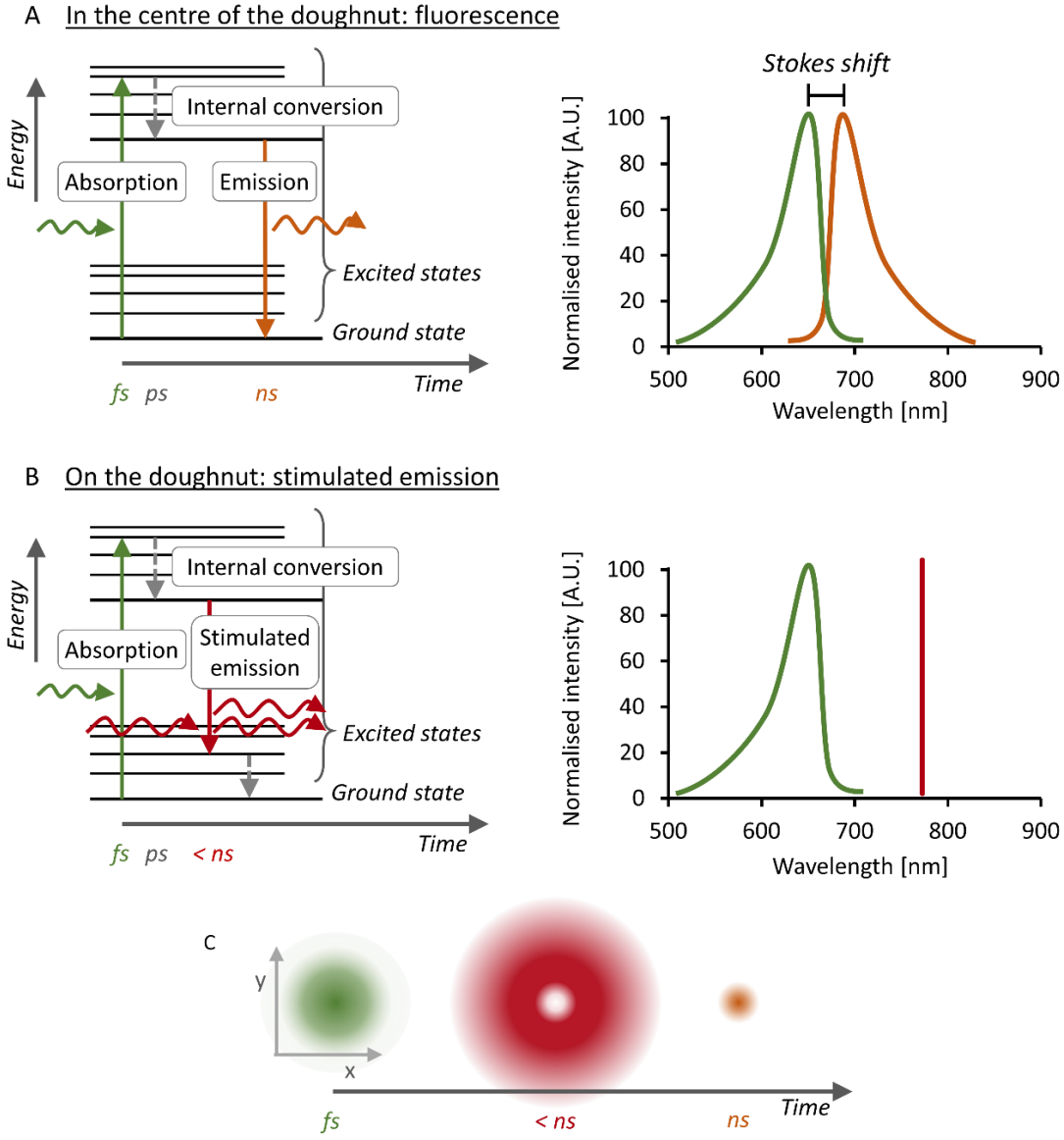

Figure 2.6: Left: Jablonski energy diagram of the energy levels of **A** fluorescence and **B** stimulated emission; right: fluorescence excitation (green), fluorescence emission spectrum (orange) and stimulated emission spectrum (red). The difference between the energy levels is inversely proportional to the wavelength of the absorbed and emitted photon. **C** The timing and the lateral intensity profiles of excitation (green), stimulated depletion (red), and fluorescence (orange).

The trick that enables STED microscopy to seemingly break the diffraction limit is that the very center of the doughnut-shaped STED beam is completely dark due to symmetry reasons (the doughnut modulation unit rotates the polarization of light). The size of the center of the doughnut (the area from which the later-detected photons originate) is thus not limited by the diffraction limit and depends mainly on the intensity of the STED laser – the higher its intensity, the smaller the size of the focal central region, leading to improved resolution.

Sadly, this doughnut-shaped 2D STED beam only improves the lateral resolution of the system, while the axial resolution still remains the same as in confocal microscopy (500 nm). To overcome this, a differently-shaped STED laser pulse is used, majorly improving the axial resolution (termed 3D STED). By combining the two shapes of the STED laser, both the lateral and axial resolution can be improved. A comparison between confocal microscopy, 2D, 3D, and 70% 3D STED (a combination of 30 % 2D STED and 70% 3D STED) is shown in Figure 2.7.

Importantly, not all fluorescent dyes are suitable for STED microscopy [64]. Besides meeting the criteria for live-cell fluorescence microscopy, the dye should not absorb photons at the wavelength of the STED laser, but it should be able to emit them (otherwise, the emission of these photons cannot be stimulated). On top of that, STED-compatible dyes should be remarkably photostable to survive the large intensities of the STED lasers (c. 10 MW/cm^2).

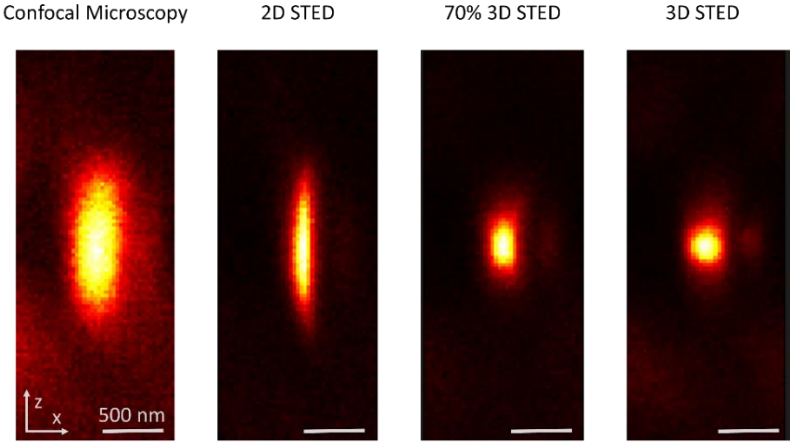

Figure 2.7: A comparison of side-view (xz) micrographs of the same 40 nm-large Crimson fluorescent bead (used to acquire the Point Spread Function of the microscope during an alignment phase), acquired by (from left to right): confocal microscopy, 2D STED, a combination of 30% 2D STED and 70% 3D STED, and 3D STED microscopy. Notice how 2D STED improves the resolution in the horizontal (lateral, x) direction, but not in the vertical direction (axial, z), 3D STED improves the resolution only in the vertical direction (z), and 70% 3D STED improves the resolution in both directions.

2.1.5 Fluorescence Lifetime Imaging Microscopy (FLIM)

An imaging technique that can provide additional functional information about the sample is fluorescence lifetime imaging microscopy (FLIM), which can be used simultaneously with any of the aforementioned fluorescence microscopy techniques. It relies on detecting the time between fluorophore excitation and the emission of photon (the so-called fluorescence lifetime), which depends not only on the fluorophore, but also on the pH, viscosity and ion

concentration in its local environment, as well as on the vicinity of other molecules that can interact with the relaxation pathways of a fluorophore or interest.

Because spontaneous photon emission is a quantum process, its timing is not always the same; it follows a monoexponential probability distribution. In practice, when enough emission events of a fluorophore are detected, the lifetime τ of the fluorophore can be determined from the time-distribution of the arrival of emitted photons: $I(t) \propto e^{-t/\tau}$ [59], [62] (see Figure 2.8). To provide a reasonably good fit to determine the lifetime with satisfactory signal-to-noise in each pixel in the image, this approach is generally slower than ordinary, intensity-based imaging.

FLIM measurements can be performed on a variety of fluorescence microscopes [59], [62]; in our confocal setup with pulsed laser excitation, we used a PMT (photomultiplier tube) single-photon detector and a time-correlated single-photon counting (TCSPC) module, which enable measurements of the time between the laser excitation and the detection of each of the emitted photons (see grey, magenta and blue elements in Figure 2.4).

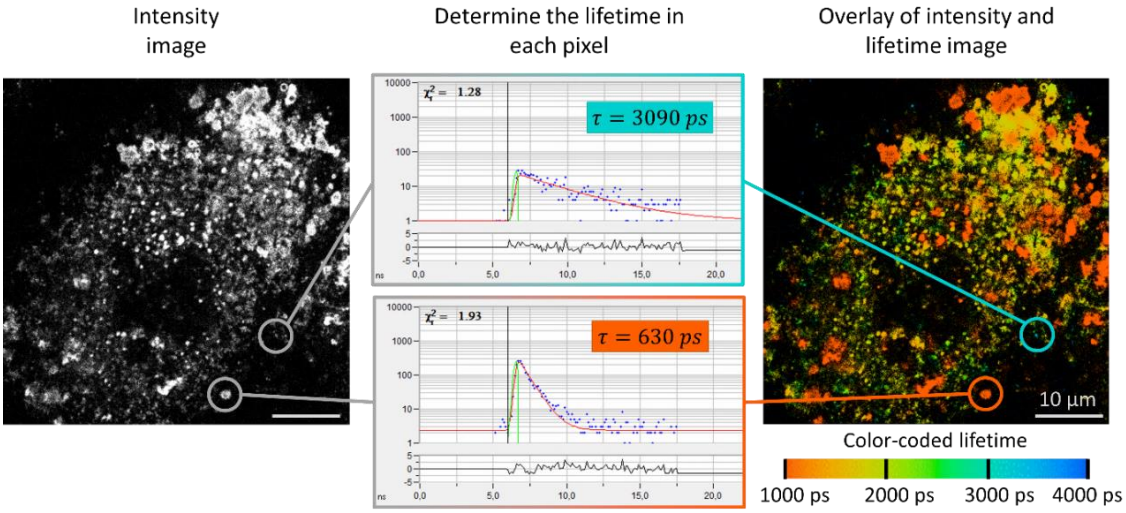

Figure 2.8: A fluorescence lifetime-coded image is obtained by fitting the time-distribution of detected photons with a monoexponential decay (middle) in each pixel of the image. Often, the fluorescence lifetime-coded image is weighted (multiplied) with the intensity image (left) for easier detection of characteristic structures in the image, as shown on the right.

2.2 Detection of Non-Fluorescent Nanoparticles

In order to enable tracking of the nanoparticles inside living cells using optical microscopy, one must be able to detect the nanoparticles as well as the cells. Although various fluorescently labelled nanoparticles are commercially available, we specifically wished to track the TiO_2 nanotubes due to their characteristic in vitro and in vivo behavior. Hence, we decided to fluorescently label them by attaching a commercial fluorophore onto the nanoparticle surface via a silane linker (see Figure 2.13 in Section 2.2.2). As this was done in-house, we were free to choose a fluorophore which is optimized for STED microscopy. To ensure stable and artefact-free fluorescent labelling, we used and refined a quality-controlled procedure, which will be discussed more in detail in Section 2.2.2).

However, for the other pre-synthesized nanoparticles, which we obtained from the specialized JRC distribution source and used to test several key events, the labelling and its optimization would require proportionately more time and effort. Hence, we devised a method to simultaneously detect both the native non-fluorescent nanoparticles and fluorescence from all the other structures on the same optical microscope. For this purpose, we relied on the fact that most nanoparticles are ordered, crystalline structures that consequently scatter light stronger than most biological structures. Thus, the nonlabelled nanoparticles could be localized by detecting the light that is scattered back from the sample (i.e., by reflectance microscopy).

2.2.1 Reflectance Microscopy

The simultaneous implementation of reflectance and fluorescence microscopy is shown in Figure 2.9. In the first setup that we devised (reflectance microscopy, shown in green), we used the same excitation lasers as for fluorescence microscopy, and directed some of the back-scattered light through a beam-splitter onto an auxiliary detector that was located before the pinhole and all the notch filters that block the excitation light. In the second setup (confocal reflectance microscopy, shown in dark red), an additional excitation laser with a higher wavelength than others was used. At this chosen wavelength, the existing filters of the fluorescence microscope setup did not block the back-scattered light, allowing us to guide the light to a detector by an additional dichroic mirror located behind the pinhole. The technical details of both setups are described in Section 2.5.4.3.

Both of these setups enabled detection of nanoparticles with a 60x water immersion objective, albeit with lower resolution, contrast and specificity than standard fluorescence microscopy of the labelled nanoparticles (Figure 2.10). Nevertheless, the image quality was still satisfactory for our research hypothesis as we were interested only in the general location of the nanoparticles (Figure 2.11). We noted, however, that at lower magnification, lower numerical aperture of the 10x air objective sadly precluded localization of nonlabelled nanoparticles (Figure 2.12).

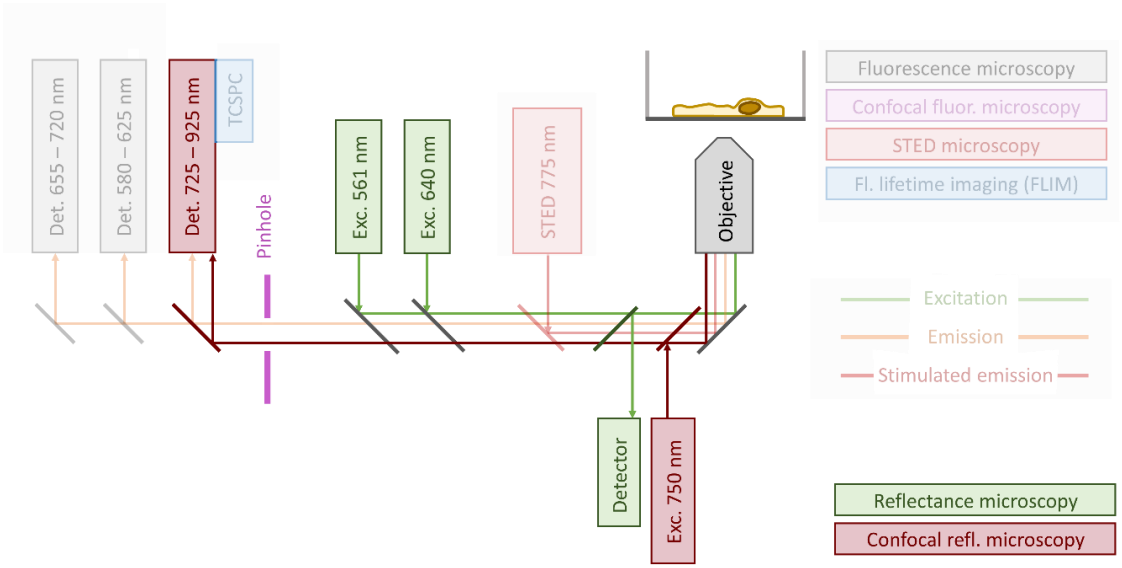

Figure 2.9: Schematic of the two setups for detecting light that is backscattered from the sample by the nanoparticles: reflectance microscopy (shown in green) and reflectance confocal microscopy (shown in dark red). "Exc." denotes excitation lasers and "Det." denotes detectors. Elements from the existing fluorescence setup shown in Figure 2.4 that are not used for detecting the backscattered light are greyed out and several elements that are also used in fluorescence microscopy are recolored for clarity.

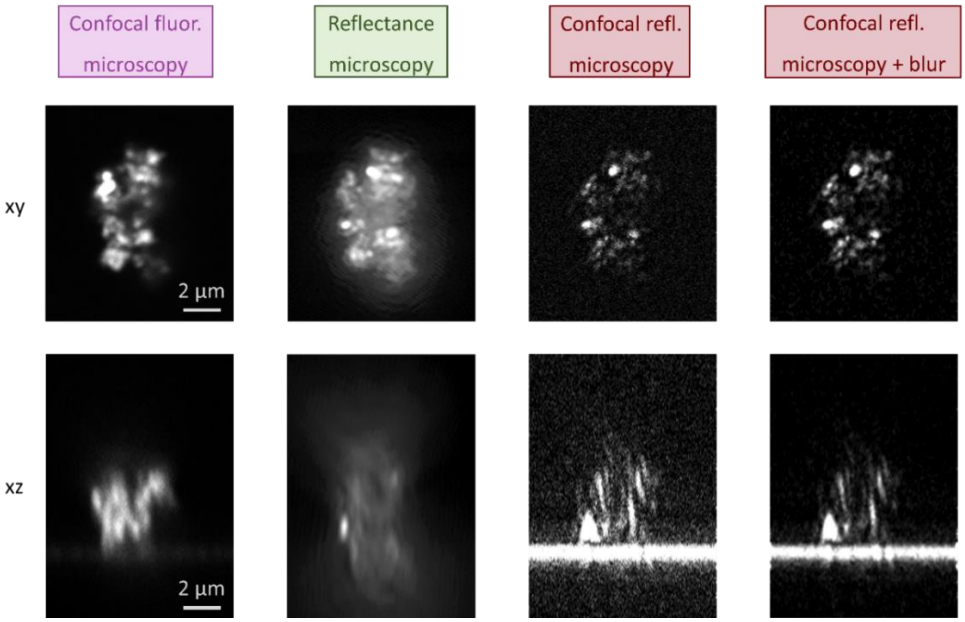

Figure 2.10: Comparison of three modes of optical detection of nanoparticles using a 60x water immersion objective. From left to right: confocal fluorescence microscopy of labelled nanoparticles, reflectance microscopy, reflectance confocal microscopy and reflectance confocal microscopy that was blurred post-acquisition using a 100 nm wide Gaussian filter. The upper row shows micrographs in the horizontal (xy) plane and the lower row in the vertical (xz) plane; the same nanoparticle aggregate is on all micrographs.

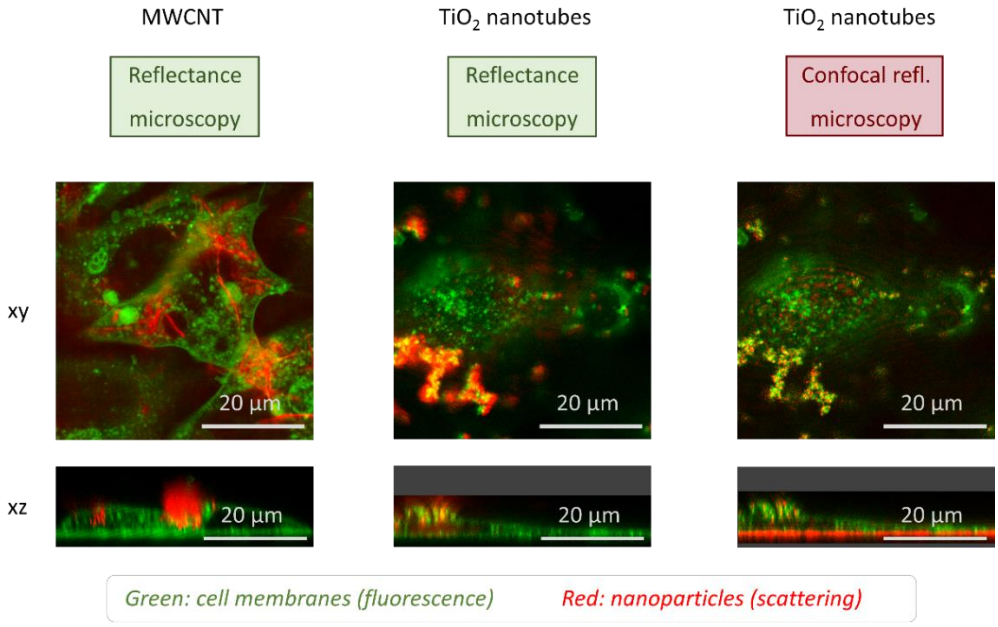

Figure 2.11: Detection of nonlabelled multi-walled carbon nanotubes (MWCNT, left) and nonlabelled TiO_2 nanotubes (middle and right) in a sample with living cells using a 60x water immersion objective. The reflectance micrographs (left and middle) and reflectance confocal micrographs (right) of nonlabelled nanoparticles (red, ratio between nanoparticle surface area and cell surface 10:1) were acquired after a 2-day incubation with LA-4 epithelial cells (fluorescently labelled using CellMask Orange, detected using fluorescence microscopy and shown in green). Some of the xz micrographs were padded with dark grey to ensure that the figures are equal in size.

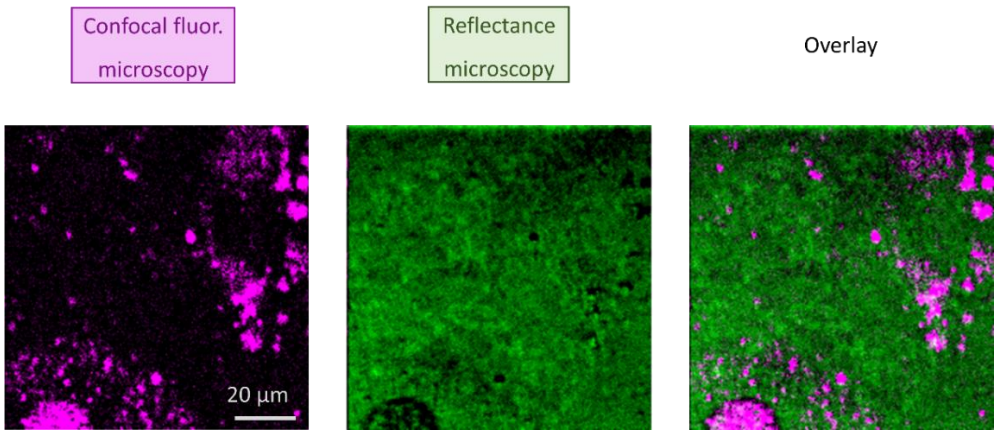

Figure 2.12: Comparison of a reflectance (green) and confocal fluorescence micrograph (magenta) of labelled TiO_2 nanotubes on a monolayer of LA-4 cells when using a low-magnification 10x air objective. In this case, the scattering from the glass and cells overpowers the scattering from the nanoparticles due to the poor axial resolution of the setup – even though the scattering from the glass was negligible compared to the scattering from nanoparticles on the 60x water immersion objective, as shown in Figure 2.11. The few regions in the overlay on the right where the signal from the confocal fluorescence micrograph and reflectance microscopy overlap are white.

2.2.2 Quality-Controlled Nanoparticle Labelling

To truly harness the potential of nanoparticle tracking in living cells using advanced fluorescence microscopy, nanoparticles should first be fluorescently labelled because they mostly do not fluoresce on their own. The common approach to fluorescently tagging already synthesized nanoparticles is to bind a fluorescent dye to the nanoparticles via a chemical linker (a silane linker works well for metal oxide nanoparticles) [53], as shown in Figure 2.13A. The benefit of this approach is that the same batch of nanoparticles can be separately labelled using various dyes, including dyes that are especially designed for advanced microscopies.

However, such nanoparticle labelling must be accompanied by an appropriate quality control procedure to prevent artefacts and erroneous conclusions which can arise from nanoparticles, inadvertently changed during the labelling procedure. We thus refined the labelling procedure of metal oxides and devised appropriate quality control checkpoints to accompany the labelling, tested the procedure on the TiO_2 nanotubes, and mimicked the effect of faulty labelling on experimental results – work, which we published in [53]. A short overview of the procedure is presented in the following paragraphs, including several examples of artefacts (see Figure 2.13 B and Figure 2.14) and approaches how to control them (see Figure 2.13 C).

As shown in the first row in Figure 2.13, the use of a charged linker and/or dye can unintentionally change the nanoparticle surface charge and consequently its interaction with biological molecules and cells [71], [72]. Because many – if not most – fluorescent dyes are charged, it is often difficult to avoid using a charged dye. Luckily, a linker with an opposite charge can be chosen to somewhat balance out the charge of the dye. Also, the general guideline in labelling nanoparticles is to change their surface chemistry as little as possible, thus minimizing the amount of linker and dye on the nanoparticles, while at the same time retaining and achieving a large fluorescence signal. To confirm that the surface charge of the nanoparticles has not been changed, the zeta potential of both the labelled and native nanoparticles should be measured over the entire range of pH values. When this is measured for the functionalized nanoparticles as well, it can indicate whether the linker has successfully bound to the nanoparticles – a valuable piece of information, which is confirmed by Fourier transform infrared spectroscopy (FTIR) measurements. Moreover, the appropriate pH of the labelling and storage medium can be easily discerned from the zeta potential measurements.

Secondly, the sonication that is often utilized to prevent nanoparticle aggregation during the labelling procedure can inadvertently change the morphology of the nanoparticles (Figure 2.13, second row), influencing also their interaction with the biological milieu [29], [73], [74]. This is best tested by comparing transmission electron microscopy (TEM) measurements of the native and labelled nanoparticles. For example, we observed that a 2-hour sonication can break the long TiO_2 nanotubes that are used throughout this work into notably shorter nanotubes, which can disrupt the cell's cytoskeleton and cause the cells to wobble when pulled using an optical tweezer (see Figure A.1 in the Appendix). Using this knowledge, we reduced the sonication to 45 minutes, which did not noticeably change the morphology of the nanotubes.

Last but not least, the presence of unbound dye in the sample causes erroneous localization of nanoparticles in the sample [75]–[78], shown also in Figure 2.13, third row. The presence of unbound dye can originate from insufficient removal of the excess dye after the labelling step or from desorption of the linker from the nanoparticles, which is an often overlooked process. The amount of unbound dye can be majorly reduced by multiple centrifugal filtrations of the sample (or a sequence of centrifugation and supernatant removal) after the reaction between the linker and probe has ended, as well as right before

the experiment. Such removal of free dye should be carefully monitored by fluorescence correlation spectroscopy (FCS) of the sample or measurements of fluorescence intensity of both the sample and removed dye.

If all the above-mentioned control checkpoints are followed, one can rest assured that the nanoparticle labelling is stable, repeatable, well-characterized, and enables reliable interpretation of experiments performed with the labelled nanoparticles.

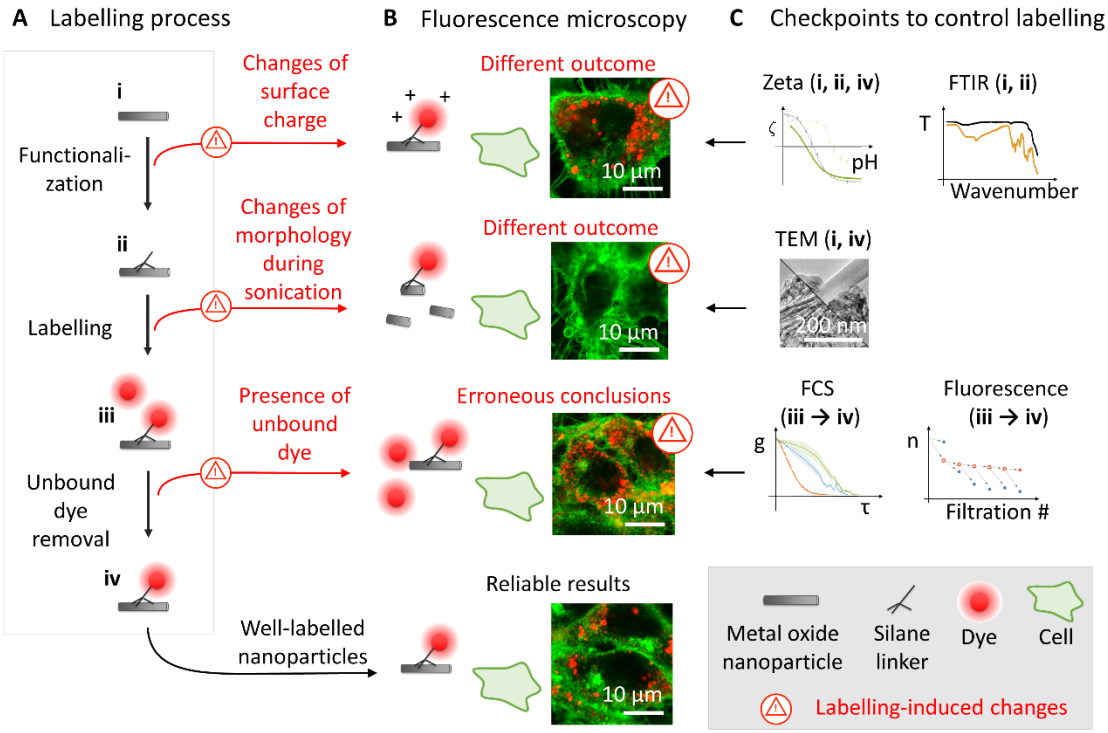

Figure 2.13: Overview of **A** the process of fluorescent labelling of nanoparticles, **B** potential experimental artefacts that originate from faulty labelling, and **C** checkpoints to control the labelling procedure and ensure reliable and reproducible experimental results. Reproduced from our published manuscript [53].

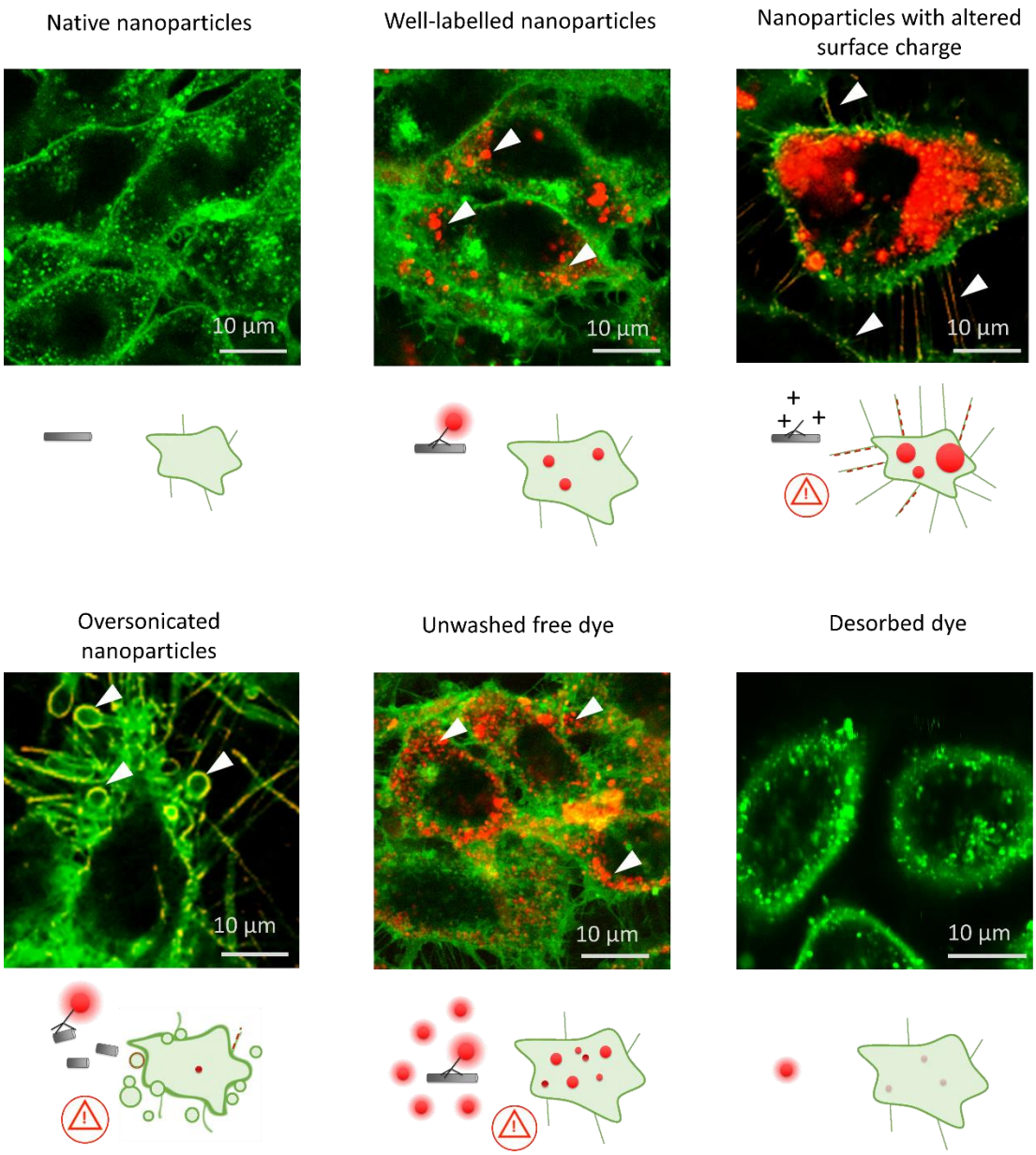

Figure 2.14: Schemes and micrographs of potential experimental artefacts that stem from faulty labelling. LA-4 epithelial cells (cell membranes were labelled with CellMask Orange) were incubated with purposefully modified TiO_2 nanotubes, labelled with Alexa Fluor 647 (shown in red).

2.3 In Vitro Model

The uniform and easily cultivatable immortalized murine cell lines of type II lung epithelial cells (LA-4) and alveolar macrophages (MH-S) were selected for the in vitro model as they enabled comparison with in vivo experiments on mice as well as with various complementary methods performed by other groups in the H2020 SmartNanoTox project [79], which we were included in. Moreover, the coculture of these cell lines was able to reproduce in vivo key events despite its simplicity, thus avoiding increasing the complexity

of the model with additional cell types (e.g. fibroblasts, capillary endothelial cells, etc.) or lung surfactant (see Figure 1.3).

The LA-4 cell line of murine alveolar type II epithelial cells (obtained from ATCC, CCL-196 [80]) was originally derived from a benign urethane-induced mouse lung adenoma (tumor) of a 28-week-old mouse [81]. Similar to type II alveolar pneumocytes, these cells contain lamellar bodies (organelles in which surfactant is stored), have a characteristic polygonal-shaped morphology, and their growth is contact-inhibited (although they do gradually lose this inhibition when cultures reach confluency) [81]. They can also synthesize a large amount of phospholipids, albeit with a different phospholipid composition than pneumocytes type II in vivo [82]. In contrast to the normal diploid mouse cells with 40 chromosomes per cell [81], the LA-4 cells have on average 114 chromosomes (between 38 and 256 chromosomes) per cell [80]. In our case, they appeared to be the perfect model system because they could reproduce the in vivo observable events related to the response of epithelial cells to metal-oxide nanoparticles.

The MH-S cell line of murine alveolar macrophages (obtained from ATCC, CRL-2019 [83]) was originally obtained from a bronchoalveolar lavage of a 7-week male mouse by culturing the adherent alveolar macrophages for several days before infecting them with the SV40 virus [84]. The contact-uninhibited, adherent MH-S share many properties with alveolar macrophages, including typical macrophage morphology, function and antigenic characteristics [84]. According to the creators of the cell line, "this cell line should facilitate studies where homogeneous populations of alveolar macrophages are desirable, especially those involved in determining the immunological functions of alveolar macrophages and their potential role in lung pathology" [84], and is as such an excellent choice for the planned experiments.

2.4 Materials

2.4.1 Chemicals

LCIS: Live Cell Imaging Solution (Invitrogen), PBS: phosphate buffer saline (Gibco), 100x dcb: 100-times diluted bicarbonate buffer (pH 10, osmolarity 5 milliosmolar, mixed in-house), F-12K cell culture medium (Gibco), RPMI 1640 cell culture medium (Gibco), FBS: fetal bovine serum (ATCC), trypsin (Sigma), penicillin-streptomycin (Sigma), non-essential amino acids (Gibco), L-glutamine (Gibco), beta mercaptoethanol (Gibco), glucose (Kemika).

2.4.2 Fluorophores and Stains:

Alexa Fluor 647 NHS ester (Termo Fisher), CellMask Orange (Invitrogen), LysoTracker Red (Invitrogen), Hoechst reagent 33342 (Invitrogen), Propidium iodide (Invitrogen), DRAQ7 (Abcam), SAG-38 (3-(Benzo[d]thiazol-2-yl)-6,8,8,9-tetramethyl-2-oxo-8,9-dihydro-2H-pyrano[3,2-g]quinoline-4-carbonitrile, kind gift from Stane Pajk, FFA, UL).

2.4.3 Nanoparticles

Synthesized in-house by Polona Umek:

- TiO_2 nanotubes (PU-nTOX-01-03) and
- TiO_2 nanocubes (PU-nTOX-01-21);

Kind gift from Ulla Vogel:

- carbon black (Printex 90, kindly provided by Evonik, Frankfurt, Germany),
- TiO_2 MKNA015 (MKN- TiO2 -A015),
- TiO_2 MKNA100 (MKN- TiO2 -A100), and
- quartz silica (SiO_2 DQ12, kindly provided by Craig Poland, IOM, Edinburgh, UK);

Kind gift from the JRC Nanomaterial Repository:

- NM-101 TiO_2 anatase (TiO2-NM101-JRCNM01001a),
- NM-105 TiO_2 rutile-anatase (TiO2-NM105-JRCNM01005a),
- NM-110 ZnO (ZnO-NM110-JRCNM62101a),
- NM 111 ZnO (ZnO-NM111-JRCNM01101a),
- NM-200 SiO_2 (SiO2-NM200-JRCNM02000a),
- NM-401 MWCNT (MWCNTs-NM401-JRCNM04001a), and
- NM-402 MWCNT (MWCNTs-NM402-JRCNM04002a).

2.4.4 Materials

#1.5H µ-dishes (Ibidi), #1.5H µ-Slide 8-well (Ibidi), #1.5H µ-Slide 18-well (Ibidi), #1.5 µ-dish 35 mm quad (Ibidi), Amicon Ultra 4 mL 100K (Millipore), Multi-Analyte ELISArray Kit (Qiagen).

2.4.5 Software

Imspector (version 16.2.8282-metadata-win64-BASE) software provided by Abberior, SPCImage 7.3 (Becker & Hickl), Fiji – ImageJ 1.52p (NIH), Mathematica 12.0 (licence L5063-5112, Wolfram), Excel (Microsoft Office 2016, Microsoft), ilastik [85].

2.5 Methods

2.5.1 Preparation and Characterization of Nanoparticles

2.5.1.1 Synthesis and Labelling of TiO_2 Nanotubes

The TiO_2 anatase nanotubes that were used in most experiments in this work were synthesized by Polona Umek in a single large batch to ensure comparability between the various experiments. She also functionalized a part of them with AEAPMS, which we later labelled with fluorescent probes by a covalent reaction between the AEAPMS silane linkers on the nanoparticles and the NHS- or SDP-ester functional group on the probe. All this was done in-house using the protocol and quality-control procedure that we described in reference [53]. Once labelled, the TiO_2 nanotubes were stored suspended in 100-times diluted bicarbonate buffer with pH 10 at 1 mg/mL in a refrigerator to minimize aggregation. The sample was filtered through the 100 kDa membrane of a centrifugal filtration device (Amicon Ultra 4 mL 100K) at 1000 g (centrifuge LC-320, Tehtnica, Železniki) before experiments to remove any desorbed probe.

2.5.1.2 Nonlabelled Nanoparticles

Other nanoparticles were obtained in powder form either directly from the JRC Nanomaterial Repository – a specialized distribution source, or as a kind gift from the scientists that performed the complementary experiments using the same batch of

nanoparticles. The nanoparticles were suspended in 4 mL PBS by a 15-minute sonication on an ice bath with a tip sonicator (Sonicator 4000, Misonix, with 419 Microtip probe) using a series of 5 s ON/ 5 s OFF steps and a power of 2 kJ per minute of sonication (30 kJ in total). All these nanoparticle suspensions were optimized to have the same specific surface area (BET) of nanoparticles per volume of PBS by varying the concentration of nanoparticles between 0.3 (BET 300 m^2/g) and 15 mg/mL (BET 18 m^2/g). Thus, cells that received the same surface dose of nanoparticles also received the same volume of the vehicle (in this case PBS).

2.5.1.3 Characterization of the Nanoparticles

The main characteristics of the nanoparticles that were used in this work – such as their dimensions, chemical composition and specific surface area (BET) – are presented in Table A.3 in the Appendix. More information on the nanoparticles can be found in the following references. The TiO_2 anatase nanotubes, TiO_2 anatase nanocubes, small and large TiO_2 nanospheres and DQ12 were well-characterized in reference [29]. Additionally, we characterized and compared the labelled TiO_2 nanotubes to the nonlabelled nanotubes in reference [53]. The Printex 90 (carbon black) nanoparticles are characterized in the reference [86], whereas the rest of the nanoparticles were obtained from the JRC Nanomaterial Repository and are thus extremely well characterized in their publically available reports [87]–[90].

2.5.2 Culturing of Cell Lines

The LA-4 cell line of murine alveolar type II epithelial cells and the MH-S cell line of murine alveolar macrophages were obtained from the American Type Culture Collection (ATCC) as CCL-196 [80] and CRL-2019 [83], respectively. Both cell lines were cultured and sub-cultured according to the ATCC guidelines and grown in an incubator with a controlled humidified atmosphere with 5% CO_2 at 37 °C. The experiments were performed when cells were between the fourth and the twentieth passage.

The LA-4 cell line was cultured in Ham's F-12K medium (Gibco) that was supplemented with 15% fetal bovine serum (FBS, from ATCC), 1% penicillin-streptomycin (Sigma), 1% non-essential amino acids (Gibco), and 2 mM L-glutamine, whereas the MH-S were cultured in a RPMI 1640 medium (Gibco), that was supplemented with 10% FBS (ATCC), 1% penicillin-streptomycin (Sigma), 2 mM L-glutamine, and 0.05 mM beta mercaptoethanol (Gibco).

2.5.3 Preparation of in Vitro Samples for Imaging and Cell Tests

First, the cells were seeded into appropriate chambers for microscopy (#1.5 and #1.5H chambers by Ibidi) and cultured in the above-mentioned conditions for at least one day to ensure that the cells have attached to the bottom of the chamber, recovered from the splitting procedure, and started proliferating. Care was taken to seed the cells as evenly as possible, especially for imaging-based viability experiments in small wells.

At least 24 hours after the splitting, nanoparticles were added to the cells at an appropriate time-point before the experiment. The stock suspension of nanoparticles would be sonicated for 10 s in an ultrasonic bath (Bransonic ultrasonic cleaner, Branson 2510EMT) before adding the appropriate volume of the nanoparticle suspension to the sample to achieve the desired surface dose ($S_{NP} : S_{cells}$) for the experiment. The cells were then continuously cultured with the nanoparticles until the measurement was performed.

In the case of cocultures, the LA-4 epithelial cells were first seeded into the imaging chamber. After one day, the almost confluent layer of cells was washed with PBS and MH-

S were added to the already attached LA-4 at a number ratio of $N_{MH\text{-}S} : N_{LA\text{-}4} = 1 : 40$ and a 1:1 ratio of F-12K and RPMI full cell culture media. When observing the response of the coculture, the nanoparticles were added after both cell lines have grown in coculture for at least one day. However, for the reuptake experiments, the LA-4 and MH-S were first cultured and exposed to the nanoparticles in separate chambers, and thoroughly washed with PBS before adding the MH-S to LA-4.

Before imaging, the cells were labelled with the desired fluorescent dyes. As most imaging sessions were short in duration (up to a few hours), the medium with the dye was replaced with live cell imaging solution (LCIS) and cells were observed in a closed heated chamber. For longer sessions, the cells were observed in a home-made stage-top incubator which provided the appropriate temperature and CO_2 levels.

In one experiment, we nebulized the nanoparticles onto the LA-4 cells (already labelled with CellMask Orange) with removed cell medium while continuously imaging the system in xz. The exposure was performed by nebulizing a 100:1 surface dose of labelled TiO_2 nanotubes (concentrated to 33 mg/mL in PBS) using a pre-wetted Aeroneb®Pro nebulizer from a VITROCELL® Cloud 6 system, mounted onto a 50 mL centrifuge tube that was pre-cut to a length of 10 cm. Due to losses in the system, the surface dose that reached the cells was estimated to be 10:1. More on the nebulizing system can be found in [91].

2.5.4 In Vitro Imaging

2.5.4.1 Confocal Fluorescence Microscopy and STED Microscopy

Most of the in vitro micrographs were acquired on a laser scanning microscope that was custom-built by Abberior around an Olympus IX83 microscope. As shown in Figure 2.4, the microscope uses two excitation lasers at 561 and 640 nm (maximal average power of 50 µW in the sample plane, pulse length 120 picoseconds). An additional laser at 775 nm (maximal power of 170 mW in the sample plane, pulse length 1.2 ns) is shaped using a spatial light modulator into the characteristic doughnut shape that is used for STED depletion. The light emitted from the sample is detected by two avalanche photodiodes (APDs, SPCM-AQRH Excelitas) in two separate wavelength ranges: 580–625 nm and 655–720 nm, as defined by the filter sets (Semrock). The objectives used in this work were a 10x air objective (UPLFLN10, NA 0.3, Olympus) and a 60x water immersion objective (UPLSAPO60, NA 1.2, Olympus).

The images were acquired and contrasted using Imspector (version 16.2.8282-win64) software that was also provided by Abberior. In each experiment, the microscopy settings were tuned to achieve the best combination of signal-to-noise, resolution, speed of acquisition, and field-of-view of the micrographs while minimizing phototoxicity and photobleaching. The most commonly used microscopy settings are listed in Table 2.1.

Table 2.1: A short overview of the settings that were most commonly used for live-cell imaging shown in this work.

Imaging Mode	**Laser powers**	**Dwell time**	**Pixel size**	**Pinhole size**
Confocal	5-10 µW	10 µs	dx, dy: 100 nm dz: 200 nm	1.1 AU
STED	Excitation: 5-10 µW STED: 20-40 mW	30 µs	dx, dy: 30 nm dz: 50 nm	1.1 AU
FLIM	5-10 µW	100 µs	dx, dy: 100 nm dz: 200 nm	1.1 AU

2.5.4.2 FLIM

The fluorescence lifetime images (FLIM) were obtained on the same custom-built STED microscope (Abberior instruments) as described above in Section 2.5.4.1 and shown in Figure 2.4. To detect the time between the excitation and emission, the fluorescence was detected using a photomultiplier tube (16-channel GaASP PMT, Becker & Hickl) that was attached to a spectrograph with a diffraction grating of 600 lines per mm to measure photons with wavelengths ranging from 560 to 760 nm. The spectral information was discarded and the information on the photon arrival time was sent to a time-correlated single-photon counting unit (TCSPC, Becker & Hickl), which also collects information on the excitation timing in real time. From there, the information on the arrival times of all the photons detected in each pixel of the image was gathered in Imspector 16.2 (Abberior Instruments). The typical microscopy settings are shown in Table 2.1.

After acquisition, the fluorescence lifetime data was analyzed using the SPCImage 7.3 software (Becker & Hickl). Firstly, the Decay matrix was obtained from the brightest pixel in the image, and was used to determine the response function of the system. Then, the spatial distribution of the mean lifetime was calculated using monoexponential fitting of the arrival times, gathered from an array of 7 x 7 pixels (700 x 700 nm large area, obtained by setting the binning parameter in the software to 3). To avoid confusion, the lifetimes were not determined if the signal in the peak was below 5 counts, which corresponds to background noise (this was obtained by setting the Threshold parameter in the software to 5). For easier comparison of lifetimes between samples, the rainbow look-up-table was scaled from 500 ps to 1000 ps for all images, and both intensity and contrast of the lifetime-coded image were adjusted to improve the visibility of the structures of interest.

2.5.4.3 Imaging of Nanoparticles with Reflectance Microscopy

As discussed in Section 2.2.1, nonlabelled nanoparticles in the sample were located by detecting the backscattered light simultaneously with the detection of fluorescence. As shown in Figure 2.9, two versions of reflectance microscopy were developed and tested on the same STED microscope that was described in Section 2.5.4.1.

In the non-confocal version (shown in green in Figure 2.9), the same 561 or 640 nm excitation laser that was used for fluorescence microscopy was directed onto the sample. Then, both the emitted and scattered light from the sample passed through a 50:50 beam-splitter that directed half of the light onto a photomultiplier tube (PMT) and half onto the APDs. Because scattering is far more likely to occur than fluorescence in our samples, almost all the signal that is detected on the PMT arises from scattering. On the other hand, almost all photons that are detected on the APDs arise from fluorescence because the light passes through several filters that block the excitation wavelengths and hence also the scattered light.

For confocal reflectance microscopy (shown in dark red in Figure 2.9), a tunable Chameleon Discovery laser (Coherent, pulse length 100 fs) with a wavelength of 750 nm was directed onto the sample. Its maximal average power of 1.7 W (measured at 850 nm) was attenuated by several neutral density filters (ND filters) and later by a 785 nm built-in dichroic filter which reflected only a minor fraction of the beam, directing it onto the sample. The emitted and backscattered light passed through the same 785 nm dichroic, which transmitted most of the light, and a 0.63 A.U.-large pinhole, until a 725 nm dichroic separated the scattered light from fluorescence. The scattered light was thus directed onto a multi-channel photomultiplier tube (the PMT described in Section 2.5.4.2), which was set to detect wavelengths between 725 and 925 nm, and the fluorescence was detected using the afore-described APDs. Because of the large coherence of the Discovery laser, the

backscattered light exhibited strong interference, which resulted in a strong speckle pattern on the micrographs that could lead to false negative colocalisation. This was later diminished by applying a 100-nm-wide Gaussian blur to the micrographs, which sadly also reduced the spatial resolution.

2.5.5 In Vitro Cell Tests

2.5.5.1 Measuring Cell Viability

Cell viability was determined on LA-4 and MH-S monocultures that were exposed to various doses of the TiO_2 nanotubes. Just before imaging, the cell medium was very slowly removed and replaced with LCIS supplemented with 1.5 g/L glucose. Then, the cells were fluorescently labelled with a mixture of two dyes: one that labels the nuclei of all cells (5 µg/mL Hoechst reagent 33342), and a second, spectrally well-separated dye, that labels the nuclei of cells with compromised plasma and nuclear membranes (0.15 µg/mL propidium iodide – PI). Since cells with a compromised plasma and nuclear membrane (PI-positive cells) are mostly necrotic or in late apoptosis, they were counted as "dead". During imaging, two fluorescence and one bright-field micrograph were acquired on each of the five well-separated locations in the sample. To enable comparison between the samples despite uneven cell density (most likely due to the meniscus effect in small wells), the images were acquired at similar locations in each well. The field-of-view of each micrograph was 760 µm x 760 µm, corresponding to ca. 100-400 cells in the negative control.

The fluorescence micrographs that were used to determine cell viability were recorded using a 10x air objective (Plan Fluor 10x, NA 0.3, Nikon) on a home-built wide-field microscope built around a Nikon TE2000-E body. A bright Xe-Hg light (Lambda LS, Sutter Instrument) was used for excitation and a EMCCD camera (Rolera-MGi, QImaging) with 512 x 512 pixels for detection. In between, a set of appropriate filters and dichroics (Brightline, Semrock) was used: 352-402/409/417-477 nm for the Hoechst reagent 33342 and 503-538/560/596-664 nm for propidium iodide.

After imaging, the number of all cells (Hoechst-positive) and the number of dead cells (colocalized Hoechst and PI signal) in each image were determined by semi-automatic counting of cells using a custom-built program in Mathematica. In short, inhomogeneous illumination was first corrected using a top-hat transform with a disk kernel (similar to the Rolling Ball algorithm implemented in ImageJ). The image was then blurred using a Gaussian filter with a radius of 4 pixels (6 µm) to even out the signal, binarised using a user-defined threshold, and the remaining holes in the image were automatically filled in. Then, the distance of each pixel to the background was calculated, and the maximal values of these distances (above a used-defined threshold distance) were used as markers for the detection of morphological components on the gradient-filtered image using the rainfall watershed algorithm. This step greatly improved the ability to separate neighboring cells from one another. Then, components on the image that were appropriately large and circular (this was also user-defined but remained constant for all images of the same cell type) were counted to obtain the number of nuclei of all cells (Hoechst-positive) and number of nuclei of dead cells (PI-positive) in each location in the sample. When determining the number of dead cells, only those PI-positive objects that colocalized with Hoechst-positive objects were counted. Lastly, the number of living cells and fraction of dead cells were both calculated from the number of all cells and the number of dead cells.

2.5.5.2 Determining the Cauliflower-Forming Potential of Nanoparticles

The fraction of nanoparticles that were quarantined on the cell surface was estimated from the fluorescence-scattering micrographs and a visual overview of the sample. After 2 days of incubation with nanoparticles, the sample was measured on the above-described STED setup using a 60x water immersion objective, and a field of view of 80 x 80 μm. CellMask Orange fluorescence from the cells and scattering of nanoparticles were measured from 18 cells in each sample and a visual overview of the entire sample was performed. For each cell, a horizontal (xy) slice and two vertical (xz, yz) slices were acquired. The evaluation of cauliflower-forming potential of the nanoparticles is described in detail in Table A.1 in the Appendix.

2.5.5.3 Detecting Released Cytokines with ELISA

The concentrations of eight cytokines (CCL2 (MCP1), CCL3 (MIP1a), CCL4 (MIP1b), CXCL12 (SDF1), TNF-α, IFN-γ, IL-1b, and IL-6) released by a coculture of LA-4 and MH-S cells after exposure to seven nanoparticles (TiO_2 nanotubes, TiO_2 nanocubes, TiO_2 MKNA015, TiO_2 NM-101, TiO_2 NM-105, ZnO NM-111, and crystalline silica – DQ12) were measured using a kinetic measurement of a sandwich ELISA (Multi-Analyte ELISArray Kit, Qiagen). Cocultures of LA-4 and MH-S cells were grown in two 96-well plates for each 96-well ELISA plate and exposed to a 10:1 surface dose of various nanoparticles. After 48 h of incubation, the medium was removed from the cells, joined together (from the multiplicates exposed to the same nanoparticles), and centrifuged at 200 g for 5 minutes (centrifuge LC-320, Tehtnica, Železniki) to remove dead cells and cell debris. Afterwards, the upper 2/3 of the sample were transferred to a new microcentrifuge tube and centrifuged at 23000 g for 20 minutes (centrifuge MR22i, Jouan) to remove the majority of nanoparticles – this helps to avoid optical interference that is caused by binding of nanoparticles to the ELISA plates. The supernatant was transferred to a new microcentrifuge tube, 0.03% Triton X-100 was added to open up any vesicles in the sample, and the sample was centrifuged for 1 minute at 100 g (centrifuge LC-320, Tehtnica, Železniki) to remove bubbles in the sample. In the assay, 12.5% FBS was used as a negative control, the antigen standards from the kit were used as a positive control, and a blank, non-exposed coculture cultured in the same manner as the exposed cocultures was used as the third control.

From here on, the ELISA assay was performed as instructed by the manufacturer. First, the samples were added to the ELISA plate along with the Assay Buffer and incubated for two hours to let the cytokines bind to the cytokine-specific capture antibodies that were attached to the bottom of each well of the ELISA plate. After washing the plate to remove unbound molecules, the Detection Antibodies (to which biotin was bound) were added to the plate and incubated for one hour to allow them to bind to the captured cytokines. Then, the sample was washed and Avidin-HRP (avidin- horseradish peroxidase) was added to the wells for 30 minutes, during which the avidin molecule was able to bind to the biotin on the Detection Antibodies. After washing, the Development Solution containing H_2O_2 and the soluble TMB substrate (3,3',5,5'-tetramethylbenzidine) was added to the wells, and immediately afterwards the time-course of the absorbance was measured at 650 nm for 1 hour in steps of 15 seconds on a spectrophotometer (Infinite M1000 Pro, Tecan). During this time, the HRP enzyme catalyzed the colorimetric reaction that transformed the colorless TMB into its oxidized state, in which it absorbs light at 650 nm. The cytokine concentrations were calculated from the initial slopes of the absorbance time-dependence of the nanoparticle-exposed cells, adjusting for the measured values in the non-exposed

coculture, negative control (just the Assay Buffer) and positive control (Antigen Standard Cocktail), as described in detail in Section A.3 in the Appendix.

2.5.6 Model of Chronic Inflammation Following Nanoparticle Exposure

The theoretical model of nanoparticle cycling in the alveolus and its effect on cell population and chronic inflammation is described in detail in Chapter 4. It is defined by a system of differential equations, which can be further simplified to describe the in vitro monocultures of epithelial cells and macrophages, as well as their in vitro coculture. The system of differential equations was solved numerically to obtain the time evolution and final states of the model (so-called characteristic endpoints) using the function *NDSolve* in Wolfram Mathematica 12.0 (license L5063-5112). The same software was also used to visualize these results.

The phase space of the three nanoparticle-specific parameters (toxicity tox, cauliflower formation cff and signaling efficiency $signalEff$), termed "nanoparticle sorter cube", was predicted by calculating the time evolution of the in vivo system for various combinations of the three nanoparticle-specific parameters. For each of these three parameters, 30 values that were equally spaced in the logarithmically distorted phase space were selected, totaling the amount of predicted time evolutions in the grid to 30 x 30 x 30 = 27.000. The values of the final states of the model were read out and used to determine the contours that delimit areas with similar characteristic endpoints in the nanoparticle sorter cube. The same approach was used to model the cross-sections and projections of the nanoparticle sorter cube.

2.5.7 Analysis of In Vivo BAL Cell Numbers

In this work, we analyzed the cell numbers from bronchoalveolar lavages (BAL) of mice, published under a CC-BY license by Danielsen et al. [29]. In the study, they intratracheally exposed 8-week old mice to several mass doses of various nanoparticles (18, 54 or 162 μg of nanoparticles per mouse). After the desired time (1, 3, 28, 90, and 180 days), they flushed the lungs of anesthetized mice to obtain the BAL fluid, from which they isolated the BAL cells and counted them [29].

To compare cell numbers between the tested nanoparticles, we decided to estimate the cell numbers at the same surface dose for all nanoparticles because the often used metrics LOAEL (Lowest Observed Adverse Effect Level, lowest dose with observed adverse effect) and NOAEL (No Observed Adverse Effect Level**,** highest dose with no observed adverse effect) can skew the toxicity grading of nanoparticles, especially when the measurements have been performed at only a few exposure doses (see Figure A.10 in the Appendix). First, the surface doses of the exposures published in [29] were calculated from the mass dose (18, 54 or 162 μg of nanoparticles per mouse), characteristic BET surface area of the nanoparticles, and the estimated lung surface area of a 20-gram 8-week old mouse (80 cm^2) [92], [93]. Then, linear interpolation between the exposure doses for the same nanoparticle was used to calculate the approximate cell numbers at a 1:1 surface dose exposure. This was possible for all nanoparticles except for DQ12, where linear extrapolation was used due to the lack of data-points – it was measured only at the highest mass dose 162 μg, whereas the 1:1 surface dose was equivalent to 800 μg, which was well out of the measured range. The cell numbers at exposure (day 0) were estimated by calculating the average cell numbers of all the negative controls – mice exposed to the sham control (vehicle without nanoparticles). For the dose dependence graphs, the cell numbers at day 0 and exposure surface dose were calculated in the same manner as described above, except for the interpolation which was not needed.

Chapter 3

Results and Discussion – Key Events in Nanoparticle-Exposed Alveolar Cells

The results presented in this and the following chapter are a part of our contribution to the interdisciplinary, international H2020 SmartNanoTox project, and formed the basis of the publication H. Kokot, B. Kokot, A. Sebastijanović et al., "Prediction of Chronic Inflammation for Inhaled Particles: the Impact of Material Cycling and Quarantining in the Lung Epithelium" [94] – one of the major outcomes of the project.

As mentioned in the Introduction, a plethora of complementary in vivo, in vitro, and in silico experiments should be performed using the same nanoparticles (mostly TiO_2 nanotubes) in order to mechanistically understand the complex network of events in the nanoparticle-exposed alveolus. Several of the findings from complementary approaches, which were performed by other members of the consortium, are included in the discussion of our experimental results with the aim of enriching the discussion and increasing the impact and validity of the conclusions. This was done with permission from the authors, who are clearly attributed in the text.

As a side note, we would like to stress that the micrographs presented in this chapter were obtained using different experimental setups. Most of them are fluorescence micrographs of the horizontal plane (denoted as xy) of an in vitro cell culture obtained using a confocal fluorescence microscope with a 60x water immersion objective; cell components on the micrographs are shown in green and nanoparticles in red. Any differences in the setup are clearly stated.

In order to understand the complex network of events that take place in the alveolus following nanoparticle exposure, we decided to imitate the latter by a combination of simple in vitro sub-systems. By focusing first on the events in monocultures of alveolar macrophages, then on monocultures of epithelial cells and, lastly, on the events in the coculture of these cells, the flow of nanoparticles and the interactions between the events are simplified, and can thus be discerned more easily (see Figure 3.1).

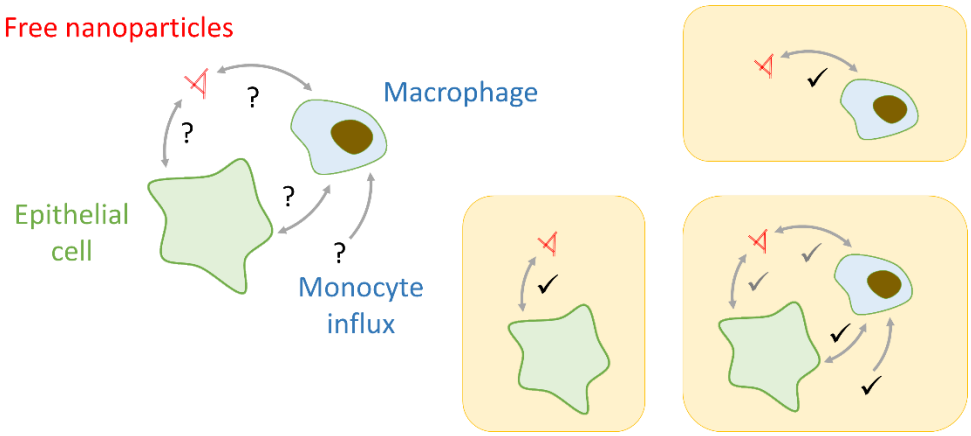

Figure 3.1: Splitting the system into simple subsystems lowers the complexity of interactions.

3.1 Macrophages Die Trying to Defend the Epithelium from Nanoparticles

Because macrophages are cells of the immune system whose role is to defend the body from foreign objects, we decided to first study and discuss the interaction between the model nanoparticles – TiO_2 nanotubes – and MH-S, a cell culture of alveolar macrophages.

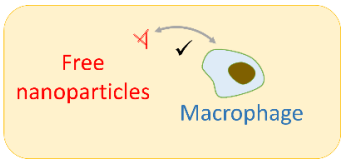

3.1.1 Macrophages Immediately Start to Internalize Nanoparticles

Macrophages are cells that are specialized for recognition, internalization and degradation of foreign bodies. It is therefore not surprising that the MH-S started to internalize TiO_2 nanotubes immediately after coming into contact with them. As seen in Figure 3.2, these macrophages can internalize various sizes of particles, from single nanotubes to aggregates of nanotubes as large as half their size. They were also observed to lift large nanotube aggregates from the floor and internalize them (Figure 3.2 A) – similarly to what macrophages are known to do with bacteria [95]. Interestingly, when a macrophage was observed interacting with and trying to internalize an aggregate much larger than itself, a haze of nanotubes could be observed inside the macrophage (Figure 3.2 C). This haze corresponded to a multitude of internalized single nanotubes, which were most likely torn from the aggregate by the macrophage and would soon be condensed into larger nanotube agglomerates, as the ones seen on the left of the macrophage.

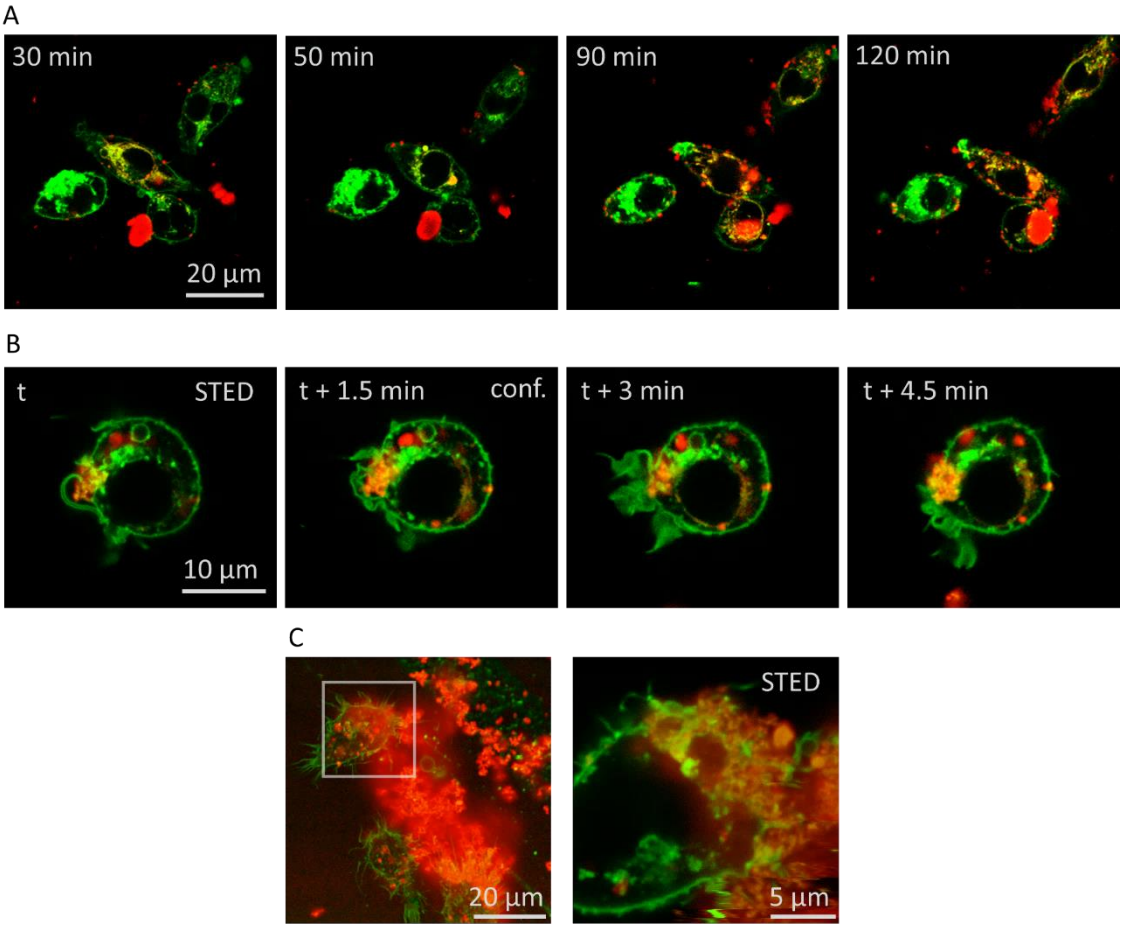

Figure 3.2: Macrophages internalize various sizes of nanotube aggregates. **A** A time-lapse of four MH-S macrophages (green) internalizing various sizes of TiO_2 nanotubes aggregates (red) very soon after exposure (1:1 surface dose – ratio between the nanoparticle and cell surface areas). **B** A time-lapse of a MH-S macrophage internalizing a 5 µm large aggregate of TiO_2 nanotubes after 2 days of exposure to a 10:1 surface dose of nanoparticles. Only the first frame is a STED micrograph, the rest are confocal (conf.). Notice how the plasma membrane ruffles and wraps around the aggregate during the internalization, as is characteristic for macropinocytosis and phagocytosis. **C** A confocal micrograph and a STED zoom-in of MH-S macrophages, engaging in internalization of a huge aggregate of TiO_2 nanotubes after 2 days of incubation with a 10:1 surface dose of nanoparticles. The red haze inside the macrophage corresponds to a multitude of single, non-aggregated nanotubes. Because 70% 3D STED was used, the improved resolution in the axial direction ensures that the red haze is inside the cell and is not an artefact of an elongated point-spread function. All fluorescence micrographs in **A, B** and **C** were acquired in the horizontal (xy) plane with a 60x wi objective, cell membranes were labelled with CellMask Orange (shown in green), and TiO_2 nanotubes with Alexa 647 (shown in red). The intensity of the nanotubes (red channel) was logarithmically scaled and cut-off below 2 counts to show both the single nanotubes as well as big aggregates.

3.1.2 The Macrophages are Full of Nanoparticles Several Days After Exposure

After several days, a large amount of the TiO_2 nanotubes was located in the MH-S macrophages, most commonly in the form of spherical aggregates of fairly uniform sizes, ranging from 0.5 μm to a few micrometers in size, as can be seen in Figure 3.3. This is different than the situation at shorter time-points, where both smaller and larger aggregates were common, suggesting that in this time, macrophages rearranged and re-aggregated the internalized nanoparticles.

A consequence of nanoparticle aggregation inside the macrophages is the reduction of the total surface of nanoparticles that can interact with biological milieu (so-called active nanoparticle dose). Also, the macrophages at that time-point did not appear to be crucially depleted of energy, judging from the vivid movement of their plasma membrane, as well as of the vesicles and nanoparticle aggregates in the macrophages (see Figure A.12 in the Appendix). This is in agreement with the transcriptomics that was performed on the same system by J. Becker's and T. Stoeger's labs (HZM Germany) [94]. According to their results (which are summed up in Figure A.13), the two most prominently up-regulated hallmark gene sets in macrophages at this time-point, i.e. two days after exposure, were Oxidative phosphorylation and mTORC1 signaling, which are both involved in energy production. The former includes genes that encode proteins involved in oxidative phosphorylation (OXPHOS): a highly efficient sequence of chemical reactions in the mitochondria that releases the energy stored in nutrients (e.g. glucose) in the presence of oxygen, and stores the energy by producing ATP. The mTORC1 signaling gene set includes genes that are up-regulated when the mTORC1 complex is activated, increasing the synthesis of proteins, lipids and nucleotides, and glycolysis (rapid and less efficient glucose metabolism in the cytoplasm that also provides intermediates for the aforementioned biomolecule synthesis), all of which are needed for cell growth and proliferation [96], [97].

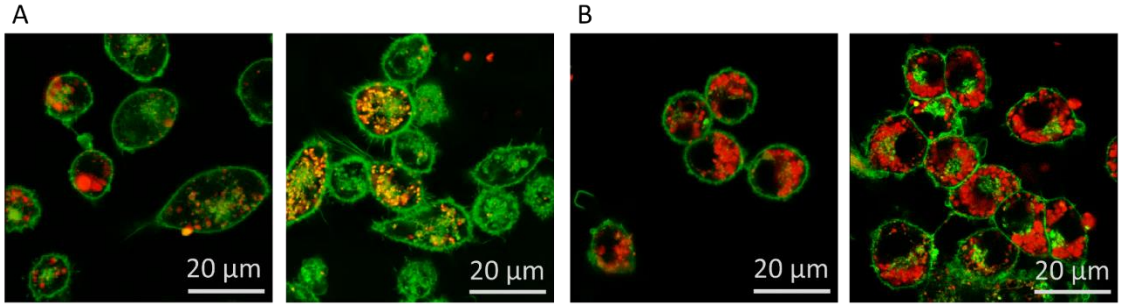

Figure 3.3: Macrophages are full of nanoparticles several days after exposure. The xy confocal fluorescence micrographs of MH-S macrophages (green) were acquired **A** after a 4-day incubation with a 1:1 surface dose of TiO_2 nanotubes (red) and **B** after a 2-day incubation with a 10:1 surface dose of the same nanoparticles. In both cases, the macrophages internalized large amounts of nanoparticles. Cell membranes were labelled with CellMask Orange (green) and TiO_2 nanotubes with Alexa 647 (shown in red, intensity is logarithmically scaled and cut-off below 2 counts).

3.1.3 Macrophages Die After Internalizing the Nanoparticles

Sometimes, a haze of nanotubes was observed inside certain macrophages, indicating the presence of a multitude of non-aggregated nanoparticles (left two columns in Figure 3.4). If these would not soon be aggregated by the cell, they could dangerously increase the nanoparticle surface dose that can interact with the cell interior and increase the risk of cell death. Several examples of dead macrophages can be observed in the right three columns in Figure 3.4.

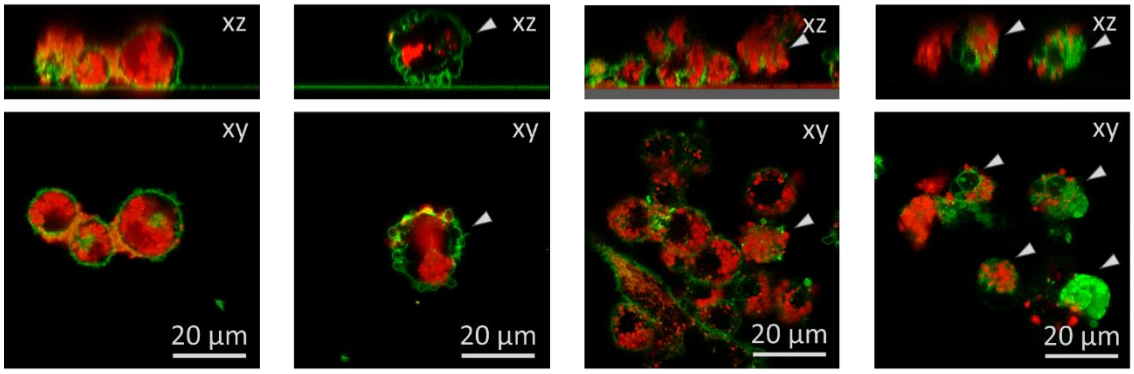

Figure 3.4: Dead macrophages and a haze of non-aggregated nanoparticles in macrophages can be observed after a few days of nanoparticle exposure. The horizontal (xy) and corresponding vertical (xz) confocal fluorescence micrographs show MH-S macrophages (membranes labelled with CellMask Orange, shown in green) after a 2-day long incubation with a 10:1 surface dose of TiO_2 nanotubes (labelled with Alexa 647 and shown in red, intensity is logarithmically scaled and cut-off below 2 counts). In the left two columns, a haze of nanoparticles can be seen inside the macrophages, and the right three columns show examples of dead and dying macrophages (denoted with arrowheads). Some of the xz micrographs were padded with grey to ensure that the figures are equal in size.

Indeed, according to the viability data shown in Figure 3.5, exposure to large surface doses of TiO_2 nanotubes (e.g. 100:1) decreases the viability of MH-S macrophages after several days of incubation. Alongside measurements of cell viability, copious amounts of cell debris found in in vitro lavages are also indicators of cell death (see Figure 3.6 A). One can also observe abundant cell debris in lavages of mice, exposed to TiO_2 nanotubes (according to C. Endes and D. Kutschke, HZM Germany, personal communication, August 2018). An important consequence of macrophage death is that the dead macrophages inevitably re-expose other macrophages to the nanoparticles they had previously internalized, consequently increasing the active dose of the nanoparticles and the death rate of the remaining macrophages.

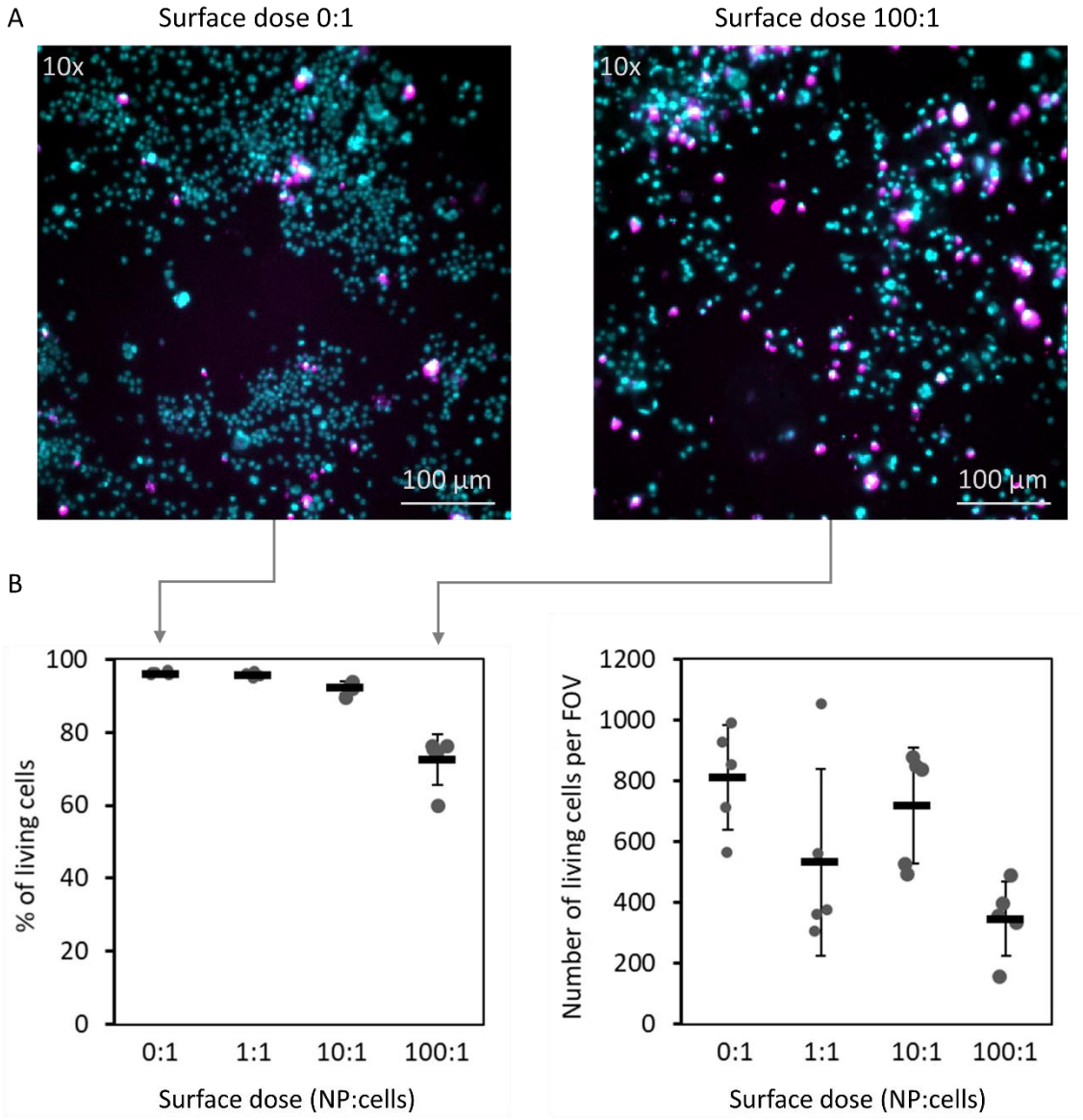

Figure 3.5: Exposure to large surface doses of TiO_2 nanotubes lowers the viability of macrophages. After a 2-day incubation of MH-S with TiO_2 nanotubes, the cell medium was gently removed and the viability of remaining cells was measured by semi-automatic counting of dead cells and all cells from micrographs. **A** In the micrographs, the nuclei of all cells were labelled with Hoechst 33342 (shown in cyan) and the nuclei of dead cells with propidium iodide (shown in magenta). **B** The percentage of dead cells and number of living (non-dead) cells per field of view (760 x 760 µm large) were calculated from the counted cell numbers. Each marker in the graphs corresponds to one of the five locations in which the sample was measured, the horizontal bars represent the mean value, and the error bars the standard deviation.

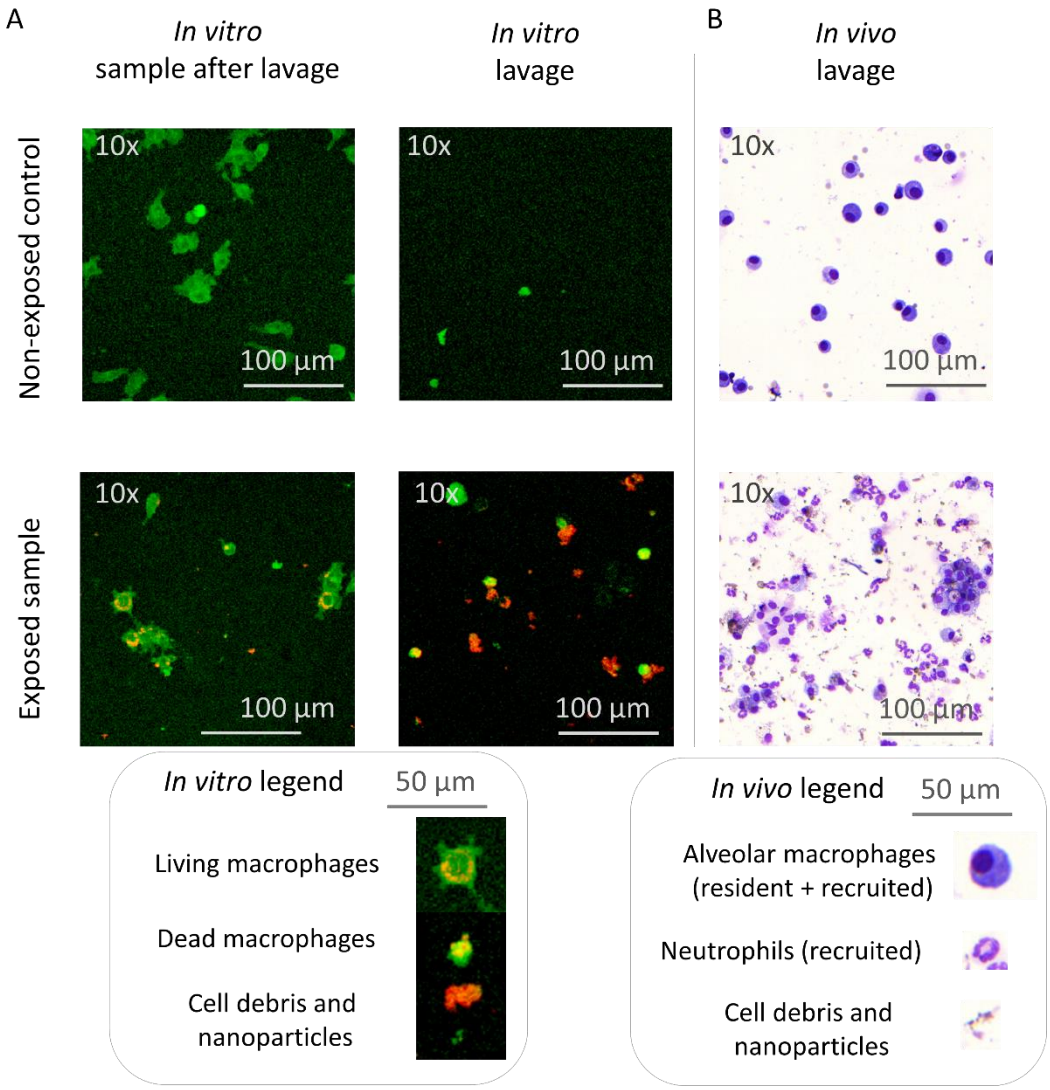

Figure 3.6: Dead cells and cell debris are present in both in vitro and in vivo lavages. **A** Fluorescence micrographs of a MH-S monoculture and its lavage (cell membranes were labelled with CellMask Orange, shown in green) after a 4-day incubation with a 10:1 surface dose of TiO_2 nanotubes (labelled with Alexa 647, shown in red). **B** Bright-field micrographs of cytospins of murine lavages one day after intratracheal exposure to a 2:1 surface dose of TiO_2 nanotubes, doped with Europium. The lavage was stained with May-Grünwald-Giemsa stain prior to imaging, which stained the negatively charged parts of the cell (e.g. nuclei) purplish-blue and the positively charged (e.g. proteins, granules) pink; unlabeled TiO_2 nanotubes appear grey and black. The exposure and lavage preparation in **B** are described in detail in [98], and the in vivo micrographs are courtesy of Carola Endes and David Kutschke.

Importantly, these TiO_2 nanotubes induce macrophage death not only in vitro, but also in instilled mice (as was shown by Danielsen et al. [29]), which creates a link between our in vitro and the in vivo results. In vivo, macrophage death can be directly observed by counting the number of macrophages in the lavages of exposed mice, as we show in Figure 3.7, Figure A.14 and Figure A.15 for data, which we re-analyzed from the raw data published in [29]. Nanoparticle-induced macrophage death is best seen with large exposure

doses, at the latest one day after the exposure. At later time-points and lower doses, the decline in macrophage numbers can be completely masked by the influx of monocytes into the alveoli as they differentiate into macrophages and raise the macrophage numbers back to the baseline or even above. According to two of the rare publications in which the BAL cell numbers were measured at very early time-points, i.e. a few hours after the exposure, the largest decline in macrophage numbers actually appears at around 12 hours after instillation, and the infiltration of neutrophils (accompanied by a significant increase in cytokine concentrations) can already be observed 3 hours after exposure (earlier time-points were not measured) [98], [99].

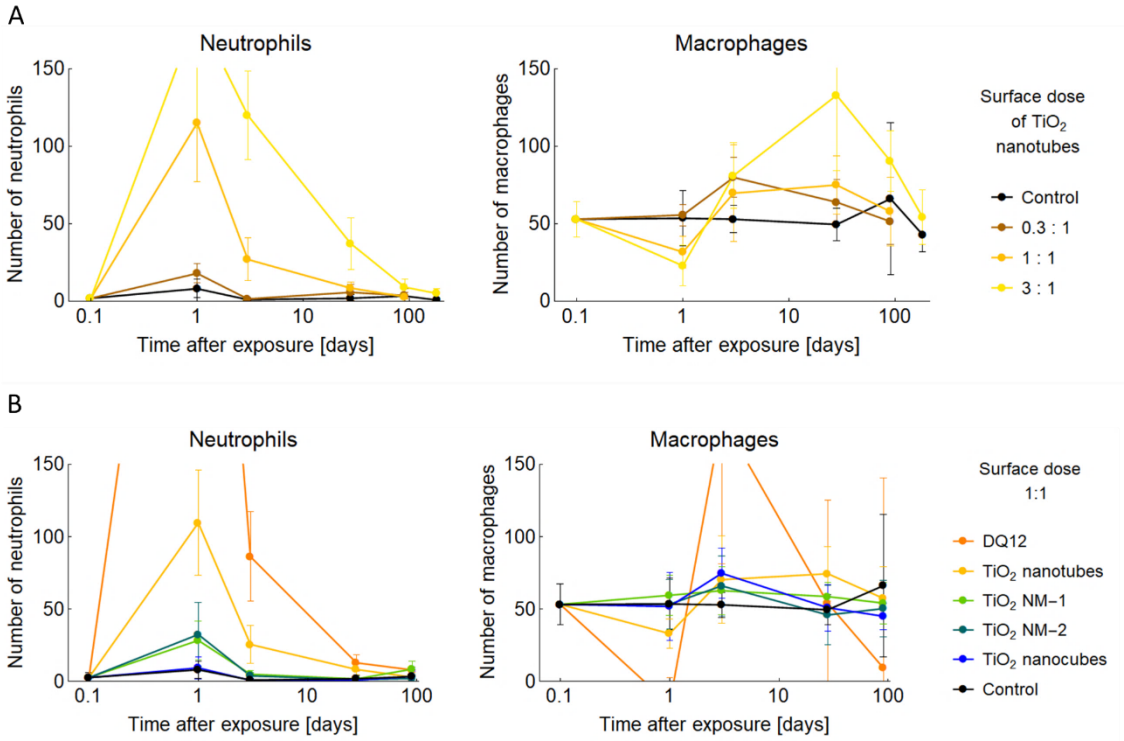

Figure 3.7: Time-courses of the macrophage and neutrophil numbers in the bronchoalveolar lavage fluid (BAL) of instilled mice. The time-courses are compared for **A** three different surface doses of the TiO_2 NTs (corresponding to 18 µg, 54 µg and 162 µg per mouse) and **B** five different metal oxides at a 1:1 surface dose (ratio between the nanoparticle and lung surface areas). We recalculated the surface doses from the raw BAL cell numbers and mass doses, published in [29] by Pernille Høgh Danielsen, Kristina Bram Knudsen, and Ulla Vogel (CC BY license). In the calculation, we assumed a lung surface area of 80 cm^2 for the 20 g heavy 8-weeks old mice [92], [93] that were used in the published work. We calculated the data for the lower graphs using linear interpolation for all nanoparticles except for DQ12, for which linear extrapolation was used – hence the non-physiological negative number of macrophages at day 1 after exposure. The values at time of exposure (day 0) were determined as the mean of all the negative controls at various time-points (mice exposed to sham control – 0 µg of nanoparticles).

An important trend that emerges from the time-courses of in vivo BAL cell counts following exposure to various doses of the TiO_2 nanotubes (Figure 3.7 A) and exposure to the same surface dose of different metal oxides (Figure 3.7 B, both recalculated from the data published in [29]) is that the exposures that caused a strong, long-lasting influx of neutrophils (and thus also prolonged inflammation) also strongly depleted macrophage

numbers one day after exposure. This effect is more pronounced with exposures to large surface doses of nanoparticles (yellow and orange markers in the dose-dependent response to TiO_2 nanotubes in Figure 3.7 A) and exposures to more toxic nanoparticles (e.g. DQ12 and TiO_2 nanotubes, denoted with orange and yellow markers in the in vivo response to various nanoparticles at the same surface dose in Figure 3.7 B). These exposures also initiated notable infiltration and differentiation of monocytes into macrophages at later time-points, which can be deduced from the increased number of macrophages. However, as shown in Figure 3.8, the connection between the initial macrophage depletion and later neutrophil numbers a month post exposure appears to be less pronounced, hinting that sustained inflammation is a consequence of not only macrophage death, but also of other processes that might include other cell types as well.

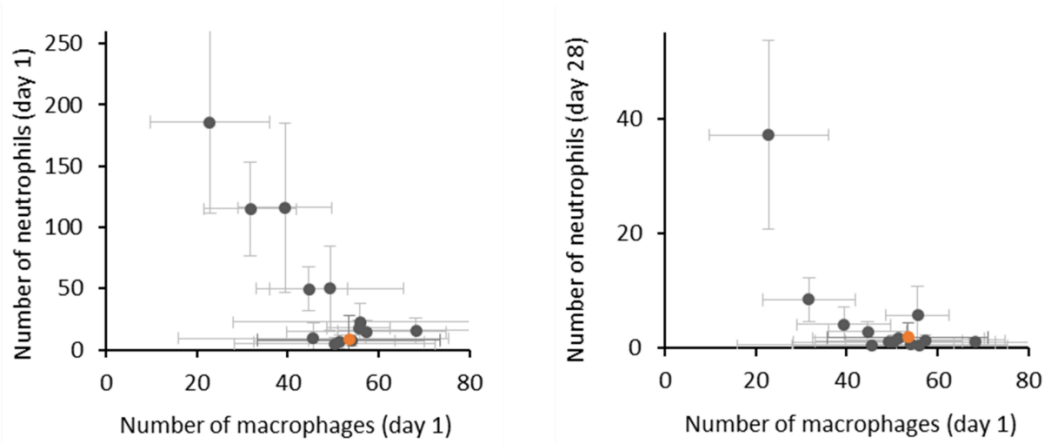

Figure 3.8: The relation between macrophage and neutrophil numbers a day after exposure (acute inflammation) is nicely discerned, whereas the relation between initial macrophage depletion and neutrophil numbers after a month of exposure (prolonged inflammation) is not as simple. We pooled together and plotted the raw data published by Danielsen et al. in [29] (CC BY) from in vivo lavages of the mice instilled with five similar metal-oxide nanoparticles at three doses. The various nanoparticle exposures are shown in black, and the control measurement in orange. Because the number of macrophages one day after exposure depends on the balance between macrophage death and influx of new macrophages, the relation on the left graph is not monotonous.

3.1.4 Macrophages Do Not Manage to Internalize All Nanoparticles

Unexpectedly, the MH-S macrophages do not manage to uptake all of the TiO_2 nanotubes – not even over the course of several days. As shown in Figure 3.9 (left), a significant amount of nanotubes was still located outside the macrophages even after several days of exposure to surface doses low enough to have no major influence on the macrophage death rate (according to the viability results shown in Figure 3.5). Interestingly, a perimeter around the macrophages was well-cleaned, whereas the rest of the sample was not. The inability of macrophages to clean the entire surface was even more pronounced at higher doses (Figure 3.9 right), where the incomplete macrophage cleaning of the surface was worsened by the effect of macrophage death, which not only lowered macrophage numbers, but also caused re-release of nanoparticles.

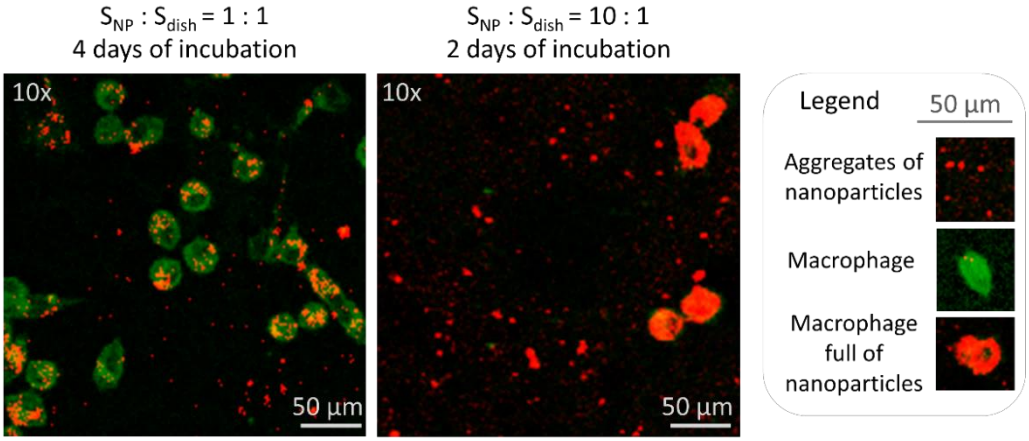

Figure 3.9: Macrophages do not manage to internalize all the nanoparticles. The fluorescence micrographs show presence of nanoparticles outside of macrophages (cell membranes labelled with CellMask Orange, shown in green) after several days of incubation with TiO_2 nanotubes (labelled with Alexa 647, shown in red).

On the one hand, the observed incomplete nanoparticle clearance could be caused by the non-physiological glass surface of the dish in which these experiments were performed. However, from the aligned fluorescence micrographs of a long-term measurement of MH-S macrophages in their coculture with LA-4 epithelial cells (which mimics the situation in the alveolus where macrophages move on top of epithelial cells), we determined the maximal speed of non-exposed macrophages to be approximately 200 nm/min (see Figure 3.10), which equals 12 µm/h and is consistent with published measurements of human monocyte-derived macrophages [100]. If macrophages systematically scanned the alveolar surface with this speed, they would scan only 5 % of the alveolar surface in one hour and would need 22 hours to scan the entire alveolar surface (the calculation of scanned surface is described in Section A.8 in the Appendix). Consequently, macrophages are inherently too slow to fully prevent nanoparticles from reaching the underlying epithelial cells.

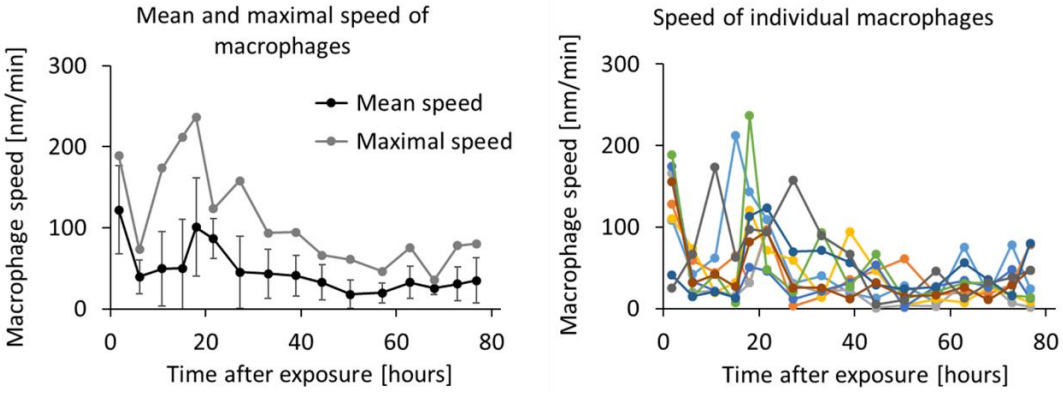

Figure 3.10: The macrophages slow down during the exposure to nanoparticles. The graphs show the time-dependence of the speed of macrophages in a coculture with epithelial cells, exposed to a 10:1 surface dose of labelled TiO_2 nanotubes. We calculated the mean and maximal speed (shown on the left graph) from the speed data (right graph), which we calculated from the positions of nine macrophages in aligned fluorescence micrographs that were acquired over a period of 80 hours (published in [94]).

An interesting observation from the graphs in Figure 3.10 is that the MH-S macrophages slowed down after exposure to TiO_2 nanotubes. One explanation could be that they were surrounded by nanotubes and hence did not need to scan the surface to find other foreign bodies. Secondly, they might be focusing mainly on repairing the internal damage caused by the internalized nanotubes in order to survive. Thirdly, the strong interactions between the cells and the nanoparticles could act as glue, binding the cells together and inhibiting their movement (see Section A.9 in the Appendix). Fourthly, because we have observed that these specific nanotubes can disrupt the actin cytoskeleton in lung epithelial cells [94], it would be of no surprise if the same process also took place in macrophages, hindering their movement and phagocytosis, thus further limiting their clearance of nanoparticles. The observed slow-down of macrophages is also in line with recently published in vivo and in vitro observations of nanoparticle-induced attenuation of phagocytosis and migration in macrophages (albeit for different macrophages – RAW 264.7 cell line, BV2 microglial cell line, primary microglial cell cultures, bone marrow-derived macrophages, macrophages in living zebrafish larva – and other nanoparticles – Au NPs, CuO, CoO, Fe3O4, CNT, Mn_2O_3, and others) [101]–[103].

Importantly, the incomplete and slow internalization of nanoparticles by macrophages inevitably causes a non-negligible fraction of nanoparticles to bypass the macrophages and consequently reach and interact with the epithelial cells. Thus, pneumocytes – lung epithelial cells – and their direct interaction with nanoparticles are likely to play a major role in nanoparticle-induced adverse outcomes as well.

3.1.5 Short Summary

Alveolar macrophages – "the defenders of the lungs" – internalize nanoparticles and their aggregates, which they then condense into large structures inside the cells. Their viability is significantly lowered when exposed to large nanoparticle doses, with the consequent cell death re-exposing the neighboring cells to the internalized nanoparticles. Because the alveolar macrophages are unable to internalize all nanoparticles, a large fraction of the nanoparticles inevitably interacts directly with the underlying lung epithelial cells.

3.2 Nanoquarantine – an Unexpected Cellular Defense Mechanism

In order to understand the role of lung epithelial cells in the nanoparticle-exposed lung, we shall again simplify the observed system and investigate the nanoparticle-induced events in a monoculture of the LA-4 cell line (type II epithelial cells) exposed to TiO_2 nanotubes. Wherever possible, we will link the observed in vitro events to the in vivo observations from mice exposed to the same nanotubes via instillation.

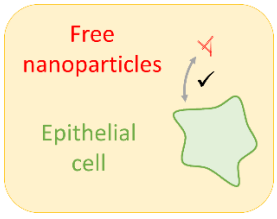

3.2.1 Epithelial Cells Immediately Start to Internalize Nanoparticles

Similar to MH-S macrophages, the LA-4 epithelial cells are also able to internalize considerable amounts of TiO_2 nanotubes. Noteworthy, they mostly internalize single nanotubes and small aggregates, but we also observed them internalizing larger nanoparticle aggregates, e.g. 5 μm in size. An hour after nanoparticle exposure, most of

the internalized TiO_2 nanotubes were located inside acidic organelles (see Figure 3.11 A) – e.g. late endosomes and/or lysosomes, which are filled with enzymes capable of degrading various biomolecules. This indicates that most TiO_2 nanotubes enter the cell by endocytosis. The remaining small portion of nanotubes inside the LA-4 cells does not co-localize with lysosomes one hour after the exposure, as shown in Figure 3.11 B, and most likely entered the cells in a different manner. However, after a few days of nanoparticle exposure, a large fraction of the nanoparticles inside epithelial cells are located outside of lysosomes/late endosomes in large nanoparticle aggregates.

Unexpectedly, when we nebulized the nanotubes directly onto a LA-4 monolayer, some nanotubes passed through the plasma membrane in an order of seconds, as shown in Figure 3.11 C. As this time scale is much quicker than the minute-long process of clathrin-mediated endocytosis, such a quick passage could arise either from clathrin-independent fast endocytic processes [104] or from a purely passive passage of single nanotubes through the membrane – a process termed direct translocation. This process is caused by the strong affinity between the nanotubes and the cell membrane that induces and mediates the process of lipid wrapping [105]–[107].

It is important to stress that even though the LA-4 cells mostly internalize the TiO_2 nanotubes by endocytosis, this does not imply that they have specific receptors for nanoparticles. On the contrary, the endocytosis process is likely triggered by a) the various biomolecules that are adsorbed to the nanoparticles in the so-called corona and can bind to the endocytotic receptors and/or b) unspecific interaction of nanoparticles with these receptors and/or the plasma membrane.

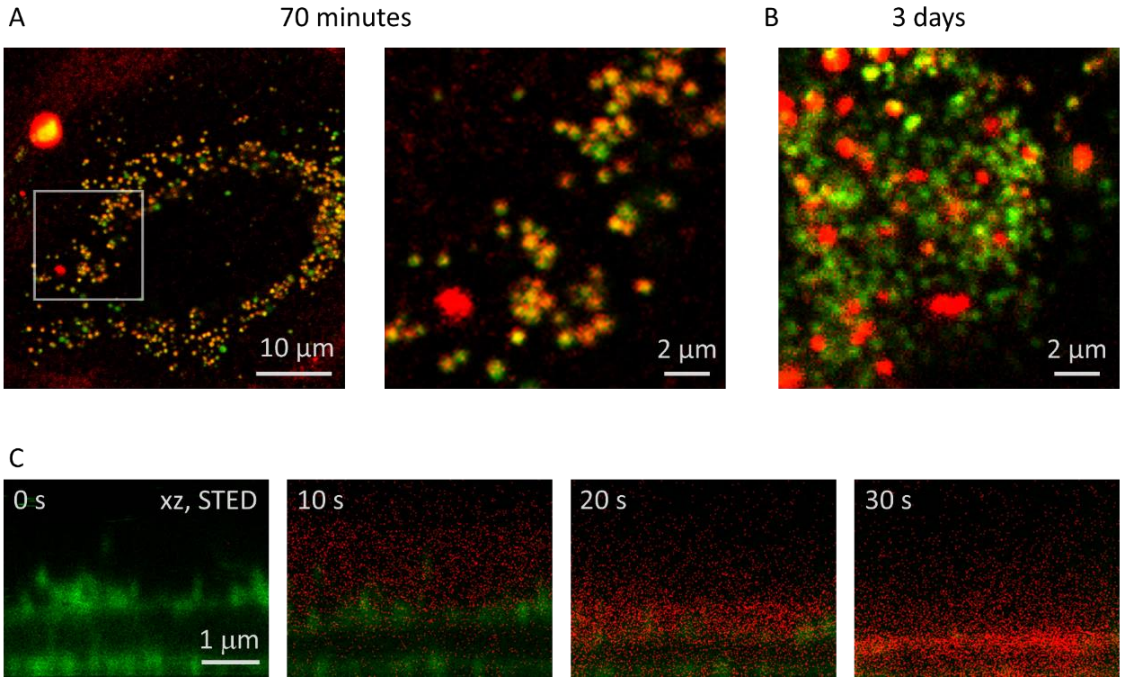

Figure 3.11: The nanotubes enter the cell through multiple mechanisms – mostly by endocytosis, but also through other routes, e.g. fast endocytic processes and direct translocation. **A** A fluorescence micrograph and a zoom-in of an LA-4 epithelial cell after a 70-minute incubation with a 1:1 surface dose of TiO_2 nanotubes. **B** An equally contrasted fluorescence micrograph of an LA-4 epithelial cell after 3 days of incubation with a 10:1 surface dose of TiO_2 nanotubes. In **A** and **B**, the TiO_2 nanotubes were labelled with Alexa 647 (shown in red) and lysosomes with LysoTracker Red (shown in green), which partitions into acidic organelles and thus also labels late endosomes. **C** Side view (xz) time-lapse of nebulization of a 1:1 surface dose of TiO_2 nanotubes (labelled with Alexa 647, shown in red, contrasted from 1 to 3 counts) directly onto a layer of LA-4 epithelial cells (cell membranes labelled with CellMask Orange, shown in green). The pronounced bleaching of the CellMask signal is due to the continuous use of STED laser during imaging (the frame rate of the original time-lapse was one frame per second). Note the presence of nanoparticles inside the cell from the second image onward.

The endocytosis-mediated entry of the nanotubes into LA-4 cells is supported by findings of P. Zawilska who observed that the majority of internalized nanotubes were localized in endosomes after 30 minutes of exposure. Moreover, when she blocked all internalization pathways except macropinocytosis and phagocytosis [108], [109] with chlorpromazine, almost no nanotubes were observed inside the LA-4 epithelial cells [94]. Interestingly though, when we re-contrasted her published micrographs, we noticed that a small fraction of single nanotubes slowly relocated into the chlorpromazine-exposed cells (see Figure 3.12), possibly being internalized through macropinocytosis or by passively passing through the membrane as described above.

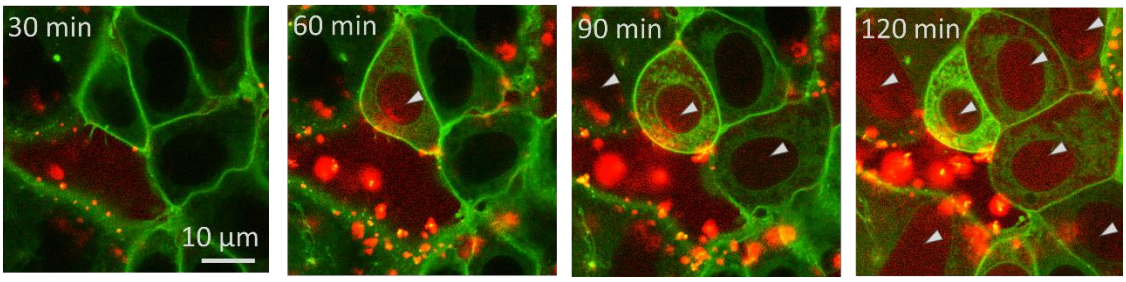

Figure 3.12: The major route of nanoparticle internalization is endocytosis, with other routes also present. Confocal time-lapse of LA-4 epithelial cells (cell membranes labelled using STAR580 DPPE, shown in green) that were pre-incubated for 15 minutes with 100 µM chlorpromazine to block multiple endocytotic pathways, and exposed to a 10:1 surface dose of TiO_2 nanotubes (labelled with Alexa 647, shown in red), with the chlorpromazine remaining in the medium during the exposure to nanoparticles as well. We re-contrasted the red channel of the original published micrographs for easier visualization of infiltration of single nanoparticles into the cell (arrowheads). Note that due to strong intensity scaling, it is impossible to discern whether the red signal near the edge of the cell corresponds to aggregates just below the plasma membrane or to aggregates on the cell surface from a single confocal slice. Original images are courtesy of Patrycja Zawilska; adapted from [94] (CC BY-NC) with permission.

3.2.2 Surface-Bound Bio-Nano Structures (Cauliflowers) Grow on Epithelial Cells In Vitro and In Vivo

Unexpectedly, a few days after exposure we observed large structures on the surface of the LA-4 epithelial cells, which were composed from TiO_2 nanotubes and biological molecules (see Figure 3.13 for several examples of these structures at various magnifications; the structures appear yellow in the micrographs). In the epithelium monoculture, these large bio-nano structures were always observed on the surface of the cells, never inside cells or freely-floating in the sample medium. Importantly, the surface-bound structures were larger when the epithelial cells were exposed to larger surface doses of nanoparticles (see Figure 3.13) and they would grow with time (see Figure 3.14). Because a literature search returned no descriptions of such a phenomenon, we termed these newly-discovered structures cauliflowers (due to their grainy texture and yellow color in our false-colored confocal fluorescence micrographs) and decided to examine them further.

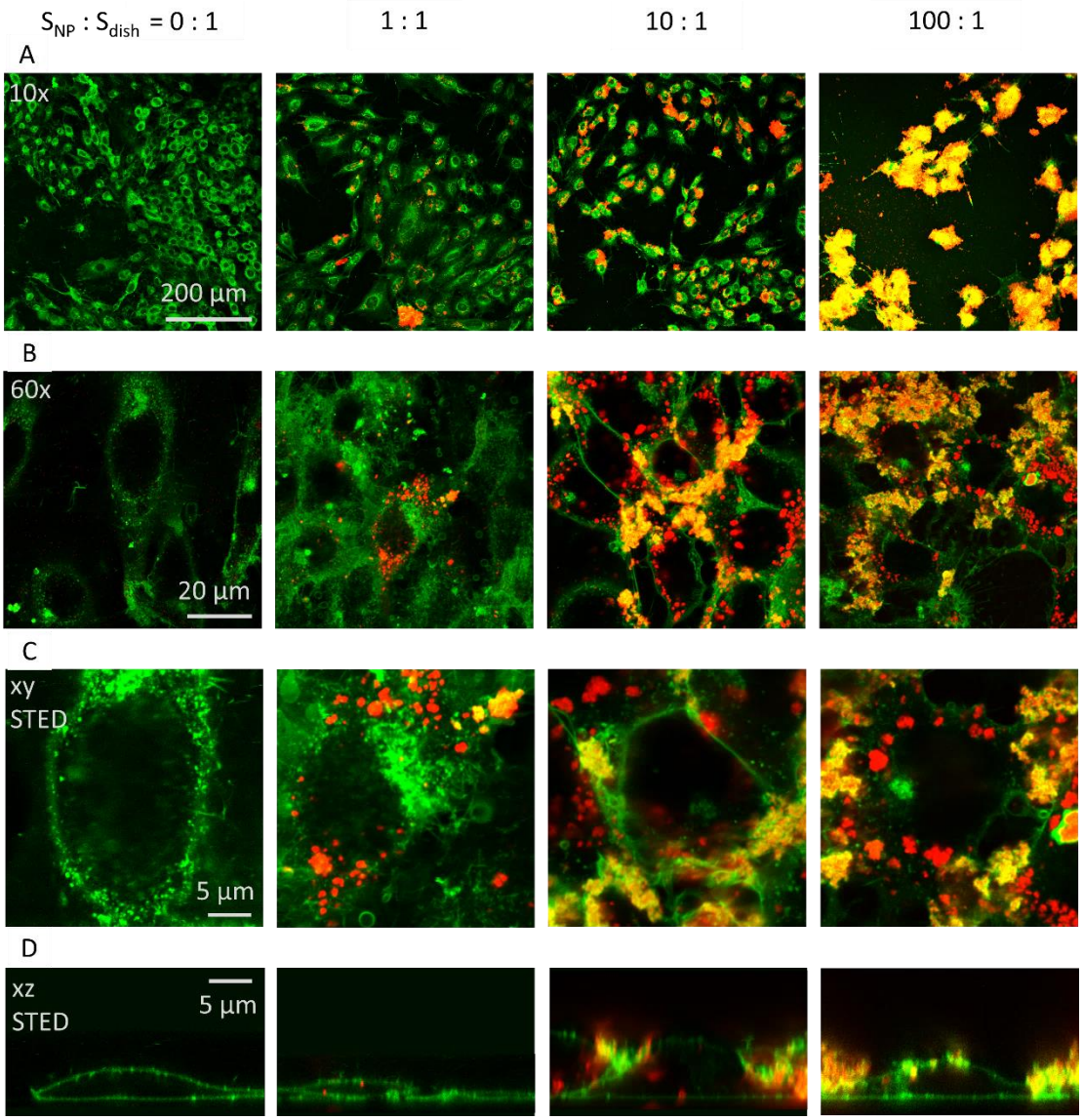

Figure 3.13: Cauliflowers are larger and more frequent at higher surface doses of exposure. The xy micrographs on **A, B** and **C** show LA-4 cells (membranes labelled with CellMask Orange, shown in green) after a 2-day incubation with various surface doses of TiO_2 nanotubes (labelled with Alexa 647, shown in red) at different magnifications. **D** The xz cross-sections corresponding to STED micrographs from **C**; both **C** and **D** were acquired using 70% 3D STED. Before imaging, the cell medium was removed and replaced with Live Cell Imaging Solution (LCIS), thus also removing any mobile nanotubes and vesicles

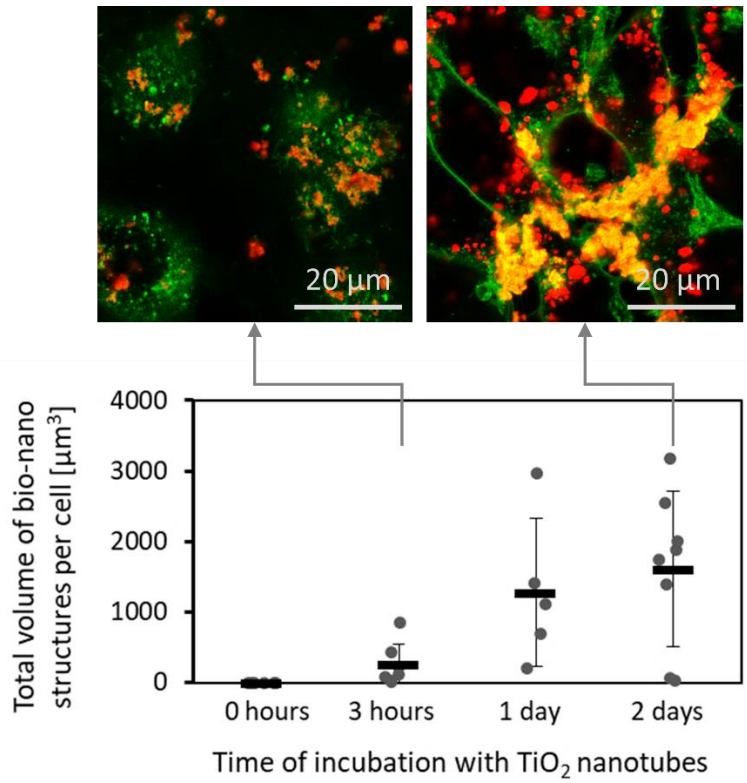

Figure 3.14: Cauliflowers grow with time. Micrographs and a graph showing the characteristic time-scale of appearance of the bio-nano structures on the surface of LA-4 epithelial cells (cell membranes labelled with CellMask Orange, shown in green) after exposure to a 10:1 surface dose of TiO_2 nanotubes (labelled with Alexa 647, shown in red). The micrographs were acquired 3 hours and 48 hours after exposure. We performed the quantification with Tanja Vajs; the resulting graph is adapted from [110] with permission.

Firstly, we noticed that the cauliflowers are observed only in LA-4 epithelial cell monoculture, but neither in the MH-S macrophage monoculture nor in a cell-free sample consisting of the TiO_2 nanotubes and the fluorescent probe (CellMask Orange, see Figure A.18 in the Appendix). Hence, we can suspect that the appearance of cauliflowers is cell-mediated, and is not an artefact of direct affinity between the nanoparticles and the fluorescent probe.

Secondly, super-resolution microscopy of the cauliflowers (Figure 3.15) revealed that these structures consisted of fairly monodispersed aggregates of TiO_2 nanotubes, which were intercalated by sheets of phospholipids. Interestingly, the structures did not move when probed by a strong STED beam, which acts as an optical tweezer and can otherwise easily move mobile nanoparticles and lipid-filled vesicles (see Figure A.1 in the Appendix). Because we were also unable to remove the cauliflowers from the sample even by vigorous washing, this led us to conclude that these bio-nano structures are not only rigid but also strongly attached to the surface of the lung epithelial cells.

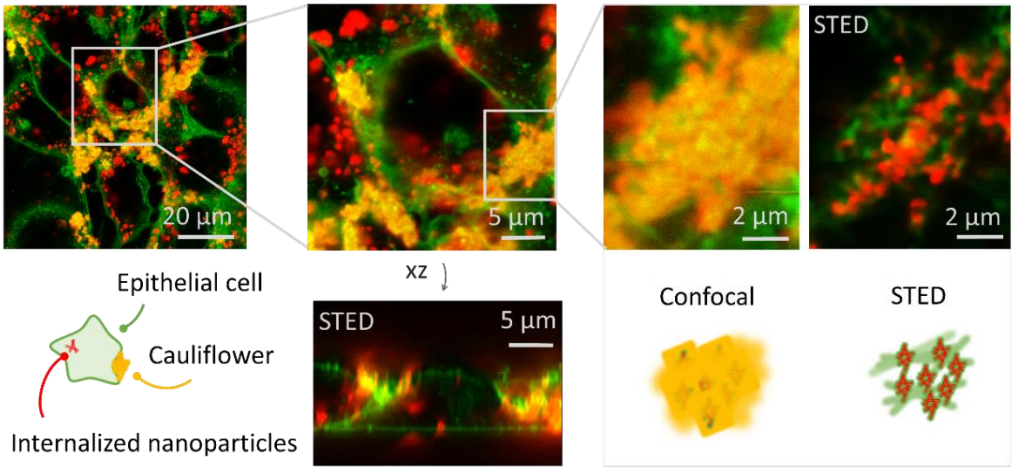

Figure 3.15: The characteristic appearance and structure of cauliflowers on the surface of lung epithelial cells. The LA-4 cells (membranes are labelled with CellMask Orange, shown in green) were exposed to a 10:1 surface dose of TiO_2 nanotubes (labelled with Alexa 647, shown in red) for 2 days.

In order to test whether the appearance of cauliflowers was merely an artefact of the in vitro setup used for the experiment, we took a closer look at the data from mice, exposed to the exact same batch of TiO_2 nanotubes [29]. In the published manuscript, Danielsen et al. noted that the alveoli were "full of micron-sized agglomerates and acellular organic debris". Also, "accumulation of proteinaceous matter in the alveolus" was observed but not explained, which sparked our interest. Indeed, the micrographs of histological sections from the same experiment show that the lumen of the alveoli was filled with large structures that were composed of nanoparticles and biological molecules (Figure 3.16). Moreover, similar to cauliflowers, they were attached to the alveolar wall, which consists of type I and type II lung epithelial cells. Crucially, the in vivo presence of structures similar to the in-vitro-observed cauliflowers provides a valuable link between in vitro and in vivo results and supports the choice of the in vitro setup used for experiments.

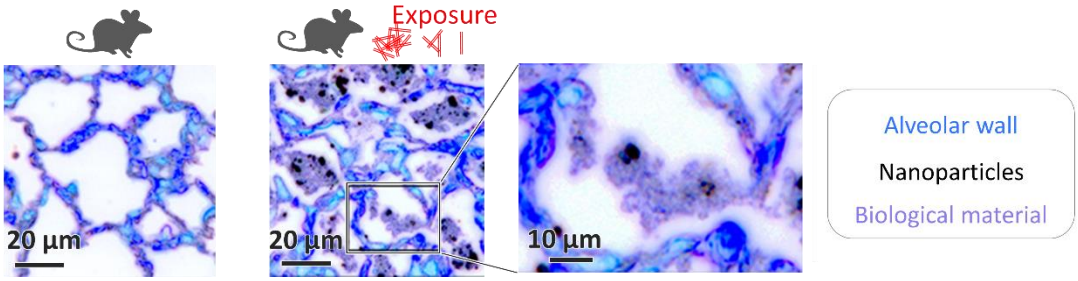

Figure 3.16: Cauliflowers are present also in the alveoli of mice, exposed to the same TiO_2 nanotubes. Right: color-inverted enhanced dark-field hyperspectral microscopy images of a histological section obtained from murine lungs one month after intratracheal instillation of a 3:1 surface dose of TiO_2 nanotubes (162 µg of nanoparticles per mouse); cauliflowers can be seen as large purple structures in the lumen of the alveolus. For comparison, a histological section of a mouse, exposed to a sham control, is shown on the left. Courtesy of Trine Berthing, Pernille Høgh Danielsen and Ulla Vogel (NRCWE, Denmark; with assistance of Jorid Birkelund Sørli), adapted from [94] (CC BY-NC) with permission.

3.2.3 Cauliflowers Form by Exocytosis of Nanoparticles

Naturally, at this point one starts to wonder how do these surface-bound cauliflowers form. One clue comes from Figure 3.17, where one can see that the characteristic size of nanotube aggregates in the cauliflowers (0.3 – 0.5 μm) is very similar to the size of lysosomes (0.3 – 0.8 μm) in which the internalized nanotubes are located shortly after exposure. This leads us to hypothesize that the nanoparticles in cauliflowers might have previously been inside the LA-4 cells. However, as mentioned in the Introduction, these TiO_2 nanotubes are known to only slightly affect the viability of the LA-4 lung epithelial cells [52], and consequently the large amount of nanoparticles in the cauliflowers cannot be attributed solely to the release of nanoparticles from the few dead cells. Therefore, the nanoparticles might have been released from living cells through exocytosis, as some cells have the ability to exocytose nanoparticles [111]–[116].

When the excretion of exocytotic vesicles was blocked using jasplakinolide (a drug that inhibits fragmentation of actin, consequently preventing the excretion of exocytotic vesicles during the final stage of exocytosis; experiment performed by A. Sebastijanović), noticeable amounts of TiO_2 nanotubes were located in exocytotic vesicles that were prepared for excretion from the cell (Figure 3.17 C) [94]. We noticed that in his micrographs, the size of the exocytotic vesicles ranged from 0.3 μm upward, which nicely corresponds to the observed size of nanotube aggregates in the cauliflowers. Moreover, almost no cauliflowers were present on the cells when exocytosis was blocked [94].

Importantly, nanoparticle exocytosis by lung epithelial cells could explain the puzzling in vivo observations that almost no nanotubes were located in lung epithelial cells 90 days after exposure, but were instead mostly located in macrophages [29]. Namely, if one takes into account the incomplete clearance of nanoparticles by macrophages (see Section 3.1.4), one would expect to observe a significant amount of nanoparticles in both the epithelial cells and macrophages. However, the epithelial cells excrete the nanoparticles into cauliflowers and macrophages do not, causing the observed amount of nanoparticles in epithelial cells to be disproportionately lower than in macrophages.

It is worth noting that similar but smaller lipid-nano structures were formed on the LA-4 cell surface soon after exposure when endocytosis was blocked using chlorpromazine and the nanotubes were mostly prevented from entering the cell (as was shown in Figure 3.12 B). In this case, the strong affinity between the nanotubes and the plasma membrane caused lipid wrapping of the nanotubes, and aggregated them into larger structures. Although this route of cauliflower formation is also possible in the usual scenario after exposure to the TiO_2 nanotubes, the route via endocytosis and exocytosis described above is more probable because of quick and efficient endocytosis.

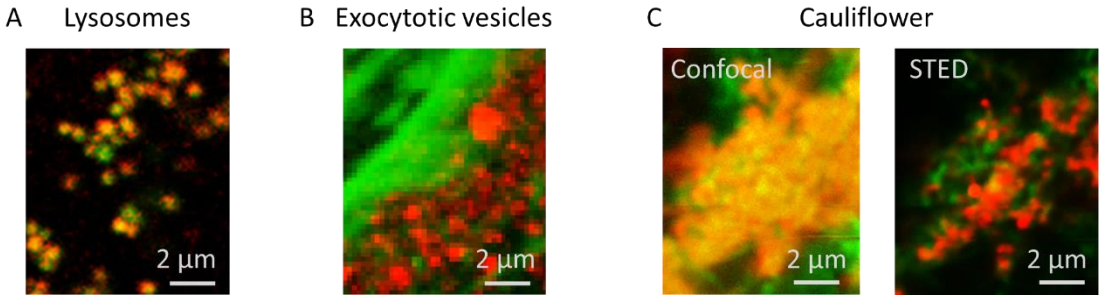

Figure 3.17: The characteristic size of nanoparticle aggregates in the cauliflowers is very similar to the size of lysosomes and exocytotic vesicles. **A** A fluorescence micrograph of the lysosomes/late endosomes in an LA-4 epithelial cell (labelled with Lysotracker Red, shown in green) after a 70-minute incubation with a 1:1 surface dose of TiO_2 nanotubes (labelled with Alexa 647, shown in red). **B** A zoomed-in fluorescence micrograph of unexcreted exocytotic vesicles inside a LA-4 epithelial cell (F-actin labelled with Sir Actin, shown in green) after one day of incubation with a 10:1 surface dose of TiO_2 nanotubes (labelled with STAR 520SXP, shown in red). Excretion of exocytotic vesicles was blocked by an overnight incubation with 1 mM jasplakinolide prior to incubation with nanoparticles, with the incubation taking place during the exposure to nanoparticles as well. Original micrograph courtesy of Aleksandar Sebastijanović [94] (CC BY-NC). **C** A confocal and STED fluorescence micrograph of a cauliflower on the surface of LA-4 epithelial cells (cell membranes labelled with CellMask Orange, shown in green) after 2 days of exposure to a 10:1 surface dose of TiO_2 nanotubes (labelled with Alexa647, shown in red). In order to distinguish the nanoparticle aggregates in the dense inner structure of cauliflowers, STED microscopy was used – hence, the structures also appear smaller than they would on a confocal micrograph.

3.2.4 Cauliflower Formation is Accompanied by Increased Lipid Synthesis

One striking feature of cauliflowers is their richness in lipids, which can be nicely observed in Figure 3.18 A by comparing the intensity of the lipid signal from the cauliflowers and the signal from the cell plasma membrane. To investigate where this unusually large amount of lipids originates from, we first focused on lipid droplets – organelles in which cells store ample amounts of fatty acids, which can later be used as building blocks for phospholipid synthesis or as an energy source. Unexpectedly, when we measured the size and number of lipid droplets in the LA-4 cells, the population of lipid droplets did not majorly differ between the exposed cells and control – even at very high surface doses of 100:1 (S_{NP}:S_{cells}), as shown in Figure 3.18 B. Consequently, we suspected that the additional phospholipids in the cauliflowers were not synthesized from the fatty acids stored in lipid droplets, but were synthesized anew.

This suspicion was confirmed by the RNA transcriptome of LA-4 cells, exposed to the same nanotubes, performed by J. Becker's and T. Stoeger's labs (HZM Germany) [94]. According to them, various aspects of lipid metabolism were increased in the LA-4 epithelial cells both after 4 and 48 hours of exposure to the nanotubes – including fatty acid metabolism, cholesterol biosynthesis and cholesterol metabolism (see Figure 3.18 C). From this we can conclude that although there was active de novo synthesis of lipids, these lipids were probably excreted, utilized for cauliflower synthesis or metabolized, which

explains our observed lack of change in the population of lipid droplets in the nanoparticle-exposed epithelial cells.

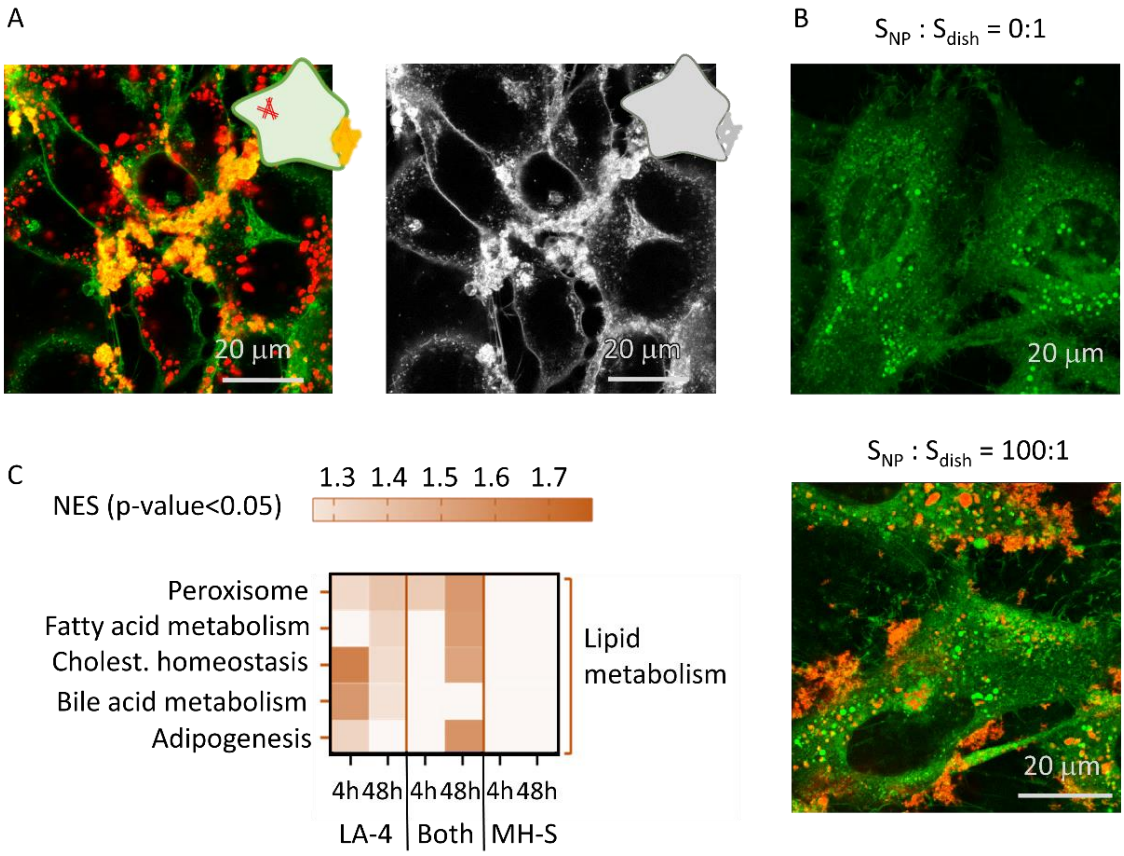

Figure 3.18: Nanoparticle exposure elevates the lipid metabolism of cells but does not majorly influence the size of lipid droplets. **A** Fluorescence micrographs of LA-4 epithelial cells (cell membranes labelled with CellMask Orange, shown in green) after 2 days of incubation with a 10:1 surface dose of TiO_2 nanotubes (labelled with Alexa 647, shown in red). The signal from cell membranes (green) is shown in grayscale on the right to show the intensity of the signal in cauliflowers in comparison to the cell plasma membranes. **B** Fluorescence micrographs of LA-4 epithelial cells (cell membranes labelled with CellMask Orange and lipid vesicles labelled with SAG-38, both shown in green) after 2 days of incubation with a 10:1 surface dose of TiO_2 nanotubes (labelled with Alexa 647, shown in red). **C** A heatmap presenting the GSEA normalized enrichment score (NES) of Hallmark pathways related to lipid metabolism and energy production in the transcriptome profile (total RNA) of mono- and cocultures of LA-4 and MH-S cells, exposed to a 10:1 surface dose of TiO_2 nanotubes for 4 and 48 hours. It is based on gene expressions that were increased at least two-fold compared to the control (non-exposed cells). **C** is courtesy of Carolina Ballester Lopez, Martin Irmler, Johannes Beckers, and Tobias Stoeger (with assistance of K. Richter and A. Krišelj), adapted from [94] (CC BY-NC) with permission.

3.2.5 Nanoquarantine Is Also Observed with Other Nanoparticles and Cell Lines

To confirm that the observed nanoquarantine is not just an exotic phenomenon, limited to our experimental setup, we tested it on other cell lines exposed to the same nanotubes. The same TiO_2 nanotubes induced formation of cauliflowers not only in the type II pneumocytes (LA-4) but also in a human neuroblastoma cell line (SH-SY5Y) that was differentiated into neurons. On the other hand, nanoquarantine was extremely rare (and noticeably less pronounced) in the cell line of murine alveolar macrophages (MH-S); examples of both are shown in Figure 3.19.

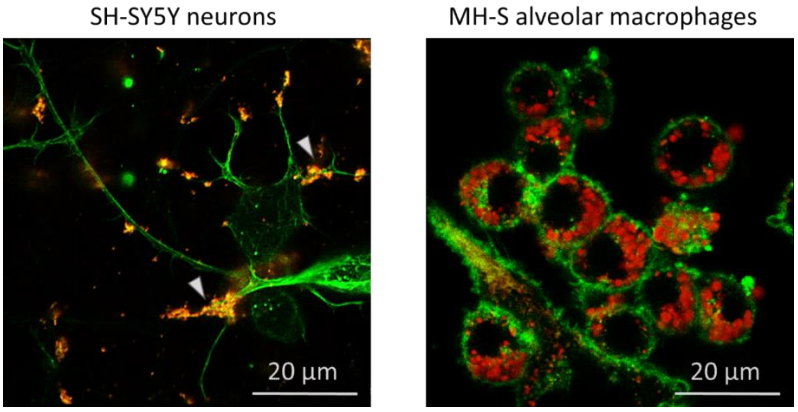

Figure 3.19: Cauliflowers can be observed in neurons, but not in macrophages. Fluorescence micrographs of SH-SY5Y neurons and MH-S alveolar macrophages (cell membranes labelled with CellMask Orange, shown in green) after 1 and 2 days of incubation with a 10:1 surface dose of TiO_2 nanotubes (labelled with Alexa 647, shown in red). Cauliflowers are marked with arrowheads. Left micrograph is courtesy of Aleksandar Sebastijanović.

To test whether the effect of nanoquarantine is characteristic only for the chosen TiO_2 nanotubes, we exposed the same LA-4 epithelial cell line to several nanoparticles of varying size, shape, chemical composition and surface functionalization. After two days, the size and frequency of nanoquarantine was assessed. Some of the metal oxides induced very sparse and small cauliflowers, others formed extremely large cauliflowers on all cells, and the rest were in between these cases (see Figure 3.20 for an overview and Table A.2 in the Appendix for characteristic micrographs). However, no cauliflowers were observed in cells exposed to hydrophobic carbonaceous nanoparticles.

Interestingly enough, a quick glance of the samples with metal oxide nanoparticles led to the observation that the nanoparticles that induce smaller cauliflowers also localize inside the cell more than others (see Table A.2 in the Appendix). This is also in line with the exocytosis-driven cauliflower formation explained in Section 3.2.3. Moreover, when the extent of nanoquarantine is compared to the number of viable epithelial cells, as shown on the graph in Figure 3.20, a slight trend can be observed which connects higher cell viability with extensive nanoquarantine for nanoparticles of the same chemical composition (denoted by the same color in the graph). Although the sparse dataset precludes any decisive conclusions, this trend hints to a possible connection between nanoquarantine and cell viability.

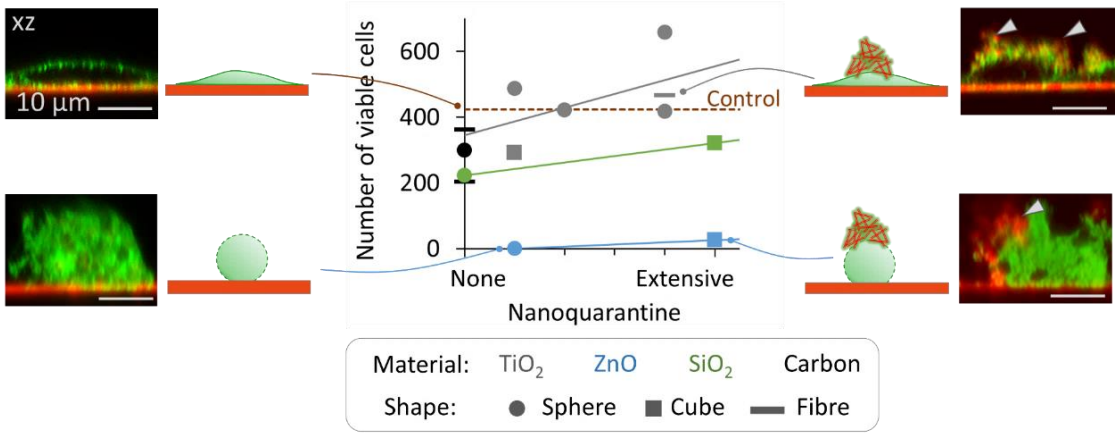

Figure 3.20: Various nanoparticles induce formation of cauliflowers. The graph shows the effect of 12 different nanoparticles on the extent of nanoquarantine and the viability of LA-4 cells after a 2-day incubation with a 10:1 surface dose of nanoparticles. A linear fit of the data-points is shown for each type of nanoparticles (TiO_2, ZnO and SiO_2), serving as a guide to the eye. To obtain the viability data, cells were counted from fluorescence micrographs obtained by Hoechst 32442 and Propidium iodide staining and bright-field reference micrographs. Characteristic xz micrographs and the corresponding schematics of the cauliflowers on cells are shown around the graph for three nanoparticles and the control. The membranes of cells in these micrographs were labelled with CellMask Orange (shown in green) and the nonlabelled nanoparticles were detected via backscattered light (shown in red).

3.2.6 Nanoquarantine – a Cell Defense Mechanism?

As mentioned in the introduction, exposure to the TiO_2 nanotubes does not seem to influence the viability of the LA-4 lung epithelial cells as much as one would expect due to their large affinity towards biomolecules leading to pronounced lipid wrapping. Strikingly, as we show in this subsection, the unexplained effect of increased cell survival could be causally connected to the appearance of cauliflowers. This is backed by the data shown in the previous subsection (Figure 3.20), as well as two sets of experiments that tracked the dose- and time-dependent changes in mitochondrial morphology, which is known to sensitively react to changes in cellular energy needs.

Firstly, the formation of cauliflowers coincides with the restoration of the morphology of the mitochondrial network following exposure of LA-4 cells to TiO_2 nanotubes. The latter was observed by M. Pušnik and T. Koklič [94] (see Figure 3.21): a few hours after exposure, the mitochondrial network of the LA-4 cells fragments, which is a typical sign of great stress to the cell [117], [118]. At this time-point, we have observed only the presence of small structures containing nanoparticles and some lipids on the cell surface. However, she observed that during the course of exposure, the mitochondrial network elongates, fully restoring two days after exposure – a process coinciding with our observed growth and formation of large cauliflowers.

On the other hand, we observed a different outcome with T. Vajs when we cultured and incubated the LA-4 cells with the same TiO_2 nanotubes in full cell medium, deficient in glutamine: after two days, only smaller cauliflowers were formed and the mitochondrial network did not restore, but rather continued to fragment with time [110]. As glutamine is a crucial component for lipid synthesis (especially for cancer cells, e.g. LA-4 cells), we

can suspect that in this case, cells were not able to synthesize a sufficient amount of phospholipids to successfully produce large cauliflowers, which prevented the restoration of the mitochondrial network.

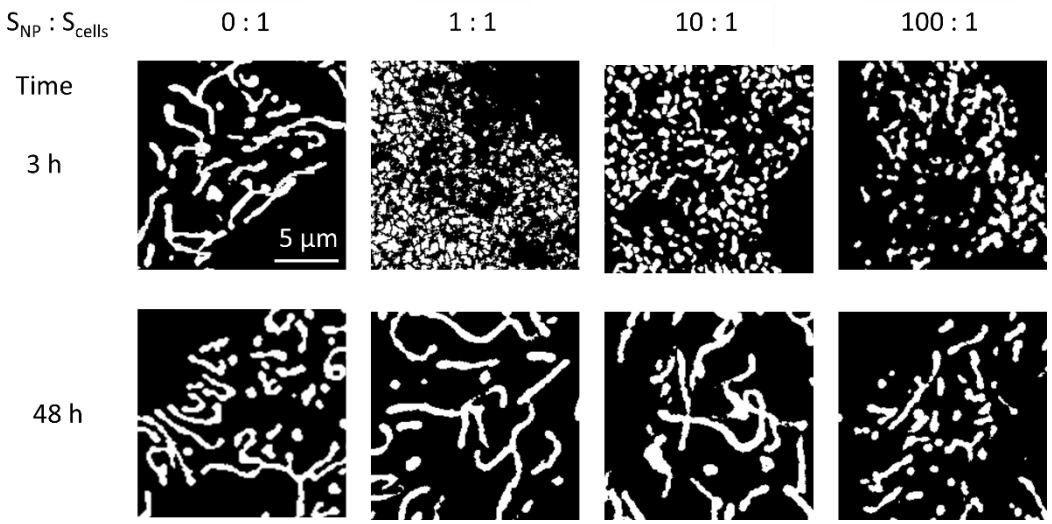

Figure 3.21: The mitochondrial network fragments soon after exposure to TiO_2 nanotubes, but is restored after two days. We rescaled binarised micrographs of the mitochondrial network of LA-4 epithelial cells, stained with MitoTracker Orange, to show the time- and dose-response of the mitochondrial network to nanoparticle exposure. Original micrographs courtesy of Mojca Pušnik and Tilen Koklič, published in [94] (CC BY-NC).

The possible causal relation between the appearance of cauliflowers and increased cell survival could be the consequence of two key cauliflower characteristics:

- the cauliflowers form when the cell excretes the nanoparticles: this temporarily lowers the amount of nanoparticles inside the cell;
- the cauliflowers are stiff and rigid: the nanoparticles that have been excreted into these structures are immobile and thus cannot move around and interact with cells. In a way, this effectively lowers the active dose of nanoparticles to which the cells are exposed, improving their chances of survival. In a way, this acts similarly to a quarantine – hence, cauliflowers can be viewed as a nano-scale form of quarantine (nanoquarantine).

On its own, nanoparticle excretion might not be a long-term solution in regard to cell viability and fitness. Although nanoparticle exocytosis might compensate for the continuous flow of nanoparticles into the cell (leading to a steady-state scenario with equal amounts of internalized and externalized nanoparticles), one might imagine that maintaining this flow of nanoparticles requires a copious amount of energy. To obtain the energy and resources needed for nanoparticle exocytosis, the cell might increase energy production or turn off various less important processes, both of which might slowly "burn out" the cell and decrease its fitness, possibly causing premature cell death in the long run.

On the other hand, the immobilization of nanoparticles in the growing cauliflowers can slowly diminish the amount of freely-floating nanoparticles, consequently also lowering the amount of nanoparticles entering the cell and the energy needed to excrete it from the cell. In the extreme case when all the nanoparticles are immobilized in cauliflowers with its

organic part not being biodegraded, the effective exposure to the cells diminishes, mimicking 100% clearance of the nanoparticles.

However, the exocytosed nanoparticles in the cauliflowers are not mobile and therefore probably cannot be cleared from the lung by the flow of lung lining fluid – cauliflower formation thus simultaneously lowers the (accessible) dose but also impairs nanoparticle clearance.

All this leads us to believe that cauliflower formation might be one of the key molecular events in the toxicity pathway (alongside the macrophage death that was discussed in Section 3.1.3).

3.2.7 Short Summary

Alveolar epithelial cells, which form the rim of the alveolus, are capable of both internalizing nanoparticles and excreting the internalized nanoparticles onto their surface. The latter process can lead to the gradual formation of stiff, lipid-rich surface-bound bio-nano structures (cauliflowers), which is accompanied by increased lipid metabolism. Because the excretion of internalized nanoparticles and their immobilization in the cauliflowers effectively lowers the active nanoparticle dose, this process of nanoquarantining could be seen as a cell defense mechanism.

3.3 Inter-Cellular Nanoparticle Cycling Governs Chronic Inflammation

So far, we have focused on the general interactions between the nanoparticles and the monocultures of macrophages or epithelial cells. What remains is to elucidate the interactions between these two cell types – both in terms of the flow of nanoparticles and signaling. Again, we seek to simplify the system as much as possible to ease the detection of individual events, and will thus focus on a coculture of epithelial cells and macrophages.

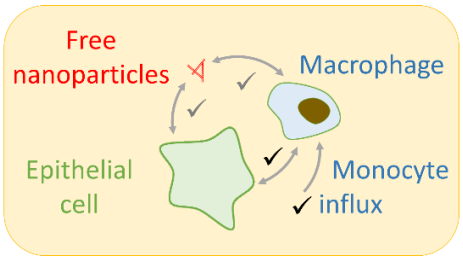

In order to correctly interpret the fluorescence micrographs of a coculture, it is important to ensure that one can visually distinguish between the different cell types. One option would be to separately label one cell type prior to adding it to the coculture by using a fluorescent entity that is well retained in cells and cannot be transferred from one cell to its neighbor – for example CellTrace, CellTracker, CFSE ((5(6)-Carboxyfluorescein diacetate N-hydroxysuccinimidyl ester), Cytopainter, NucLight fluorescence proteins, etc. However, in our case the shape and size of the two cell lines were very distinct: macrophages are either spherical or spindle-shaped (elongated in one direction), whereas the epithelial cells are flat and star-shaped at low confluences, or flat and elongated in dense samples (see Figure 3.22 for some characteristic images of both cell types). Hence, we decided to rely on the characteristic shape and size of cells to visually distinguish between these two cell types.

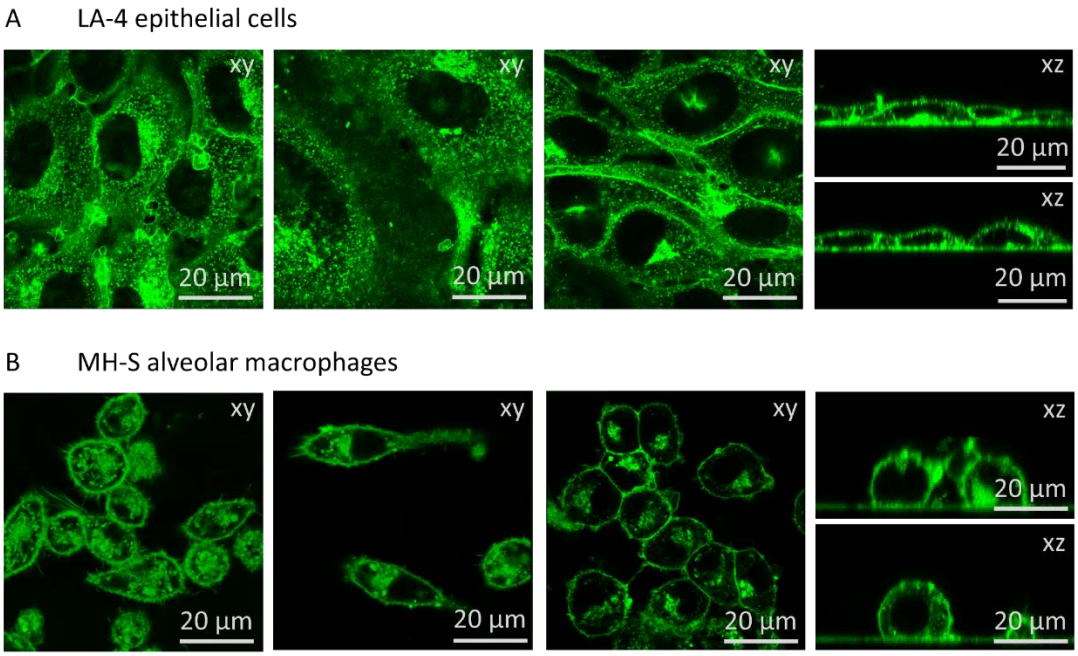

Figure 3.22: The LA-4 epithelial cells and MH-S macrophages can be distinguished by their morphology. Fluorescence micrographs of **A** LA-4 epithelial cells and **B** MH-S alveolar macrophages with cell membranes labelled with CellMask Orange, shown in green). Some cells were exposed to nanoparticles, which are not shown in the figures. Note the distinct flat and spread-out shape of the epithelial cells and spherical shape of macrophages.

3.3.1 Dying Cells Re-Expose Other Cells by Releasing the Nanoparticles

As mentioned in the previous sections, nanoparticles that are released from dead/dying cells can be taken up by other cells in the sample. To prove this, we added thoroughly washed macrophages, pre-filled with nanoparticles, to non-exposed epithelial cells. Not surprisingly, some nanoparticles could be found inside a few epithelial cells two days later (Figure 3.23). The low amount of nanoparticles inside the epithelial cells does not come as a surprise because not all macrophages died during the duration of coculture with epithelial cells, and the released nanoparticles were distributed among the remaining cells in the coculture. Based on this, one can assume that the nanoparticles that are released in the case of either macrophage or epithelial cell death can be re-internalized by any of these cell types.

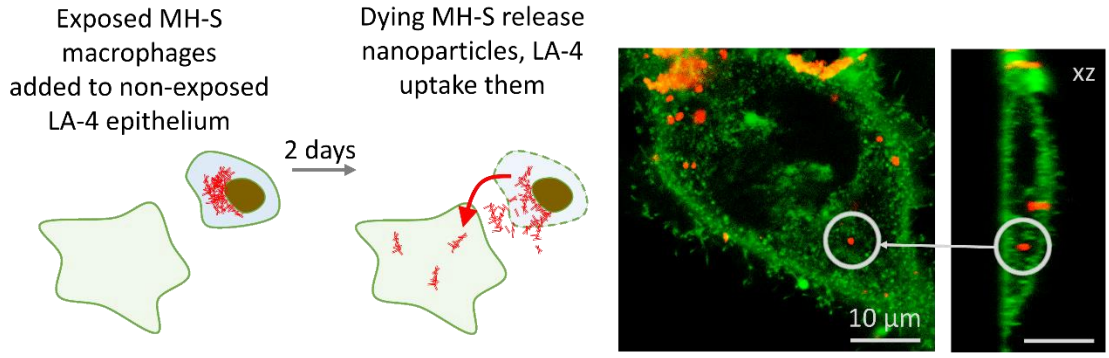

Figure 3.23: Nanoparticles that are released from macrophages are internalized into epithelial cells. Schematic and fluorescence micrographs of the coculture of nanoparticle-filled MH-S macrophages and unexposed LA-4 epithelial cells after 2 days of coculture (cell membranes of both are labelled with CellMask Orange, shown in green). Prior to coculture, only the MH-S were exposed to a 10:1 surface dose of TiO_2 nanotubes (labelled with Alexa 647, shown in red) for 2 days. The nanoparticles, released from MH-S into the LA-4, are encircled on the micrographs.

3.3.2 Macrophages Degrade and Internalize Cauliflowers

To answer whether nanoparticles can also flow in the other direction (from epithelial cells to macrophages), we added non-exposed macrophages to a sample of nanoparticle-exposed epithelial cells. Because the sample was thoroughly washed prior to adding the macrophages, most of the nanoparticles at that time were immobilized in cauliflowers, and the rest were inside the epithelial cells. After two days in coculture, many macrophages were filled with nanoparticles and appeared to be engaging with the cauliflowers, proving that macrophages can internalize the nanoparticles that had previously been in the epithelial cells (see Figure 3.24). The nanoparticles in macrophages were found in large spherical aggregates, similar to the case when macrophages internalized and compacted freely-floating nanoparticles (an example of which was shown in Figure 3.3).

Fluorescence lifetime imaging on the same sample revealed that the nanoparticles in the aggregates inside macrophages had a shorter lifetime than the nanoparticles in cauliflowers, as seen in Figure 3.24. Because the fluorescence lifetime of the labelled nanotubes depends on how close the nanotubes are to each other (the shorter the lifetime, the closer the distance), this indicates that the nanoparticles from cauliflowers were internalized by the macrophages and were aggregated inside them.

It is important to stress that the uptake and degradation of cauliflowers by macrophages could explain why the cauliflowers are often less prominent in cocultures and in vivo situations. Even more importantly, it is this uptake and degradation of cauliflowers that de-quarantines the nanoparticles that had been quarantined by the epithelial cell, and returns them into the cycling of nanoparticles inside the system, again increasing the active dose of nanoparticles.

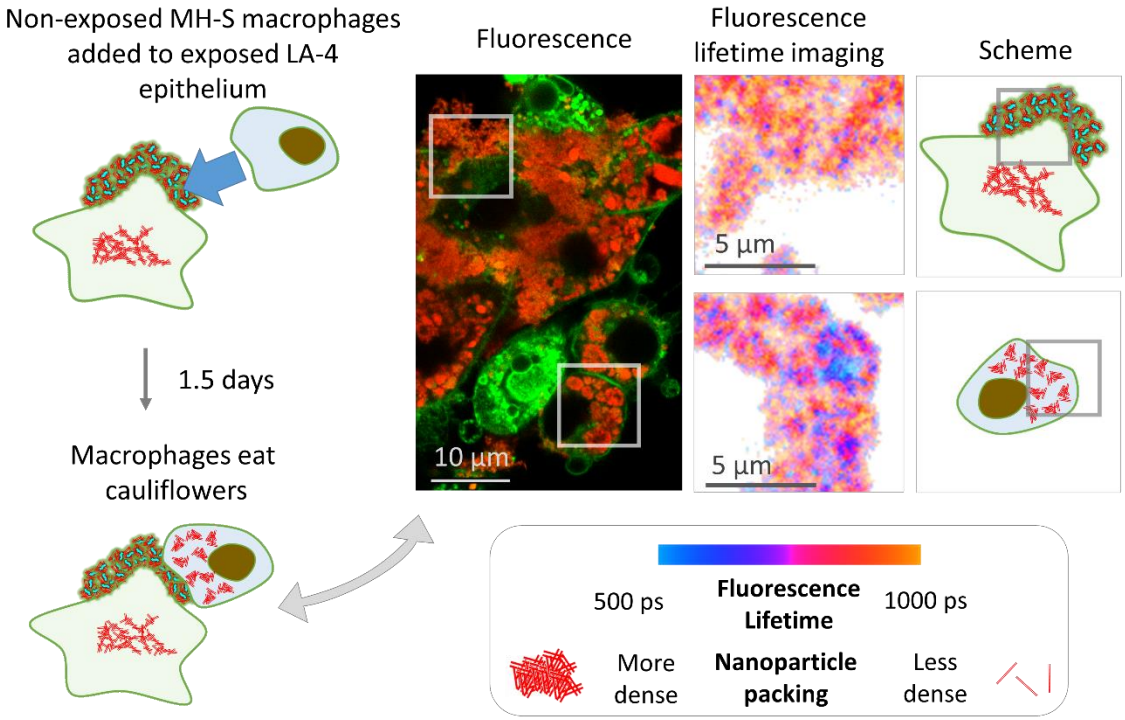

Figure 3.24: Macrophages internalize and condense nanoparticles from cauliflowers. The fluorescence micrographs and fluorescence lifetime micrographs (FLIM) of a coculture of nanoparticle-exposed LA-4 epithelial cells and non-exposed MH-S macrophages were acquired after 1.5 days of coculture (cell membranes of both were labelled with CellMask Orange, shown in green). Prior to coculture, only the LA-4 were exposed to a 10:1 surface dose of TiO_2 nanotubes (labelled with Alexa 647, shown in red) for 2 days, and thoroughly washed before the MH-S were added.

3.3.3 Epithelial Cells Are the Major Modulator of Signaling for Immune Cell Influx

A crucial component of chronic inflammation is prolonged pro-inflammatory signaling, which leads to the continuous influx of immune cells. To get a better view of the modulated inflammatory signaling in our system and the involved cytokines, transcriptomics was performed by J. Becker's and T. Stoeger's labs (HZM Germany) on the coculture of epithelial cells and macrophages, as well as on their monocultures after 4 and 48 hours of nanoparticle exposure. Interestingly, the transcription of several cytokines was strongly up-regulated both in the exposed epithelial monoculture and the coculture, whereas very few were up-regulated in the macrophage monoculture, with several even being strongly downregulated (see Figure 3.25 A). Also, the epithelial cells seem to have a greater number of up-regulated inflammatory pathways than macrophages, as can be observed in Figure 3.25 B.

Knowing that 1) the surface of epithelial cells in the alveolus is larger than the surface of macrophages, 2) the epithelial cells can excrete cytokines and other pro-inflammatory mediatory directly into the lymph [119], [120], and 3) epithelial cells have been shown to majorly influence the response of macrophages, neutrophils and other immune cells [26], it is not so surprising that the main modulator of pro-inflammatory signaling following

nanoparticle exposure are epithelial cells, not macrophages – an observation that has been reported for other nanoparticles as well [98].

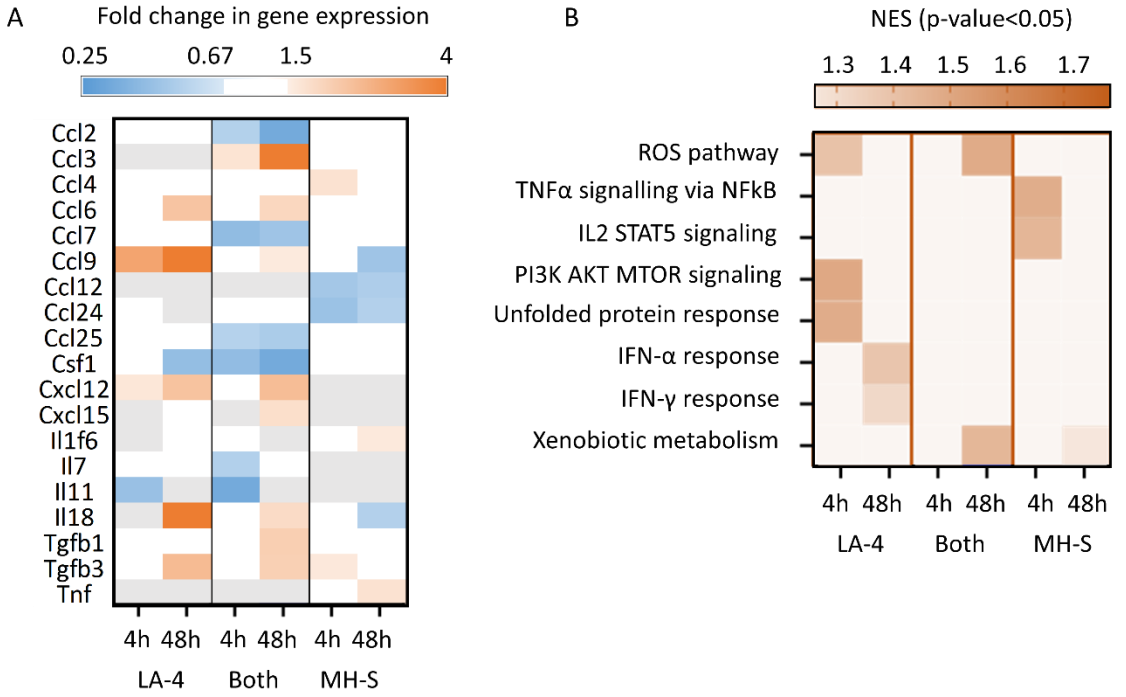

Figure 3.25: Inflammatory signaling is strongly modulated in the cell cultures. The heatmaps present the changes in **A** the transcription of genes encoding cytokines and **B** the hallmark gene sets related to stress response and inflammation for in vitro mono- and cocultures of LA-4 and MH-S cells, exposed to a 10:1 surface dose of TiO_2 nanotubes for 4 and 48 hours. In **A**, we plotted only the gene expressions of cytokines (chemokines (XCL, CCL, CXCL, CX3CL), interferons (IFN), interleukins (IL), tissue necrosis factors (TNF), and GM-CSF (CSF2)) that were increased or decreased at least 1.5-fold compared to the control in at least one of the nanoparticle-exposed samples. Significant up- or down-regulation is denoted with an orange and blue color, respectively, whereas gene expressions that were below the detection limit are shown in gray. Raw data in **A** and heatmap in **B** are courtesy of Carolina Ballester Lopez, Martin Irmler, Johannes Beckers, and Tobias Stoeger (with assistance of K. Richter and A. Krišelj), published in [94] (CC BY-NC).

3.3.4 Short Summary

In a coculture of macrophages and lung epithelial cells, the additional interactions between the cell types lead to the transfer of nanoparticles from one cell type to the other: dying cells re-expose other cells to the nanoparticles they had previously internalized, and macrophages internalize the nanoparticles that had previously been quarantined by the epithelial cells.

3.4 Combining it All Together – the Chronic Cycle of Inflammation

Based on the experimental findings described in detail in the previous sections, we can display the most important events in the coculture of epithelial cells and macrophages in a simplified scheme showing the main processes (Figure 3.26).

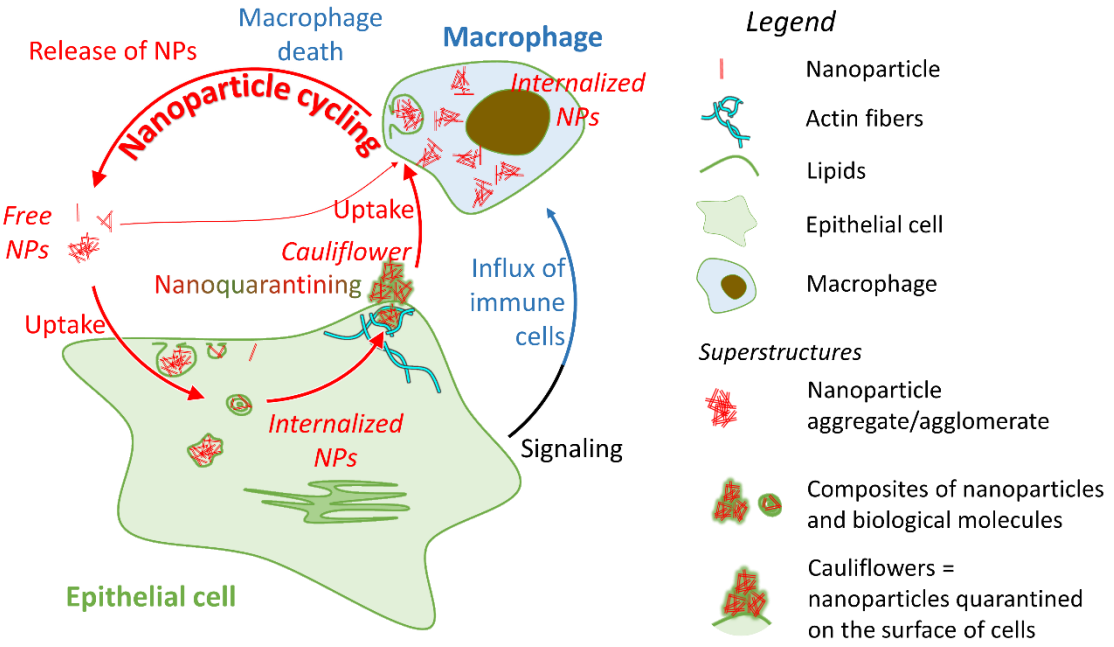

Figure 3.26: Simplified schematic of the cycle of events with the most important events leading to chronic inflammation; "NPs" stands for nanoparticles.

The major events of the pathway leading to chronic inflammation explained in the previous sections are nicely extracted from the scheme above:

- **Nanoquarantining**: excretion and immobilization of nanoparticles by lung epithelial cells. It lowers the active dose of nanoparticles, increases cell viability and forms the **first part of nanoparticle cycling**.
- **(Macrophage) cell death**: a consequence of nanoparticle internalization. It results in the release of nanoparticles from dying cells, thus forming the **second part of nanoparticle cycling**.
- **Signaling-induced influx of new cells**: the release of chemo-attractants which in vivo attract immune cells to the site of exposure. It enables replacement of the dead macrophages and, consequently, the **continuation of nanoparticle cycling**.

In the absence of macrophages, more and more nanoparticles would be transferred into cauliflowers through nanoquarantine, protecting the epithelial cells. However, macrophages internalize the cauliflowers and re-expose the cells to the nanoparticles when they die. The release of nanoparticles leads to a continuation of nanoparticle cycling and prolongs the inflammation. On top of this, the epithelial cells recruit new immune cells to the site of exposure through chemo-attractants. These replace the dead macrophages and enable the continuation of nanoparticle cycling, extending the duration of inflammation.

Chapter 4

Results and Discussion – Development of the Predictive Model

Now that the key processes in the nanoparticle-exposed lung that lead to prolonged inflammation have been discerned, we can use this knowledge and understanding to describe the system in a mathematical manner – by using differential equations. What makes this approach worthwhile is its potential for time-propagation and accounting for inter-system differences, enabling animal-free prediction of the in vivo adverse outcomes based on in vitro determination of the key model parameters.

4.1 Mathematical Equations Describe the Network of Events

The in vivo system, shown in the scheme in Figure 3.26, can be mathematically described using six differential equations, connecting the cycling of nanoparticles and cell viability. In the derivation of the mathematical model that describes the processes in the nanoparticle-exposed biological systems, we strived for maximal simplicity of the equations, reducing the amount of parameters, variables and terms to the bare minimum. For derivation of the equations, we leaned heavily on the experiments described in Chapter 3, and added some additional simplifications/approximations. The main simplified assumptions of the model are as follows:

- Epithelial cells and macrophages internalize nanoparticles equally quickly.
- Macrophages internalize freely floating nanoparticles and nanoparticles in cauliflowers equally quickly.
- The probability of cell death is proportional to the surface area of nanoparticles per cell surface (toxicity rate) and is the same for epithelial cells and macrophages.
- The amount of nanoparticles that an epithelial cell can exocytose per day is limited; macrophages do not exocytose the nanoparticles.
- The main modulation of inflammatory signaling arises from the epithelial cells; the influx of new immune cells is proportional to cauliflower growth (the synthesis of new lipids by epithelial cells) and is delayed compared to if by a few hours.
- All epithelial cells in the model are capable of quarantining nanoparticles and signaling for immune cell influx.

- All the immune cells in the model are categorized as macrophages, regardless of their actual cell type.
- Epithelial cells replicate until they form a confluent monolayer, macrophages do not replicate in vivo.

In order to simplify the system, we decided not to include equations that describe intermediate events such as transport of nanoparticles through the cell, their aggregation inside the cell, and interaction with organelles. Instead, the effect of these events is included in the other equations and characteristic parameters of the system.

The system of equations thus consists of six first-order nonlinear ordinary differential equations – one for each of the six variables – with time as the independent variable (Table 4.1). Four of the variables represent the surface areas of nanoparticles in the four distinct compartments: inside epithelial cells ($npLa4(t)$), in cauliflowers ($npCF(t)$), inside macrophages ($npMhs(t)$), and mobile, freely-floating nanoparticles ($npFree(t)$). The other two variables correspond to the surface (i.e. projected area) of viable macrophages ($sMhs(t)$) and of epithelial cells ($sLa4(t)$). For easier scalability and more intuitive values, all used variables are presented in units of surface, normed to the surface area of the alveolus.

Table 4.1: An overview and description of the variables used in the system.

Variable	**Description**	**Value at $t = 0$**
$npFree(t)$	Surface area of freely-floating nanoparticles normed to the surface area of the lung	10 (corresponds to an exposure to a 10:1 surface dose of nanoparticles at $t = 0$)
$npLa4(t)$	Surface area of nanoparticles inside epithelial cells normed to the surface area of the lung	0
$npCF(t)$	Surface area of nanoparticles in cauliflowers normed to the surface area of the lung	0
$npMhs(t)$	Surface area of nanoparticles inside macrophages normed to the surface area of the lung	0
$sLa4(t)$	Surface (i.e. projected area) of epithelial cells normed to the surface area of the lung	1
$sMhs(t)$	Surface (i.e. projected area) of macrophages (and other immune cells) normed to the surface area of the lung	1/40 [121]
t	Time measured in days	0

The ten parameters that are used in the system are described in Table 4.2, and we suspect that only three of them are strongly dependent on the nanoparticle properties: the rate of cauliflower formation: cff, signaling efficiency: $signalEff$, and toxicity: tox. As will be shown in Section 4.2, the model can successfully replicate the typical in vivo outcomes by modifying only these three parameters. This justifies our choice of the minimal set of nanoparticle-dependent parameters and our decision to ignore the weaker influence of nanoparticle properties on the remaining parameters.

Table 4.2: An overview and description of the 10 parameters used in the system. Of these parameters, three are nanoparticle-dependent (NP-dependent), five are nanoparticle-independent, and two change the units in the equations.

Parameter	Description	Value	Reasoning behind the choice of value
cff	Rate of cauliflower formation	NP-dependent [day^{-1}]	This is the key rate describing nanoquarantining.
cfuEff	Ratio between the rates of internalization of cauliflowers and free nanoparticles	Set to 1 [ ]	The internalization rates of cauliflowers and free nanoparticles are roughly the same; their ratio is therefore approximately 1.
delay	Delay between excretion of nanoparticles (release of cytokines) and infiltration of new macrophages	Set to 0.1 [days] (equal to 2.4 hours)	Neutrophils infiltrate nanoparticle-exposed lungs 3 hours after exposure, possibly even sooner [98], [99]. Therefore, the delay between the source of signaling and the infiltration should be somewhat less than 3 hours (0.15 days).
endo	Rate of nanoparticle internalization	Set to 1 [day^{-1}]	The characteristic time of nanoparticle internalization is approximately one day.
la4Max	Maximal surface of epithelial cells compared to the lung surface area	Set to 1 [ ]	In the equations, epithelial cells replicate until they reach a certain threshold ($la4Max$). In reality, epithelial cells grow until they cover the entire available surface. Hence, their growth saturates when $Sla4 = 1$.
la4Rep	Replication rate of epithelial cells	Set to 0.3 [day^{-1}]	The doubling time of our exponentially growing monoculture of LA-4 cells was approximately 2 days, which corresponds to a replication rate of 0.3 (i.e. if they were seeded at 30% confluency, they would grow to confluency in around 3 days). Equally quick cell growth was observed in an ex vivo coculture of type II pneumocytes and fibroblasts, specially conditioned to induce proliferation in the pneumocytes [122].
macrophage Surface	Norming factor for surface of macrophages	Set to 1/40 [ ]	This factor is set to the initial surface of macrophages (and other immune cells). It is used to norm the units in the equation and transform the value of $signalEff$ to more intuitive values: if one surface area of nanoparticles is quarantined, $signalEff = 1$ causes the influx of an

			additional 100% of the initial number of macrophages.
signalEff	Signaling efficiency (ratio between the surface of infiltrated immune cells and newly quarantined nanoparticles)	NP-dependent [ ]	This is the key parameter connecting the influx of immune cells and nanoquarantine.
timecf	Norming factor for exocytosis saturation	Set to 1 [day]	Defines the saturation limit of nanoparticle exocytosis ($cff\ timecf$) and corrects the units in the equation: if the surface area of internalized nanoparticles in epithelial cells per cell surface is much smaller than the saturation limit, the exocytosis is proportional to the surface area of internalized nanoparticles, and if it is much larger, the exocytosis is constant (saturated).
tox	Toxicity of nanoparticles	NP-dependent [day^{-1}]	This is the key rate describing the probability of cell death due to internalization of nanoparticles.

The simplified system of six differential equations that describe the complex processes in a nanoparticle-exposed lung is as follows:

1. $$\frac{d}{dt} npFree(t) = tox\ npLa4(t)\, npLa4(t)/sLa4(t) + tox\ npMhs(t)\, npMhs(t)/sMhs(t) - endo\ sLa4(t)\ npFree(t) - endo\ sMhs(t)\ npFree(t) \tag{4.1}$$

2. $$\frac{d}{dt} npLa4(t) = endo\ sLa4\ npFree(t) - cff\ sLa4(t)\ \tanh[npLa4(t)/sLa4(t)\ cff\ timecf] - tox\ npLa4(t) npLa4(t)/(sLa4(t)) \tag{4.2}$$

3. $$\frac{d}{dt} npCF(t) = cff\ sLa4(t)\ \tanh[npLa4(t)\ /\ (sLa4(t)\ cff\ timecf)] - endo\ cfuEff\ sMhs(t)\ npCF(t) \tag{4.3}$$

4. $$\frac{d}{dt} npMhs(t) = endo\ sMhs(t)\ npFree(t) + endo\ cfuEff\ sMhs(t)\ npCF(t) - tox\ npMhs(t)\ npMhs(t)\ /\ sMhs(t) \tag{4.4}$$

5. $$\frac{d}{dt} sLa4(t) = la4Rep\ sLa4(t)\ (1 - sLa4(t)/la4Max) - tox\ npLa4(t) \tag{4.5}$$

6. $$\frac{d}{dt} sMhs(t) = signalEff\ macrophageSurface * cff\ sLa4(t - delay) * \tanh[npLa4(t - delay)\ /\ (sLa4(t - delay)\ cff\ timecf)] - tox\ npMhs(t) \tag{4.6}$$

where nanoparticle-dependent parameters are shown in red, and other parameters are shown in green. The meaning of each equation can be described as follows:

1. The surface area of free nanoparticles increases due to cell death of epithelial cells and macrophages, and decreases by internalization into epithelial cells and macrophages.
2. The surface area of nanoparticles in living epithelial cells increases through internalization of nanoparticles by epithelial cells and decreases due to exocytosis (cauliflower formation) and death of epithelial cells.
3. The surface area of nanoparticles in cauliflowers increases due to exocytosis (cauliflower formation) and decreases due to macrophages internalizing cauliflowers.
4. The surface area of nanoparticles in living macrophages increases through internalization of free nanoparticles and cauliflowers, and decreases due to death of macrophages.
5. The surface of living epithelial cells increases through replication until they are confluent and decreases due to the death of epithelial cells.
6. The surface of living macrophages increases through signaling-induced influx of immune cells and decreases due to macrophage death.

4.2 The Model Can Replicate the Typical In Vivo Outcomes – Acute and Chronic Inflammation, and the "All Dead" Situation

By playing around with the model parameters, we soon find out that this simple model is flexible enough to be able to reproduce all four endpoints in regard to inflammation: no inflammation (e.g. Figure 4.1 F), acute inflammation (e.g. Figure 4.1 C, I), prolonged inflammation (Figure 4.1 G) and severe loss of epithelium viability, possibly causing rupturing of alveolar walls and internal bleeding (denoted as "all dead", e.g. Figure 4.1 A). The theoretical endpoint can be visually determined from the time traces below according to the predicted surface of newly arrived immune cells (black curve) and the surface of epithelial cells (green curve) at day 1 after the exposure for acute processes and at day 10 – when the acute processes subside – for chronic processes. Crucially, this diverse behavior can be achieved by modelling a one-time exposure and changing only the three nanoparticle-specific parameters (rate of cauliflower formation, toxicity and signaling efficiency) – confirming that the model is not overly-simplified.

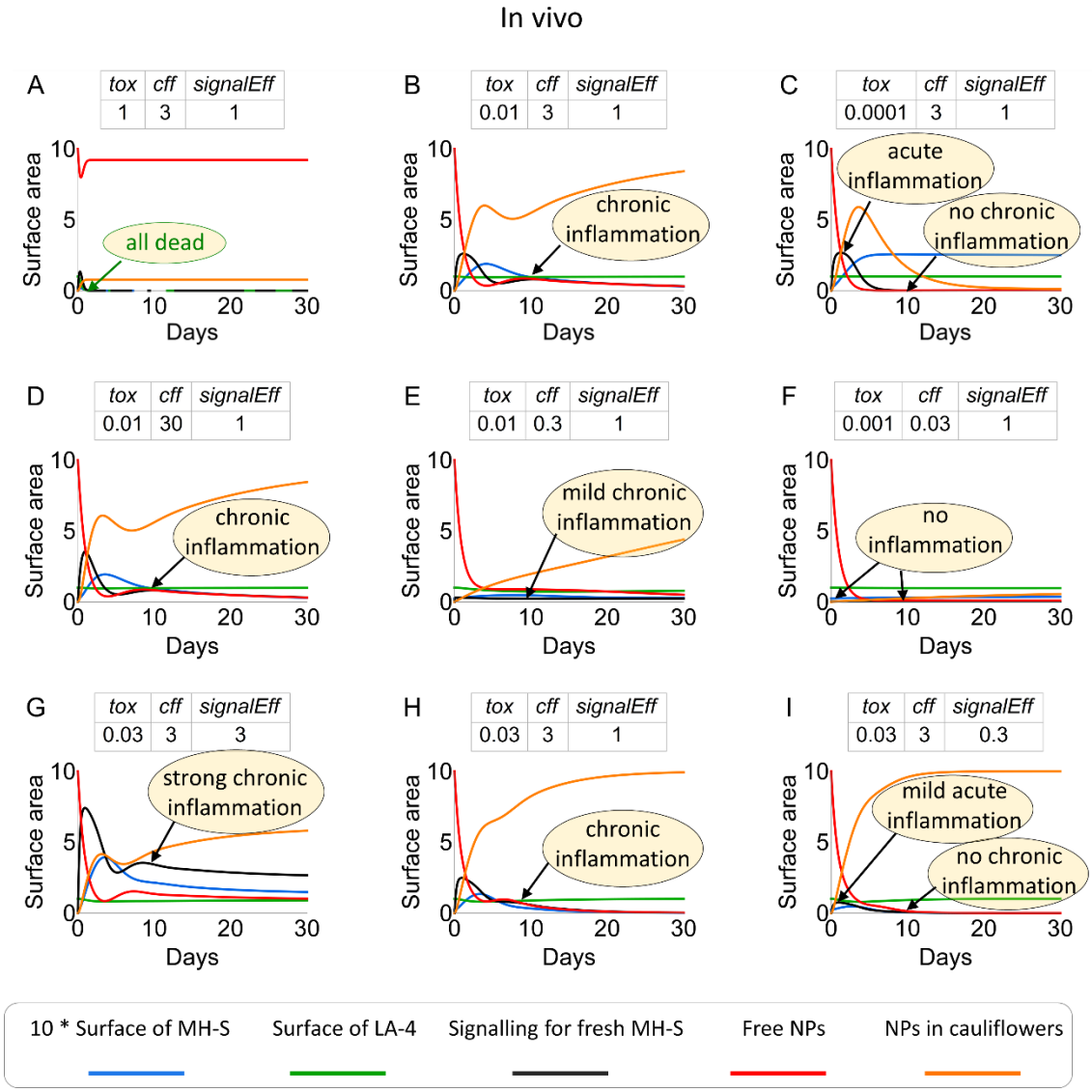

Figure 4.1: Theoretical in vivo time-courses for nine chosen sets of nanoparticle (NP) parameters. The black curves correspond to immune signaling $signalEff\ cff\ sLa4(t) * tanh[npLa4(t)/sLa4(t)\ cff\ timecf]$; the rate of increase in MH-S surface which follows it three hours later is 40-times smaller than this signal. The color and position of arrows denote the time traces and the time-points from which the endpoints are visually determined: if the surface of epithelial cells (green curve) falls below 0.3, the endpoint is "all dead" (i.e. severe loss of epithelial function); if not, the length and severity of inflammation are determined from the time-course of the black curve, which represents the inflammatory signaling; it is usually read-out at day 1 and day 10 for acute and chronic inflammation, respectively.

4.3 Phase Space of the Three Nanoparticle-Dependent Parameters: the Nanoparticle Sorter Cube

To obtain a deeper understanding of how the three key nanoparticle-specific parameters (*tox, cff* and *signalEff*) influence the outcome, we decided to investigate the phase space of long-term outcomes that they span in more detail. We simulated the short- and long-term outcomes of a one-time exposure for a wide range of nanoparticle parameters and plotted the results in a 3-dimensional cube with the three parameters on the axes (shown below). This phase space, termed the nanoparticle sorter cube, not only connects the outcomes to specific values of nanoparticle parameters, but also allows sorting and grouping of nanoparticles.

For better orientation, we separated the phase space in the cube according to the predicted theoretical endpoints with several boundary planes:

- the area above the black plane corresponds to strong in vivo inflammation (normed surface of newly arrived immune cells $> 2/40$)
- the area between the grey and black plane corresponds to mild inflammation ($0.5/40 <$ normed surface of newly arrived immune cells $< 2/40$)
- the area below the grey plane corresponds to negligible inflammation (normed surface of newly arrived immune cells $< 0.5/40$)
- the area on the left of the yellow plane corresponds to severe loss of epithelium viability ("all dead") (normed surface of epithelium < 0.3).

The read-out time-points for acute and chronic inflammation were selected at 1 day and 10 days post exposure: according to Figure 4.1, acute processes peak at around one day after exposure, and most of them significantly fade before 10 days after exposure.

As can be seen in Figure 4.2, the chronic inflammation in the nanoparticle sorter cube is located in a bent U-shaped valley. The toxicity and quarantining rate determine whether development of chronic inflammation is possible at all, while signaling efficiency determines the strength of inflammation when it is present.

Not surprisingly, very few nanoparticles with a low toxic effect on cells (located on the right part of the cube) exhibit chronic inflammation at dose 10:1. This makes sense as they do not kill many cells, thus slowing down the nanoparticle cycling.

On the other hand, nanoparticles with an extremely small quarantining rate (located near the back of the cube) also do not induce inflammation at dose 10:1 – because most of the epithelium-internalized nanoparticles remain inside the epithelial cells, the nanoparticles are more evenly distributed between all the cells, thus lowering the dose per macrophage and slowing down the nanoparticle cycling. However, the lack of quarantining also increases the dose per epithelial cell, which increases the epithelium death rate, which can be seen as a right-shift of the "all dead" plane near the back of the cube.

The "all dead" area to the left of the yellow plane corresponds to nanoparticles with extremely high toxicity towards cells. Here, the quarantining rate and signaling efficiency can only slightly reduce the damage to the system, but are sooner or later overpowered by the strong toxic effect to the cells, which disrupts the epithelium layer.

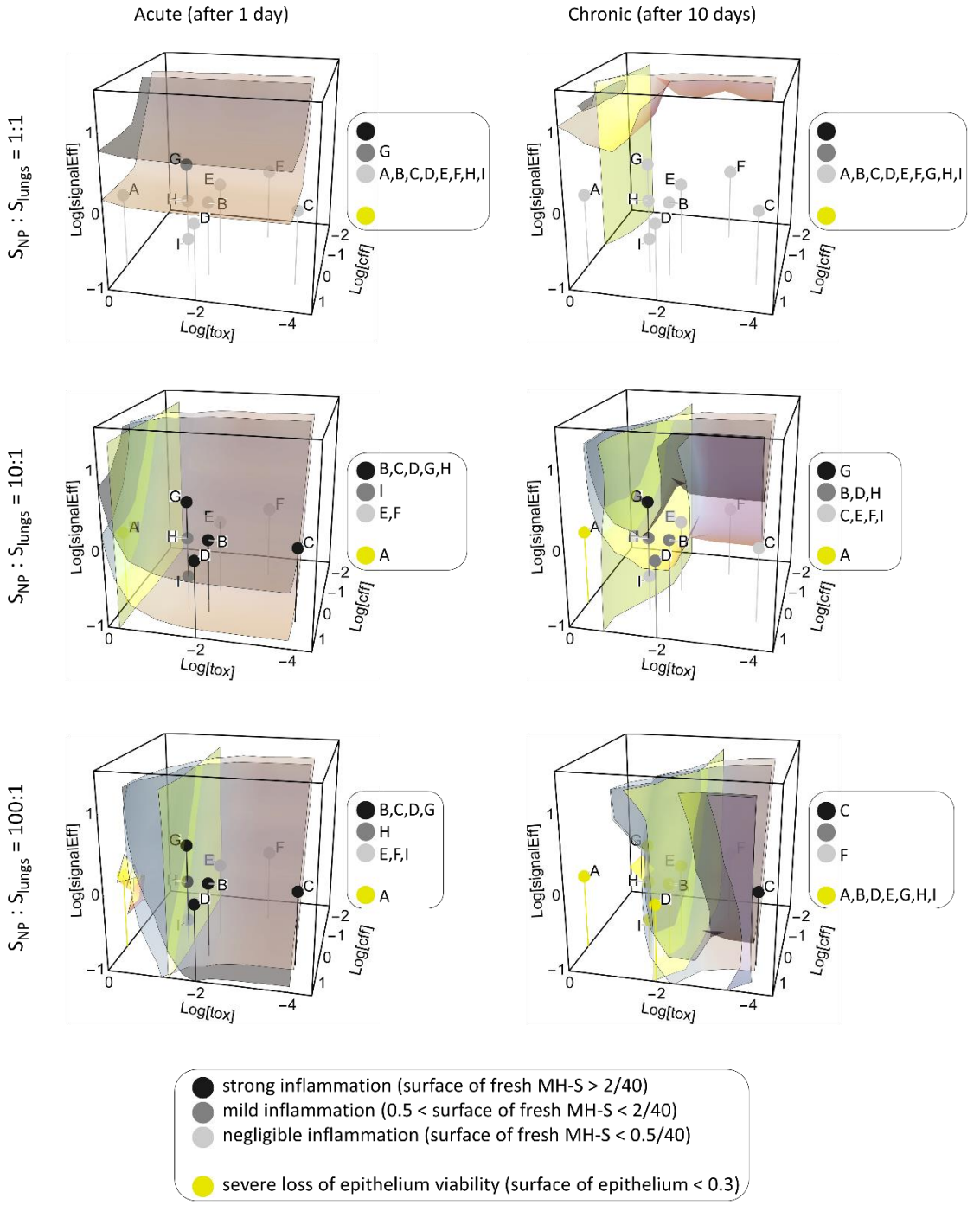

Figure 4.2: The nanoparticle sorter cube with theoretical end-points at three different exposure doses (nanoparticle-to-alveolus 1:1, 10:1 and 100:1) and two time-points corresponding to acute and chronic inflammation (1 day and 10 days after exposure, respectively). Spheres, marked with letters from A to I, correspond to the set of nanoparticle parameters whose time-traces are depicted in Figure 4.1, with the color of the sphere corresponding to the observed end-point. The grey and yellow contours separate the sorter cube into areas with a similar outcome.

4.4 Translating the Model to In Vitro Conditions

Now that we have verified the potential of the model to mimic various in vivo inflammatory outcomes, one might wonder how to use this theoretical model for theoretically predicting inflammation of real-world nanoparticles of interest. To do this, the three key nanoparticle-specific model parameters (rate of cauliflower formation: cff, signaling efficiency: $signalEff$, and toxicity: tox) that govern the behaviour of the theoretical system must first be determined for exactly those nanoparticles. A direct approach would be to measure macrophage and neutrophil numbers in the bronchoalveolar lavage, and the size of cauliflowers in histological samples a few days after exposure, and use the model for time propagation of the determined variables. However, because we strive to develop an alternative to animal testing, extraction of these parameters from in vivo experiments is not desirable, and we shall focus on in vitro experiments instead.

In order to extract the three key nanoparticle-specific model parameters from in vitro coculture experiments, we must first slightly rewrite the in vivo equations into in vitro equations to accommodate for the differences between the two systems. Most notably, the in vivo influx of immune cells triggered by signaling is replaced by macrophage replication ($mhsRep$; the rate of which is equal to $la4Rep$), so the key parameter $signalEff$ is left out as well. However, a quick glance at the equations (shown below) shows that extraction of the other two key parameters (tox, cff) from a coculture is also not trivial because the equations are still very intertwined with each other:

1. $$\frac{d}{dt}npFree(t) = tox\ npLa4(t)\, npLa4(t)/sLa4(t) + tox\ npMhs(t)\, npMhs(t)/sMhs(t) - endo\ sLa4(t)\ npFree(t) - endo\ sMhs(t)\ npFree(t) \tag{4.7}$$

2. $$\frac{d}{dt}npLa4(t) = endo\ sLa4\ npFree(t) - cff\ sLa4(t)\ \tanh[npLa4(t)/sLa4(t)\ cff\ timecf] - tox\ npLa4(t)npLa4(t)/(sLa4(t)) \tag{4.8}$$

3. $$\frac{d}{dt}npCF(t) = cff\ sLa4(t)\ \tanh[npLa4(t)\ /\ (sLa4(t)\ cff\ timecf)] - endo\ cfuEff\ sMhs(t)\ npCF(t) \tag{4.9}$$

4. $$\frac{d}{dt}npMhs(t) = endo\ sMhs(t)\ npFree(t) + endo\ cfuEff\ sMhs(t)\ npCF(t) - tox\ npMhs(t)\ npMhs(t)\ /\ sMhs(t) \tag{4.10}$$

5. $$\frac{d}{dt}sLa4(t) = la4Rep\ sLa4(t)\ (1 - sLa4(t)/la4Max) - tox\ npLa4(t) \tag{4.11}$$

6. $$\frac{d}{dt}sMhs(t) = mhsRep\ sMhs(t)\Big(1 - \frac{sMhs(t)}{mhsMax}\Big) - tox\ npMhs(t); \tag{4.12}$$

the nanoparticle-dependent parameters in the equations are shown in red and the rest in green. The meaning of each equation is:

1. The surface area of free nanoparticles increases due to cell death of epithelial cells and macrophages, and decreases by internalization into epithelial cells and macrophages.

2. The surface area of nanoparticles in living epithelial cells increases through internalization of nanoparticles by epithelial cells and decreases due to exocytosis (cauliflower formation) and death of epithelial cells.
3. The surface area of nanoparticles in cauliflowers increases due to exocytosis (cauliflower formation) and decreases due to macrophages internalizing cauliflowers.
4. The surface area of nanoparticles in living macrophages increases through internalization of free nanoparticles and cauliflowers, and decreases due to death of macrophages.
5. The surface of living epithelial cells increases through replication until they are confluent and decreases due to the death of epithelial cells.
6. The surface of living macrophages increases through replication until they are confluent and decreases due to macrophage death.

A possible approach here would be to measure the time-trace of some of the variables in the coculture (see Figure A.19 in the Appendix) and extract the key parameters from these observables through one of the methods for solving nonlinear inverse problems. However, we decided to conceptually simplify the approach by extracting the parameters from the simpler equations of monocultures and, hopefully, in return further increase the throughput of the method and improve the determination of parameters.

The models of the in vitro monocultures are less complex because many of the terms are omitted from the equations. The epithelium monoculture can thus be described using the following system of only four equations (again, nanoparticle-dependent parameters shown in red and the rest in green):

1. $$\frac{d}{dt} npFree(t) = tox\ npLa4(t)\, npLa4(t)/sLa4(t) - endo\ sLa4(t)\ npFree(t) \tag{4.13}$$

2. $$\begin{aligned} \frac{d}{dt} npLa4(t) = endo\ sLa4\ npFree(t) - \\ cff\ sLa4(t)\ \tanh[npLa4(t)/sLa4(t)\ cff\ timecf] - \\ tox\ npLa4(t) npLa4(t)/(sLa4(t)) \end{aligned} \tag{4.14}$$

3. $$\frac{d}{dt} npCF(t) = cff\ sLa4(t)\ \tanh[npLa4(t)\ /\ (sLa4(t)\ cff\ timecf)] \tag{4.15}$$

4. $$\frac{d}{dt} sLa4(t) = la4Rep\ sLa4(t)\ (1 - sLa4(t)/la4Max) - tox\ npLa4(t) \tag{4.16}$$

which describe the following processes:

1. The surface area of free nanoparticles increases due to cell death of epithelial and decreases by internalization into epithelial cells.
2. The surface area of nanoparticles in living epithelial cells increases through internalization of nanoparticles by epithelial cells and decreases due to exocytosis (cauliflower formation) and death of epithelial cells.
3. The surface area of nanoparticles in cauliflowers increases due to exocytosis (cauliflower formation).
4. The surface of living epithelial cells increases through replication until they are confluent and decreases due to the death of epithelial cells.

The system of equations describing the macrophage monoculture is even more simple, containing only three equations and variables (nanoparticle-dependent parameter shown in red and the rest in green):

1. $$\frac{d}{dt} npFree(t) = tox\ npMhs(t)\, npMhs(t)/sMhs(t) - endo\ sMhs(t)\ npFree(t) \tag{4.17}$$

2. $$\frac{d}{dt} npMhs(t) = endo\ sMhs(t)\ npFree(t) - tox\ npMhs(t)\ npMhs(t)\ /\ sMhs(t) \tag{4.18}$$

3. $$\frac{d}{dt} sMhs(t) = mhsRep\ sMhs(t)\ (1 - sMhs(t)/mhsMax) - tox\ npMhs(t) \tag{4.19}$$

where each equation describes:

1. The surface area of free nanoparticles increases due to cell death of macrophages, and decreases by internalization into macrophages.
2. The surface area of nanoparticles in living macrophages increases through internalization of free nanoparticles, and decreases due to death of macrophages.
3. The surface of living macrophages increases through replication until they are confluent and decreases due to macrophage death.

To provide a better overview of the four aforementioned models (in vivo, in vitro coculture, and two in vitro monocultures), the tables below summarize their variables and parameters. The tables are supported by the graphical comparison of the theoretical time courses of the different models, shown in Figure A.19, Figure A.20, and Figure A.21 (in the Appendix) for the same set of nanoparticle parameters as already shown in Figure 4.1 and Figure 4.2. The simplicity of the systems and equations is nicely reflected in the number of variables, parameters and the simplicity and tameness of the time-traces, confirming that it is desired to use the least complex systems possible for determining the nanoparticle-specific parameters through measuring observables (variables) – both from an experimental and numerical point of view.

Table 4.3: An overview of the variables in all four models.

Model	**Variables / observables**
in vivo	*t, npFree, npLa4, npCF, sLa4, npMhs, sMhs*
in vitro coculture	*t, npFree, npLa4, npCF, sLa4, npMhs, sMhs*
in vitro epithelial cell monoculture	*t, npFree, npLa4, npCF, sLa4*
in vitro macrophage monoculture	*t, npFree, npMhs, sMhs*

Table 4.4: An overview of the parameters in all four models..

Model	Nanoparticle-specific parameters	Other parameters
in vivo	*tox, cff, signalEff*	*endo, la4Max, la4Rep, timecf, cfuEff, delay, macrophageSurface*
in vitro coculture	*tox, cff*	*endo, la4Max, la4Rep, mhsRep, timecf, cfuEff*
in vitro epithelial cell monoculture	*tox, cff*	*endo, la4Max, la4Rep, timecf*
in vitro macrophage monoculture	*tox*	*endo, la4Max, mhsRep*

4.5 Determination of the Nanoparticle-Specific Model Parameters Using Targeted In Vitro Tests

As shown in the tables and time-courses above, one should be able to fairly easily discern the three nanoparticle-specific model parameters from targeted measurements in appropriate in vitro systems. The plan, shown in Figure 4.3 and explained in detail below, is to start with the simplest systems and build from there. Hence, the parameter *tox* should first be determined from a macrophage monoculture. Knowing the value of *tox*, the parameter cff can be determined from an epithelium monoculture. Lastly, $signalEff$ is determined from a coculture using the known *tox* and cff and a pre-calibration to in vivo data.

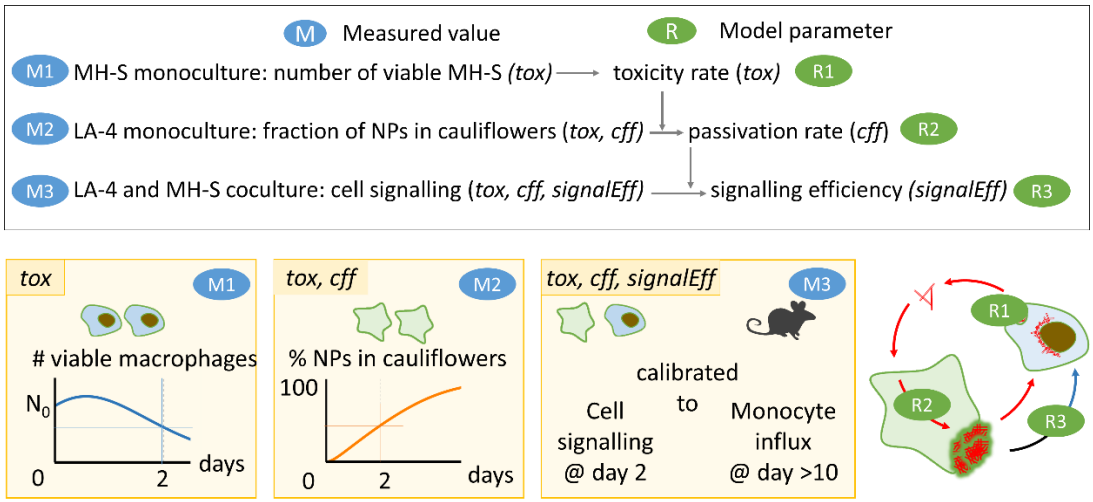

Figure 4.3: By using a multi-step approach, the model parameters can easily be determined from targeted in vitro tests.

4.5.1 Determination of the Toxicity Rate (*tox*)

In line with the "simple is better" approach, one should first extract the toxicity rate (*tox*) from in vitro macrophage monoculture, because it is the only in vitro model that is governed by solely one nanoparticle-specific parameter, making it easier to extract the value of the *tox* parameter from the data. Although the toxicity rate could in principle be extracted from the more complex epithelial cell monoculture or even the coculture, such an approach seems as an unnecessary complication.

The possible observables in the macrophage monoculture are the surface area of free nanoparticles, surface area of nanoparticles in macrophages, and surface of viable macrophages, of which the latter seems by far the easiest to measure. By using the measured surface of viable macrophages at a known time, the known initial conditions, and the known equations that govern the time-development of the system, the toxicity rate (the only unknown parameter in the system) can be determined by solving the so-called "inverse problem".

One way to extract the unknown parameter would be to use any of the existing mathematical and numerical approaches. An alternative approach (which in our case functions well due to the tameness of our system) is to model the time-course of the system for a large number of different values of the unknown parameter, thus producing a pre-generated table that connects the values of the unknown variable (e.g. toxicity rate) with the value of the measured observable (e.g. surface of viable macrophages). The value of the unknown variable can then be either extracted from this table by interpolation, or read-out from a graphical representation of the pre-generated table, as shown in Figure 4.4.

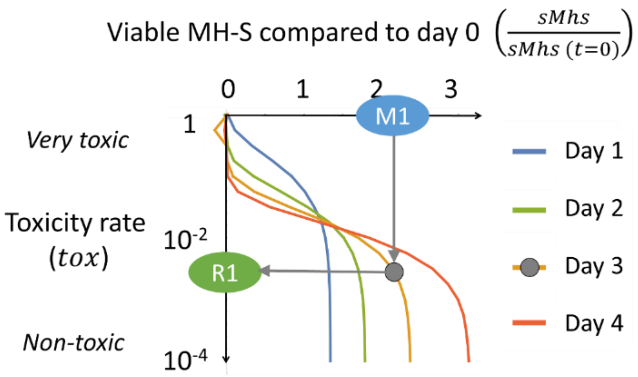

Figure 4.4: The toxicity rate *tox* (R1) can be determined from the measured relative increase of surface of viable macrophages (M1) in a macrophage monoculture after 1 – 4 days of exposure to the nanoparticles (surface dose 10:1). Different time-points offer different zones of sensitivity – shorter time-points are more suitable for more toxic nanoparticles and longer exposures for less toxic, where more nanoparticles need to be internalized to cause cell death.

In practice, the surface of viable macrophages can be determined by fluorescently labelling the exposed macrophages with a combination of three spectrally well separated dyes: one that labels the nuclei of all cells (e.g. Hoechst 33342, DRAQ5, etc.), another that labels the nuclei of "dead" cells (cells with compromised plasma membrane, e.g. propidium iodide, DRAQ7, etc.), and a third that labels the membranes/cytoplasm/organelles of all cells (e.g. CellMask, Mitotracker, Lysotracker, Citotracker, Nile Red, etc.), from which the area of the cell can be clearly seen. Then, using segmentation, the surface of living cells

can be determined, as shown in Figure 4.5. The key in this in vitro test is to use dyes that do not adhere strongly to the nanoparticles – a property that can easily be checked in the micrographs. As an alternative but less precise method, the number of viable macrophages can be counted by using only the two nuclear dyes, and multiplying the number of living macrophages with the average macrophage size, determined by an independent experiment. A third method – labelling the nuclei of dead cells and the membranes of all cells – is also appropriate, but requires fairly advanced segmentation approaches on the acquired micrographs, especially in dense samples and setups with low confocality (which is usually the case when imaging with a 10x objective which provides the large field of view needed to increase statistics). The sample density is not a concern for the former methods because the nuclei are well separated even in confluent cells.

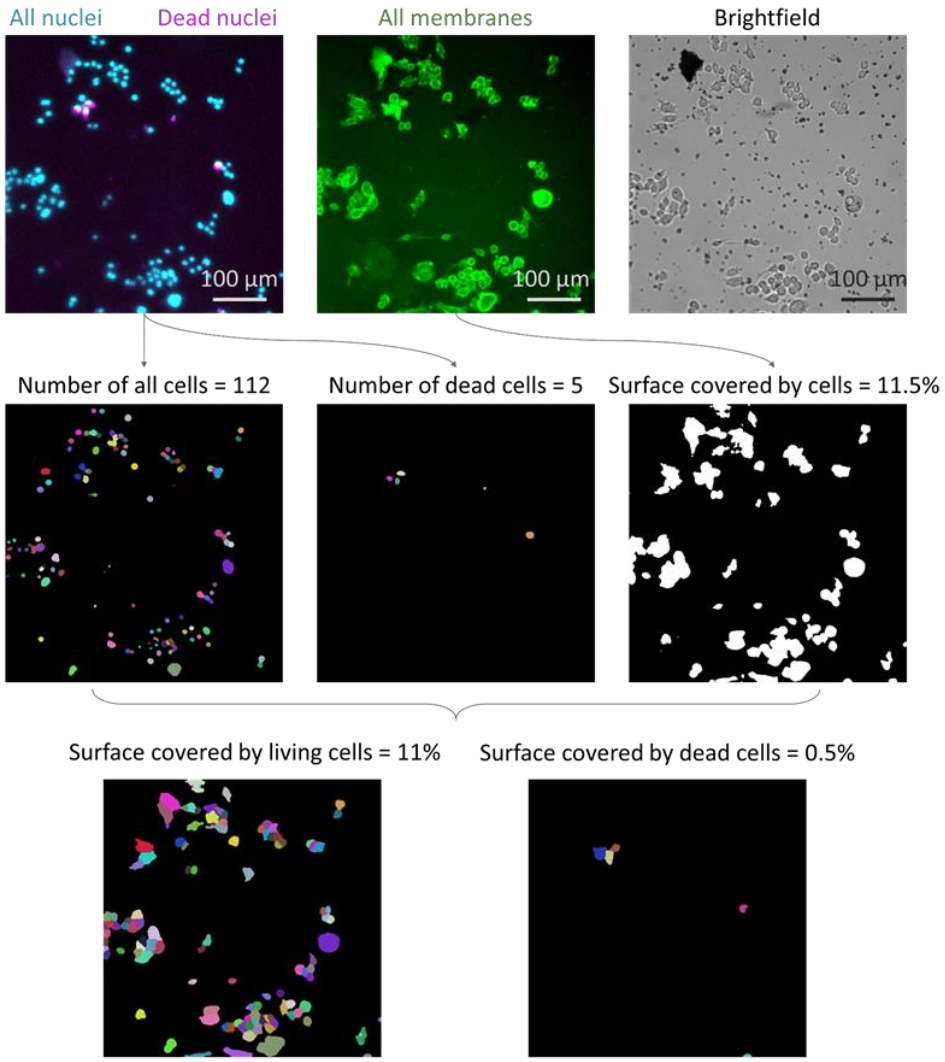

Figure 4.5: The viability and surface coverage of macrophages can be determined from fluorescence micrographs (top row, 10x objective). MH-S macrophages were incubated with a 10:1 surface dose of TiO_2 nanotubes for 2 days, after which the nuclei of dead cells were labelled with Propidium iodide (magenta, top left), nuclei of all cells with Hoechst 33342 (cyan, top left), and membranes of cells with CellMask Green (green, top middle). A brightfield image (top right) was acquired as well to provide an additional overview of the sample. As shown in the middle row, cell numbers and the total surface covered by all cells can be obtained by appropriate segmentation of the acquired fluorescence micrographs; note that in the segmented micrographs in the middle and lower row, each cell is shown in a different color to discern them more easily. These segmented images can then be used for further segmentation of the surface coverage to obtain the surface covered by living cells (bottom row). In our case, the obtained number coincides with the surface coverage of living cells, estimated from the total surface coverage and the fraction of living cells. Only a small field of view is shown here for clarity; usually, multiple larger fields of view are used for a more accurate determination of nanoparticle toxicity.

4.5.2 Determination of the Quarantining Rate (Cauliflower Formation Rate, cff)

To determine the quarantining rate cff, we again choose the simplest still appropriate model – the epithelial monoculture. If we were to try to determine the cff from a coculture with macrophages, the macrophage internalization of nanoparticles would unnecessarily complicate the system and equations. In the epithelial monoculture, the easiest-to-measure observable is the surface (viability) of the epithelial cells ($sLa4$), which unfortunately strongly depends on the value of the tox parameter and is on the other hand only weakly influenced by the quarantining rate cff (see Figure 4.6 A). Because of this, even the slightest error of the tox parameter or the measured surface of the epithelial cells can result in a major change in the determined cff, which is highly undesirable.

As an alternative, the next easiest observed variable is chosen – the amount of quarantined nanoparticles ($npCF$). From the measured $npCF$ and previously determined tox, the cff can be determined by solving the inverse problem or by using appropriate pre-generated tables (see Figure 4.6 B), derived in the same manner as described in Section 4.5.1.

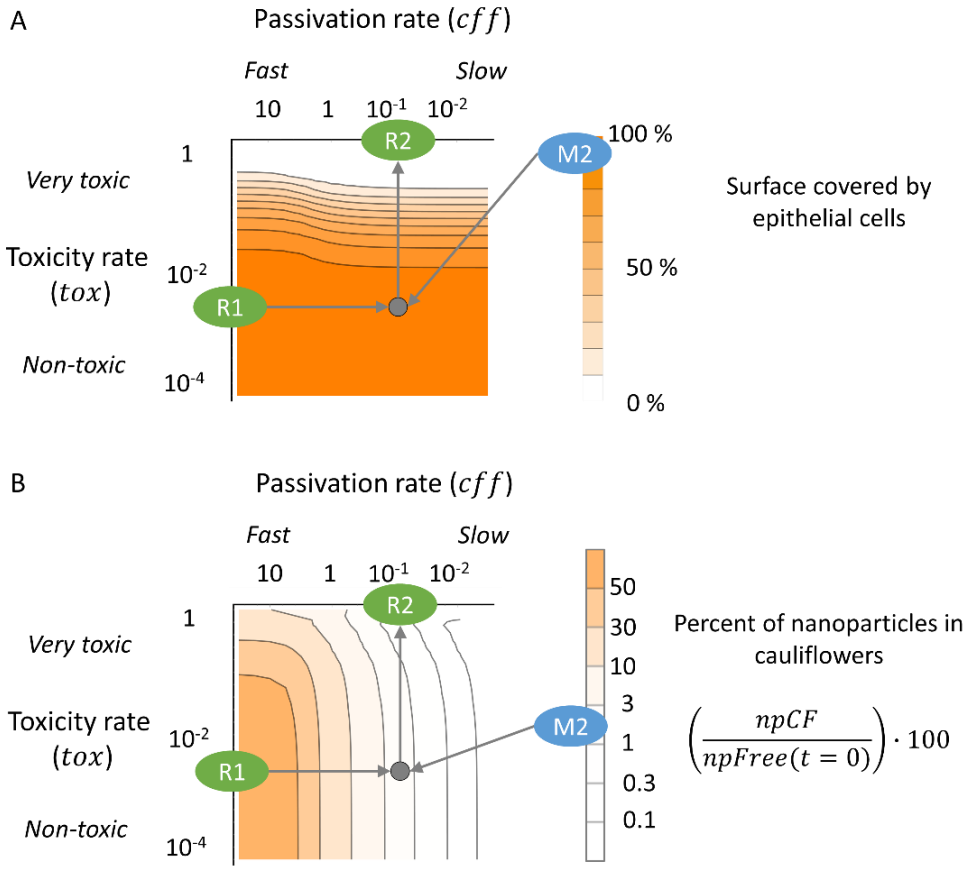

Figure 4.6: Determining the cff from the epithelial monoculture. **A** The surface covered by epithelial cells only weakly depends on the quarantining rate cff. **B** The quarantining rate cff (R2) can be determined from the measured percentage of nanoparticles located in cauliflowers (M2) and the toxicity rate tox (R1) determined previously. The graphs are shown for cells after a 2-day incubation with a 10:1 surface dose of nanoparticles.

An approach to quantify the percentage of quarantined nanoparticles is to combine fluorescence and reflectance microscopy. First, the medium from the exposed cells is removed and the amount of nanoparticles in this "lavage" is determined by reflectance microscopy. Then, the exposed cells are labelled with a fluorescent dye that labels both the cell and the cauliflowers, which enables one to determine the location of the nonlabelled nanoparticles, detected via reflectance microscopy. The ratio between the amount of nanoparticles in cauliflowers and the total detected nanoparticles can then be used as $npCF$ in the model. Alternatively, machine learning and/or advanced image analysis could be employed to differentiate nanoparticles in cauliflowers from free nanoparticles, eliminating the need for the lavage step.

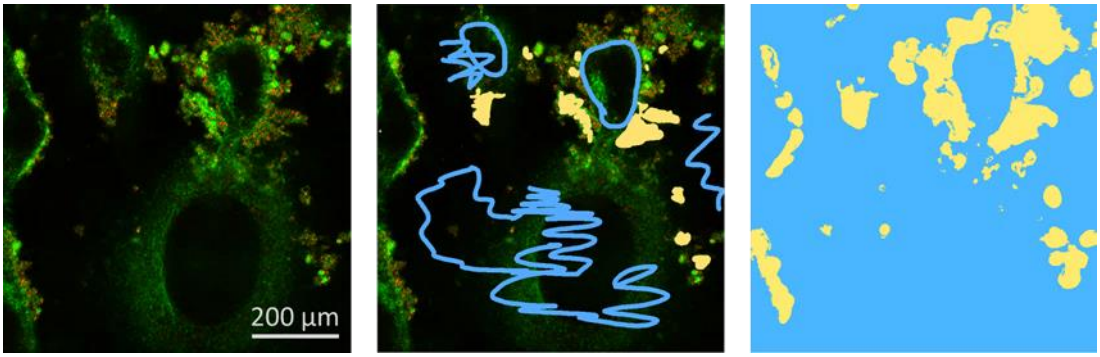

Figure 4.7: A proof-of-concept example of machine-learning-based detection of cauliflowers in a fluorescence micrograph. On the left is an xy fluorescence micrograph of LA-4 cells (cell membranes labelled with CellMask Orange, green) after a 2-day incubation with a 10:1 surface dose of TiO_2 nanotubes (detected by reflectance microscopy, red). During model training in Ilastik (middle figure), the user manually defines some of the areas in the micrograph that correspond to cauliflowers (yellow) and some of the areas that correspond to the rest of the sample (blue). Then, the integrated trained random forest classifier provides masks of the cauliflower regions for the entire micrograph (right figure, yellow), which can be used to determine the amount of nanoparticle signal in cauliflowers in that micrograph. The same trained model can then be used to detect nanoparticles in cauliflowers in other cross sections as well as in other micrographs.

Importantly, as shown in Figure 4.8, tox and cff together can already detect the nanoparticles that have the potential to cause chronic inflammation if their signaling efficiency is high enough (grey regions in Figure 4.8). Moreover, they also detect nanoparticles that significantly lower epithelium viability (yellow region in Figure 4.8) and nanoparticles that are safe regardless of their signaling efficiency (regions in Figure 4.8 that are neither grey nor yellow). However, this two-parameter prediction can consider some safe nanoparticles as potentially hazardous (false positives) if they are located in the grey regions in Figure 4.8. If one wishes to discern these nanoparticles from the truly hazardous nanoparticles, further testing should be done to determine their signaling efficiency ($signalEff$), as will be described in the following section.

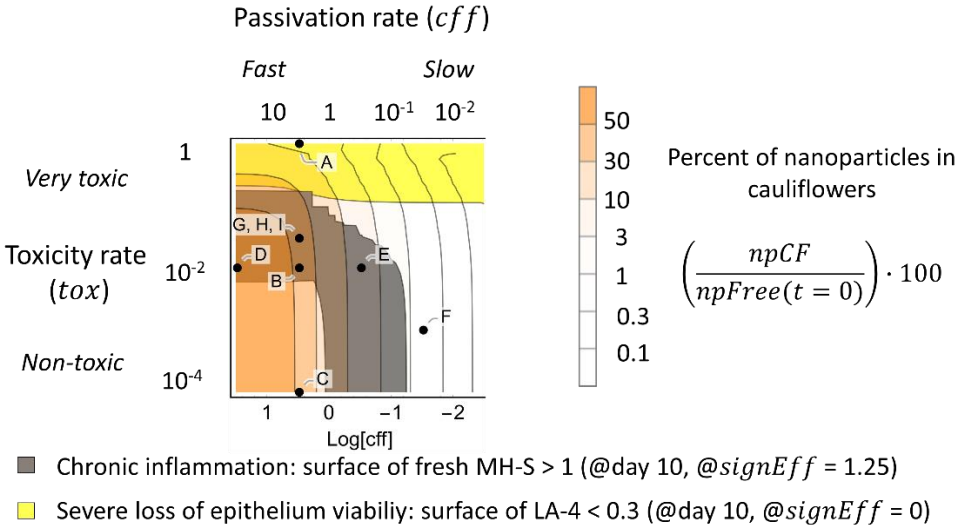

Figure 4.8: Theoretically predicted endpoints for nanoparticles A-I (same as in Figure 4.1 and Figure 4.2) performed on the basis of two nanoparticle parameters – *tox* and *cff*.

4.5.3 Determination of Signaling Efficiency (*signalEff*)

Lastly, the third nanoparticle-dependent parameter, signaling efficiency $signalEff$, should be determined. Because it is not included in any of the in vitro equations, it requires a special approach.

The observable in our in vivo model that is closest to the available data from already published in vivo experiments is the signaling-induced influx of immune cells into the lung:

$$influxMhs/macrophageSurface = signalEff * \ cff * \ \ sLa4(t - delay) * \\ \tanh[npLa4(t - delay) \ / \ (sLa4(t - delay) \ \ cff \ timecf)], \tag{A.20}$$

which roughly corresponds to the relative number of polymorphonuclear cells (PMN), most commonly neutrophils, in cell counts of in vivo bronchoalveolar lavages – a metric commonly used to quantify the extent and severity of inflammation. Although the amount of free nanoparticles *npFree* in bronchoalveolar lavages would also be a relatively easily measured observable, it is not commonly measured, leading us to lean towards using $influxMhs$ as the observable due to the large amount of published in vivo data.

One way to determine the $signalEff$ is by a similar process as the previous parameters: an appropriate table is pre-calculated from the predetermined *tox* and cff, which are used to determine the $signalEff$ from the relative number of PMN cells measured in vivo at a 1:1 surface dose (a high enough dose to induce a PMN influx, but low enough to be included in the range of doses that are typically measured), as shown in Figure 4.9. However, as we strive for an animal-free prediction, the use of in vivo data for large-scale nanoparticle testing is not desirable and should only be used for calibration and validation of the model.

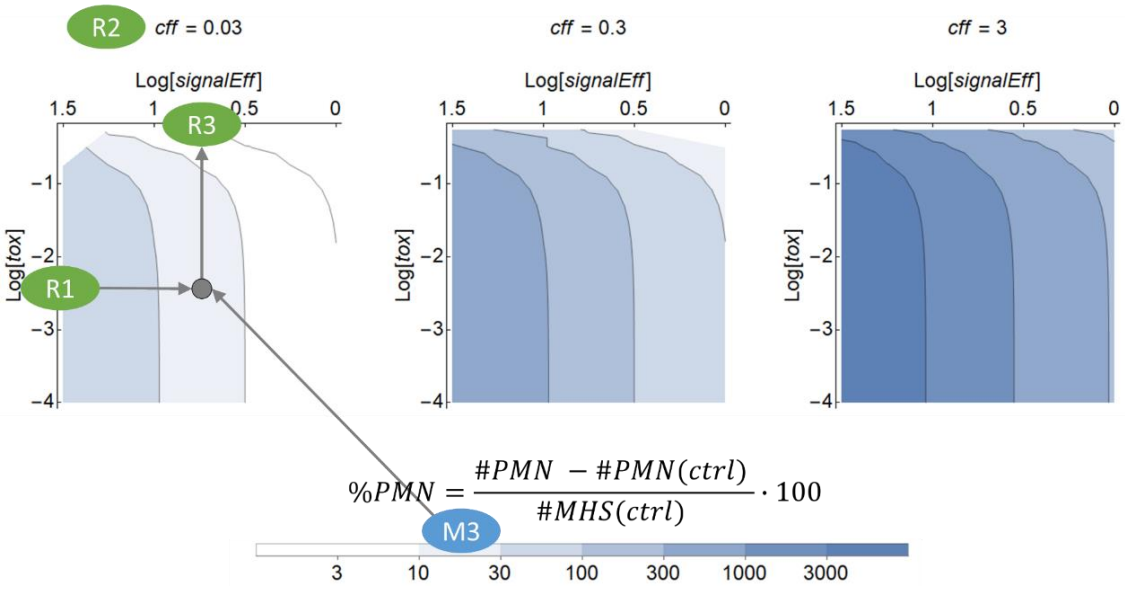

Figure 4.9: The signaling efficiency $signalEff$ (R3) can be determined from the measured percent of PMN in bronchoalveolar lavages after one day (M3), combined with the previously determined tox (R1) and cff (R2).

To devise an in vitro test for determining the signaling efficiency $signalEff$, we utilised the knowledge that although no immune cells can be infiltrated in vitro, some of the signaling which could initiate it should still be present in the cell cultures. To detect it, we decided to use a sandwich ELISA assay (Enzyme-Linked Immunosorbent Assay) as it is more cost-efficient than transcriptomics (the results of which were shown multiple times in Chapter 3 for the TiO_2 nanotubes). In short, this colorimetric assay works by binding specific cytokines (that were released from the cells) onto specific antibodies that are attached to the bottom of each well. Then, an enzyme is attached onto the bound specific cytokines, which catalyzes a colorimetric reaction that is monitored by measuring the time-dependence of the sample absorbance.

In contrast to transcriptomics, where one obtains the entire list of genes and their expression levels and can search the obtained results for specific cytokines, ELISA requires the molecules of interest to be determined prior to the measurement. Using the transcriptomics results from TiO_2 nanotubes and a literature search, we narrowed down the long list of cytokines to eight cytokines. These selected cytokines, on which we performed the ELISA measurements, were: CCL2 (MCP1), CCL3 (MIP1a), CCL4 (MIP1b), CXCL12 (SDF1), TNF-α, IFN-γ, IL-1b, and IL-6. The seven metal oxides for which we measured the concentrations of cytokines (TiO_2 nanotubes, TiO_2 nanocubes, TiO_2 MKNA015, TiO_2 NM-101, TiO_2 NM-105, ZnO NM-111, and crystalline silica – DQ12) were chosen to cover a wide spectrum of induced PMN influx in vivo one day after exposure (see Table A.4 in the Appendix).

Interestingly, the calculated effective cytokine concentrations increase more for the nanoparticles that induce milder inflammation in vivo (as determined from the calculated relative number of PMN and the measured cytokine levels shown in Figure 4.10). This could be caused by adherence of cytokines to the nanoparticles. Also, it is worth noting that the ELISA results do not necessarily overlap with the transcriptomics because transcriptomics measures genes that are being actively transcribed, whereas ELISA measures the excreted cytokines. For example, the cytokines that have already been synthesized and are prepared for quick secretion are visible in ELISA but not in

transcriptomics. On the other hand, the cytokines which are transcribed but are excreted in vesicles or adhere strongly to the nanoparticles can be visible in the transcriptomics but not in the ELISA.

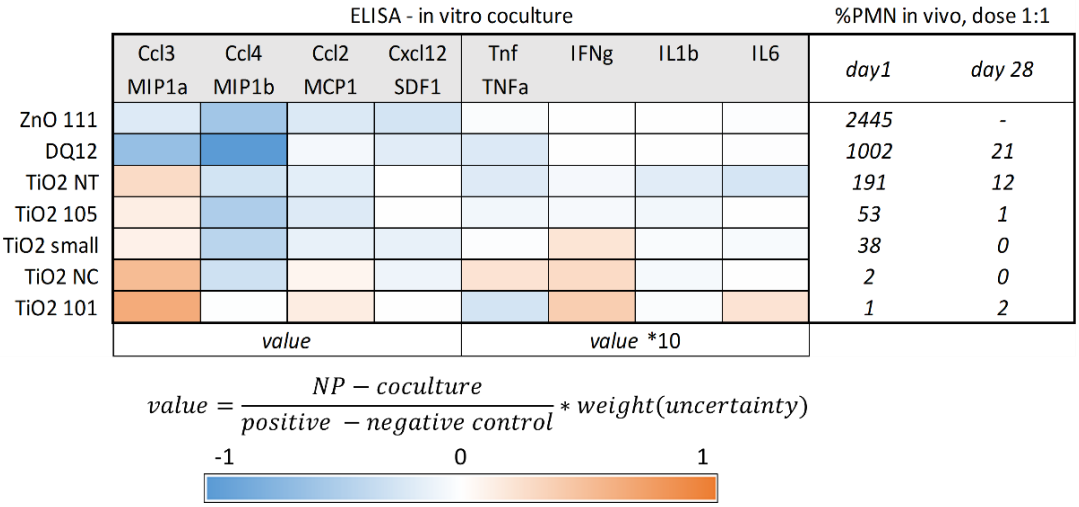

Figure 4.10: Effective change in cytokine concentrations, calculated from the fitted measured time course of TMB absorption. This effective change takes into account the positive, negative and blank controls, as well as the uncertainty of each measurement, and should be fairly independent from the properties of the cocultures and measuring devices. The %PMN represents the quotient between the number of PMN cells after exposure (normed to the control) and the total number of cells in the control at the same time-point to enable comparison between different sets of experiments. It was calculated by interpolating/extrapolating publically available in vivo data to a 1:1 surface dose. More details are available in Section A.3 in the Appendix.

The combination of these calculated effective cytokine changes can then be tied to the corresponding in vivo PMN influxes by Karhunen-Loève decomposition (KLD, a version of principal component analysis), as described in detail in Section A.3 in the Appendix. In short, after performing the KLD on the set of values in Figure 4.10, one obtains a transformation matrix $transfMatrix$ and a vector of weights $weights$ that can be used to estimate the in vivo PMN influx after 1 day of exposure to a 1:1 surface dose of nanoparticles $\%PMN$ from the ELISA measurements $elisaData$ for a metal oxide nanoparticle:

$$\%PMN = elisaData\ (transfMatrix\ \ weights)^T. \tag{4.21}$$

In the future, the measurements of these eight cytokines would ideally be substituted by measurements of all the cytokines, which would however be financially quite costly. As an alternative, they could be replaced by imaging the cellular responses to the entire cocktail of cytokines that were released into the medium. In this way, the system (living cells) would already appropriately sum up the contributions of various cytokines to produce a meaningful measureable outcome. Examples of possible imaging-based approaches are measurements of chemotaxis induced by chemokines and measurements of cellular activation, e.g. through specific markers or distinct changes of morphology, such as the M1 and M2 subtypes in macrophages. Also, potential in vitro cellular assays that correlate well with acute PMN influx in vivo could efficiently replace the lengthier and less cost-efficient ELISA measurements. In any case, the measured values should be calibrated with the in

vivo PMN influx, and the relationship between the measured values and the PMN influx should be at least roughly monotonous.

Chapter 5

Conclusions

From this work, it is evident that the use of (advanced) live-cell microscopy combined with complementary methods (such as omics) can help detect and understand the complex mechanisms of nanoparticle toxicity – an essential factor in the development of predictive nanotoxicology. Crucially, the here-described key processes have been observed both in vitro and in vivo with the same nanoparticles, increasing the relevance of our findings.

We have shown that chronic inflammation that follows nanoparticle exposure stems from continuous cycling of nanoparticles in the alveoli, which is formed by an interplay of several key events:

- **nanoparticle internalization** by alveolar macrophages and epithelial cells,
- **nanoparticle excretion and lipid-mediated quarantine** by epithelial cells (i.e. nanoquarantine, a newly-described cellular defense mechanism); this aids cell survival and leads to formation of large stiff immobile composites of nanoparticles and biomolecules on the cell surface (termed cauliflowers),
- **internalization and degradation of cauliflowers** by macrophages,
- **toxicity of the internalized nanoparticles** towards alveolar macrophages and epithelial cells, causing their **death and re-release of nanoparticles** that can be taken up by neighboring cells.

Because this continuous nanoparticle cycling is accompanied by pro-inflammatory signaling, it also causes a **continuous influx of immune cells**, replacing the dead macrophages in the above-mentioned processes. Ironically, because these cells internalize the already quarantined nanoparticles in cauliflowers, they enable the continuation of nanoparticle cycling.

Importantly, these processes and their relations can be described and mimicked by a theoretical model, consisting of several differential equations with three nanoparticle-specific parameters. By determining these parameters through a set of three simple, quick and cost-efficient in vitro tests, and solving these differential equations, the nanoparticle-specific theoretical course of inflammation is obtained, providing an insight on the severity and length of inflammation. The nature of the differential equations also allows one to detect the nanoparticles with high inflammatory potential even when omitting the costliest and most labor-intensive test (ELISA assay of eight cytokines). Although this approach produces several false positives (non-toxic nanoparticles labelled as toxic), it is useful as a low-effort pre-sorter of nanoparticles for more extensive testing.

Our initial hypotheses, that i) the lung epithelial cells possess defense mechanisms that enable them to survive exposures to nanoparticles even at extremely large doses and that

ii) alveolar macrophages do not employ the aforementioned defense mechanisms, have been confirmed with the discovery of nanoparticle excretion and lipid-mediated nanoquarantine, which are present in epithelial cells but not in macrophages. This is most likely due to different individual roles of these cells: lung epithelial cells produce and repair lipid-rich lung surfactant, whereas macrophages internalize and degrade foreign matter. However, the difference between the viability of both cell lines is not as pronounced as one might expect, suggesting that the macrophages might employ other defense mechanisms, one of which could be the here-observed aggregation of internalized nanoparticles inside cells.

The third initial hypothesis, that iii) re-exposure of cells to the nanoparticles that have been released from other dying cells (e.g. macrophages) prolongs the inflammation, was also confirmed. However, this process alone is not sufficient for the development of chronic inflammation from a single nanoparticle exposure. Our simulations show that adequate pro-inflammatory signaling and an appropriate rate of nanoquarantining are also needed for the development of chronic inflammation.

5.1 Prediction Model

The next step in the development of this model should be its calibration with in vitro measurements and validation against in vivo data for a wide range of nanoparticles. We suspect that hydrophobic nanoparticles such as carbon nanotubes induce inflammation in a different manner than described in this work due to their inherently different interactions with the biological milieu. For these nanoparticles, a similar approach as shown here should be applied to develop an alternative, suitable model. Moreover, the solubility of certain nanoparticles such as zinc oxide could also be included in the model to extend its applicability. For instance, we have observed that zinc oxide nanoparticles severely lower cell viability when freshly prepared, but are non-toxic when given the time to dissolve before incubation with the cells. We suspect this to be a consequence of a higher local dose of zinc in the cells when internalized non-dissolved nanoparticles are degraded in the lysosome, where the protective bio-molecular corona is removed from the particles and their dissolution is increased by the low pH [123].

Two major elements which are lacking in our current theoretical model are clearance of nanoparticles and cells from the alveoli and the short life-span of neutrophils (1-5 days, depending on the cytokine concentrations). One consequence of this is that when the inflammation signaling decreases, the immune cells remain in the alveoli instead of migrating away/dying, which is why it was difficult to match in vivo BAL cell numbers to the prediction model. This could be corrected by adding a constant decay term to the number of immune cells, which would be small enough to be easily overpowered by signaling-induced influx of immune cells in the inflammatory state, but large enough to clear the excess immune cells when the inflammation subsides. Another consequence of the lack of clearance is that the amount of nanoparticles in the model remains constant – in contrast to the in vivo case, where the amount of nanoparticles decreases with time, lowering the inflammation as well. Because the rate of nanoparticle clearance varies greatly among different nanoparticles, it would be interesting to test whether the here-observed decrease in macrophage speed and mobility in vitro could be a predictor for the (lack of) in vivo clearance. If so, this could be used as an additional in vitro test to determine the clearance rate; one of the processes that is known to majorly influence the length and severity of inflammation. A third element which could be added to the model is additional signaling that originates from dying macrophages.

Lastly, we would like to briefly discuss the complex topic of the appropriate dose metric in terms of cellular toxicity. In the model, the probability for cell death was chosen to be

proportional to the surface area of nanoparticles per cell surface, in line with the surface dose metric. This metric makes perfect sense in the initial interactions, which are most likely surface-based (except for the dissolution of special nanoparticles, which is discussed above). However, when the cells internalize and aggregate the nanoparticles, the volume of the nanoparticles compared to the volume of the cell could be a more appropriate metric, especially in macrophages which fill a notable volume of the cell with nanoparticles.

5.2 Methodology

A critical methodological step in the determination of the key events and their relations was the development of a procedure for stable and well-characterized fluorescent labelling of the model nanoparticles, TiO_2 nanotubes, which enabled us to track them in living cells with high precision and resolution. At the same time, the application of reflectance microscopy was central in testing the resolved toxicity mechanisms on other nanoparticles, albeit at a lower spatial resolution. Although indispensable for the study of toxicity mechanisms performed here, both of these approaches to nanoparticle tracking have their strengths and weaknesses. Developing a reliable fluorescent labelling procedure for a manufactured nanoparticle is a lengthy process which, if not properly controlled, can lead to a variety of experimental artefacts and misinterpretations. On the upside, it enabled us to locate very small aggregates on a confocal fluorescence microscope and even single nanotubes with STED microscopy. Reflectance microscopy, on the other hand, can be used to detect any non-soluble nanoparticles without lengthy nanoparticle preparation. However, the resolution and precision are typically lower than with fluorescently detected labelled nanoparticles, and most microscope setups cannot accommodate this type of measurements without a well-thought-out modification.

During the course of this work, the field of microscopy has advanced tremendously and setups previously seen as advanced are becoming more and more widespread. According to our experience, the most useful currently available features of a confocal fluorescence microscope for understanding toxicity mechanisms would be:

- a variety of excitation/detection options and multiple simultaneous detection schemes (for visualization of multiple organelles and processes simultaneously with tracking nanoparticles),
- a setup with low loss and excellent detection efficiency (this lowers the exposure of cells to light),
- a stage-top incubator and a stable auto-focus system with automated image acquisition of multiple regions (for tracking processes in multiple cells over the course of days),
- possibility of 3D stack acquisition (for additional insight regarding inter-cellular localization of nanoparticles and shapes of 3D structures),
- and, possibly, additional advanced modules, e.g. hyperspectral imaging, FLIM imaging, high resolution microscopy, etc. (for additional information on the system).

Such automated multi-channel 3D-time image acquisition – when coupled with automated image analysis – increases the statistics and provides a much-needed boost for scanning of the phase space of possible interactions and events.

5.3 Open Questions

As is common in science, this work opens a myriad of questions, some of which are gathered and discussed briefly below.

We noticed that cells in the MH-S monoculture are notably more viable than expected from in vivo data – the reduction in cell numbers in vitro is comparable to the lung-averaged reduction of cell numbers in vivo at 30-times lower exposure doses. Is this solely the consequence of the innate differences between in vitro and in vivo systems (and delivery efficiency) or would a different in vitro macrophage monoculture – be it a different cell line or primary cells – be more vulnerable and thus more appropriate for toxicity testing? If so, it would be interesting to observe the key differences between the responses of these macrophage monocultures and how they relate to cell viability, possibly revealing other novel innate cell-defense mechanisms.

Because we have shown that the LA-4 cell line of type II pneumocytes and the SH-SY5Y neurons are capable of nanoquarantining the nanoparticles – in contrast to the MH-S cell line of alveolar macrophages – we wonder which cell types and cell lines are also capable of nanoquarantining. Even more importantly, which characteristic of cells governs the ability of cells to quarantine nanoparticles? Is nanoquarantining an evolutionary beneficial cell-defense mechanism against foreign matter or is it merely a coincidental sequence of regular cellular processes that serve a different purpose but are hijacked/triggered by the nanoparticles, producing a fortunate outcome?

In this work, nanoparticles have been shown to enter the cells through various routes, giving rise to the question how much and in what way does the route of internalization influence the internal fate of nanoparticles and their toxic effect on cells? If we generalize the question – to what extent does the cell state (e.g. stage of the cell cycle, M1 and M2 phase in macrophages) influence the outcomes and in what way? Along these lines, one can wonder about an often noticed increase in the number of cells compared to the control cells at low doses of exposure (e.g. 1:1 surface dose). What is the mechanism behind this and does nanoparticle exposure trigger cell division? It is known that during cell division, the internalized nanoparticles in vesicles are asymmetrically divided between the cells [124]. As this results in an overall lower nanoparticle dose per each daughter cell and most likely increased likelihood of cell survival, it could be seen as another potential cell-defense mechanism – again, deliberate or accidental.

One can also wonder what happens if cells are devoid of nutrients (such as in autophagy). And vice-versa: how does nanoparticle internalization influence the energy levels and metabolism of the cells? A promising approach is by simultaneously monitoring the fluorescence intensity of NADH and FAD to determine their ratio, spectral/lifetime shift of NADH to determine the fraction of bound NADH, and mitochondrial morphology [125], all of which should be possible to be measured on the same cell over the course of a few days.

Also, because we found no influence on the size and number of lipid droplets in LA-4 epithelial cells after exposure to TiO_2 nanotubes despite the observed changes in lipid metabolism, this could be a marker of changes in the lipid composition in the cells. In turn, such an effect should influence the fluidity of cell membranes, critically regulating the uptake of nanoparticles and the rate of nanoparticle wrapping. In this case, it would be interesting to see whether the changes in membrane fluidity improve or impede cell survival. A changed fluidity of cell membranes could, for example, be detected by FCS (fluorescence correlation spectroscopy) [126] or via a shift in the emission spectrum [127] or lifetime [128] of specially designed fluorescent dyes.

Another intriguing topic is the influence of nanoparticle exposure on intra- and intercellular communication. We have observed that nanoparticle exposure fragments the actin network and that cytokines can adhere to the nanoparticles. Do any changes occur on the tubulin network and does nanoparticle exposure influence intercellular transport and communication? Do nanoparticles change the movement and/or clustering of organelles in the cell? How does the adherence of cytokines and vesicles to the nanoparticles (and cauliflowers) influence cell-to-cell communication? Does the presence of cauliflowers limit the supply of nutrients to the cell?

Several questions also arise when discussing the differences between the in vitro and in vivo settings. How does the presence of other cells (e.g. endothelial cells, fibroblasts, neutrophils, etc.) and surfactant modulate the here-described processes? How does the mechanic stimulation of cells during breathing and aerosolized deposition of nanoparticles modulate the processes? Also, does the presence of large cauliflowers in the alveoli obstruct the exchange of gas, nutrients and signals in the alveoli and present a noticeable obstacle for macrophage movement? Do these stiff structures induce enough additional strain to the alveolar walls to impede breathing and potentially damage the cells? All of these events could potentially lead to other adverse outcomes that are seemingly unrelated to the inflammation in the alveolar region.

5.4 Final Remarks

All in all, the work presented here illustrates the importance of including live-cell imaging-based methods in resolving the complex mechanisms in biological systems as they offer an alternative perspective to the more commonly used spectroscopic methods and omics, thus aiding the detection of novel events and discerning their interrelations. Moreover, the here-described combination of mechanism-based modelling and simple cell-based in vitro tests presents a useful basis for further refinement and, hopefully, widespread use for predictive nanotoxicology.

Appendix A

Supplementary Information

A.1 Over-Sonicated TiO_2 Nanotubes Can Disrupt the Cell's Cytoskeleton

One can see in the experiment shown in Figure A.1 that the TiO_2 nanotubes that have been broken into shorter pieces by a 2-hours long sonication can in fact disrupt the cell's cytoskeleton: when they were incubated with LA-4 cells at a 1:1 surface dose, the cells lost their stiffness and would wobble when scanned with a STED beam. Due to its shape, the STED beam always acts as an optical tweezer, but is too weak to cause any movement in healthy cells. It can, however, move mobile objects such as nanoparticles [52] and lipid-filled vesicles.

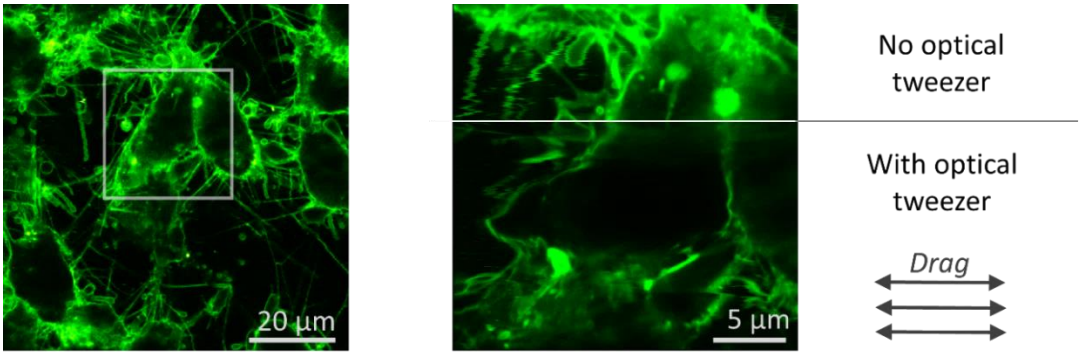

Figure A.1: Nanoparticles can disrupt the cell's cytoskeleton. After incubating LA-4 cells (membranes labelled with CellMask Orange, shown in green) with TiO2 nanotubes, that have been broken into shorter pieces by sonication, the cell membrane can be dragged by an optical tweezer (a 775 nm STED laser beam in this case).

A.2 Nanoquarantine is Observed with Many Nanoparticles

Exposure of LA-4 cells to nanoparticles can lead to the formation of variously common cauliflowers, ranging from large and very common cauliflowers to none at all. Table A.2 presents an overview of the extent of nanoquarantine (CFP, left-most column) and characteristic micrographs of LA-4 cells after a 2-day incubation with a 10:1 surface dose of the 12 tested nonlabelled nanoparticles. The CFP was determined qualitatively by visually scanning the sample with a 60x objective using bright-field and fluorescence, and

from the obtained micrographs. The criteria for determining the CFP are described in Table A.1 and the main characteristics of the tested nanoparticles are shown in Table A.3.

Table A.1: Table of criteria for the qualitative determination of the extent of quarantine, termed "Cauliflower-Forming Potential" (CFP).

CFP	**Extent of nanoquarantine – Cauliflower-Forming Potential (CFP)**
5	Most cells have large cauliflowers
4	Most cells have small cauliflowers OR up to 10% cells have large cauliflowers
3	Up to 10% cells have small cauliflowers
2	Up to 1 % cells have small cauliflowers
1	A few cauliflowers per 1 cm^2
0	No cauliflowers in 1 cm^2

Table A.2: The determined extent of nanoquarantine (CFP, left column) and typical xy micrographs of LA-4 cells (cell membranes labelled with CellMask Orange, shown in green) after a 2-day incubation with a 10:1 surface dose of various nonlabelled nanoparticles (detected via backscattered light, shown in red). The Field of view in the micrographs is 80 x 80 µm. The two samples where the majority of cells was non-viable (both were exposed to ZnO nanoparticles) are marked with an asterisk.

CFP	**Examples of micrographs**		
5 – Extensive	SiO_2 DQ12 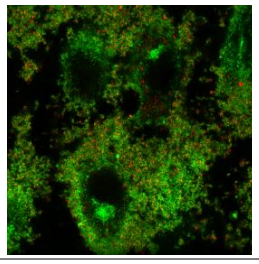	ZnO raw NM-110* 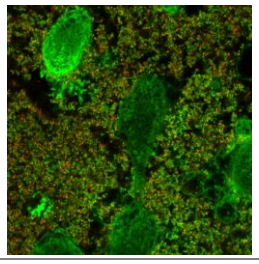	
4 – Strong	TiO_2 an. MKNA100 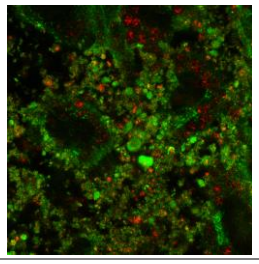	TiO_2 ru-an. NM-105 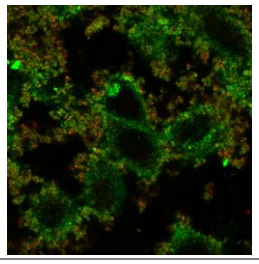	
3 – Mild	TiO_2 an. MKNA015 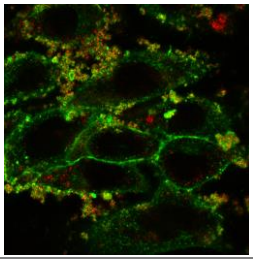	TiO_2 nanotubes 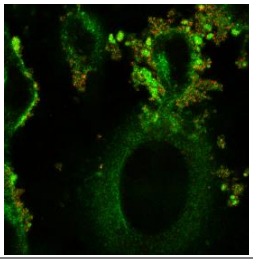	
1 - Weak	TiO_2 nanocubes 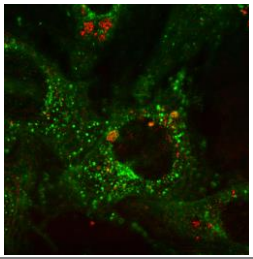	TiO_2 an. NM-101 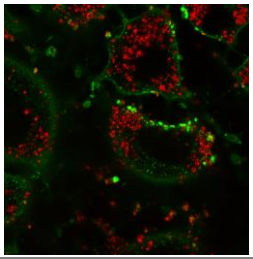	ZnO coat. NM-111* 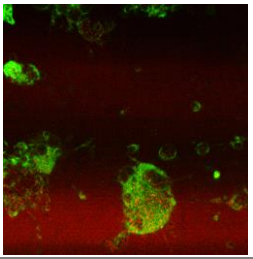

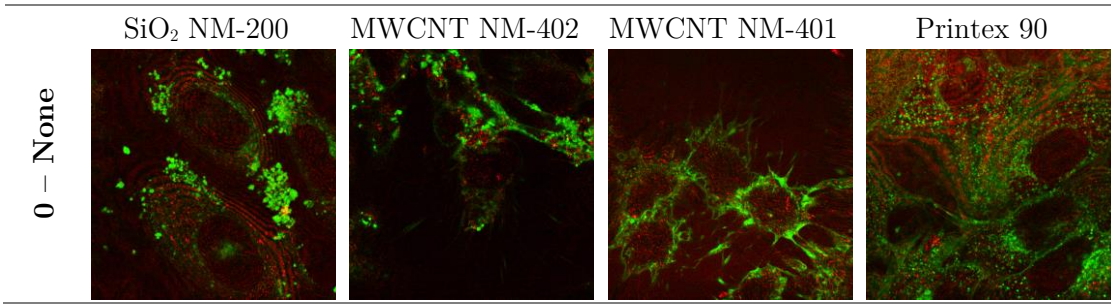

Although false positives and false negatives sometimes appear in the detected scattering due to interference and scattering off cell structures (see the red interference rings on the image of non-exposed cells below), they can be distinguished from the signal scattered by nanoparticles by their lower intensity and ring-like pattern.

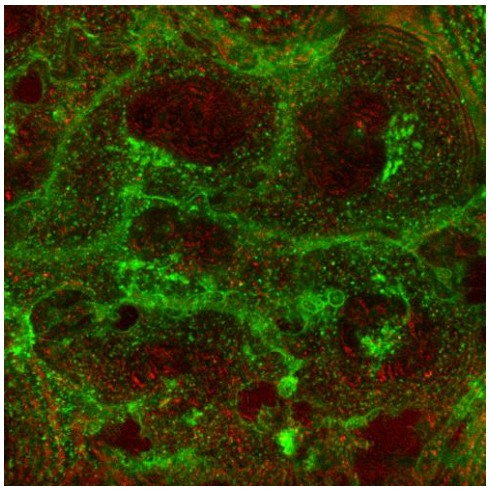

Figure A.2: A micrograph of the control – non-exposed LA-4 – with a more contrasted red channel (scattering) than figures in the table above.

Table A.3: Overview of the main characteristics of the tested nanoparticles, including the observed CFP.

NP name	**Characteristics**	**NP ID**	**BET surface area (m^2/g)**	**NP size D x L (nm)**	**CFP**
MWCNT NM-401	Thick nanotubes	JRCNM04001a	18	67 x 4000	0
MWCNT NM-402	Thin nanotubes	JRCNM04002a	226	11 x 1400	0
Printex 90	Carbon black		300	14	0
SiO_2 DQ12	Crystalline quartz		10	14	5
SiO_2 NM-200	Amorphous silica	JRCNM02000a	189	20	0

TiO_2 an. NM-101	Anatase	JRCNM01001a	230	5	1
TiO_2 an. MKNA015	Anatase nanospheres	MKN-TiO2-A015	85	12-50	3
TiO_2 an. MKNA100	Anatase nanospheres	MKN-TiO2-A100	74	16-28	4
TiO_2 nanocubes	Anatase nanocubes		97	15 x 20	1
TiO_2 nanotubes	Anatase nanotubes		154	10 x 100	3
TiO_2 rut-an. NM-105	Rutile-anatase	JRCNM01005a	46	20	4
ZnO raw NM-110	Non-coated	JRCNM62101a	12	70-110	5
ZnO coated NM-111	Coated with a hydrophobic triethoxycaprylsilane coating	JRCNM01101a	15	60-90	1

A.3 ELISA

A.3.1 Selection of Nanoparticles for the ELISA Assay

To select the seven nanoparticles for the ELISA assay, we gathered published, publically available in vivo data on BAL cell counts for a multitude of nanoparticles. Then, we calculated the percentage of PMN at a 1:1 surface dose ($S_{nanoparticles}$: S_{lungs}) by linear interpolation (or extrapolation in the case of SiO_2 DQ12 and ZnO NM-111). Because we strived for a linear metric of inflammation, we decided to calculate the percentage of PMN at a certain time- and dose-point as the quotient between the number of PMN in the BAL, corrected for the number of PMN in the controls, and the number of macrophages in the control BAL (non-exposed mouse) at the same time-point (%PMN; this metric is discussed in detail in Section A.2 in the Appendix). From the nanoparticles, we selected seven metal oxides that uniformly covered a wide range of inflammatory signatures, the properties of which are shown in the table below.

Table A.4: A table of chosen nanoparticles for ELISA assay, information on their physicochemical characteristics and the inflammation they induce in vivo at a 1:1 surface dose. Orange color corresponds to PMN > 5%, indicating inflammation. The %PMN was calculated from data, published in the references in the right-most column. *The values were extrapolated from the measured doses due to lack of data-points. **Data was not available.

NP name	Characteristics	NP ID	BET surface area (m2/g)	NP size D x L (nm)	%PMN @ 1:1 dose, 1 day	%PMN @ 1:1 dose, 28 days	Ref.
ZnO coated NM-111	Coated with a hydrophobic triethoxycaprylsilane coating	JRCNM 01101a	15	60-90	2445*	**	[129], CC-BY
SiO_2 DQ12	Crystalline quartz		10	14	1002*	21*	[29], CC-BY
TiO_2 nanotubes	Anatase nanotubes		154	10 x 100	191	12	[29], CC-BY
TiO_2 rut-an. NM-105	Rutile-anatase	JRCNM 01005a	46	20	53	1	[130], CC-BY-NC
TiO_2 an. MKNA015	Anatase nanospheres	MKN-TiO2-A015	85	12-50	38	0	[29], CC-BY
TiO_2 nanocubes	Anatase nanocubes		97	15 x 20	2	0	[29], CC-BY
TiO_2 an. NM-101	Anatase	JRCNM 01001a	230	5	1	2	[130], CC-BY-NC

A.3.2 Obtaining Concentrations from Time-Resolved ELISA Measurements

The sandwich ELISA used for the measurements relies on measuring the absorbance of the TMB substrate which is transformed from a form which does not absorb light in the visible spectrum to a blue-colored absorbing molecule. Usually, after a certain amount of time, a Stop Solution is added to all wells to change the pH of the sample and stop the conversion of TMB by the enzyme, simultaneously also changing the absorption spectrum of the oxidized TMB [131].

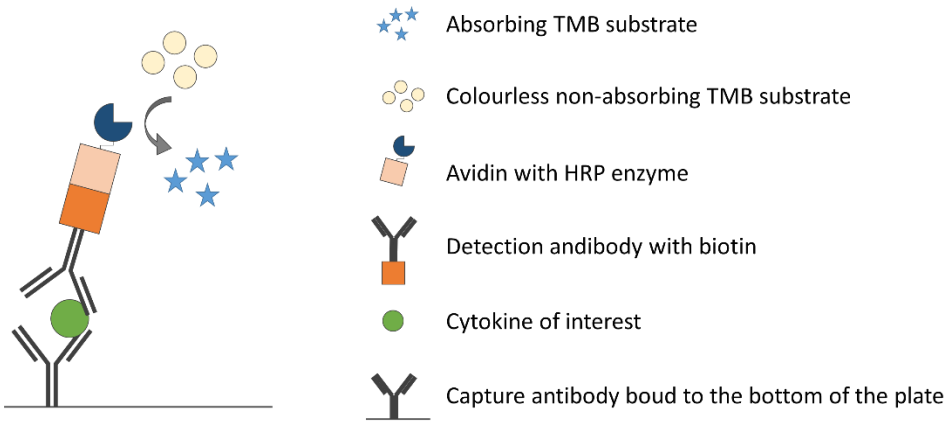

Figure A.3: A scheme of the TMB substrate reaction in the sandwich ELISA.

Because one can gain much more information from a time measurement than a single measurement in time, we measured the time evolution of TMB absorption at 650 nm in each well (examples in figure below).

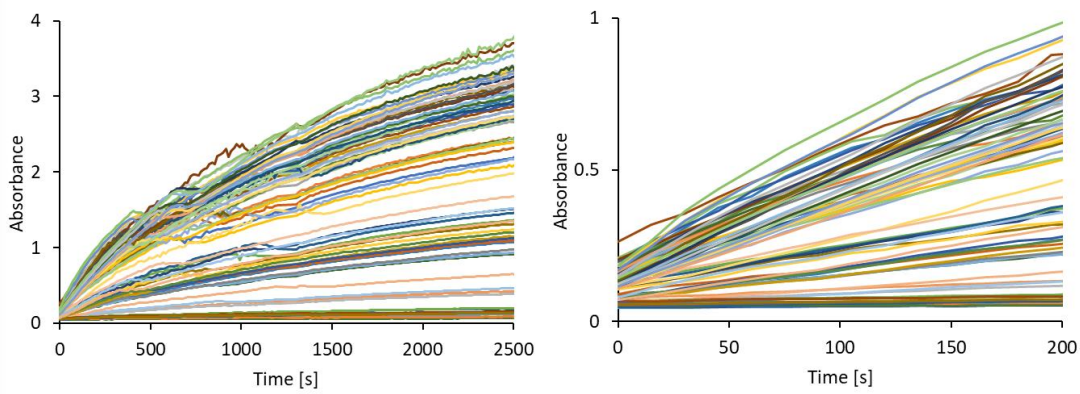

Figure A.4: Time evolution of the absorbance of TMB in several samples and the zoom-in on the first 200 seconds. Note the instabilities of the spectrofluorimeter spanning mostly from ca. 300 s to 1300 s, which are highly undesirable both in the time-resolved and endpoint ELISA measurements.

If we assume the conversion of the substrate TMB from non-absorbing *substrate* to absorbing *substrate** to be of first order (with rate k) and with a short lifetime of the intermittent complex with the enzyme, and that the enzyme concentration is proportional to the cytokine concentration $[cytokine]$, we can write the equations that govern the time-course of the detected absorbance *Absorbance*:

$$\begin{aligned} Absorbance(t) &= log_{10}\frac{I(t)}{I(0)} = \varepsilon l[substrate^*](t) \\ \frac{d[substrate^*](t)}{dt} &= k\ [substrate](t)\ [cytokine] \\ \frac{d[substrate](t)}{dt} &= -k\ [substrate](t)\ [cytokine], \end{aligned} \tag{A.1}$$

where I is the detected intensity and ε and l are the molar absorptivity of the TMB substrate and the height of the sample in the well, respectively.
By solving this system of equations, we find that

$$\begin{aligned} Absorbance(t) &= \varepsilon l \;\; [substrate]_{t=0} \; (1 - e^{-t \; k \; [cytokine]}) = \\ &= Absorbance(\infty) \; (1 - e^{-t \; k \; [cytokine]}), \end{aligned} \tag{A.2}$$

and thus

$$\begin{aligned} -\ln\left(1 - \frac{Absorbance(t)}{\varepsilon l \;\; [substrate]_{t=0}}\right) &= k \; [cytokine] \; t \\ -\ln\left(1 - \frac{Absorbance(t)}{Absorbance(\infty)}\right) &= b \; t; \quad b = k \; [cytokine], \end{aligned} \tag{A.3}$$

where a is the absorbance after an infinitely long time and b is the fitted ELISA slope.

Hence, we fitted a curve to the measurements performed in the first 200 seconds, after which our measuring system experienced severe instabilities measuring system (see the time-courses in Figure A.4 between 300 and 1300 seconds). Importantly, time-resolved ELISA helps to avoid artefacts from such instabilities as they can be more easily recognized in the curves than from endpoint measurements. The resulting fitted slopes b are shown in Figure A.5. It is important to stress here that the four leftmost cytokines (Ccl3, Ccl4, Ccl2 and Cxcl12) are so abundant both in the exposed and non-exposed cocultures that their slopes are similar to the slopes of the positive control and are thus most likely out of the range where the slope is linear to the cytokine concentration, although it should still be monotonous. On the other hand, the four rightmost cytokines (Tnf, IFNg, IL1b and IL6) are present in very low concentrations that are comparable to the negative controls.

	Ccl3 MIP1a	Ccl4 MIP1b	Ccl2 MCP1	Cxcl12 SDF1	Tnf TNFa	IFNg	IL1b	IL6
negative control	1.8E-05	1.7E-05	1.9E-06	8.5E-05	6.2E-06	2.3E-06	1.4E-05	1.5E-05
positive control	5.2E-04	2.2E-04	6.7E-04	1.0E-04	4.5E-04	4.1E-04	3.1E-04	4.8E-04
coculture	5.8E-04	2.6E-04	6.9E-04	7.0E-04	1.7E-05	7.2E-06	1.6E-05	2.7E-05
ZnO 111	4.8E-04	1.5E-04	5.5E-04	4.6E-04	1.2E-05	6.4E-06	1.5E-05	2.0E-05
DQ12	2.6E-04	5.6E-05	6.5E-04	5.2E-04	5.6E-06	6.9E-06	1.6E-05	2.1E-05
TiO2 NT	7.2E-04	2.1E-04	5.8E-04	7.2E-04	5.9E-06	3.6E-06	2.3E-06	7.0E-06
TiO2 105	6.5E-04	1.6E-04	5.6E-04	6.6E-04	1.0E-05	3.8E-06	6.0E-06	2.4E-05
TiO2 small	6.4E-04	1.8E-04	6.0E-04	5.5E-04	1.3E-05	1.6E-05	8.8E-06	1.7E-05
TiO2 NC	8.4E-04	2.0E-04	7.5E-04	5.7E-04	2.9E-05	1.9E-05	7.0E-06	2.3E-05
TiO2 101	9.1E-04	2.5E-04	7.9E-04	6.8E-04	3.9E-06	2.3E-05	9.2E-06	4.6E-05

Figure A.5: The slopes b of the measured samples; they are proportional to concentrations of cytokines for each cytokine separately. The concentrations of positive controls were 2 ng/ml.

A.3.3 Obtaining a Measure for the Effective Change in Cytokine Concentrations Between the Samples and Controls

The concentrations of cytokines were compared to their concentrations in the non-exposed (sham) cocultures and were also compared to the value in the positive and negative control to achieve a metric which was as independent on the coculture variability and measuring device as possible. This allows for comparison of results, measured on different days or even months. Various metrics were tested.

After many attempts, the best metric was found not to favor neither high nor low absolute values, also taking into account the interval of trust for each measurement – this is especially crucial for cytokines which naturally come in low abundancies. The best metric including these trust factors was found to be

$$value = \frac{NP - coc}{pos - neg}(1 - e^{-(NM-coc)^2/(2\ neg^2)})(1 - e^{-(pos-neg)^2/2\ neg^2}), \tag{A.4}$$

where NP denotes the slope of the sample, incubated with the nanoparticles, coc is the slope of the non-exposed cocultures, pos is the slope of the positive control and neg is the slope of the negative control. For the low-abundant cytokines (the four rightmost cytokines in Figure A.6), the *value* shown was multiplied by 10 for clarity.

The resulting values are shown in the table below. In the next step, these values should be calibrated to the in vivo %PMN values.

	ELISA - in vitro coculture								%PMN in vivo, dose 1:1	
	Ccl3 MIP1a	Ccl4 MIP1b	Ccl2 MCP1	Cxcl12 SDF1	Tnf TNFa	IFNg	IL1b	IL6	*day1*	*day 28*
ZnO 111	-0.20	-0.57	-0.22	-0.27	-0.03	0.00	0.00	-0.02	*2445*	-
DQ12	-0.64	-1.02	-0.06	-0.18	-0.21	0.00	0.00	-0.01	*1002*	*21*
TiO2 NT	0.28	-0.27	-0.16	0.00	-0.20	-0.06	-0.18	-0.25	*191*	*12*
TiO2 105	0.13	-0.49	-0.20	0.00	-0.08	-0.05	-0.08	0.00	*53*	*1*
TiO2 small	0.11	-0.42	-0.13	-0.14	-0.02	0.20	-0.03	-0.04	*38*	*0*
TiO2 NC	0.52	-0.30	0.08	-0.10	0.22	0.28	-0.06	0.00	*2*	*0*
TiO2 101	0.65	-0.01	0.14	0.00	-0.26	0.38	-0.03	0.22	*1*	*2*
	value				*value* *10					

Figure A.6: Resulting values, calculated from the fitted slopes of measured time traces of TMB absorption.

A.3.4 Coupling the Effective Measure *value* to the In Vivo PMN Data

Next, Karhunen Loève decomposition (KLD), a version of principal component analysis (PCA) was performed on the set of values shown in Figure A.6 to provide an orthogonal (uncorrelated) base for the comparison with the measured PMN influx later on. Karhunen Loève decomposition (KLD) was chosen because PCA pre-transforms the data so the sum of the columns of the PCA matrix is zero. This is undesirable in our case since it prevents comparing measurements from different measurement sets.

For the dataset

$elisaData =$

	MIP1a	MIP1b	MCP1	SDF1	TNFa	IFNg	IL1b	IL6
ZnO 111	−0.201757	−0.566553	−0.215463	−0.267965	−0.0272834	−0.00102794	−0.000141161	−0.0171957
DQ12	−0.639341	−1.01507	−0.0643014	−0.18184	−0.211658	−0.0000595959	-2.22848×10^{-6}	−0.0115273
TiO2 NT	0.27876	−0.269182	−0.164644	0.000226045	−0.201044	−0.0600546	−0.181297	−0.253592
TiO2 105	0.134532	−0.492964	−0.204411	−0.0038633	−0.0758339	−0.0546474	−0.078761	−0.0018705
TiO2 small	0.108771	−0.419323	−0.134334	−0.138535	−0.0150773	0.204056	−0.0309345	−0.0438645
TiO2 NC	0.521118	−0.296265	0.082082	−0.101959	0.216344	0.276982	−0.0587199	−0.00346255
TiO2 101	0.647586	−0.00797015	0.143435	−0.00102897	−0.264505	0.381295	−0.0260235	0.217278

the transformed input data in the basis of principal component vectors (denoted here as PC1-8, ordered by decreasing variance) was found to be

$transfData =$

	PC1	PC2	PC3	PC4	PC5	PC6	PC7	PC8
ZnO 111	0.533504	0.0711123	0.129878	0.00284931	0.0463852	0.0960701	0.388481	0.11
DQ12	1.09405	0.25924	−0.0604481	0.26608	0.0322441	0.136383	0.388481	0.11
TiO2 NT	−0.0116006	−0.296756	−0.0432407	0.220489	−0.0276537	0.126532	0.388481	0.11
TiO2 105	0.207533	−0.0793662	0.0465097	0.186371	0.210485	0.155781	0.388481	0.11
TiO2 small	0.138241	0.113859	0.129718	0.106538	−0.0012236	0.215353	0.388481	0.11
TiO2 NC	−0.317247	0.203426	0.338566	0.261054	0.0435666	0.117196	0.388481	0.11
TiO2 101	−0.611543	0.28938	−0.205498	0.140548	0.059552	0.130264	0.388481	0.11

and the transformation between the values for cytokines and principal components is defined by the following transformation matrix:

$transfMatrix =$

	MIP1a	MIP1b	MCP1	SDF1	TNFa	IFNg	IL1b	IL6
PC1	−0.779229	−0.545773	−0.147823	−0.121286	−0.0445006	−0.221993	0.0382684	−0.0751382
PC2	−0.137743	−0.188513	0.464577	−0.181248	0.0809134	0.585787	0.258545	0.529403
PC3	0.128402	−0.162311	−0.103592	−0.235904	0.921254	0.0331433	0.0199118	−0.201447
PC4	0.202824	−0.513089	0.554253	0.492829	0.0145973	−0.0389776	−0.251325	−0.283953
PC5	0.219985	−0.257645	−0.267242	0.362409	0.150874	−0.405182	0.111061	0.695124
PC6	−0.0177794	−0.163692	−0.564789	0.464047	−0.0253583	0.645981	0.0388249	−0.138277
PC7	0.427118	−0.479146	−0.2322	−0.546341	−0.291381	0.104557	−0.367995	0.0657914
PC8	0.291659	−0.232879	−0.00818185	−0.0934795	−0.185043	−0.112066	0.84786	−0.29365

The relationship between the $data$, $transfData$ and $transfMatrix$ is

$$transfMatrix \;\; elisaData^T = transfData^T. \tag{A.5}$$

As seen in the lower figures, the line which connects the nanoparticles ordered by their PMN influx is complex for both the single principal components (PC) and their pairs, indicating a complex underlying biological system, which should be described by at least a few principle components.

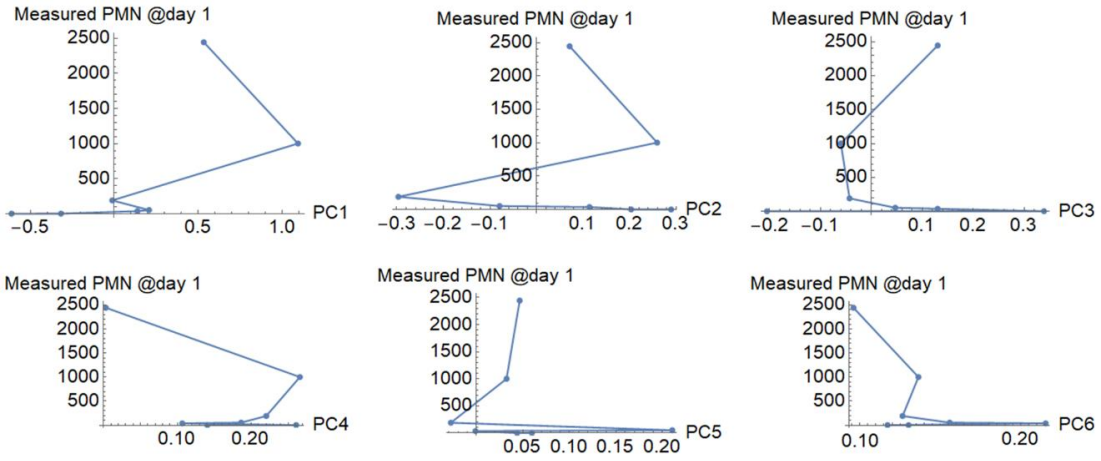

Figure A.7: Graphs of PMN influx compared to the six largest principal components (PC1 – PC6). The line that connects the nanoparticles in order of their PMN influx is non-monotonous.

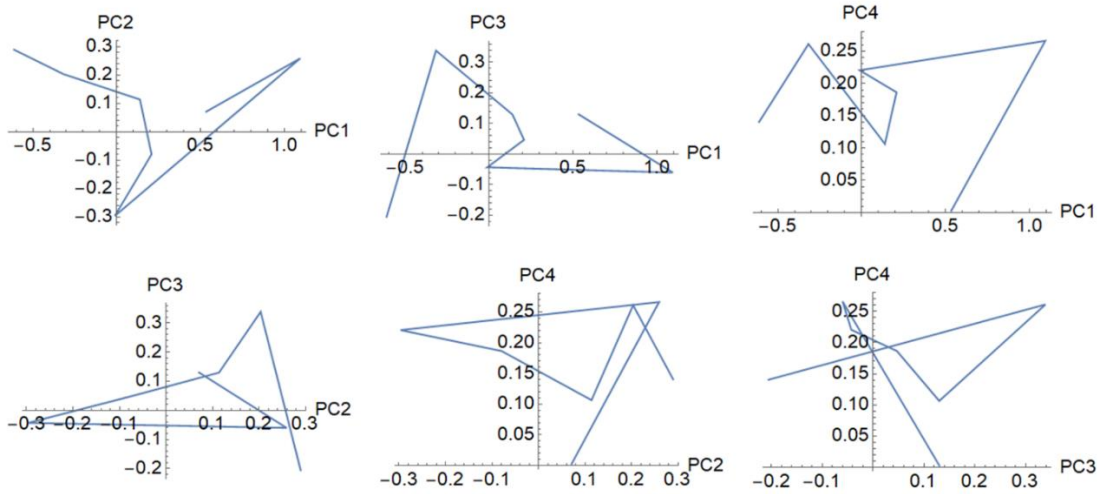

Figure A.8: Graphs of PMN influx compared to various combinations of the first four principal components. The line that connects the nanoparticles in order of their PMN influx is non-monotonous.

To obtain the appropriate linear combination of the principal component vectors which corresponds to the measured PMN influx, a set of linear equations defined by

$$\%PMN = (elisaData \;\; transfMatrix^{\,T}) \;\; weights \tag{A.6}$$

was solved using the Least Squares approach in Wolfram Mathematica for an increasing number of principal component vectors. As the results in Figure A.9 show, the non-monotonous relationship between the measured ELISA signals and PMN numbers in vivo and the complex system complicate the analysis, resulting in the system being described by at least seven principal component vectors, with the vector of weights being

$$weights = \{998.204, 303.065, 426.709, -5659.81, -1206.09, -12540.7, 8011.57\}.$$

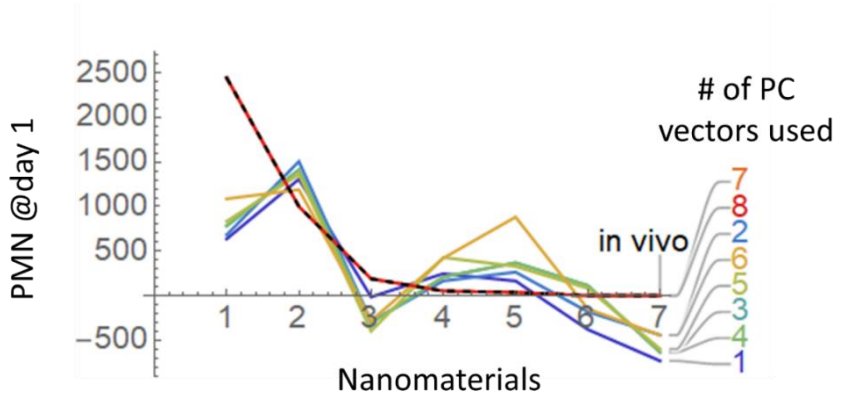

Figure A.9: The results of solving a set of linear equations using an increasing number of principal component vectors.

The weights needed to describe the PMN influx using seven principle component vectors and the above-described transformation between the cytokine values and principal components are saved and can later be used to transform other measurements. Solving the equation (A.6) for any appropriately measured ELISA data using the pre-determined

weights and transformation matrix then yields a table of predicted PMN influx for the measured materials.

A.4 The Metric for Comparing the In Vivo Inflammatory Potential of Various Nanoparticles

A.4.1 The Issue with LOAEL and NOAEL

Two often used metrics for comparing the toxicity of various nanoparticles are LOAEL ("lowest observed adverse effect level"), which represents the lowest dose with observed adverse effect, and NOAEL ("no observed adverse effect level"), which is the highest dose with no observed adverse effect. In the case of experiments where the doses are densely sampled, these two metrics perform well. However, most of the large-scale in vivo experiments are performed using the same small set of logarithmically-scaled mass doses of nanoparticles per mouse lung (e.g. 18 µg, 54 µg and 162 µg in reference [29]) for all the tested nanoparticles. This can in certain cases lead to severe mis-estimations of toxicity, as shown in Figure A.10 A.

Moreover, when these mass doses are re-calculated into surface doses for comparison of nanoparticles, the toxicity of nanoparticles can also be skewed. For instance, when same mass doses are applied to the lungs, nanoparticles with larger BET surfaces are applied at larger surface doses. Consequently, the measurements of these nanoparticles often start at relatively large surface doses where the adverse effects are already pronounced. Due to the lack of data, the lowest measured surface dose is thus chosen as the LOAEL of the nanoparticle, potentially severely underestimating the nanoparticle's toxicity (see Figure A.10 B).

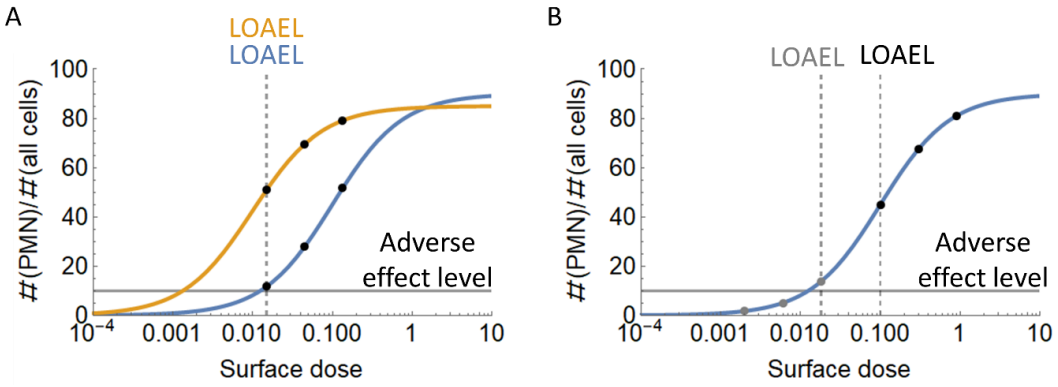

Figure A.10: Graphical representation of the problematic nature of LOAEL and NOAEL as toxicity metrics. **A** An example of the dose response of two nanoparticles with markedly different toxicities – a factor 10 difference in the dose needed to induce the same PMN influx, which was chosen as the observed adverse effect for inflammation. However, due to the sparseness of experimental data (black points in the graphs), the determined LOAEL is the same for both nanoparticles. **B** An example of the dose response of two nanoparticles with the same toxicity that are measured at the same three mass doses. Because these correspond to different surface doses (gray and black points), the determined LOAELs are noticeably different.

A.4.2 An Alternative: % PMN at a Defined Surface Dose

We thus decided to use an alternative metric for comparing the toxicity of various nanoparticles: the observed adverse effect at a fixed surface dose, which can be determined by interpolation of the measurements. The fixed surface dose was chosen to be a 1:1 surface dose (ratio between the nanoparticle surface area and the surface area of lungs – 80 cm^2 for 6 weeks old mice) for two reasons: most nanoparticles exhibit at least some acute inflammation at this surface dose which improves sorting of nanoparticles, and secondly, the 1:1 surface dose is in the range of the mass doses that are most commonly tested (0-150 μg per mouse) for nanoparticles with BET surface areas above 54 m^2/g, which includes a large portion of nanoparticles.

The observed adverse effect that reflects pulmonary inflammation with great sensitivity is the number of neutrophils (PMN) in the bronchoalveolar lavages (BAL) [132]; an example of the typical dose-response curve is shown in Figure A.11 A. However, because the use of different experimental techniques causes the control BAL cell numbers to majorly differ between studies, the total number of PMN in the BAL is not an appropriate metric for pooling together results from different studies as we planned to do in this work.

An often used alternative metric that enables comparison of various studies is the percentage of PMN in the BAL of exposed mice compared to the total number of cells in the same BAL [44]

$$\%PMN1 = \frac{\#PMN\ (dose, t)}{\#all\ cells\ (dose, t)} = \tag{A.7}$$

$$= \frac{\#PMN\ (dose, t)}{\#PMN\ (dose, t) + \#other\ cells\ (dose, t)} = \frac{x}{x + a}.$$

However, as this metric is intrinsically non-linear, the dose-response curve on the semi-log graph is sigmoidal, saturating at larger doses where the number of PMN in the BAL becomes comparable to the number of other cells in the BAL (see Figure A.11 B). In practice, the response curve usually saturates to values between 50% and 80% [44], aggravating the sorting of materials.

In this work, we define and use a metric that combines the best of both the abovementioned metrics: it is linear in the number of PMN in the BAL and normed to enable comparison of various studies. This metric is defined as

$$\%PMN = \frac{\#PMN\ (dose, t) - \#PMN(ctrl)}{\#macrophages\ (ctrl)}, \tag{A.8}$$

and its dose-dependence curve is shown in Figure A.11 C. The number of PMN in the control BAL was included in the metric to separate the effect of the vehicle and normal background from the effect of the nanoparticles, but it is not necessary. For the norming factor, one could also use the number of all cells in the control. However, because there is approximately one macrophage per alveolus in mice, the metric that is normed to the number of macrophages can be interpreted as the additional number of PMN cells per alveolus – a very intuitive metric.

It is worth noting that this metric saturates only as a reflection of the natural saturation of the influx of PMN into the alveolus, but remains linear much longer than the previously described $\%PMN1$. The largest $\%PMN$ after one day that we calculated from data found with a short literature search was 296 [133], indicating that the biological saturation maximum is equal or even larger.

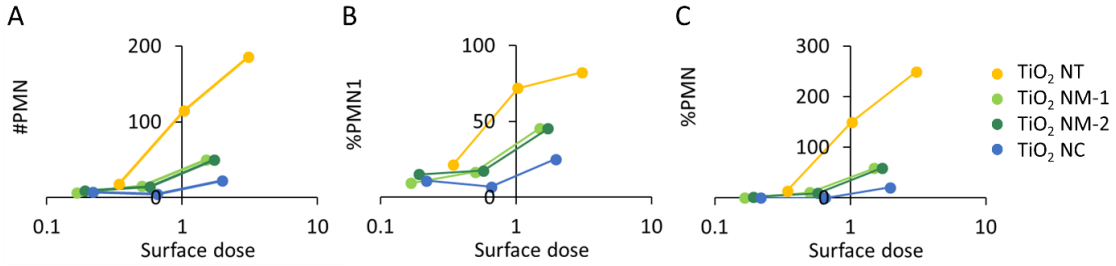

Figure A.11: A comparison of dose-dependence curves for three toxicity metrics. **A** #PMN, **B** %PMN1 and, **C** %PMN. The metrics #PMN and %PMN are linear, and the metrics %PMN1 and %PMN can be compared between different studies.

A.5 Dynamic Interior of Macrophages After Two Days

The dynamic movement inside MH-S macrophages after 2-4 days of incubation with TiO_2 nanotubes (for micrographs from Figure 3.3 in the main text) is shown below by overlaying two differently colored micrographs of nanoparticles obtained at two different times.

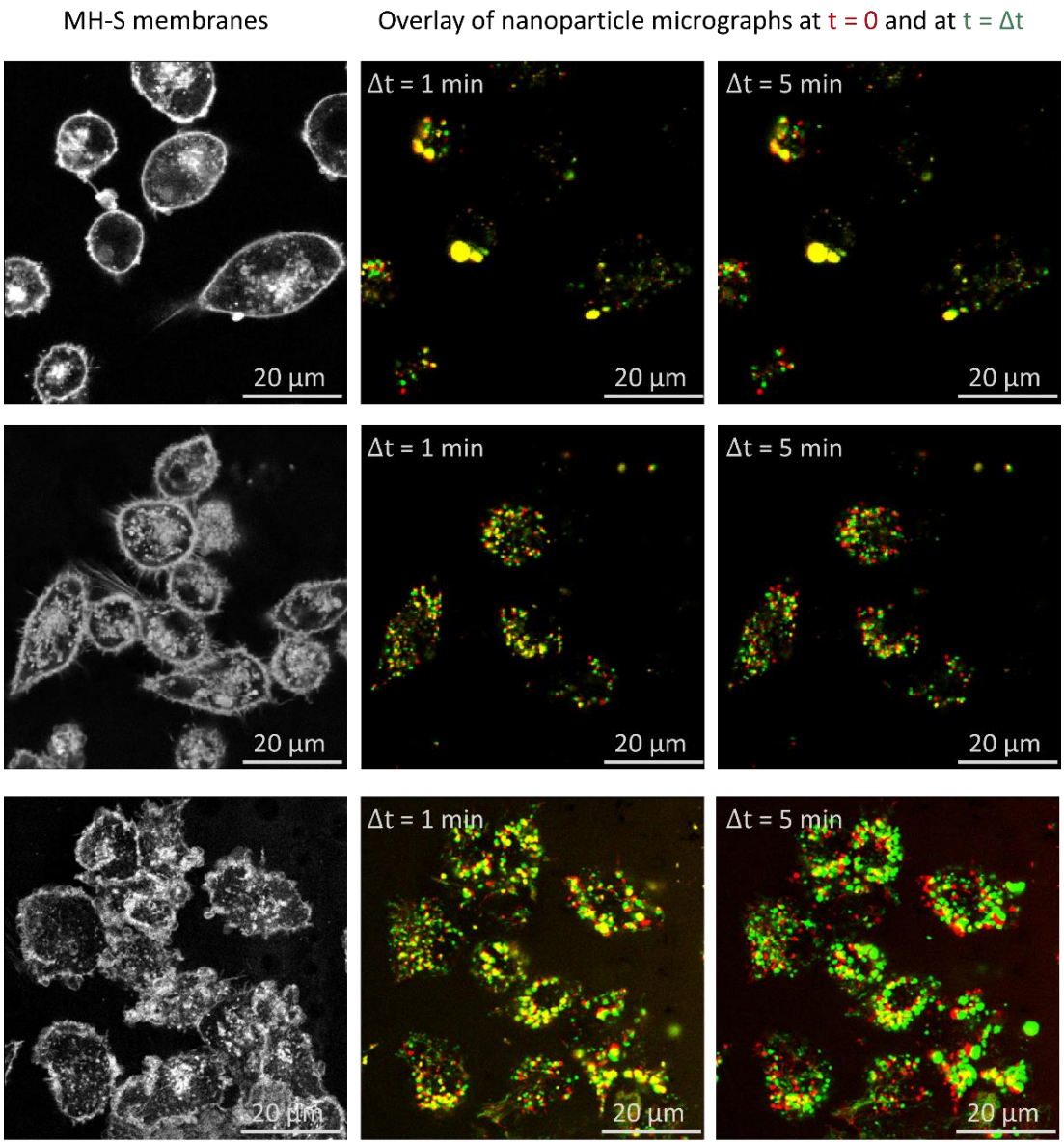

Figure A.12: The micrographs show the dynamics of MH-S cells (membranes labeled with CellMask Orange, left micrograph) after several days of incubation with TiO_2 nanotubes (labelled with Alexa 647, middle and right micrographs). The red color denotes the initial location of the nanoparticles whereas the green corresponds to the location of the nanoparticles after a certain time Δt. The nanoparticles that have not moved during this time appear yellow, whereas moving nanoparticles appear red and green.

A.6 Transcriptomics

The combined overview of the upregulated Hallmark gene set pathways as determined by the GSEA analysis of the transcriptomics data is shown below. Courtesy of Carolina Ballester Lopez, Martin Irmler, Johannes Beckers, and Tobias Stoeger (with assistance of K. Richter and A. Krišelj), reproduced from [94].

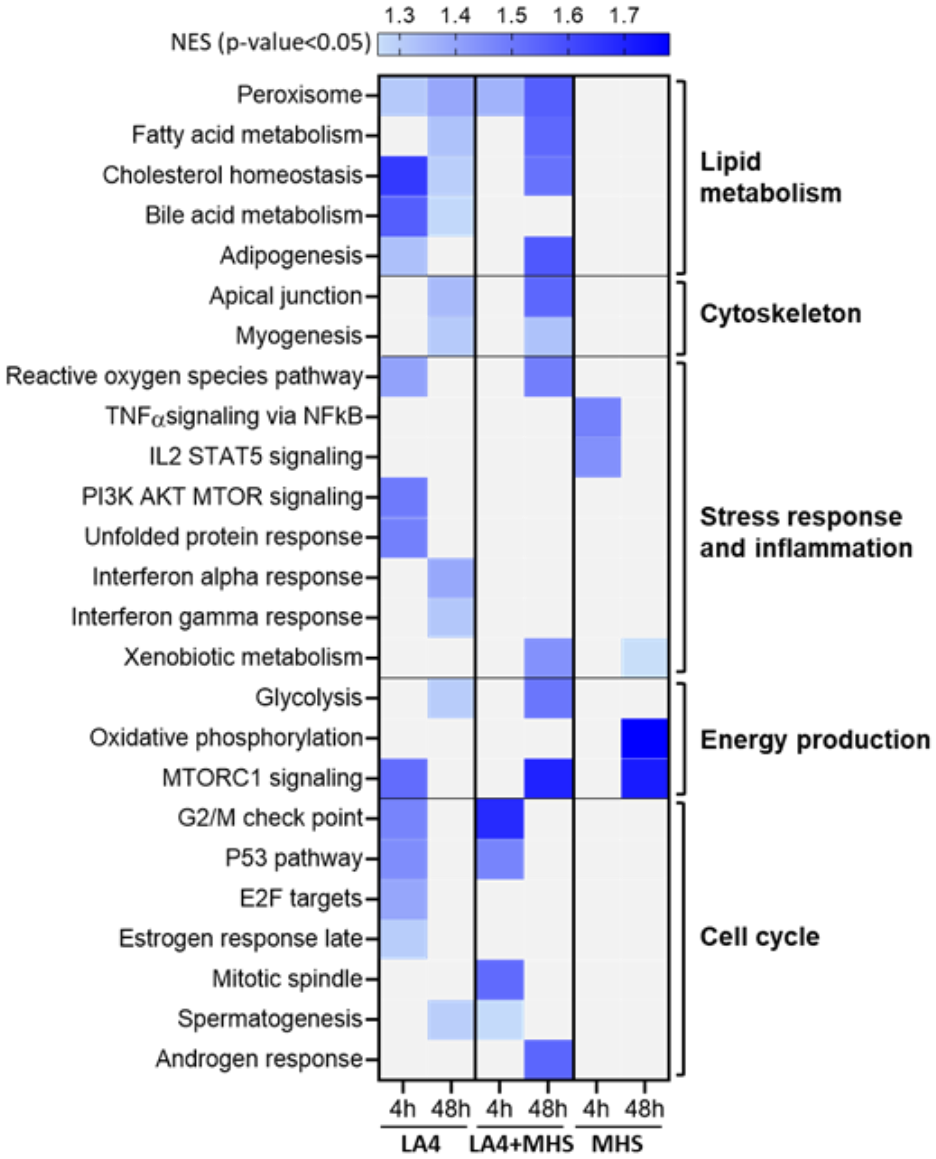

Figure A.13: A heatmap presenting the GSEA normalized enrichment score (NES) of the upregulated Hallmark pathways in the transcriptome profile (total RNA) of mono- and cocultures of LA-4 and MH-S cells, exposed to a 10:1 surface dose of TiO_2 nanotubes for 4 and 48 hours. It is based on gene expressions that were increased at least two-fold compared to the control (non-exposed cells). Reproduced from [94] (CC BY-NC) with permission.

A.7 In Vivo BAL Cell Numbers

In Figure 3.7 in the main text, only the time-courses of neutrophils and macrophages in the bronchoalveolar lavages of instilled mice were shown. The time-courses of the remaining cell types – eosinophils, lymphocytes, epithelial cells and total BAL cells – are shown below. The cell numbers were recalculated from data by Pernille Høgh Danielsen, Kristina Bram Knudsen, and Ulla Vogel, that was published under a CC-BY license [5]. Notably, the

influx of eosinophils and lymphocytes peaks later than the influx of neutrophils: they peak at 3 and 28 days, respectively.

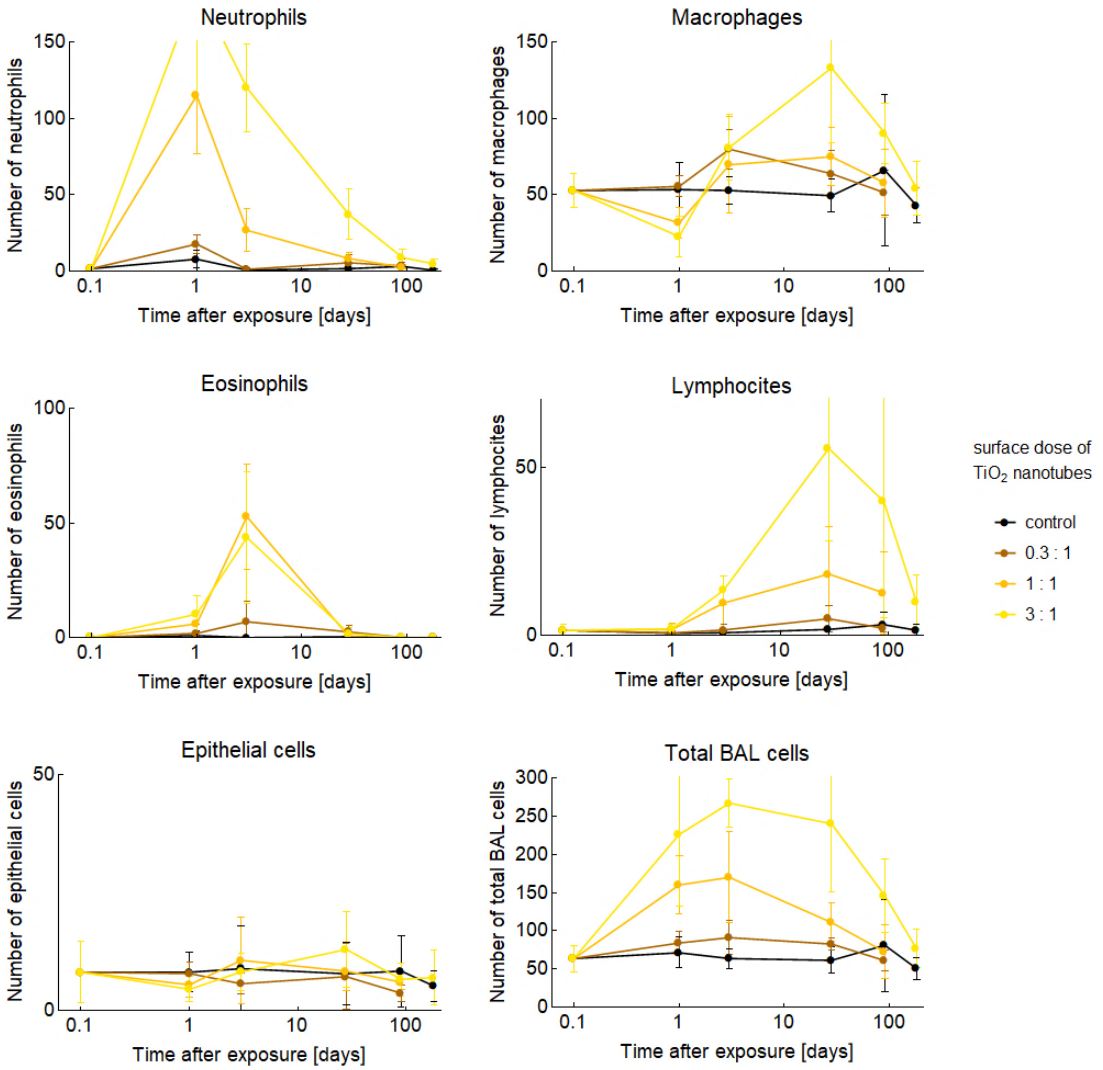

Figure A.14: Time-courses of the numbers of various cell types in the bronchoalveolar lavage fluid (BAL) of instilled mice. The plotted values were recalculated from data courtesy of Pernille Høgh Danielsen, Kristina Bram Knudsen, and Ulla Vogel, that was published under a CC-BY license [5]. The time-courses are compared for three different surface doses of the TiO_2 NTs (corresponding to 18 µg, 54 µg and 162 µg per mouse). We obtained the raw data from [5] and calculated the surface doses from the published mass doses using a lung surface area of 80 cm^2 for the 20 g heavy 8-weeks old mice [7], [8]. We calculated the data for the lower graphs using linear interpolation for all nanoparticles except for DQ12, for which linear extrapolation was used – hence the non-physiological negative number of macrophages at day 1 after exposure. We determined the values at time of exposure (day 0) as the mean of all the negative controls at various time-points (mice exposed to sham control – 0 µg of nanoparticles).

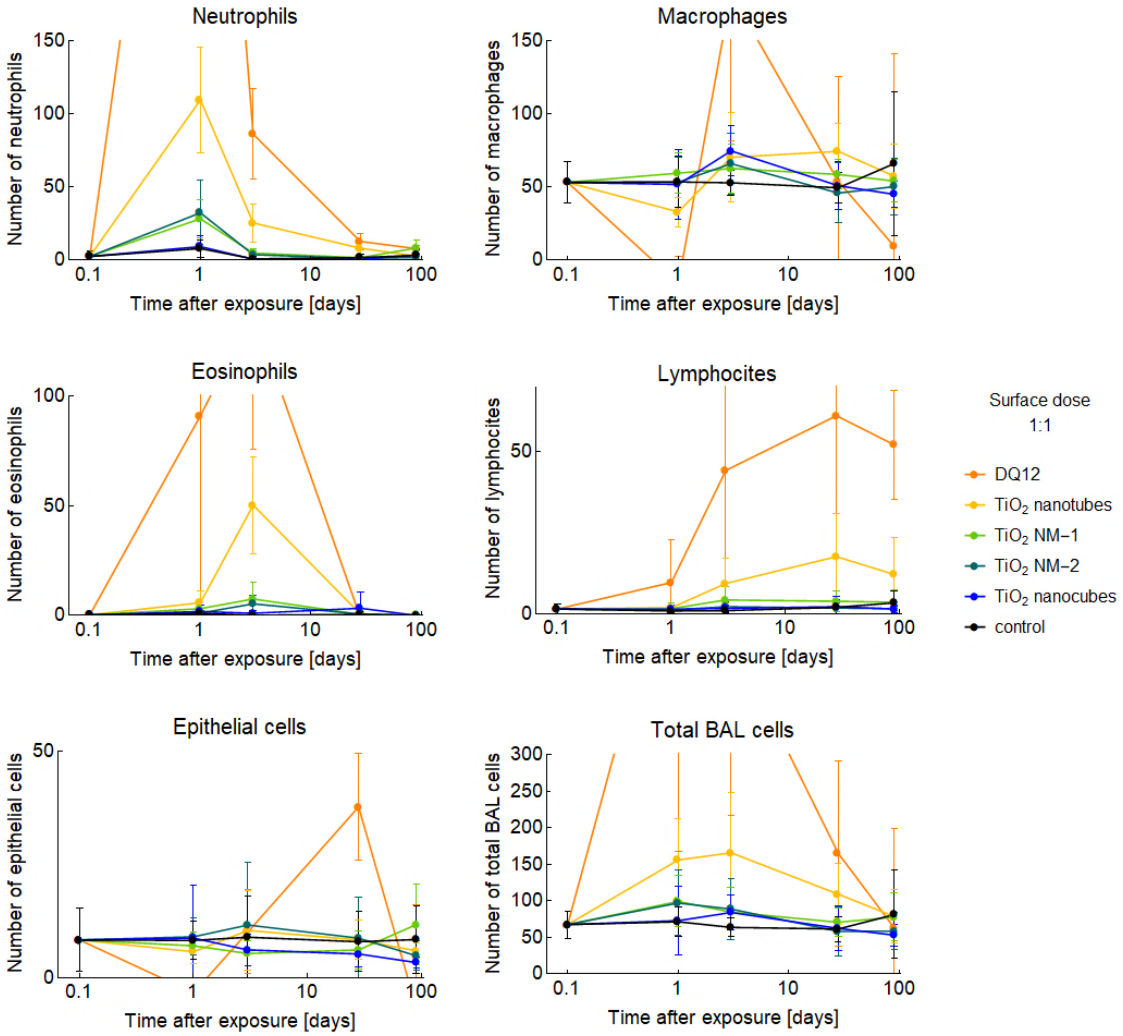

Figure A.15: The time-courses are compared for five different metal oxides at the same surface dose (ratio between the nanoparticle and lung surface being 1:1). More details in caption of Figure A.14.

A.8 Speed of Macrophages

As depicted in Figure 3.10, the maximal velocity of the macrophages decreases from 200 to 100 nm/min during the exposure to nanoparticles. Even at full speed, the non-exposed macrophages need a day to fully scan the alveolus surface (see calculation below). Even the fastest measured animal cell (human neutrophil) with the migration speed of 9 µm/min [134] would need 30 minutes to fully scan the alveolar surface, inevitably leaving enough time for the epithelium to internalize some of the nanoparticles. The data and reasoning behind this estimation are as follows:

The velocity of macrophages: $v = 200\ nm/min$ (measured from time-series, shown in Figure 3.10, consistent with other published measurements);

The ratio between the surface of macrophages S_M and the surface area of alveoli in mice S_A; $S_M/S_A = \alpha = 0.03$ (from reference [135]);

The diameter of macrophages: $2r = 10\ \mu m$ (estimated from microscopy images);

The time in which macrophages fully scan the alveolar surface by systematic scanning (the time is even longer in the case of random motion) is thus 22 hours:

$$t = \frac{path}{velocity} = \frac{\left(\frac{S_A}{2r}\right)}{v} = \frac{\left(\frac{S_M}{2r\alpha}\right)}{v} = \frac{\pi r^2}{2r\alpha v} = \frac{\pi r}{2\alpha v} = \\ = \frac{3.14 \ * \ 5 \ \mu m}{2 \ * \ 0.03 \ * \ 0.2 \ \mu m/min} = 1300 \ minutes = 22 \ hours. \tag{A.9}$$

A.9 Can Nanoparticles Between Macrophages Glue Them Together?

Interestingly, the labelled TiO_2 nanotubes were in some cases observed not only inside the MH-S macrophages, but also between them (see Figure A.16). Whether this phenomenon is a consequence of all the macrophages in the micrograph attacking the same nanoparticle aggregate, or is it caused solely by a combination of the vicinity of multiple macrophages and the affinity of the nanoparticles to the cell membrane is, of course, debatable. However, if the interactions between the nanoparticles and the cells are strong enough, the nanoparticles between cells could in this case act as glue – clustering the macrophages together and constraining their movement, which would further lower their ability to clear the nanoparticles.

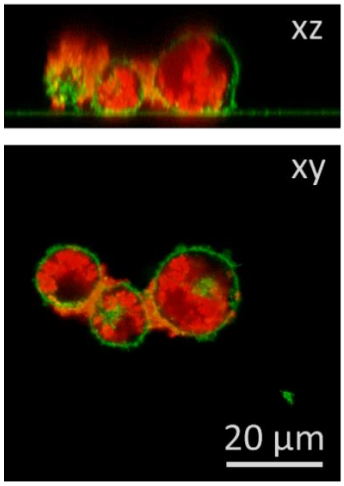

Figure A.16: Presence of nanoparticles between macrophages – does it glue them together? The horizontal (xy) and corresponding vertical (xz) confocal fluorescence micrographs show MH-S macrophages (membranes labelled with CellMask Orange, shown in green) after a 2-day long incubation with a 10:1 surface dose of TiO_2 nanotubes (labelled with Alexa 647 and shown in red, intensity is logarithmically scaled and cut-off below 2 counts).

Clusters of immune cells can also be observed in cytospins of in vivo lavages of mice, instilled with europium-doped TiO_2 nanotubes, shown in Figure A.17 (courtesy of Carola Endes and David Kutschke. Because the preparation of cytospins requires centrifuging and dispersing the cells followed by applying the cell dispersion onto a microscope slide during centrifugation, such a procedure nicely disperses the cells in the control. Although the

resolution and contrast does not enable one to see the nanoparticles clearly, we can suspect that there are fairly large attraction forces that hold together the cells in the BAL of exposed mice – otherwise, the cells in the cytospins micrographs would not appear in such large clusters.

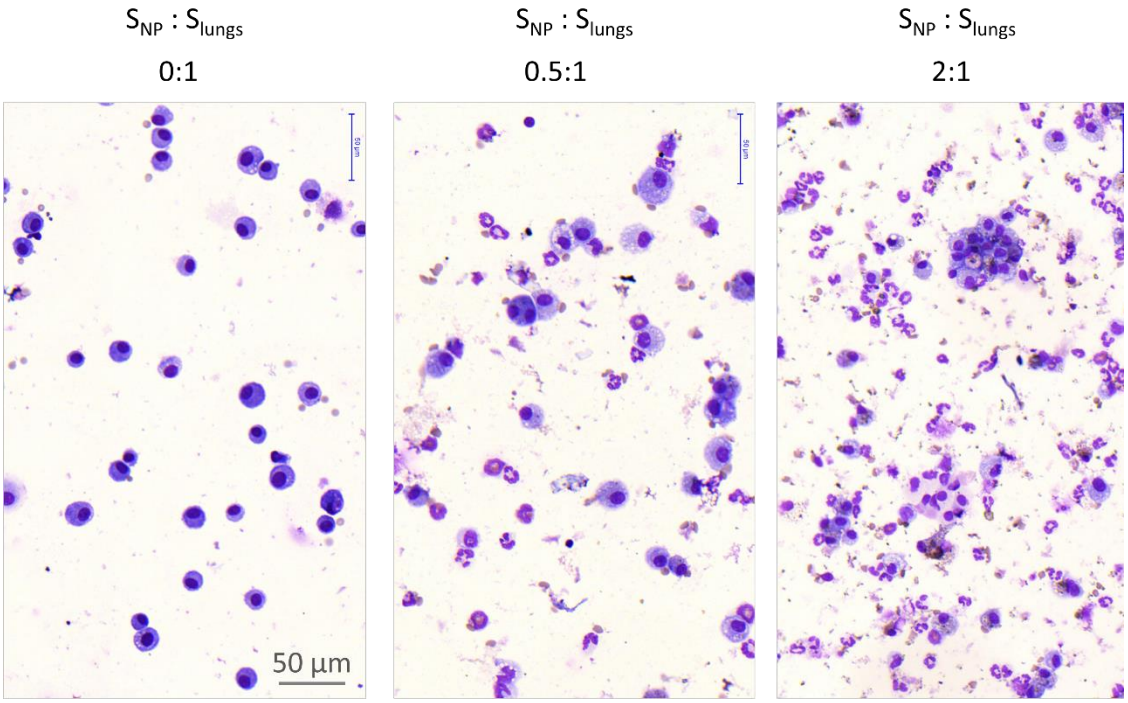

Figure A.17: Clustering of cells in BAL cytospins after nanoparticle exposure hints on large attraction between the cells. Bright-field micrographs of cytospins of mouse lavages one day after intratracheal exposure to a (from left to right): 0:1, 0.5:1 and 2:1 surface dose of TiO_2 nanotubes, doped with Europium. The lavage was stained with May-Grünwald-Giemsa stain prior to imaging, which stained the negatively charged parts of the cell (e.g. nuclei) purplish-blue and the positively charged (e.g. proteins, granules) pink; unlabeled TiO_2 nanotubes appear grey and black. Courtesy of Carola Endes and David Kutschke.

To test whether the observed cauliflowers could be an artefact of the affinity of the amphiphilic probe CellMask Orange towards the surface of the nanotubes, we incubated TiO_2 nanotubes with CellMask Orange in the same volumes and concentrations as used in the majority of the experiments. Although we observed some binding of the CellMask Orange to the nanotubes, its intensity and labelling pattern differed majorly from the observed cauliflowers, from which we concluded that cauliflowers are not purely TiO_2 aggregates that are labelled with CellMask Orange, and that there are definitely other molecules (at least lipids) present in cauliflowers, which cause stronger labelling of the structures with CellMask Orange.

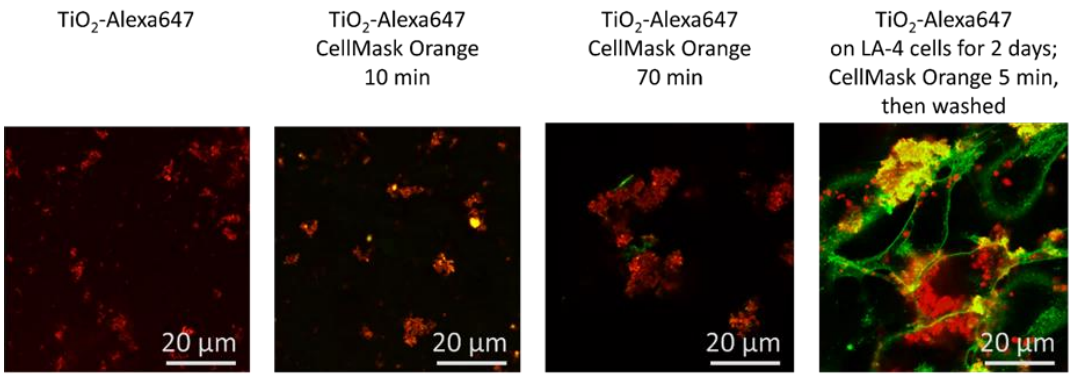

Figure A.18: A control measurement of the affinity of CellMask Orange to the TiO_2 nanotubes. The micrographs show a comparison of the signal intensity and distribution of a 10:1 surface dose of TiO_2 nanotubes (labelled with Alexa 647) after a few hours in LCIS **A** before adding CellMask Orange, and **B** 10 minutes and **C** 70 minutes after adding 1.5 µg/ml CellMask Orange to the nanotubes. **D** A micrograph of LA-4 cells after two days of incubation with TiO2 nanotubes. The concentrations of the nanotubes (red) and CellMask Orange (green) are the same in all experiments, and the micrographs are scaled in the same manner to enable comparison.

A.10 Theoretical Time-Courses of In Vitro Mono- and Co-Cultures

The theoretical time-courses of nanoparticle-exposed in vitro monocultures of LA-4 epithelial cells and MH-S macrophages, as well as the time-course of their respective coculture are shown below. Each system is modelled for an exposure to a 10:1 surface dose of nanoparticles, with the chosen set of the three nanoparticle-dependent parameters being the same as in Figure 4.1 and Figure 4.2.

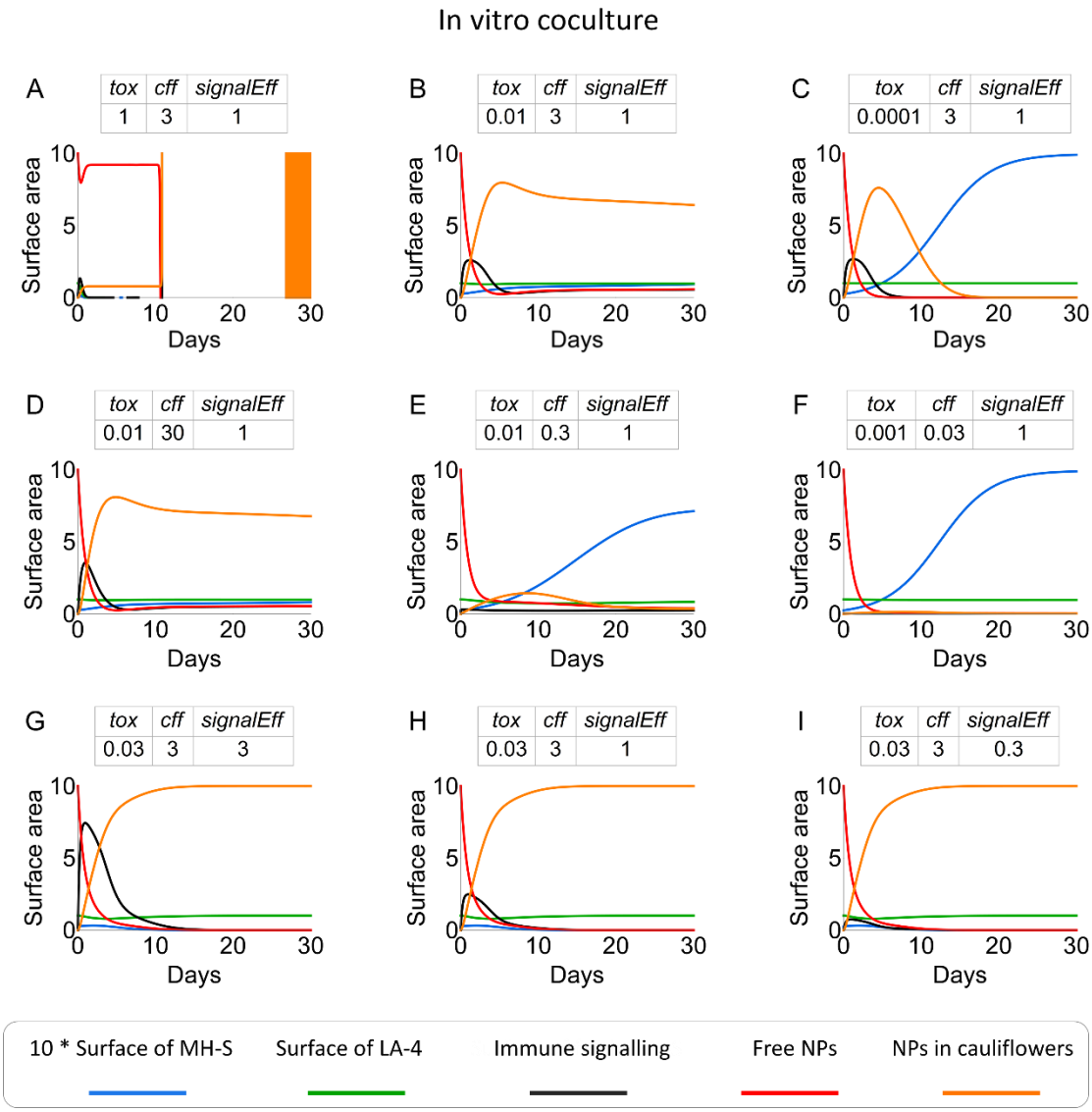

Figure A.19: Theoretical time-courses of an in vitro coculture of epithelial cells and macrophages for the chosen sets of nanoparticle parameters. The divergence and oscillations that appear in A after day 10 are the consequence of numerical error and would not appear in the real coculture. The black curves correspond to the in vitro immune signaling $signalEff\ cff\ sLa4(t) * tanh[npLa4(t)/sLa4(t)\ cff\ timecf]$.

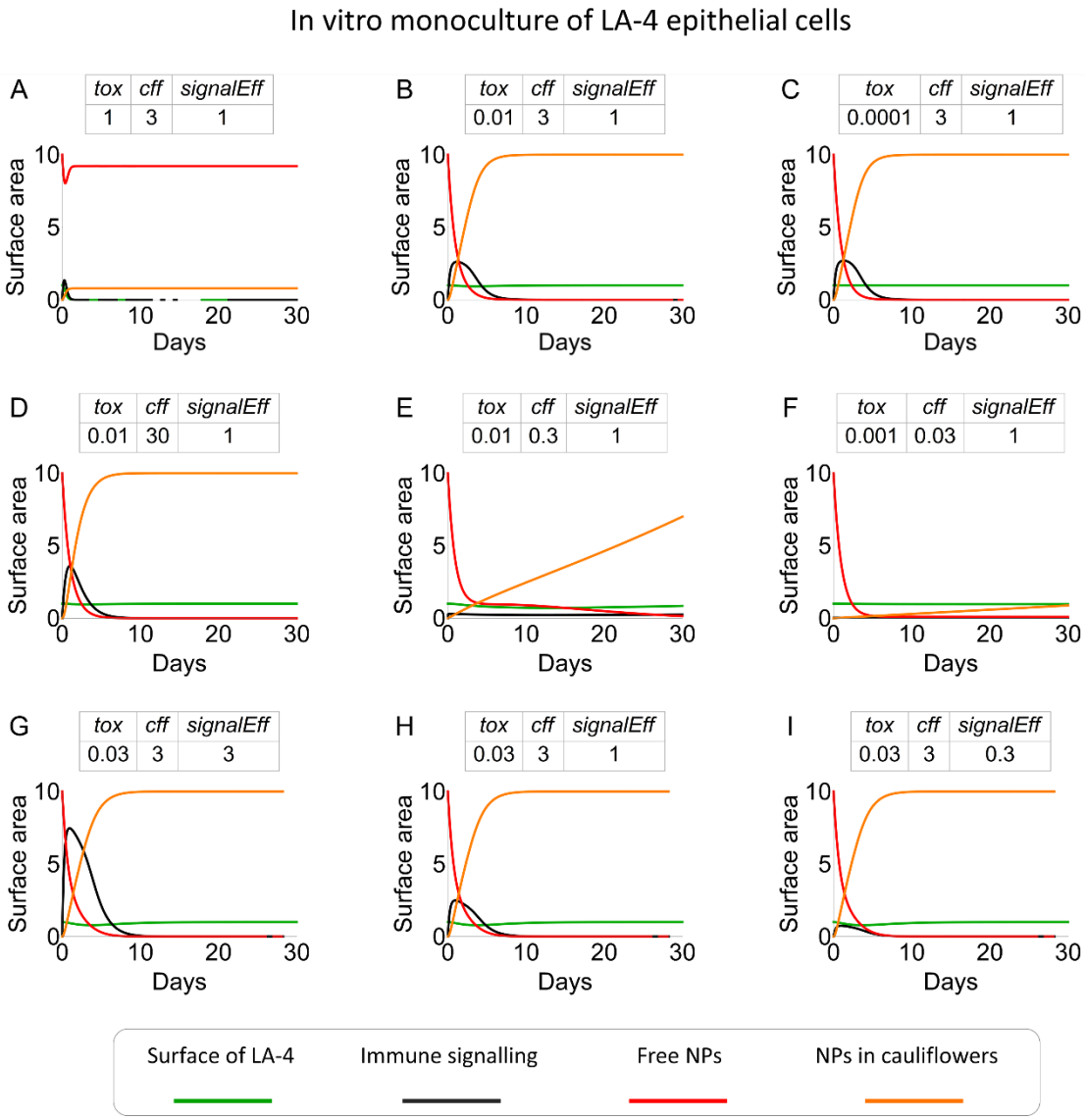

Figure A.20: Theoretical time-courses of an in vitro monoculture of epithelial cells for the chosen sets of nanoparticle parameters. The black curves correspond to the in vitro immune signaling $signalEff\ cff\ sLa4(t) * tanh[npLa4(t)/sLa4(t)\ cff\ timecf]$.

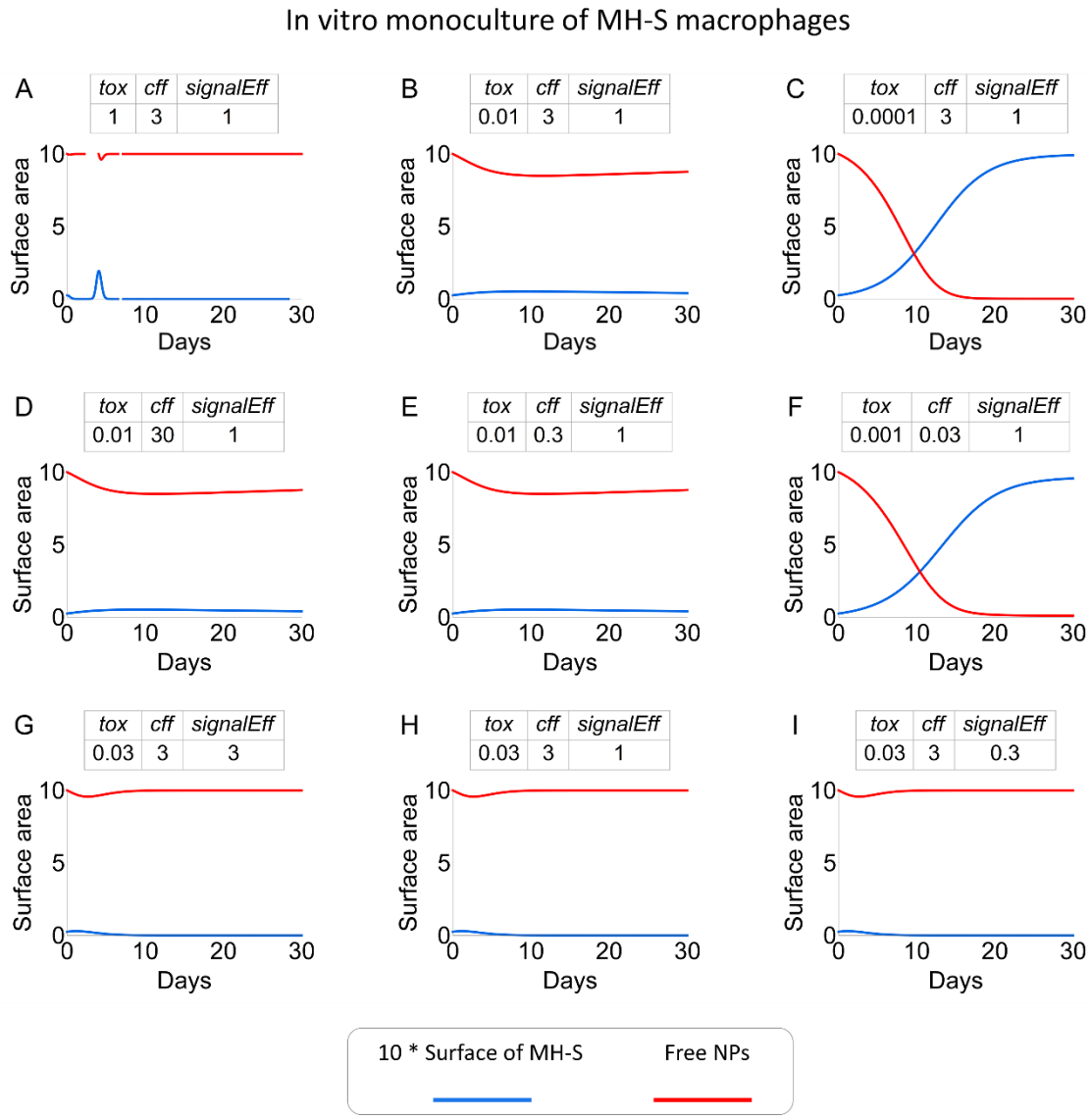

Figure A.21: Theoretical time-courses of an in vitro macrophage monoculture for the chosen set of nanoparticle parameters.

References

[1] H. F. Krug and P. Wick, "Nanotoxicology: An Interdisciplinary Challenge," *Angew. Chem. Int. Ed.*, vol. 50, no. 6, pp. 1260–1278, Feb. 2011, doi: 10.1002/anie.201001037.

[2] G. Oberdörster, E. Oberdörster, and J. Oberdörster, "Nanotoxicology: An Emerging Discipline Evolving from Studies of Ultrafine Particles," *Environ. Health Perspect.*, vol. 113, no. 7, pp. 823–839, Mar. 2005, doi: 10.1289/ehp.7339.

[3] R. Chen *et al.*, "Beyond PM2.5: The role of ultrafine particles on adverse health effects of air pollution," *Biochim. Biophys. Acta BBA - Gen. Subj.*, vol. 1860, no. 12, pp. 2844–2855, Dec. 2016, doi: 10.1016/j.bbagen.2016.03.019.

[4] S. J. Klaine *et al.*, "Nanomaterials in the environment: Behavior, fate, bioavailability, and effects," *Environ. Toxicol. Chem.*, vol. 27, no. 9, pp. 1825–1851, 2008, doi: 10.1897/08-090.1.

[5] P. Biswas and C.-Y. Wu, "Nanoparticles and the Environment," *J. Air Waste Manag. Assoc.*, vol. 55, no. 6, pp. 708–746, Jun. 2005, doi: 10.1080/10473289.2005.10464656.

[6] R. D. Handy, R. Owen, and E. Valsami-Jones, "The ecotoxicology of nanoparticles and nanomaterials: current status, knowledge gaps, challenges, and future needs," *Ecotoxicology*, vol. 17, no. 5, pp. 315–325, Jul. 2008, doi: 10.1007/s10646-008-0206-0.

[7] J. Kolosnjaj-Tabi *et al.*, "Anthropogenic Carbon Nanotubes Found in the Airways of Parisian Children," *EBioMedicine*, vol. 2, no. 11, pp. 1697–1704, Nov. 2015, doi: 10.1016/j.ebiom.2015.10.012.

[8] F. Ahmad and Y. Zhou, "Pitfalls and Challenges in Nanotoxicology: A Case of Cobalt Ferrite (CoFe2O4) Nanocomposites," *Chem. Res. Toxicol.*, vol. 30, no. 2, pp. 492–507, Feb. 2017, doi: 10.1021/acs.chemrestox.6b00377.

[9] S. N. A. Shah, Z. Shah, M. Hussain, and M. Khan, "Hazardous Effects of Titanium Dioxide Nanoparticles in Ecosystem," *Bioinorganic Chemistry and Applications*, 2017. https://www.hindawi.com/journals/bca/2017/4101735/ (accessed Aug. 04, 2017).

[10] M. Ema, M. Gamo, and K. Honda, "A review of toxicity studies of single-walled carbon nanotubes in laboratory animals," *Regul. Toxicol. Pharmacol.*, vol. 74, pp. 42–63, Feb. 2016, doi: 10.1016/j.yrtph.2015.11.015.

[11] T. S. Peixe, E. de S. Nascimento, K. L. Schofield, A. S. A. Arcuri, and R. P. Bulcão, "Nanotoxicology and Exposure in the Occupational Setting," *Occup. Dis. Environ. Med.*, vol. 03, no. 03, p. 35, 2015, doi: 10.4236/odem.2015.33005.

[12] Y. Song, X. Li, and X. Du, "Exposure to nanoparticles is related to pleural effusion, pulmonary fibrosis and granuloma," *Eur. Respir. J.*, vol. 34, no. 3, pp. 559–567, Sep. 2009, doi: 10.1183/09031936.00178308.

[13] J. Lelieveld, A. Pozzer, U. Pöschl, M. Fnais, A. Haines, and T. Münzel, "Loss of life expectancy from air pollution compared to other risk factors: a worldwide perspective," *Cardiovasc. Res.*, vol. 116, no. 11, pp. 1910–1917, Sep. 2020, doi: 10.1093/cvr/cvaa025.

[14] J. Lelieveld *et al.*, "Cardiovascular disease burden from ambient air pollution in Europe reassessed using novel hazard ratio functions," *Eur. Heart J.*, vol. 40, no. 20, pp. 1590–1596, May 2019, doi: 10.1093/eurheartj/ehz135.

[15] A. Santamaria, "Historical Overview of Nanotechnology and Nanotoxicology," in *Nanotoxicity: Methods and Protocols*, J. Reineke, Ed. Totowa, NJ: Humana Press, 2012, pp. 1–12. doi: 10.1007/978-1-62703-002-1_1.

[16] H. L. Karlsson, J. Gustafsson, P. Cronholm, and L. Möller, "Size-dependent toxicity of metal oxide particles—A comparison between nano- and micrometer size," *Toxicol. Lett.*, vol. 188, no. 2, pp. 112–118, Jul. 2009, doi: 10.1016/j.toxlet.2009.03.014.

[17] M. Schneider, F. Stracke, S. Hansen, and U. F. Schaefer, "Nanoparticles and their interactions with the dermal barrier," *Dermatoendocrinol.*, vol. 1, no. 4, pp. 197–206, 2009.

[18] L. J. Mortensen, G. Oberdörster, A. P. Pentland, and L. A. DeLouise, "In Vivo Skin Penetration of Quantum Dot Nanoparticles in the Murine Model: The Effect of UVR," *Nano Lett.*, vol. 8, no. 9, pp. 2779–2787, Sep. 2008, doi: 10.1021/nl801323y.

[19] D. J. McClements and H. Xiao, "Is nano safe in foods? Establishing the factors impacting the gastrointestinal fate and toxicity of organic and inorganic food-grade nanoparticles," *Npj Sci. Food*, vol. 1, no. 1, pp. 1–13, Nov. 2017, doi: 10.1038/s41538-017-0005-1.

[20] A. Elder *et al.*, "Translocation of Inhaled Ultrafine Manganese Oxide Particles to the Central Nervous System," *Environ. Health Perspect.*, vol. 114, no. 8, pp. 1172–1178, Aug. 2006, doi: 10.1289/ehp.9030.

[21] B. A. Maher *et al.*, "Magnetite pollution nanoparticles in the human brain," *Proc. Natl. Acad. Sci.*, vol. 113, no. 39, pp. 10797–10801, Sep. 2016, doi: 10.1073/pnas.1605941113.

[22] R. Nho, "Pathological effects of nano-sized particles on the respiratory system," *Nanomedicine Nanotechnol. Biol. Med.*, vol. 29, p. 102242, Oct. 2020, doi: 10.1016/j.nano.2020.102242.

[23] E. Lopez-Rodriguez, G. Gay-Jordi, A. Mucci, N. Lachmann, and A. Serrano-Mollar, "Lung surfactant metabolism: early in life, early in disease and target in cell therapy," *Cell Tissue Res.*, vol. 367, no. 3, pp. 721–735, Mar. 2017, doi: 10.1007/s00441-016-2520-9.

[24] A. Hidalgo, A. Cruz, and J. Pérez-Gil, "Pulmonary surfactant and nanocarriers: Toxicity versus combined nanomedical applications," *Biochim. Biophys. Acta BBA - Biomembr.*, vol. 1859, no. 9, Part B, pp. 1740–1748, Sep. 2017, doi: 10.1016/j.bbamem.2017.04.019.

[25] H. Fehrenbach, "Alveolar epithelial type II cell: defender of the alveolus revisited," *Respir. Res.*, vol. 2, p. 33, 2001, doi: 10.1186/rr36.

[26] B. Ruaro *et al.*, "The History and Mystery of Alveolar Epithelial Type II Cells: Focus on Their Physiologic and Pathologic Role in Lung," *Int. J. Mol. Sci.*, vol. 22, no. 5, p. 2566, Mar. 2021, doi: 10.3390/ijms22052566.

[27] M. Geiser, M. Casaulta, B. Kupferschmid, H. Schulz, M. Semmler-Behnke, and W. Kreyling, "The Role of Macrophages in the Clearance of Inhaled Ultrafine Titanium Dioxide Particles," *Am. J. Respir. Cell Mol. Biol.*, Dec. 2012, doi: 10.1165/rcmb.2007-0138OC.

[28] H. M. Braakhuis, M. V. Park, I. Gosens, W. H. De Jong, and F. R. Cassee, "Physicochemical characteristics of nanomaterials that affect pulmonary inflammation," *Part. Fibre Toxicol.*, vol. 11, p. 18, Apr. 2014, doi: 10.1186/1743-8977-11-18.

[29] P. H. Danielsen *et al.*, "Effects of physicochemical properties of TiO2 nanomaterials for pulmonary inflammation, acute phase response and alveolar proteinosis in intratracheally exposed mice," *Toxicol. Appl. Pharmacol.*, vol. 386, p. 114830, Jan. 2020, doi: 10.1016/j.taap.2019.114830.

[30] S. J. Seok *et al.*, "Genomic responses in mouse models poorly mimic human inflammatory diseases," *Proc. Natl. Acad. Sci. U. S. A.*, vol. 110, no. 9, pp. 3507–3512, Feb. 2013, doi: 10.1073/pnas.1222878110.

[31] F. Yue *et al.*, "A comparative encyclopedia of DNA elements in the mouse genome," *Nature*, vol. 515, no. 7527, pp. 355–364, Nov. 2014, doi: 10.1038/nature13992.

[32] A. D. Maynard and R. J. Aitken, "'Safe handling of nanotechnology' ten years on," *Nat. Nanotechnol.*, vol. 11, no. 12, pp. 998–1000, Dec. 2016, doi: 10.1038/nnano.2016.270.

[33] B. Drasler, P. Sayre, K. G. Steinhäuser, A. Petri-Fink, and B. Rothen-Rutishauser, "In vitro approaches to assess the hazard of nanomaterials," *NanoImpact*, vol. 8, pp. 99–116, Oct. 2017, doi: 10.1016/j.impact.2017.08.002.

[34] A. Astashkina and D. W. Grainger, "Critical analysis of 3-D organoid in vitro cell culture models for high-throughput drug candidate toxicity assessments," *Adv. Drug Deliv. Rev.*, vol. 69–70, pp. 1–18, Apr. 2014, doi: 10.1016/j.addr.2014.02.008.

[35] aop-wiki, "AOP-Wiki." https://aopwiki.org/ (accessed Jan. 12, 2021).

[36] A. E. Nel and T. F. Malloy, "Policy reforms to update chemical safety testing," *Science*, vol. 355, no. 6329, pp. 1016–1018, Mar. 2017, doi: 10.1126/science.aak9919.

[37] A. J. Clippinger *et al.*, "Expert consensus on an in vitro approach to assess pulmonary fibrogenic potential of aerosolized nanomaterials," *Arch. Toxicol.*, vol. 90, pp. 1769–1783, 2016, doi: 10.1007/s00204-016-1717-8.

[38] M. A. Bañares *et al.*, "CompNanoTox2015: novel perspectives from a European conference on computational nanotoxicology on predictive nanotoxicology," *Nanotoxicology*, vol. 11, no. 7, pp. 839–845, Aug. 2017, doi: 10.1080/17435390.2017.1371351.

[39] "EPA/600/R-12/056F Provisional Assessment of Recent Studies on Health Effects of Particulate Matter Exposure." 2012.

[40] J. D. Ede *et al.*, "Translating Scientific Advances in the AOP Framework to Decision Making for Nanomaterials," *Nanomaterials*, vol. 10, no. 6, Jun. 2020, doi: 10.3390/nano10061229.

[41] S. Halappanavar *et al.*, "Adverse outcome pathways as a tool for the design of testing strategies to support the safety assessment of emerging advanced materials at the nanoscale," *Part. Fibre Toxicol.*, vol. 17, no. 1, p. 16, Dec. 2020, doi: 10.1186/s12989-020-00344-4.

[42] S. Mülhopt *et al.*, "Characterization of Nanoparticle Batch-To-Batch Variability," *Nanomaterials*, vol. 8, no. 5, p. 311, May 2018, doi: 10.3390/nano8050311.

[43] S. VEGRO, "JRC Nanomaterials Repository," *EU Science Hub - European Commission*, Dec. 17, 2014. https://ec.europa.eu/jrc/en/scientific-tool/jrc-nanomaterials-repository (accessed Jun. 29, 2021).

[44] O. Schmid and T. Stoeger, "Surface area is the biologically most effective dose metric for acute nanoparticle toxicity in the lung," *J. Aerosol Sci.*, vol. 99, pp. 133–143, Sep. 2016, doi: 10.1016/j.jaerosci.2015.12.006.

[45] K. M. Waters *et al.*, "Macrophage Responses to Silica Nanoparticles are Highly Conserved Across Particle Sizes," *Toxicol. Sci.*, vol. 107, no. 2, pp. 553–569, Feb. 2009, doi: 10.1093/toxsci/kfn250.

[46] K. J. Ong *et al.*, "Widespread Nanoparticle-Assay Interference: Implications for Nanotoxicity Testing," *PLOS ONE*, vol. 9, no. 3, p. e90650, Mar. 2014, doi: 10.1371/journal.pone.0090650.

[47] A. Kroll, M. H. Pillukat, D. Hahn, and J. Schnekenburger, "Interference of engineered nanoparticles with in vitro toxicity assays," *Arch. Toxicol.*, vol. 86, no. 7, pp. 1123–1136, Jul. 2012, doi: 10.1007/s00204-012-0837-z.

[48] R. Guadagnini *et al.*, "Toxicity screenings of nanomaterials: challenges due to interference with assay processes and components of classic in vitro tests," *Nanotoxicology*, vol. 9, no. sup1, pp. 13–24, May 2015, doi: 10.3109/17435390.2013.829590.

[49] M. Rösslein *et al.*, "Use of Cause-and-Effect Analysis to Design a High-Quality Nanocytotoxicology Assay," *Chem. Res. Toxicol.*, vol. 28, no. 1, pp. 21–30, Jan. 2015, doi: 10.1021/tx500327y.

[50] "Titanium Dioxide Uses & Applications, Application of Tio2," *Hangzhou Harmony Chemical Co.,Ltd.* http://www.ti-line.net (accessed Jun. 29, 2021).

[51] "Mineral commodity summaries 2020," U.S. Geological Survey, Reston, VA, USGS Unnumbered Series, 2020. [Online]. Available: http://pubs.er.usgs.gov/publication/mcs2020

[52] I. Urbančič *et al.*, "Nanoparticles Can Wrap Epithelial Cell Membranes and Relocate Them Across the Epithelial Cell Layer," *Nano Lett.*, vol. 18, no. 8, pp. 5294–5305, Aug. 2018, doi: 10.1021/acs.nanolett.8b02291.

[53] B. Kokot *et al.*, "How to control fluorescent labeling of metal oxide nanoparticles for artefact-free live cell microscopy," *Nanotoxicology*, vol. 15, no. 8, pp. 1102–1123, Oct. 2021, doi: 10.1080/17435390.2021.1973607.

[54] M. Garvas, A. Testen, P. Umek, A. Gloter, T. Koklic, and J. Strancar, "Protein Corona Prevents TiO2 Phototoxicity," *PLOS ONE*, vol. 10, no. 6, p. e0129577, Jun. 2015, doi: 10.1371/journal.pone.0129577.

[55] J. B. Pawley, Ed., *Handbook of Biological Confocal Microscopy*. Boston, MA: Springer US, 2006. doi: 10.1007/978-0-387-45524-2_14.

[56] C. M. Brown, "Fluorescence microscopy - avoiding the pitfalls," *J. Cell Sci.*, vol. 120, no. 10, pp. 1703–1705, May 2007, doi: 10.1242/jcs.03433.

[57] M. M. Frigault, J. Lacoste, J. L. Swift, and C. M. Brown, "Live-cell microscopy – tips and tools," *J. Cell Sci.*, vol. 122, no. 6, pp. 753–767, Mar. 2009, doi: 10.1242/jcs.033837.

[58] S. Cox, "Super-resolution imaging in live cells," *Dev. Biol.*, vol. 401, no. 1, pp. 175–181, May 2015, doi: 10.1016/j.ydbio.2014.11.025.

[59] M. Y. Berezin and S. Achilefu, "Fluorescence Lifetime Measurements and Biological Imaging," *Chem. Rev.*, vol. 110, no. 5, pp. 2641–2684, May 2010, doi: 10.1021/cr900343z.

[60] C. Eggeling, K. I. Willig, and F. J. Barrantes, "STED microscopy of living cells – new frontiers in membrane and neurobiology," *J. Neurochem.*, vol. 126, no. 2, pp. 203–212, 2013, doi: 10.1111/jnc.12243.

[61] A. G. Godin, B. Lounis, and L. Cognet, "Super-resolution Microscopy Approaches for Live Cell Imaging," *Biophys. J.*, vol. 107, no. 8, pp. 1777–1784, Oct. 2014, doi: 10.1016/j.bpj.2014.08.028.

[62] W. Becker, *The bh TCSPC Handbook 8th ed.* 2019. Accessed: Aug. 23, 2021. [Online]. Available: https://www.becker-hickl.com/literature/documents/flim/the-bh-tcspc-handbook/

[63] Robert D. Goldman, Jason R. Swedlow, and David L. Spector, Eds., *Live Cell Imaging: A Laboratory Manual, Second Edition / Edition 2|Paperback*. USA: Oxford University Press, 2010. Accessed: Aug. 23, 2021. [Online]. Available: https://www.barnesandnoble.com/w/live-cell-imaging-robert-d-goldman/1101420630

[64] M. V. Sednev, V. N. Belov, and S. W. Hell, "Fluorescent dyes with large Stokes shifts for super-resolution optical microscopy of biological objects: a review," *Methods Appl. Fluoresc.*, vol. 3, no. 4, p. 042004, Oct. 2015, doi: 10.1088/2050-6120/3/4/042004.

[65] J. R. Lakowicz, Ed., *Principles of Fluorescence Spectroscopy*. Boston, MA: Springer US, 2006. doi: 10.1007/978-0-387-46312-4.

[66] W. Liu *et al.*, "Breaking the Axial Diffraction Limit: A Guide to Axial Super-Resolution Fluorescence Microscopy," *Laser Photonics Rev.*, vol. 12, no. 8, p. 1700333, 2018, doi: 10.1002/lpor.201700333.

[67] S. Pajk, H. Majaron, M. Novak, B. Kokot, and J. Štrancar, "New coumarin- and phenoxazine-based fluorescent probes for live-cell STED nanoscopy," *Eur. Biophys. J.*, vol. 48, no. 5, pp. 485–490, Jul. 2019, doi: 10.1007/s00249-019-01354-7.

[68] J. A. Kilgore, N. J. Dolman, and M. W. Davidson, "A Review of Reagents for Fluorescence Microscopy of Cellular Compartments and Structures, Part III: Reagents for Actin, Tubulin,

Cellular Membranes, and Whole Cell and Cytoplasm," *Curr. Protoc. Cytom.*, vol. 67, no. 1, p. 12.32.1-12.32.17, 2014, doi: 10.1002/0471142956.cy1232s67.

[69] S. W. Hell and J. Wichmann, "Breaking the diffraction resolution limit by stimulated emission: stimulated-emission-depletion fluorescence microscopy," *Opt. Lett.*, vol. 19, no. 11, pp. 780–782, Jun. 1994, doi: 10.1364/OL.19.000780.

[70] V. Okhonin, "Method of investigating specimen microstructure, Patent SU 1374922," Apr. 10, 1986 Accessed: Jul. 01, 2021. [Online]. Available: https://www.researchgate.net/publication/272021175_STED_Priority_1986_Eng_Transl

[71] A. Verma and F. Stellacci, "Effect of Surface Properties on Nanoparticle–Cell Interactions," *Small*, vol. 6, no. 1, pp. 12–21, 2010, doi: 10.1002/smll.200901158.

[72] M. Zhu, G. Nie, H. Meng, T. Xia, A. Nel, and Y. Zhao, "Physicochemical Properties Determine Nanomaterial Cellular Uptake, Transport, and Fate," *Acc. Chem. Res.*, vol. 46, no. 3, pp. 622–631, Mar. 2013, doi: 10.1021/ar300031y.

[73] O. R. Vasile *et al.*, "Influence of the size and the morphology of ZnO nanoparticles on cell viability," *Comptes Rendus Chim.*, vol. 18, no. 12, pp. 1335–1343, Dec. 2015, doi: 10.1016/j.crci.2015.08.005.

[74] S. Pujari-Palmer, X. Lu, and M. K. Ott, "The Influence of Hydroxyapatite Nanoparticle Morphology on Embryonic Development in a Zebrafish Exposure Model," *Nanomaterials*, vol. 7, no. 4, Apr. 2017, doi: 10.3390/nano7040089.

[75] P. Pietzonka, B. Rothen-Rutishauser, P. Langguth, H. Wunderli-Allenspach, E. Walter, and H. P. Merkle, "Transfer of Lipophilic Markers from PLGA and Polystyrene Nanoparticles to Caco-2 Monolayers Mimics Particle Uptake," *Pharm. Res.*, vol. 19, no. 5, pp. 595–601, May 2002, doi: 10.1023/A:1015393710253.

[76] T. Tenuta *et al.*, "Elution of Labile Fluorescent Dye from Nanoparticles during Biological Use," *PLOS ONE*, vol. 6, no. 10, p. e25556, Oct. 2011, doi: 10.1371/journal.pone.0025556.

[77] S. Grafmueller *et al.*, "Transfer studies of polystyrene nanoparticles in the ex vivo human placenta perfusion model: key sources of artifacts., Transfer studies of polystyrene nanoparticles in the ex vivo human placenta perfusion model: key sources of artifacts," *Sci. Technol. Adv. Mater. Sci. Technol. Adv. Mater.*, vol. 16, 16, no. 4, 4, pp. 044602–044602, Aug. 2015, doi: 10.1088/1468-6996/16/4/044602, 10.1088/1468-6996/16/4/044602.

[78] S. Shahabi, L. Treccani, and K. Rezwan, "A comparative study of three different synthesis routes for hydrophilic fluorophore-doped silica nanoparticles," *J. Nanoparticle Res.*, vol. 18, no. 1, p. 28, Jan. 2016, doi: 10.1007/s11051-016-3334-0.

[79] "SmartNanoTox | Smart Tools for Gauging Nano Hazards." http://www.smartnanotox.eu/ (accessed Jul. 09, 2021).

[80] "LA-4 | ATCC." https://www.atcc.org/products/ccl-196 (accessed Jun. 30, 2021).

[81] G. D. Stoner, Y. Kikkawa, A. J. Kniazeff, K. Miyai, and R. M. Wagner, "Clonal Isolation of Epithelial Cells from Mouse Lung Adenoma," *Cancer Res.*, vol. 35, no. 8, pp. 2177–2185, Aug. 1975.

[82] G. D. Stoner, M. Hallman, and M. C. Troxell, "Lecithin biosynthesis in a clonal line of lung adenoma cells with type II alveolar cell properties," *Exp. Mol. Pathol.*, vol. 29, no. 1, pp. 102–114, Aug. 1978, doi: 10.1016/0014-4800(78)90030-8.

[83] "MH-S | ATCC." https://www.atcc.org/products/crl-2019 (accessed Jun. 30, 2021).

[84] I. N. Mbawuike and H. B. Herscowitz, "MH-S, a Murine Alveolar Macrophage Cell Line: Morphological, Cytochemical, and Functional Characteristics," *J. Leukoc. Biol.*, vol. 46, no. 2, pp. 119–127, 1989, doi: https://doi.org/10.1002/jlb.46.2.119.

[85] S. Berg *et al.*, "ilastik: interactive machine learning for (bio)image analysis," *Nat. Methods*, vol. 16, no. 12, pp. 1226–1232, Dec. 2019, doi: 10.1038/s41592-019-0582-9.

[86] J. A. Bourdon *et al.*, "Carbon black nanoparticle instillation induces sustained inflammation and genotoxicity in mouse lung and liver," *Part. Fibre Toxicol.*, vol. 9, no. 1, p. 5, Feb. 2012, doi: 10.1186/1743-8977-9-5.

[87] K. Rasmussen *et al.*, "Multi-walled Carbon Nanotubes, NM-400, NM-401, NM-402, NM-403: Characterisation and Physico-Chemical Properties," Publications Office of the European Union, EUR - Scientific and Technical Research Reports, 2014. doi: 10.2788/10753.

[88] K. Rasmussen *et al.*, "Synthetic Amorphous Silicon Dioxide (NM-200, NM-201, NM-202, NM-203, NM-204): Characterisation and Physico-Chemical Properties," Publications Office of the European Union, EUR - Scientific and Technical Research Reports, 2013. doi: 10.2788/57989.

[89] K. Rasmussen *et al.*, "Titanium Dioxide, NM-100, NM-101, NM-102, NM-103, NM-104, NM-105: Characterisation and Physico-Chemical Properties," Publications Office of the European Union, EUR - Scientific and Technical Research Reports, 2014. doi: 10.2788/79554.

[90] C. Singh *et al.*, "NM-Series of Representative Manufactured Nanomaterials - Zinc Oxide NM-110, NM-111, NM-112, NM-113: Characterisation and Test Item Preparation," Publications Office of the European Union, EUR - Scientific and Technical Research Reports, 2011. doi: 10.2787/55008.

[91] M. Leroux *et al.*, "Optimized operating procedure of an innovative aerosol-cell exposure system applied to semi-adherent cells pre-coated with lung surfactant for RNA extraction preceding transcriptomic assay.," *Prep.*, 2022.

[92] J. Knust, M. Ochs, H. J. G. Gundersen, and J. R. Nyengaard, "Stereological Estimates of Alveolar Number and Size and Capillary Length and Surface Area in Mice Lungs," *Anat. Rec.*, vol. 292, no. 1, pp. 113–122, 2009, doi: 10.1002/ar.20747.

[93] J. E. Phillips, "Inhaled efficacious dose translation from rodent to human: A retrospective analysis of clinical standards for respiratory diseases," *Pharmacol. Ther.*, vol. 178, pp. 141–147, Oct. 2017, doi: 10.1016/j.pharmthera.2017.04.003.

[94] H. Kokot *et al.*, "Prediction of Chronic Inflammation for Inhaled Particles: the Impact of Material Cycling and Quarantining in the Lung Epithelium," *Adv. Mater.*, vol. 32, no. 47, p. 2003913, 2020, doi: https://doi.org/10.1002/adma.202003913.

[95] J. Möller, T. Lühmann, M. Chabria, H. Hall, and V. Vogel, "Macrophages lift off surface-bound bacteria using a filopodium-lamellipodium hook-and-shovel mechanism," *Sci. Rep.*, vol. 3, no. 1, pp. 1–8, Oct. 2013, doi: 10.1038/srep02884.

[96] R. A. Saxton and D. M. Sabatini, "mTOR Signaling in Growth, Metabolism, and Disease," *Cell*, vol. 168, no. 6, pp. 960–976, Mar. 2017, doi: 10.1016/j.cell.2017.02.004.

[97] I. Ben-Sahra and B. D. Manning, "mTORC1 signaling and the metabolic control of cell growth," *Curr. Opin. Cell Biol.*, vol. 45, pp. 72–82, Apr. 2017, doi: 10.1016/j.ceb.2017.02.012.

[98] S. Chen *et al.*, "No involvement of alveolar macrophages in the initiation of carbon nanoparticle induced acute lung inflammation in mice," *Particle and fibre toxicology*, Jun. 21, 2016. https://pubmed.ncbi.nlm.nih.gov/27328634/ (accessed Aug. 20, 2020).

[99] B. L. Baisch *et al.*, "Equivalent titanium dioxide nanoparticle deposition by intratracheal instillation and whole body inhalation: the effect of dose rate on acute respiratory tract inflammation," *Part. Fibre Toxicol.*, vol. 11, p. 5, Jan. 2014, doi: 10.1186/1743-8977-11-5.

[100] K. M. Adlerz, H. Aranda-Espinoza, and H. N. Hayenga, "Substrate elasticity regulates the behavior of human monocyte-derived macrophages," *Eur. Biophys. J.*, vol. 45, no. 4, pp. 301–309, May 2016, doi: 10.1007/s00249-015-1096-8.

[101] B. D. Thrall *et al.*, "Modulation of susceptibility to lung bacterial infection by engineered nanomaterials: In vitro and in vivo correspondence based on macrophage phagocytic

function," *NanoImpact*, vol. 14, Feb. 2019, doi: https://doi.org/10.1016/j.impact.2019.100155.

[102] J. Xu *et al.*, "Nanoparticles retard immune cells recruitment in vivo by inhibiting chemokine expression," *Biomaterials*, vol. 265, p. 120392, Jan. 2021, doi: 10.1016/j.biomaterials.2020.120392.

[103] J. C. Villegas, L. Álvarez-Montes, L. Rodríguez-Fernández, J. González, R. Valiente, and M. L. Fanarraga, "Multiwalled Carbon Nanotubes Hinder Microglia Function Interfering with Cell Migration and Phagocytosis," *Adv. Healthc. Mater.*, vol. 3, no. 3, pp. 424–432, 2014, doi: https://doi.org/10.1002/adhm.201300178.

[104] S. Watanabe and E. Boucrot, "Fast and ultrafast endocytosis," *Curr. Opin. Cell Biol.*, vol. 47, pp. 64–71, Aug. 2017, doi: 10.1016/j.ceb.2017.02.013.

[105] Y. Guo, E. Terazzi, R. Seemann, J. B. Fleury, and V. A. Baulin, "Direct proof of spontaneous translocation of lipid-covered hydrophobic nanoparticles through a phospholipid bilayer," *Sci. Adv.*, vol. 2, no. 11, p. e1600261, Nov. 2016, doi: 10.1126/sciadv.1600261.

[106] C.-F. Su, H. Merlitz, H. Rabbel, and J.-U. Sommer, "Nanoparticles of Various Degrees of Hydrophobicity Interacting with Lipid Membranes," *J. Phys. Chem. Lett.*, vol. 8, no. 17, pp. 4069–4076, Sep. 2017, doi: 10.1021/acs.jpclett.7b01888.

[107] J. Lin and A. Alexander-Katz, "Cell Membranes Open 'Doors' for Cationic Nanoparticles/Biomolecules: Insights into Uptake Kinetics," *ACS Nano*, vol. 7, no. 12, pp. 10799–10808, Dec. 2013, doi: 10.1021/nn4040553.

[108] J. J. Rennick, A. P. R. Johnston, and R. G. Parton, "Key principles and methods for studying the endocytosis of biological and nanoparticle therapeutics," *Nat. Nanotechnol.*, vol. 16, no. 3, pp. 266–276, Mar. 2021, doi: 10.1038/s41565-021-00858-8.

[109] J. A. Daniel *et al.*, "Phenothiazine-Derived Antipsychotic Drugs Inhibit Dynamin and Clathrin-Mediated Endocytosis," *Traffic*, vol. 16, no. 6, pp. 635–654, 2015, doi: 10.1111/tra.12272.

[110] T. Vajs, "Methodology development to study the correlation between mitochondrial activation and assembly of bio-nano composites in lung epithelial cells exposed to nanomaterials.," University of Maribor, Maribor, 2021.

[111] C. Strobel, H. Oehring, R. Herrmann, M. Förster, A. Reller, and I. Hilger, "Fate of cerium dioxide nanoparticles in endothelial cells: exocytosis," *J. Nanoparticle Res.*, vol. 17, no. 5, 2015, doi: 10.1007/s11051-015-3007-4.

[112] M. Orecna *et al.*, "Toxicity of carboxylated carbon nanotubes in endothelial cells is attenuated by stimulation of the autophagic flux with the release of nanomaterial in autophagic vesicles," *Nanomedicine Nanotechnol. Biol. Med.*, vol. 10, no. 5, pp. e939–e948, Jul. 2014, doi: 10.1016/j.nano.2014.02.001.

[113] C. S. Kim *et al.*, "The role of surface functionality in nanoparticle exocytosis," *Adv. Healthc. Mater.*, vol. 3, no. 8, pp. 1200–1202, Aug. 2014, doi: 10.1002/adhm.201400001.

[114] N. Oh and J.-H. Park, "Endocytosis and exocytosis of nanoparticles in mammalian cells," *International Journal of Nanomedicine*, May 06, 2014. https://www.dovepress.com/endocytosis-and-exocytosis-of-nanoparticles-in-mammalian-cells-peer-reviewed-fulltext-article-IJN (accessed Jan. 25, 2021).

[115] R. Sakhtianchi, R. F. Minchin, K.-B. Lee, A. M. Alkilany, V. Serpooshan, and M. Mahmoudi, "Exocytosis of nanoparticles from cells: Role in cellular retention and toxicity," *Adv. Colloid Interface Sci.*, vol. 201–202, pp. 18–29, Dec. 2013, doi: 10.1016/j.cis.2013.10.013.

[116] U. R. Dahiya and M. Ganguli, "Exocytosis - a putative road-block in nanoparticle and nanocomplex mediated gene delivery," *J. Controlled Release*, vol. 303, pp. 67–76, Jun. 2019, doi: 10.1016/j.jconrel.2019.04.012.

[117] J. N. Meyer, T. C. Leuthner, and A. L. Luz, "Mitochondrial fusion, fission, and mitochondrial toxicity," *Toxicology*, vol. 391, pp. 42–53, Nov. 2017, doi: 10.1016/j.tox.2017.07.019.

[118] T. Wai and T. Langer, "Mitochondrial Dynamics and Metabolic Regulation," *Trends Endocrinol. Metab.*, vol. 27, no. 2, pp. 105–117, Feb. 2016, doi: 10.1016/j.tem.2015.12.001.

[119] F. Colombo *et al.*, "Polarized cells display asymmetric release of extracellular vesicles," *Traffic*, vol. 22, no. 4, pp. 98–110, 2021, doi: 10.1111/tra.12775.

[120] A. W. Chow, J. F. Liang, J. S. Wong, Y. Fu, N. L. Tang, and W. Ko, "Polarized Secretion of Interleukin (IL)-6 and IL-8 by Human Airway Epithelia 16HBE14o- Cells in Response to Cationic Polypeptide Challenge," *PLoS ONE*, vol. 5, no. 8, p. e12091, Aug. 2010, doi: 10.1371/journal.pone.0012091.

[121] D. L. Laskin, R. Malaviya, and J. D. Laskin, *Comparative Biology of the Normal Lung*, 2nd Edition. San Diego, CA, USA: Academic Press, 2015. Accessed: Jun. 30, 2021. [Online]. Available: https://www.elsevier.com/books/comparative-biology-of-the-normal-lung/parent/978-0-12-404577-4

[122] P. F. Bove *et al.*, "Breaking the In Vitro Alveolar Type II Cell Proliferation Barrier while Retaining Ion Transport Properties," *Am. J. Respir. Cell Mol. Biol.*, vol. 50, no. 4, pp. 767–776, Apr. 2014, doi: 10.1165/rcmb.2013-0071OC.

[123] S.-W. Bian, I. A. Mudunkotuwa, T. Rupasinghe, and V. H. Grassian, "Aggregation and Dissolution of 4 nm ZnO Nanoparticles in Aqueous Environments: Influence of pH, Ionic Strength, Size, and Adsorption of Humic Acid," *Langmuir*, vol. 27, no. 10, pp. 6059–6068, May 2011, doi: 10.1021/la200570n.

[124] Y. Yan *et al.*, "Particles on the Move: Intracellular Trafficking and Asymmetric Mitotic Partitioning of Nanoporous Polymer Particles," *ACS Nano*, vol. 7, no. 6, pp. 5558–5567, Jun. 2013, doi: 10.1021/nn401800u.

[125] Z. Liu *et al.*, "Mapping metabolic changes by noninvasive, multiparametric, high-resolution imaging using endogenous contrast," *Sci. Adv.*, vol. 4, no. 3, p. eaap9302, doi: 10.1126/sciadv.aap9302.

[126] P. Winckler, A. Cailler, R. Deturche, P. Jeannesson, H. Morjani, and R. Jaffiol, "Microfluidity mapping using fluorescence correlation spectroscopy: A new way to investigate plasma membrane microorganization of living cells," *Biochim. Biophys. Acta BBA - Biomembr.*, vol. 1818, no. 11, pp. 2477–2485, Nov. 2012, doi: 10.1016/j.bbamem.2012.05.018.

[127] I. Urbančič, A. Ljubetič, Z. Arsov, and J. Štrancar, "Coexistence of Probe Conformations in Lipid Phases—A Polarized Fluorescence Microspectroscopy Study," *Biophys. J.*, vol. 105, no. 4, pp. 919–927, Aug. 2013, doi: 10.1016/j.bpj.2013.07.005.

[128] I. E. Steinmark *et al.*, "Targeted fluorescence lifetime probes reveal responsive organelle viscosity and membrane fluidity," *PLOS ONE*, vol. 14, no. 2, p. e0211165, Feb. 2019, doi: 10.1371/journal.pone.0211165.

[129] I. Gosens *et al.*, "Comparative Hazard Identification by a Single Dose Lung Exposure of Zinc Oxide and Silver Nanomaterials in Mice," *PLOS ONE*, vol. 10, no. 5, p. e0126934, May 2015, doi: 10.1371/journal.pone.0126934.

[130] L. Rahman, D. Wu, M. Johnston, A. William, and S. Halappanavar, "Toxicogenomics analysis of mouse lung responses following exposure to titanium dioxide nanomaterials reveal their disease potential at high doses," *Mutagenesis*, vol. 32, no. 1, pp. 59–76, Jan. 2017, doi: 10.1093/mutage/gew048.

[131] R. W. Bally and T. C. J. Gribnau, "Some Aspects of the Chromogen 3,3´,5,5´-Tetramethylbenzidine as Hydrogen Donor in a Horseradish Peroxidase Assay," vol. 27, no. 10, pp. 791–796, Jan. 1989, doi: 10.1515/cclm.1989.27.10.791.

[132] R. F. Henderson, “Use of bronchoalveolar lavage to detect respiratory tract toxicity of inhaled material,” *Exp. Toxicol. Pathol.*, vol. 57, pp. 155–159, Jul. 2005, doi: 10.1016/j.etp.2005.05.004.

[133] Y. Cao *et al.*, “Vascular Effects of Multiwalled Carbon Nanotubes in Dyslipidemic ApoE−/− Mice and Cultured Endothelial Cells,” *Toxicol. Sci.*, vol. 138, no. 1, pp. 104–116, Mar. 2014, doi: 10.1093/toxsci/kft328.

[134] R. M. & R. Philips, “» How fast do cells move?” http://book.bionumbers.org/how-fast-do-cells-move/ (accessed Aug. 13, 2020).

[135] D. L. Laskin, R. Malaviya, and J. D. Laskin, “Chapter 32 - Pulmonary Macrophages,” in *Comparative Biology of the Normal Lung (Second Edition)*, R. A. Parent, Ed. San Diego: Academic Press, 2015, pp. 629–649. doi: 10.1016/B978-0-12-404577-4.00032-1.

Bibliography

Publications Related to the Thesis

Journal Articles

B. Kokot*, **H. Kokot***, P. Umek, K. P. van Midden, S. Pajk, M. Garvas, C. Eggeling, T. Koklič, I. Urbančič, and J. Štrancar, "How to control fluorescent labeling of metal oxide nanoparticles for artefact-free live cell microscopy," Nanotoxicology, vol. 15, no. 8, pp. 1102–1123, Oct. 2021, doi: 10.1080/17435390.2021.1973607.

H. Kokot*, B. Kokot*, A. Sebastijanović*, C. Voss, R. Podlipec, P. Zawilska, T. Berthing, C. Ballester-López, P. Høgh Danielsen, C. Contini, M. Ivanov, A. Krišelj, P. Čotar, Q. Zhou, J. Ponti, V. Zhernovkov, M. Schneemilch, Z. Doumandji, M. Pušnik, P. Umek, S. Pajk, O. Joubert, O. Schmid, I. Urbančič, M. Irmler, J. Beckers, V. Lobaskin, S. Halappanavar, N. Quirke, A. P. Lyubartsev, U. Vogel, T. Koklič, T. Stoeger, and J. Štrancar, "Prediction of Chronic Inflammation for Inhaled Particles: the Impact of Material Cycling and Quarantining in the Lung Epithelium," Adv. Mater., vol. 32, no. 47, p. 2003913, 2020, doi: https://doi.org/10.1002/adma.202003913.

I. Urbančič, M. Garvas, B. Kokot, **H. Majaron**, P. Umek, H. Cassidy, M. Škarabot, F. Schneider, S. Galiani, Z. Arsov, T. Koklic, D. Matallanas, M. Čeh, I. Muševič, C. Eggeling, and J. Štrancar, "Nanoparticles Can Wrap Epithelial Cell Membranes and Relocate Them Across the Epithelial Cell Layer," Nano Lett., vol. 18, no. 8, pp. 5294–5305, Aug. 2018, doi: 10.1021/acs.nanolett.8b02291.

Other Publications

Journal Articles

S. Pajk, **H. Kokot**, M. Novak, B. Kokot, and J. Štrancar, "New coumarin- and phenoxazine-based fluorescent probes for live-cell STED nanoscopy," Eur. Biophys. J., vol. 48, no. 5, pp. 485–490, Jul. 2019, doi: 10.1007/s00249-019-01354-7.

Conference Papers

S. Pajk, **H. Kokot**, B. Kokot, A. Pišlar, H. Esih, A. Gabrič, D. Urbančič, I. Urbančič, J. Štrancar, "Development of coumarin-based membrane probes for live-cell STED nanoscopy", vol. 11, suppl. s1, p. 26. Symposia on 45th FEBS Congress, Molecules of Life: Towards New Horizons, July 2021, Ljubljana, Slovenia. doi: 10.1002/2211-5463.13206.

R. Podlipec, N. Klinger, R. Heller, **H. Kokot**, P. Pelicon, J. Štrancar, J. von Borany, "Correlative microscopy of lung epithelial in vitro model exposed to nanoparticles by

using super-resolution optical and advanced ion/electron based techniques", in Conference on Multimodality Imaging in Life Sciences 2019, p. 13, November 2019, Vienna, Austria.

Zorec, Š. Zupančič, S. Pajk, **H. Kokot**, J. Štrancar, R. Dreu, "Preparation and characterisation of simvastatin matrix and core-shell particles by electrospraying", in Abstractbook, p. 42. 13th PSSRC Annual Meeting, Düsseldorf, Germany, 2019.

H. Kokot, B. Kokot, T. Koklič, M. Pušnik, A. Sebastijanović, J. Štrancar, "3D STED microscopy reveals that cell membranes can deactivate nanomaterial by forming bio-nano agglomerates" in European biophysics journal vol. 38, suppl. 1, p. s209. Joint 12th EBSA Congress and 10th ICBP-IUPAP Congress, July 2019, Madrid, Spain.

B. Kokot, **H. Kokot**, J. Štrancar, "In vitro nanoparticle tracking in live LA-4 epithelial cells using superresolution one-photon and two-photon excitation STED microscopy" in European biophysics journal vol. 38, suppl. 1, p. s203. Joint 12th EBSA Congress and 10th ICBP-IUPAP Congress, July 2019, Madrid, Spain.

J. Mirtič, K. N. Grilc, **H. Kokot**, S. Pajk, J. Štrancar, J. Kristl, "Following the layer-by-layer polyelectrolyte coating of bacterial cells using STED microscopy" in: Book of abstracts, p. 356. 32nd Conference of The European Colloid and Interface Society, September 2018, Ljubljana, Slovenia.

H. Kokot, B. Kokot, T. Koklič, J. Štrancar, "A relevant in vitro model of the alveolus enables reliable studies of nanomaterial-cell interactions" in Book of abstracts, p.54. 8th Regional Biophysics Conference, May 2018, Zreče, Slovenia.

B. Kokot, **H. Kokot**, J. Štrancar, "Uncontrolled nanoparticle-labeling lead to misinterpreted STED images of exposure studies" in Book of abstracts p. 159. 8th Regional Biophysics Conference, May 2018, Zreče, Slovenia.

S. Pajk, M. Novak, **H. Kokot**, B. Kokot, J. Štrancar, "New fluorescent probes for superresolution stimulated emission depletion microscopy based on 4-cyanocoumarin and nile blue fluorophores" in Book of abstracts p. 119. 8th Regional Biophysics Conference, May 2018, Zreče, Slovenia.

M. Garvas, T. Koklič, P. Umek, **H. Kokot**, R. Podlipec, J. Štrancar, "Europium doped anatase TiO_2 nanoparticles for NP localization in vitro in living cells and ex vivo tissues", in Book of abstracts. 8th Regional Biophysics Conference, May 2018, Zreče, Slovenia.

H. Kokot, B. Kokot, I. Urbančič, P. Umek, T. Koklič, M. Garvas, J. Štrancar, "Fluorescent labelling of nanoparticles for reliable bio-nano interactions study", in European biophysics journal. 2017, vol. 46, suppl. 1, p. 189. Presented at 19th IUPAB and 11th EBSA Congress, July, 2017, Edinburgh, Scotland.

H. Kokot, I. Urbančič, M. Zadnik, Z. Arsov, R. Podlipec, J. Štrancar, "Towards molecular conformational imaging in non-spherical vesicles" in European Conferences on Biomedical Optics (ECBO) p.39. June 2017, Munich, Germany.

H. Kokot, L. Cmok, M. Vilfan, D. Lisjak, A. Mertelj, "Particle diffusion in ferromagnetic liquid crystals" in Liquids 2017: book of abstracts: posters p. 3045. 2017, Ljubljana.

M. Vilfan, **H. Kokot**, D. Lisjak, A. Mertelj, "Measurements of diffusion in anisotropic fluids", in Book of abstracts p. 26. Flowing matter, January 2016, Porto, Portugal.

H. Kokot, M. Vilfan, D. Lisjak, A. Mertelj, "Opazovanje difuzije v feromagnetnih tekočih kristalih", in Zbornik povzetkov, 10. konferenca fizikov v osnovnih raziskavah, p. 57, Otočec, November 2016, str. 57

H. Kokot, M. Vilfan, D. Lisjak, A. Mertelj, "Observation of diffusion in ferromagnetic liquid crystals", in 26th International Liquid Crystal Conference, ILCC 2016, July 31 - August 5, 2016, Kent, OH, USA.

Preprints

I. Rybkin J. Mirtič, **H. Kokot**, Jitka Hreščak, Miran Čeh, Janez Štrancar, Julijana Kristl, Tomaž Rijavec, Aleš Lapanje, "Strain-dependent selective antimicrobial action of cationic polyelectrolytes on Gram-negative bacteria," bioRxiv, 2021. doi: 10.1101/2021.04.19.440400.

Master's Thesis

H. Kokot, "Anizotropna difuzija kroglic v feromagnetnem tekočem kristalu", Faculty of Mathematics and Physics, University of Ljubljana, 2016.

Co-mentor for Master's Theses

N. Mraz, "Suitability of selected fluorescent probes for long-term live-cell imaging", Faculty of Pharmacy, University of Ljubljana, 2021.

T. Vajs, "Methodology development to study the correlation between mitochondrial activation and assembly of bionano-composites in lung epithelial cells exposed to nanomaterials", Faculty of Natural sciences and Mathematics, University of Maribor, 2022.

Editor

H. Kokot, P. Čotar, M. Koren, N. Golmajer Zima., "Book of abstracts. 8th Regional Biophysics Conference, 16th to 20th May, 2018, Zreče, Slovenia." Slovenian Biophysical Society, Ljubljana 2018.

Biography

Hana Kokot (née Majaron), M.Sc.Phys., is a PhD student of Nanosciences and Nanotechnologies at the Jožef Stefan International Postgraduate School, Slovenia, and is currently performing research in the field of Predictive Nanotoxicology in the Laboratory of Biophysics at the Jožef Stefan Institute, Slovenia.

Her work is tightly connected to the H2020 SmartNanoTox project and focuses on predicting nanoparticle-induced adverse outcomes by pinpointing the key events in the interactions of nanoparticles and cells, understanding how they lead to diseases, and ultimately devising models and simple tests to predict them.

Education

10/2017 – present **PhD study of Nanosciences and Nanotechnologies**
Jožef Stefan International Postgraduate School, Ljubljana, Slovenia

- Advanced courses in nanobiophysics, experimental methods in biophysics, microscopies and microanalytical methods and science communication.

10/2013 – 5/2016 **Master of Science in Physics (M.Sc.Phys.)**
Faculty of Mathematics and Physics, University of Ljubljana, Slovenia

- Advanced courses in physics, computational physics, optics, photonics, and a basic course in human physiology.

10/2010 – 9/2013 **Bachelor of Science in Physics**
Faculty of Mathematics and Physics, University of Ljubljana, Slovenia

- Basic courses in physics, mathematics, programming, chemistry and mathematical physics.

Summer schools and workshops

- EBSA 2019 Summer Biophysics School – Biophysics in the 21st Century. El Escorial, Spain, July 17th – 19th 2019.
- Project meeting and training school within H2020 project SmartNanoTox. Bohinj, Slovenia, March 19th – 23rd 2018.
- Exploring the molecular world by advanced fluorescence microscopy approaches. Ljubljana, Slovenia, September 12th – 15th 2017.
- Project meeting and training school within H2020 project SmartNanoTox. Edzell, Scotland, September 24th – 26th 2016.

Research

5/2016 – present **Professional associate / PhD student**
Laboratory of Biophysics, Jožef Stefan Institute, Ljubljana, Slovenia

- Experimental work on the interaction between nanoparticles and cells or model biological systems connected to the H2020 SmartNanoTox project.
- Experimental work using various experimental methods, including microscopies, spectroscopies and nanoscopies (STED).
- Programming and advanced image analysis.

5/2015 – 5/2016 **Master student**
Department of Complex Matter, Jožef Stefan Institute, Ljubljana, Slovenia

- Experimental work on the characterization of anomalous diffusion in ferromagnetic liquid crystals and its dependence on the external magnetic field.
- Development of correlative analysis.

Conferences

Oral lectures

- Project meeting within H2020 project SmartNanoTox. Nancy, France, March 19th – 22nd 2019.
- 8th Regional Biophysics Conference - RBC 2018. Zreče, Slovenia, May 16th – 20th 2018.
- Project meeting and training school within H2020 project SmartNanoTox. Bohinj, Slovenia, March 19th – 23rd 2018.

Other

- SmartNanoTox International Online Conference. Online, 24th June 2020.
- 12th EBSA, 10th ICBP-IUPAP Biophysics Congress. Madrid, Spain, July 20th – 24th 2019 (poster).
- 4th Days of Biophysics. Rogla, Slovenia, October 23rd – 24th 2017 (poster).
- 19th IUPAB congress and 11th EBSA congress. Edinburgh, Scotland, July 16th – 20th 2017 (poster).
- Project meeting and training school within H2020 project SmartNanoTox. Edzell, Scotland, September 24th – 26th 2016.